UNIVERSITAT DE BARCELONA

Study of the effects of mechanical force on nucleo-cytoplasmic transport

Ignasi Granero Moya

Study of the effects of mechanical force on nucleo-cytoplasmic transport

UNIVERSITAT DE BARCELONA

Memòria de tesi doctoral presentada per n'Ignasi Granero Moya per optar al grau de Doctor en Biomedicina per la Universitat de Barcelona

Barcelona, setembre del 2022.

Realitzada a l'Institut de Bioenginyeria de Catalunya

IBEC
Institute for Bioengineering of Catalonia

Dirigida pels Dr. Pere Roca-Cusachs Soulere i Dr. Ion Andreu Arzuaga

Tutoritzada per en Dr. Pere Roca-Cusachs Soulere

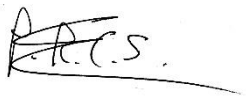

Agraïments

First, I would like to thank Dr. Daniel Navajas, Dr. Miki Ebisuya, Dr. Javier Fernández Martínez, Dr. Mª Isabel Geli and Dr. Raimon Sunyer, for accepting to evaluate my work to obtain the title of *Doctor en Biomedicina per la Universitat de Barcelona*.

I would like to thank Dr Anna Labernadie and Dr Verena Ruprecht for being part of my Thesis Advisory Committe and giving us a valuable external view on my PhD thesis.

Gràcies Pere per haver-me acceptat com a candidat per a fer el doctorat al laboratori i per dirigir amb entusiasme aquesta tesi. Però sobretot, gràcies per fer-nos col·laborar entre tots nosaltres que és essencial en aquesta tasca de recerca que fem. En particular, gràcies per fer-nos treballar en equip al Nuclear Pore Team que per a mi és molt important, tan científicament com personal. Gràcies també per escollir tan bona gent amb la que he pogut treballar cada dia.

Eskerrik asko Ion, por hacer tan fácil el trabajar contigo. Por supervisar mi trabajo desde 2017 hasta esta tesis doctoral. Por tratarme como a un igual desde el inicio y por tener en cuenta mis opiniones científicas, sobre todo teniendo en cuenta que la diferencia de experiencia era evidente. Gracias por los ratos en las salas de microscopios especulando sobre lo que estábamos viendo en los resultados y por esa curiosidad insaciable. Gracias por insistir y por convencerme de que me apuntara al Medi, aunque nade como un waterpolista, nadar ha sido un puntal para mi salud mental y física estos años.

Gràcies Marc per fer aquest camí amb mi colze a colze. Pel suport material, fent gels i el millor PBS de tots i passant les cèl·lules quan eren comunes; pel suport digital, corregint-me la meva tendència escriure correus passiu-agressius i textos de tota mena; i pel suport emocional, fent la conya un divendres a la tarda, o compartint memes i fent stickers per a riure una bona estona. Espero haver sigut com a mínim la meitat de bon company amb tu, com tu ho has estat amb mi.

Grazas Miguel por unirte al equipo a mitad de camino como si nada, como si hubieras estado ahí desde el inicio. Es una suerte tenerte de compañero. Gracias por todo el apoyo, desde pasar células a revisar esta tesis. Gracias por estar siempre dándole vueltas a los resultados y estar dispuesto a que te dé la chapa (sin avisar) con resultados recién salidos del horno. Te deseo lo mejor para tu doctorado, y por la parte que me toca, trabajaré para que así sea.

Als tots tres del Nuclear Pore Team, gràcies per treballar en equip i fer tant fàcil tot.

Gràcies Susana, Anghara, Natàlia, Oriol i Mònica, i a la gent de Core Facilities per fer una feina essencial, i sovint massa poc reconeguda, per a que puguem fer experiments sense haver de preocupar-nos més enllà que dels nostres resultats. Especialment, gràcies a tu Susana, per ajudar-nos tant i anar sempre un pas per davant nostre.

Thanks to our collaborators in Verena Ruprecht's lab for hosting me so well. And our collaborators in Jacco van Rheenen's lab, especially Guillaume for creating the cells lines that are an amazing tool for these studies.

Gràcies Xarxa i Víctor per acollir-me al lab quan vaig arribar i per crear molt bon ambient a la Peixera (o Sala González-Tarragó) i per aconsellar-me des de la vostra experiència. Abans des de dins del lab i ara des de fora.

Gràcies Juanfra i Leone, per ajudar-me i aconsellar-me tant, i per ser científics tant íntegres. És una sort conèixer-vos, i a més, haver compartit laboratori amb vosaltres. He après moltíssim escoltant-vos (crec no us en podeu fer càrrec de quant) i no dubto que seguirà sent així d'ara endavant.

Thanks Nimesh, for your help and for being so enthusiastic with so many interesting things, also for gathering us all around a table in a bar or around a bag of chips in the best park of Barcelona, ...tothom sap que és el Parc Industrial.

Gràcies Gerardo per les bromes i l'alegria que ens aportes cada dia al laboratori. Per estar obert a respondre qualsevol pregunta que em pugui venir al cap i per ajudar-me i aconsellar-me en mil coses. Ja saps que seguiré preguntant-te perquè m'és igual que sovint no tinguis raó en les discussions.

Thanks Amy, for being always so helpful and nice. Thanks for reviewing this thesis and for all the interesting questions you ask, and the new insights you give me when I present new data.

Merci Laura pour tes conseils pendant tout ce temps-là au labo et pour m'emmener à danser salsa et faire les jours au labo plus joyeux. Si on n'avait pas souffert une pandémie, peut-être on serait des danseurs professionnels.

Thanks Alice, for being a lovely desktop neighbor, for enthusiastically taking over our spot in the PhD Committee and for always remembering about my political limitations in food consumption.

Thanks Zarina, for visiting us very often in la Peixera to have a chat and for being such a nice person with me.

Gràcies Ona i Aina per ser tan bones companyes i per les discussions tant interessants sobre mecànica del nucli. És una sort poder debatre idees amb vosaltres. Espero que gaudiu tant del doctorat com ho he fet jo.

Dank je wel Bart for pushing this project forward these last months. Working with you has helped me to correct things and rethinks many details in Chapter 2. Without your collaboration there would not be so many results in the second part of this work. Be sure that they are also yours.

Gràcies Xavi per tenir un grup farcit de bona gent, als que considero tan companys com la gent del grup del Pere.

Gràcies a tota la gent del laboratori PRC-XT per sumar al bon ambient que regna en un grup tant gran. Thanks to all the people of the PRC-XT lab for creating such a good and helpful work environment. I think it was a great decision to do a PhD thesis in this lab, I have enjoyed it a lot both personally and scientifically.
Thanks to all of you, Sri, Miquel, Jenny, Sefora, Macià, Ariadna, Natxo, Isabela, Carlos, Marija, Thomas, Anna, Jorge, Pau, Elena, Tom, Raimon, Manu, Anabel-Lise, Meng, Mamatha, Kenta, Özge, Clément, Ernest, Marilena, Marina U, Roger, Ali, Dobryna, Marina P, Aurora, Joan.

Gràcies Morena, per estar sempre disposada a escoltar sobre petits grans descobriments i experiments fallits. Per ser la meva revisora externa de confiança i revisar innumerables pòsters, xerrades, tallers, figures, abstracts i, com no, aquesta tesi. Ets una científica excel·lent i tenir el teu punt de vista sobre les coses que faig és un privilegi.

Thanks to the fellows from LCF, for being so nice people and for sharing this trip with me. It has been very helpful to get your support.

Thanks to the PhD Committee people for doing such an important job in making people know each other and socializing inside of IBEC. It fosters collaborations and creates a warmer work environment.

Per la part personal vull agrair el suport incondicional de família i amics. Dels amics i amigues (o família que he tingut la sort d'escollir), a alguns ja us he mencionat perquè sou companys de feina. Però a tots per igual vull agrair-vos el vostre suport i la vostra amistat. Espero haver correspost tota la vostra estima i suport durant aquest període, i seguir fent-ho en el futur. Ja sigui amb un whatsapp preguntant "Com va?" una tarda d'un dimarts aleatori o fent una calçotada un dissabte assolellat.

A la família, vull agrair-vos tot el suport i l'amor que m'heu donat per a poder fer aquesta tesi. Mama, Papa, Marcel, gràcies per tant. Gràcies Iaia Amèlia, Yaya Loli y Yayo Enrique, gràcies per haver-me fet el camí tant fàcil per arribar fins aquí i poder dedicar el meu temps a la ciència. Sé que si pudierais coger y hojear este librito ininteligible estaríais orgullosos de mí.

Finalment, suposo que hauria d'agrair al sistema la meva pertinença a la classe mitjana. Això m'ha donat el privilegi de poder estudiar tranquil·lament sense haver de treballar alhora, el que ha fet que pogués tenir notes suficientment bones. Les quals han fet que aconseguís una beca amb un sou digne que m'ha permès viure decentment Barcelona, i el privilegi de poder dedicar temps a la ciència sense haver de preocupar-me de gaire res més.

Financial support

The project that gave rise to these results received the support of a fellowship from “la Caixa” Foundation (ID 100010434). The fellowship code is LCF/BQ/DR19/11740009.

Abbreviations

AFM	Atomic Force Microscope
ANOVA	Analysis of Variance
ATP	Adenosine triphosphate
BFP	Blue Fluorescent Protein
DAPI	4’,6-diamidino-2-phenylindole
DMEM	Dulbecco's Modified Eagle Medium
DNA	Deoxyribonucleic acid
DN-KASH	Dominant Negative KASH
EGFP	Enhanced Green Fluorescent Protein
EPC	epidermal stem/progenitor cells
ER	Endoplasmic reticulum
FACS	Fluorescent Activated Cell Sorting
FBS	Fetal Bovine Serum
FCS	Fetal Calf Serum
FG	Phenyl-Alanine Glycine
FLIP	Fluorescent Loss In Photobleaching
FRAP	Fluorescent Recovery After Photobleaching
GDP	Guanosine-5'-diphosphate
GFP	Green Fluorescent Protein
GTP	Guanosine-5'-triphosphate
IF	Immuno Fluorescence
INM	Inner Nuclear Membrane
KPNA	Karyopherins alpha general gene code
KPNB	Karyopherin beta gene code
LAD	Lamina Associated Domains
LB	Lamin B
LEM	LAP2-emerin-MAN1
LEXY	light-inducible nuclear export construct
LINC	Linker of Nucleoskeleton and Cytoskeleton
LMNA	Lamin A gene code
LMNB	Lamin Bs gene code
LPD	lipid packing defects
MEF	Mouse Embrionary Fibroblasts
MW	Molecular Weight
NA	Numerical Aperture
N/C ratio	Nuclear-to-Cytoplasmic ratio
NE	Nuclear Envelope
NES	Nuclear Export Signal
NL	Nuclear Lamina
NLS	Nuclear Localization Signal
NPC	Nuclear Pore Complex

NR	Nucleoplasmic Reticulum
NTR	Nuclear Transport Receptor
NUP	Nucleoporin
ONM	Outer nuclear membrane
PBS	Phosphate-Buffered Saline
PCR	Polymerase Chain Reaction
PDMS	Polydimethylsiloxane
PEG	Polyethylene glycol
PM	Plasma membrane
PNS	Perinuclear Space
PTM	Post-Translational Modifications
RAN	RAs-related nuclear protein
RANBP	RAN binding protein
RANGAP	RAN GTPase-activating protein 1
RCC1	Regulator of Chromosome Condensation
RNA	Ribonucleic acid
ROI	Region of interest
RT	Room temperature
RT-qPCR	Quantitative reverse transcription Polymerase Chain Reaction
SEM	Standard Error of the Mean
SV	Simian Virus
TAN	Transmembrane Actin-Associated Nuclear
TF	Transcription Factor
UL	Ultra-low
UV	Ultraviolet
WT	Wild type

Resum de la tesi en llengua catalana

Estudi de l'efecte d eles forces mecàniques al transport nucleocitoplasmàtic

La força mecànica controla processos cel·lulars fonamentals tant en cèl·lules sanes com en malaltes, i cada cop més evidències mostren que el nucli experimenta i sent les forces que se li apliquen. Aquestes forces poden conduir a la translocació nuclear de proteïnes, però encara desconeixem si la força controla el transport nucleocitoplasmàtic i com ho fa. El Capítol 1 d'aquesta tesi mostra que les forces nuclears controlen de manera diferent el transport nucleocitoplasmàtic passiu i el facilitat, establint les regles per a la mecanosensibilitat de les proteïnes de transport. Utilitzant desenes de constructes artificials produïts *ad hoc*, demostrem que la força nuclear augmenta la permeabilitat a través dels complexos de porus nuclears, amb una dependència del pes molecular que és més forta per a la difusió passiva que per a la difusió facilitada. A causa d'aquest efecte diferencial, les forces produeixen la translocació de càrregues a dins o a fora del nucli dins d'un determinat rang de pes molecular i d'afinitat pels receptors de transport nuclear. A més, mostrem que la mecanosensibilitat de diversos reguladors transcripcionals es pot explicar amb aquest mecanisme i dissenyar-se de manera exògena mitjançant la introducció de senyals de localització nuclear adequats. El nostre treball revela un mecanisme de senyalització induïda mecànicament, que probablement funciona en paral·lel amb altres mecanismes, i amb una aplicabilitat potencial a través de les vies de senyalització.

El Capítol 2 d'aquesta tesi aprofundeix en com les forces afecten el transport nucleocitoplasmàtic, mitjançant l'ús de microscòpia confocal avançada per a obtenir imatges en 3D que permeten la segmentació dels nuclis cel·lulars. Utilitzant un dels constructes artificials analitzats en el Capítol 1 i la segmentació nuclear, podem correlacionar els diferents paràmetres de forma del nucli amb la regulació del transport actiu i de YAP com a paradigma de regulador de transcripció mecanosensible. Aquestes dades ens obren la porta a poder cercar més específicament quins són els mecanismes moleculars a nivell de la membrana nuclear que augmenten el transport a través del complex del porus nuclear.

Index of content

Preface

The thesis you are reading now is the outcome of almost five years of work in the Cellular and molecular mechanobiology laboratory at the Institut de Bioenginyeria de Catalunya (IBEC). The reason why I ended up here is because when I was choosing my MSc final project, I came across Alberto Elosegui-Artola and colleagues' article. It was titled "Mechanical regulation of a molecular clutch defines force transmission and transduction in response to matrix rigidity." and I was amazed by the very precise biological and physical measurements. Probably, I was so amazed because of my urge to quantitatively define anything that comes across. My work in the laboratory started in 2017 as a MSc project, and soon I realised I would work towards a PhD thesis in the same subject. From the very beginning, Pere put Ion and me together, in principle, as a simple Postdoc-Predoc supervising relationship. However, the supervision and collaboration with Ion ended up being very fruitful and rewarding professional and personal relationship. Ion is now co-director of this PhD thesis, and we are co-authors of the work that embodies the first chapter of this thesis.

In the present work, I have written an Introduction aimed to cover the basic knowledge to understand the mechanical structure of the nucleus and nucleocytoplasmic transport. And also, how the different components and the transport respond and mechanotransduce when submitted to forces. Then I expose the hypothesis and the aims, and later the results separated in two clear chapters.

Our work included in Chapter 1 studies regulation and mechanisms by which nucleocytoplasmic transport is regulated by forces in the nucleus, studying separately passive and active transport. Alberto Elósegui's work in the laboratory was the starting point for this research (Elosegui-Artola et al., 2017). The work I present here involved several people in the laboratory and a collaboration with Barak Raveh's group and was published in June 2022, with Ion Andreu and me as co-first authors: "Mechanical force application to the nucleus regulates nucleocytoplasmic transport" (Andreu, Granero-Moya, Chahare, et al., 2022). From the work of Chapter 1 we selected and obtained a construct among the many we had produced and tested. This construct is the cornerstone of Chapter 2. And we also produced a Review article commenting on the subject (Andreu, Granero-Moya, Garcia-Manyes, et al., 2022).

The work presented in Chapter 2 started in 2020 and overlapped with the final steps of the work in Chapter 1. The aim of Chapter 2 is to study how the mechanical regulation of nucleocytoplasmic transport applies in multicellular systems, but more specifically to decipher how that happens by analysing nuclear shape parameters. It involves 3D imaging of thousands of cells, computational segmentation of the nuclei, and measurement of nucleocytoplasmic ratios and nuclear shape parameters.

Regarding the appendixes, in Appendix A, there is the information needed to understand the modeling process in Chapter 1. In Appendix B, I included the explanation on how all the constructs for Chapter 1 were produced. And Appendix C includes deeper information of how the data of Chapter 2 are processed.

1. Introduction

The cell nucleus is a membrane-surrounded organelle that contains the cell's genetic material and is home for basic biological functions inside of the cell, such as DNA replication or RNA transcription. All this information we know now, as the reader may expect, could not have been discovered by a single individual during their lifespan, it was rather the slow addition by many people of layers of knowledge one on top of the previous throughout the years, some being refuted, and some not being added to the general knowledge after decades of publication. Here I take the pleasure to make a brief historical introduction on how we have arrived at the current knowledge about the cell nucleus.

The nucleus was the first cell organelle to be discovered, as it was already pointed out in the XVII century by Antonie van Leeuwenhoek works in cod and salmon cells (Leeuwenhoek, 1719). Later, in 1831, Robert Brown was the first person to coin the term *nucleus*, when he noticed it while observing the fertilization process in Orchidaceae and Asclepiadaceae plant families. However, even if the structure had been recognized, its basic functions were not defined yet. As a piece of historical context, it was in 1858 that Rudolf Virchow proposed his theory postulating that all cells come from a previously existing one (*Omnis cellula e cellula*), and in 1861 that Louis Pasteur discarded spontaneous generation with his famous swan-necked bottle experiment. First glimpses on nuclei function included the discovery of mitosis (Hanso, 2016; Mohl, 1837), and the behaviour of chromosome during the process by Fleming in 1879, and the observation of nuclei fusing during fertilization process by Oscar Hertwig, months before, in 1878. In parallel, in 1874, Johann Friedrich Miescher discovered a substance from white blood cells that precipitated with acid conditions and resolubilized with alkaline conditions, he termed it "nuclein". Pushing further this work, in the late years of the 19th century Albrecht Kossel was able to isolate and identify the components of "nuclein", as we know today: adenine, guanine, cytosine, thymine, and uracil. This research gained him a Nobel prize in 1910.

In the early XXth century, Mendelian rules were rediscovered, and Hämmerling experimented in the 1930's and 1940's using a single-cell alga to demonstrate that the nucleus hosts the genetic information in nuclei-containing cells, of note, Eukarya term was not coined yet. This attributed to the nucleus an essential role in cell division and life proliferation. At that time, cell biology also devoted to the study of organelles of the cell and the origin of all of them, for example Wallis proposed a bacterial origin for mitochondria (Wallin, 1925); and biochemistry made the first steps to understand how a cell worked in the inside, for example, Lohmann discovered ATP in 1929 (Langen & Hucho, 2008). After that, during the second half of the 20th century we learned about nuclear role in biochemical regulation of the cell. For example, the discovery of RNA polymerases transcribing genes (Roeder & Rutter, 1969) and protein translation (Crick, 1958).

From a phylogenetic view, in 1990, Carl Woese and colleagues (Woese et al., 1990) proposed the three life domains: Bacteria, Archaea and Eukarya. This last domain, was classified and named after the nucleus, which is one of its defining characteristics (from εὖ, well; and κάρυον, kernel; term coined by Dougherty but in more vague classification) (Dougherty, 1957).

For some time, nucleus was considered as a simple container of the genetic material, just in charge of protecting the DNA during interphase. Later we learned about biochemical regulation functions of the nucleus. And latest, we have started looking for its role in the biophysical regulation of the

cell and nuclear processes; one of the first examples of this would be the demonstration of the connection between integrins-cytoskeleton-nucleoskeleton that stabilized the nucleus (Maniotis et al., 1997).

This work is placed in this last-mentioned field of knowledge, that is known as mechanobiology. Mechanobiology studies how mechanical cues influence biological functions. In this frame, physical characteristics of the nucleus are of utter importance to understand its functions. First, the nucleus is considered the biggest and stiffest organelle in most metazoan cells (Caille et al., 2002; Guilak et al., 2000), and defines its minimal space requirements (Lomakin et al., 2020; McGregor et al., 2016). Also, it is under forces coming from outside the cell (*e.g.*, hydrostatic pressure, shear flow, cell compression) and from inside the cell (cytoskeleton). When a eukaryotic cell senses forces (through any of its mechanisms) it is very likely that the biochemical signalling cascade has one of its ends in the nucleus. In this case, the nucleus exerts a function after receiving the signal but does not sense the triggering effect. Nonetheless, the nucleus can also act as a mechanoSensor and start a biochemical signalling cascade when it is under a mechanical input; as a first example of this, this study demonstrates nuclei stiffening and the importance of the nuclear lamina and emerin (Guilluy et al., 2014).

Even though this organelle is present in the whole Eukarya domain, this work is specifically placed in the field of nuclear mechanobiology in mammalian cells. For that, I will explain the importance of nuclear morphology, introduce nuclear structure, mechanical characteristics, and mechanosensing events happening in it, while the cell is in interphase.

1.1. Nuclear morphology

The nucleus is one of the biggest organelles in the cell, and it is delimited by the NE which makes its identification and visualization easier than other structures. As any deformable body, the shape of the nucleus is directly coupled to the forces applied to it and its mechanical properties. Shape and size of the nucleus are controlled by homeostasis in healthy cells and changes in them can be a signal of forces being applied to the nucleus.

Since the 19th century, nuclear morphology has been a marker for disease, when studies by Lionel S. Beale pointed out morphological abnormalities in malignant cells. Nowadays, excessive nuclear size, morphological irregularities, or abnormal distribution of chromatin are still used as markers for diagnosis in cancer and laminopathies (Alvarado-Kristensson & Rosselló, 2019; Burke & Stewart, 2014; Dey, 2005, 2010; Fischer et al., 2010; Zink et al., 2004).

Most depicted nuclear morphology is of ellipsoid or spherical nature: this is true for many cell types such as fibroblast, lymphocytes, macrophages, splenocytes. However, there are many other cell types that deviate from the nuclear morphology par excellence. We can find lobed nuclei in the granulocyte lineage, from myelocytes to neutrophils, or in monocytes and giant multinucleated macrophages, among others. We can find fusiform nuclei in fibrocytes or smooth muscle. And in sperm we can find a variety of different nuclear morphologies changing from species to species, even inside the mammalian clade.

A good example on how shape affects function are lobed nuclei. We know that lobes in the nuclei help the nucleus to deform, for example, lobes help neutrophils to pass through small gaps (K.

Hoffmann et al., 2007), and granulocytes deficient in lamin B present less lobes and are poorer at passing through small spaces (K. Hoffmann et al., 2002). Also, down-regulation of lamins leads to abnormal nuclei shapes (Lammerding et al., 2004, 2006), therefore, the state of the nuclear lamina is key for nuclear shape. However, lobed shape is not strictly necessary for other migrating cell types such as monocytes or lymphocytes. The answer for this, as explained by Benjamin Skinner and Emma Johnson (Skinner & Johnson, 2017), would lay in the fact that the flexibility of the nucleus in lobed nuclei is achieved in exchange of shortening the lifespan of the cells (Harada et al., 2014), which other longer-lived cell types cannot afford. In the case of T-lymphocytes, which have a longer lifespan, and a spherical and fairly stiff nucleus, they forcefully squeeze the nucleus through the extracellular matrix via myosin-dependent contractions (Jacobelli et al., 2013; Lämmermann et al., 2008). Another type of immune cells, dendritic cells, with high migration capacity, long-term survival and non-lobed nuclei, pass through narrow constrictions and probably disrupt the lamina for that (Thiam et al., 2016).

Regarding volume, we know that different cell types have different nuclear volumes, and that nuclear volume changes during the cell cycle and scales with cellular volume (Finan & Guilak, 2010; M. Guo et al., 2017; Jorgensen et al., 2007; Levy & Heald, 2010; Neumann & Nurse, 2007). The dimensionality of the multicellular structure (Katiyar et al., 2019) and cell shape affect nuclear volume (Roca-Cusachs et al., 2008). Nonetheless, in some cases such as nuclei flattening during fibroblast spreading (Y. Li et al., 2015), nuclei compression by the microenvironment (Lomakin et al., 2020), or migration through narrow pores the nuclear volume stays constant (Davidson et al., 2015; Y. Li et al., 2015), probably due to the resistance of chromatin and other structures (Chan et al., 2017; Mazumder et al., 2008; Tamada et al., 2007) and the osmotic coupling between the cytoplasm and the nucleus (Finan et al., 2009, 2011; Finan & Guilak, 2010).

In the last decades we have started to understand how structure and function are related; nuclear structure can be modified by cell activity and environment, and also how the morphology of the cell affects gene expression and cell responses (Dahl et al., 2008). One of the first evidences that the nucleus receives tension was published in 1992 by Ingber and colleagues (Sims et al., 1992), where they showed that altering actomyosin forces altered cell and nuclear shape. In 1997, they proved that pulling on integrins at the plasma membrane cause nuclear position and shape changes (Maniotis et al., 1997). Forces external to the cell have been shown many times to clearly affect nuclear shape, where F-actin cytoskeleton plays a major role in transmitting force from the plasma membrane to the LINC (Linker of the Nucleoskeleton to the Cytoskeleton) complex (Guilak, 1995; Lammerding et al., 2004, 2006; Lammerding & Lee, 2008; Lombardi et al., 2011; Pajerowski et al., 2007; Poh et al., 2012). Also, the LINC complex, as an essential link in the force transmission chain, is thought to be essential in maintaining nuclear shape and positioning (Fischer-Vize & Mosley, 1994; Lombardi et al., 2011; Lombardi & Lammerding, 2011; Malone et al., 1999; Mosley-Bishop et al., 1999).

We know from studies in mechanobiology that deformation of the cell nucleus due to external geometric constraints and mechanical forces affects chromatin dynamics and gene and pathway activation (Uhler & Shivashankar, 2017). In cells seeded on 2D substrates the highest forces experienced by the LINC complex are at the apical and equatorial plane (Arsenovic et al., 2016). When Nesprin-1 (component of the LINC complex) is depleted, the pulling force arriving to the nucleus is reduced and the nucleus has a more relaxed rounded shape (Chancellory et al., 2010).

Also in 2D substrates, the magnitude of the changes in nuclear shape depend also on the forces exerted by the cytoskeleton, that increase with the stiffness of the substrate (Chancellory et al., 2010; Elosegui-Artola et al., 2017; Lombardi et al., 2011; Lovett et al., 2013; Maniotis et al., 1997). In vivo, nuclear shape changes are seen during processes such as cell cycle (Fidorra et al., 1981; Steen & Lindmo, 1978), embryogenesis (E. R. Smith et al., 2017), migration of the cells out of the intestinal crypt (Tipoe & White, 1998), epithelial to mesenchymal transition (Leggett et al., 2016), or wound healing (Rosińczuk et al., 2016).

To roughly describe nuclear shapes, there are some general determinants in cells that are seeded on 2D substrates: (1) Cell spreading drives nuclear flattening, and actomyosin forces alter nuclear shapes (Takaki et al., 2017), (2) Cell and nuclear 2D aspect ratios are positively correlated (Chen et al., 2015), (3) Nuclei orient with the longest cell axis (Chen et al., 2015).

Interestingly, there are conflicting results with the hypothesis that the nuclear shape is kept via cytoskeletal tension. Results from Tanmay P. Lele and his team question that view. When they excised nuclei from fibroblasts and breast cancer cells using microdissection, leaving them free of the cytoplasm and cytoskeletal structures, the nuclei did not relax to a spherical shape (Tocco et al., 2018). Plus, stress fibres are absent in the apical surface when the nucleus flattens during cell spreading in fibroblasts, and myosin and the LINC complex are dispensable as long as the cell can spread (Y. Li et al., 2015). Several of their articles have proven a causal relationship between the movement of cell boundaries and nuclear deformation and movement (Alam et al., 2015; Y. Li et al., 2015; Tocco et al., 2018). At the timescale of cell motility, the cytoplasm has a viscosity up to 10^6 times of that of water (Berret, 2016; Mofrad & Kamm, 2006), and the tension of the cytoskeleton would slowly dissipate due to binding turnover. That is why Lele and collaborators suggest that the nucleus does not store elastic energy when deformed, and that the nuclear shape is not the outcome of the elasticity of the nucleus versus the tension exerted by the neighbouring stress fibres (Dickinson et al., 2022). They propose that: (1) there is an excess of nuclear lamina surface area, (2) there is a viscous coupling between the nuclear surface and the cell surface involving the cytosol and the cytoskeleton, (3) the excess surface area of the lamina explains the easiness for the nuclei to elongate or flatten from an initial spherical shape until the volume would be reduced or the lamina stretched, (4) the apparent mechanical properties of the nuclei depend on nuclear deformation and the timescale at which they are measured.

1.2. Nuclear components

The nucleus is a differentiated compartment inside of the cell, that has a key role in the functioning of the cell machinery. To understand how forces affect it we need to understand its building components. From the outside to the inside: a double lipidic membrane delimits the nucleus and holds the connections from the cytoskeleton to the nucleoskeleton. The nuclear lamina is the main element of the nucleoskeleton and is placed at the inner side of the envelope and brings shape and mechanical stability to the nucleus. Connecting with the lamina, spread over most of the volume of the nucleus, we can find chromatin, which is the association of DNA with proteins.

As a whole, the components not only form a barrier between the nucleoplasm and the cytoplasm, but also are key components in nuclear structural integrity, molecule transport between the compartments, mechanotransduction, gene expression and can act as signalling platforms and

hubs. However, this barrier is permeable to some extent: the nucleoplasm is not completely isolated from the cytoplasm, since nucleopores located at the double lipidic membrane allow soluble small molecules and water to freely diffuse, and they regulate the passage of bigger soluble molecules. With this information in mind, I proceed to a more detailed description of the nuclear components depicted in Figure 1**Error! No s'ha trobat l'origen de la referència.**.

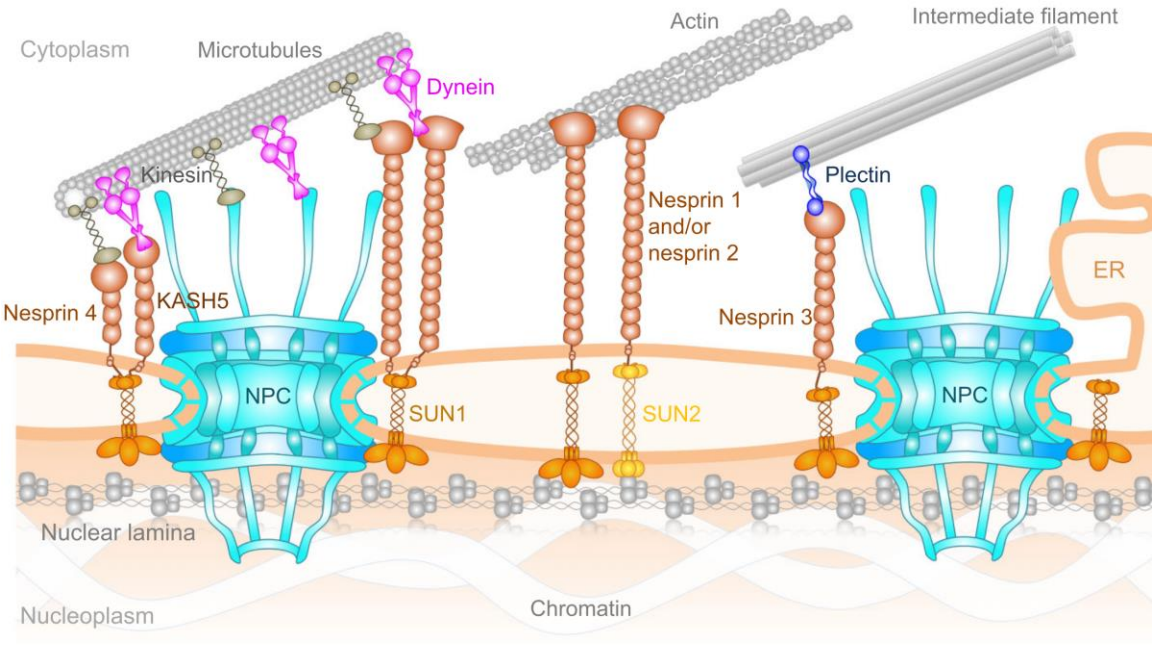

Figure 1 Composition of the cell nucleus at its interface with the cytoplasm (extracted from Jahed et al., 2016)

1.2.1. Nuclear envelope

The nuclear envelope (NE) is a double membrane formed by: an outer lipid bilayer, the outer nuclear membrane (ONM), and an inner lipid bilayer, the inner nuclear membrane (INM) (See Figure 1). Between both membranes we find the perinuclear space (PNS). From a topological point of view the NE is a continuum of the endoplasmic reticulum (ER). The ER is contiguous to the ONM, which in turn connects the lumen of the ER with the PNS. In some cell types, the NE creates inward invaginations towards the nucleoplasm which are named as nucleoplasmic reticulum (NR) (Echevarria et al., 2003; Malhas et al., 2011). Also, the inner and outer membrane are continuous at hundreds of locations, where they bend to connect each other. These ring-shaped holes in the double membrane correspond to the locations of the nuclear pore complexes (NPC), which are barrel-like protein complexes traversing both membranes and the perinuclear space.

The distance between the ONM and INM seems to be strongly regulated by the cell and goes from 30 to 50 nm (C. M. Feldherr & Akin, 1990; Franke et al., 1981; Sosa et al., 2012). Two protein complexes span through the NE: NPCs and Linker of the Nucleoskeleton to the Cytoskeleton (LINC) complexes (NPC and LINC will be introduced in the following sections). At NPC sites the distance is determined by NPC structure at around 50nm. Apart from NPCs, the LINC complexes hold both

membranes at a stablished distance (Rothballer et al., 2013): the depletion of the LINC complex increases the PNS to a 100 nm wide in HeLa cells (Crisp et al., 2006), but does not affect *C. elegans* cells not submitted to forces (Cain et al., 2014). Which leads to think that even if LINC it is not what determines the distance between the ONM and the INM, it is a key component to keep them at the stablished distance when the nuclear envelope is under forces. In the cases where there is no force, Ashutosh Agrawal, and Tanmay P. Lele (Agrawal & Lele, 2019) propose that the regular spacing between NPCs (250 to 500 nm), NPC length, membrane tension, and the low ability of the membrane to buckle if the spacing between NPC is lower than 500 nm (Torbati et al., 2016) is what keeps the spacing stable. In the cases where the space is higher, a buckling instability arises leading to a membrane fusion and creation of a new NPC (Fichtman et al., 2010; Funakoshi et al., 2011).

Regarding composition and physical properties, the NE is more compliant, and more fluid compared to the plasma membrane (PM) (Dazzoni et al., 2020). The NE composition has more unsaturated acyl chains than the PM (Khandwala & Kasper, 1971; Van Meer et al., 2008) and much less negatively charged lipids (Holthuis & Levine, 2005). In turn, the PM contains more saturated chains that the NE (Khandwala & Kasper, 1971). In the PM, the acyl chains tend to be saturated, and cholesterol allows for dense lipid packing. The NE has lipid packing defects (LPDs), and less electrostatic charges than the PM. These differences in composition define different ways of interacting with proteins. Whereas the NE favours interaction of proteins with LPD, the PM uses electrostatic interactions (Bigay & Antonny, 2012).

While we know about the differential composition of the NE versus the PM, the different composition between INM and ONM is more elusive. Electron microscopy for a long time has been the sole method for certain localization of transmembrane proteins which has limited its research (Tingey et al., 2019). However, it is known that the INM contains a unique set of proteins compared to the ONM, but whether they have different lipid composition among them or with the ER is not known (Bahmanyar & Schlieker, 2020).

Finally, regarding NE mechanically-relevant interactions, it has been long known that the INM interacts directly with chromatin-binding nuclear membrane proteins (Gant & Wilson, 1997; Stewart & Stewart, 2002) and with Lamin B, plus, the NE hosts LINC complexes and NPCs; all of them introduced below.

1.2.2. LINC (Linker of Nucleoskeleton and Cytoskeleton) complex

The LINC complex is a protein complex placed in the NE (See Figure 1). It spans from the nucleoplasm to the cytoplasm and is formed by two families of transmembrane proteins: SUN (Sad1/UNC-84) domain proteins at the INM and KASH (Klarsicht/ANC-1/SYNE homology) domain proteins at the ONM (Crisp et al., 2006). As it was first described, SUN proteins bind the nuclear lamina (Crisp et al., 2006), partner proteins (Haque et al., 2010), and chromatin (Chi et al., 2007; Ding et al., 2007; Schmitt et al., 2007; Xiong et al., 2008) in the nucleoplasmic side. In the PNS, they form a coiled coil that finishes with a globular head adjacent to the ONM (Sosa et al., 2012; W. Wang et al., 2012; Zhou et al., 2012). KASH domain proteins are tail-anchored to the ONM and bind SUN proteins. They show a short luminal portion of around 30 residues that contacts the globular head of SUN at the PNS (Crisp et al., 2006; Padmakumar et al., 2005; Sosa et al., 2012; W. Wang et al., 2012). On the cytoplasmic side, KASH proteins bind the cytoskeleton: Nesprin-1/2 bind actin (Crisp et al., 2006;

Padmakumar et al., 2005; Qiuping Zhang et al., 2002), Nesprin-3 can bind actin and intermediate filaments via plectin (Ketema et al., 2007; Wilhelmsen et al., 2005) and Nesprin-3 and Nesprin-4 bind microtubule motors (Yu et al., 2011; X. Zhang et al., 2009).

It has been long accepted that a 3:3 stoichiometric SUN:KASH proportion forms the LINC complex and bridges the nucleoskeleton to the cytoskeleton (Sosa et al., 2012; W. Wang et al., 2012; Zhou et al., 2012). However, more recent studies have also proposed bigger assemblies (Gurusaran & Davies, 2021) and showed SUN proteins binding multiple KASH domains *in vitro* (Cruz et al., 2020). If LINC complexes are able to organize in higher multimeric orders and bind different cytoskeletal structures at the same time, this would mean they could withstand higher and complex loads.

Regarding the molecular insights of the binding between SUN and KASH, it has three main contributors. First, the three KASH peptides are anchored in the SUN binding pockets (Sosa et al., 2012). Second, the "KASH-lid", a β-hairpin and the core of the SUN subunit clamp the central part of the peptides (Sosa et al., 2012). And third, many metazoan LINC complexes have a conserved extra lock, a disulphide bond between SUN and KASH proteins, which may provide extra resistance to withstand force peaks (Sosa et al., 2012).

1.2.3. Nuclear Pore Complex

The Nuclear Pore Complex (NPC) is a large protein complex placed in thousands in the NE (See Figure 1). It presents eight-fold symmetry, measures around 100nm wide and 40nm tall. It is formed by 550 copies of around 30 different proteins named nucleoporins (also termed Nups) (S. J. Kim et al., 2018; Ori et al., 2013; Rout et al., 2000). We can imagine the NPC as a donut embedded in the nuclear envelope. The NPC defining characteristic is that it connects the nucleoplasm to the cytoplasm with a central channel which is 40-60nm wide (Schuller et al., 2021; Zimmerli et al., 2021). As an essential piece for the correct functioning of a cell, the NPC can vary in its structural components; peripheral modules can be plugged in and out to the central core, giving rise to achieve different functions and structures. NPC variability can be either among cell-types or even inside the same single cell (Akey et al., 2022; Fernandez-Martinez & Rout, 2021; Varberg et al., 2022).

Its distribution, density, and composition are not as well studied as its structure, although the first data on the matter date from the 70's. It is clear, though, that NPC distribution is non-random. In metazoans is mediated at least by the Nuclear Lamina (Aaronson & Blobel, 1974, 1975; Daigle et al., 2001; Kittisopikul et al., 2021). However, both plants and fungi lack lamin and still have a regulated NPC distribution, which leads to think that more elements play a role. The most likely molecule to be doing this function is LAP2-emerin-MAN1 (LEM) domain protein, that associates with the INM in pore-free islands of the NE (Maeshima et al., 2006; Varberg et al., 2022). NPC density is variable between species and cell types (Garcia-Segura et al., 1989; G. G. Maul & Deaven, 1977), and does not correlate with nuclear size nor DNA content, whereas it may correlate with metabolic activity (G. G. Maul et al., 1980).

1.2.3.1. Phenyl-Alanine Nucleoporins (FG-Nups)

The central channel of NPCs is full of Nup disordered regions rich in phenylalanine and glycine (FG-repeats) named FG-nups. The FG-nups are anchored to the NPC scaffold on one end and the other end is freely hanging on the channel. There are around 200-300 FG-nups in the NPC occupying the whole diameter of the channel (Hoogenboom et al., 2021) (See Figure 2). The different types of FG-nups present varying lengths, net charge and Stoke radius (Yamada et al., 2010), but in general, both hydrophobicity and unfolding are conserved (Denning & Rexach, 2007). Their variability enriches possible interactions among them and to bind other molecules. Their main functions include regulation of molecule passage, and interaction with cargoes and transport molecules (Rout & Wente, 1994; Sakiyama et al., 2017), which will be introduced thoroughly in 1.3 Transport trough NPC.

	Yeast	*Human*
Cytoplasmic Filament	Nup159, Nup82, Nsp1, Nup42, Nup116, Gle2, Gle1	NUP214, NUP88, NUP62, CG1, NUP98, RAE1, CLE1, NUP358
Outer Ring	Nup85, Nup120, Nup125C, Sec13, Nup133, Nup84, Seh1	NUP85, NUP160, NUP96, SEC13, NUP133, NUP107, SEH1, NUP37, NUP43
Inner Ring	Nup188, Nup192, Nup157, Nup170, Nup53, Nup59, Nic96	NUP188, NUP205, NUP155, NUP35, NUP93
Membrane Ring	Ndc1, Pom152, Pom34, Pom33	NDC1, GP210, POM121
Nuclear Basket	Nup1, Nup60, Nup2, Mlp1, Mlp2	NUP153, NUP50, TPR
Central Channel	Nup57, Nup49, Nsp1, Nup100, Nup145N	NUP54, NUP58, NUP62, NUP98

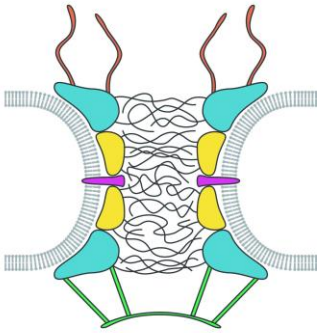

Figure 2 Molecular composition of the NPC (extracted from Matsuda & Mofrad, 2022). Nup names for the different building block in yeast and human NPCs.

1.2.3.2. Scaffold

The FG-nups are held in place by the inner ring. The inner ring spans from the FG nups to the nuclear membrane and is the central structure of the NPC (Fernandez-Martinez & Rout, 2021) (See Figure 2). It is formed by eight symmetric spokes connected by flexible linkers with a limited cross-spoke interaction (Kosinski et al., 2016; Lin et al., 2016). Parallel to the inner ring there is the membrane ring, which is formed by integral membrane Nups that are embedded in the membrane continuum between the INM and the ONM. Its arrangement had not been elucidated until recently, and data in yeast and *Xenopus* oocytes show it can be surprisingly diverse (Hao et al., 2018; Upla et al., 2017; Y. Zhang et al., 2020).

On both the nucleoplasmic and the cytoplasmic side of the inner ring, there are the outer rings. The outer rings are formed by several copies of the Y-complex, named after its Y shape (Lutzmann et al., 2002; Siniossoglou et al., 2000). In humans, each ring is formed by two staggered rings of eight repeats of the Y-complex, adding up to 32 copies per NPC (Bui et al., 2013; Ori et al., 2014). These repeats arrange in a head-to-tail fashion (Fernandez-Martinez et al., 2012) and contact the NE at the tips of the complex (Drin et al., 2007). And whereas the inner ring is connected by flexible linkers, the outer rings stick together thanks to extensive surface interactions (Lin et al., 2016).

On the nuclear side, the NPC contains a fibrous structure called the nuclear basket. It is made of eight large coiled-coil proteins named Tpr (Frosst et al., 2002; Krull et al., 2004). These filaments interact at their distal ends forming the "basket" (Goldberg & Allen, 1996; Ris & Malecki, 1993). Its structure is still considered to be poorly defined due to its intrinsic flexibility (Fernandez-Martinez & Rout, 2021). On the cytoplasmic side, there are eight cytoplasmic filaments formed by the Nup82/84 channel that fold on top of the NPC channel and have a role in RNA export (Fernandez-Martinez et al., 2016).

1.2.3.3. NPC interactions

Apart from many structural studies, there are some publications relating to NPC interactions to other molecules and structures that are putative force transmitting interactions. Starting from the cytoplasmic side, NPCs bind dynein motor proteins via Nup358; Nup358 faces the cytoplasm and is part of the structure known as cytoplasmic filaments (Goldberg, 2017; Joseph & Dasso, 2008). In the nuclear envelope, it has been shown that the LINC complex component Sun1, but not Sun2, colocalizes with Nup153 (P. Li & Noegel, 2015; Qian Liu et al., 2007; Lu et al., 2008), which could be a force transmitting link. Furthermore, Sun1 depletion leads to NPC clustering in HeLa cells (Qian Liu et al., 2007). Then, Sun1 is required to tether the NPC or to organize them correctly.

In the nucleoplasmic side the NPC interacts with the lamina and chromatin. It has been long known that the NPC interaction with the lamina plays a main role in NPC positioning in the NE and avoids its free movement (Daigle et al., 2001; Dwyer & Blobel, 1976; Gerace et al., 1984; Scheer et al., 1976). Interactions with lamins create pore-free islands in nuclei at G1 state in multiple cell types that gradually disappear to obtain an even distribution before mitosis (Maeshima et al., 2006; Mimura et al., 2017). Overexpression of Lamin A induces the formation of the pore-free island while siRNA depletion of Lamin A and C leads to an even distribution of NPCs (Maeshima et al., 2006). Also, the expression of defective forms of Lamin A/C or Lamin B1 depletion promote the formation of nuclear blebs containing an expanded Lamin A/C meshwork, but without Lamin B1 or NPCs (Goldman et al., 2004; L. C. Mounkes et al., 2003; Raharjo et al., 2001; Shimi et al., 2008). Together with the fact that some cells that are naturally defective of Lamin A/C have an even distribution of NPCs, these results would suggest that NPCs preferentially interact with Lamin B. Nonetheless, other studies prove that different lamins can act redundantly to ensure NPC distribution (Y. Guo et al., 2014) or that NPCs have preference for Lamin A over Lamin B, and that the importance of Lamin A over Lamin B-NPC interactions is bigger that Lamin B over Lamin A-NPC interactions (Kittisopikul et al., 2021).

Even though the direct molecular connection between NPC and lamina has not been elucidated yet, some probable interactors are ELYS, NUP153, and TPR (Roux et al., 2012). ELYS is placed in the nucleoplasmic ring and NUP153 and TPR in the nuclear basket. In a recent study by Robert D. Goldman's team, knocking down every one of them separately had a different and unique effect in NPC distribution and lamin meshwork structure; ELYS knockdown created NPC clusters that excluded lamin A/C fibres but included LB1 and LB2 fibres, and knockdown of TPR or NUP 153 altered the arrangement of lamin fibres and NPCs (Kittisopikul et al., 2021), which suggests an interdependence between Lamina structure and NPC number and distribution in metazoans.

Regarding NPC-chromatin interactions, it needs to be pointed out that there are Nups that can promiscuously interact with chromatin out of the NPC (Griffis et al., 2004). However, for the aim of this thesis the most significant are direct NPC-chromatin interaction and putative Nup-chromatin interactions outside of the NPC caused by a mechanical reaction in the NPC.

In the 80s, the "gene gating hypothesis" proposed that NPC could be organizing open chromatin and functioning as a gate for efficient transcription-translation coupling (Blobel, 1985). This hypothesis was proposed after observing that chromatin is differently organised along the nuclear lamina compared to the NPC sites. Particularly, condensed chromatin was observed along the nuclear lamina but not on the regions near NPCs (Gerd G. Maul et al., 1971).

In support of this hypothesis, a genome-wide study in yeast showed evidence that several Nups and Nup-associated proteins associated with genes of high transcriptional activity (Casolari et al., 2004). In this line, structural Nups such as Elys, which contains a conserved DNA-binding domain, interact directly with chromatin (Franz et al., 2007; Zierhut et al., 2014). In metazoans, some studies point the NPC as a scaffold for transcription factors (TF) and chromatin modifying complexes (Capelson et al., 2010; Kalverda & Fornerod, 2010; Mendjan et al., 2006; Vaquerizas et al., 2010). Some examples are Nup153, linked to the function of Polycomb group (PcG) proteins (Jacinto et al., 2015), Nup93 binds chromatin together with Nup98 and Elys (Pascual-Garcia et al., 2017), TPR maintains heterochromatin exclusion sites close to NPCs (Krull et al., 2004), and Nup98 mediates enhancer-promoter looping of inducible genes (Pascual-Garcia et al., 2017), and also contacts repressed genes (Liang et al., 2013). The contacts imply direct genomic binding of the NPC to both heterochromatin and euchromatin, which fosters the idea that *dynamic Nups* that bind-unbind the NPC (Rabut et al., 2004) interact mainly with active transcription sites in the nucleoplasm, but *NPC-bound-Nups* interact with both active and silent regions either sequentially or simultaneously regulated by histone modifications (Köhler & Hurt, 2010; Kuhn & Capelson, 2019; Pascual-Garcia et al., 2017). This would allow a swift gene regulation to biochemical cues (Kadota et al., 2020). However, the correlation between NPC-chromatin interaction and transcriptional state does not prove any direct mechanical connection or force-transmitting effect, yet.

NPC role as gateway for biochemical exchange will be discussed in point 1.3 Transport trough NPC.

1.2.4. Nuclear Lamina

At the inner side of the envelope, we can find the nuclear lamina (NL) (see Figure 1). The NL is the main element of the nucleoskeleton and brings mechanical stability to the nucleus. It has vital roles in integrity of NE, NPC positioning, DNA replication, RNA transcription, chromatin organization, cell development, differentiation, migration and apoptosis (Fiserova & Goldberg, 2010; Gruenbaum et al., 2003; Harada et al., 2014; Hutchison, 2002; Vahabikashi et al., 2022). The NL is formed by lamins which are type V intermediate filament (IF) proteins, as classified by sequence homology (Herrmann & Aebi, 2016). In mammals, there are two types of lamins: A and B; in a simplified way, type A includes lamin A and lamin C which are alternative splicing variants of the *LMNA* gene, and type B includes genes *LMNB1* and *LMNB2* that translate into lamin B1, the first, and lamin B2 and B3, the second. Lamin B1 and B2 are expressed in all mammalian cell types, and B3 is a a germ cell-specific isoform, whereas A and C are present in most differentiated cell types (Adam, 2017).

Lamin monomers are formed by a central coiled coil (rod) domain composed of four α-helix subdomains (1A, 1B, 2A, 2B) that are separated by flexible linker regions (Ahn et al., 2019). The difference between lamins and other cytoplasmic IF is the presence of six heptad repeats more in the central rod domain (Worman, 2012). We can find a head at the N-terminal side and a C-terminal tail containing a nuclear localization signal (NLS), an immunoglobulin domain, and a CaaX motif present in lamins A, B1 and B2, but not in Lamin C, (Gruenbaum & Foisner, 2015). CaaX stands for C, Cysteine; a, aliphatic amino acid; X, any amino acid. This domain is important for the post-translational modifications (PTM) and correct functioning of the lamina. First the cysteine is farnesylated and then the -aaX are removed from the lamins A, B1 and B2. Then the cysteine is methylated to finish the processing of the CaaX motif (de Leeuw et al., 2018). Lamin Bs remain farnesylated, which is needed for their ability to bind the INM and to accomplish their function (Gruenbaum & Foisner, 2015). Pre-Lamin A needs to have the last 15 residues removed (including the cysteine) to become mature Lamin A (Pendás et al., 2002). Among the many PTM that lamins undergo, a primordial one for mature lamins is phosphorylation, which defines lamin solubility (Torvaldson et al., 2015) and lamin A localization into the nucleoplasm (Dechat et al., 2010).

Studies of lamins in their native microenvironment by cryo-ET in Mouse Embryonic Fibroblasts (MEFs) cells, have shown that lamins organize in 3.5 nm thick tetrameric filament with an average length of 380 nm, forming a meshwork of around 14 nm just below the INM. One feature of this filament is its short persistent length of less than 200 nm (Turgay et al., 2017), which makes them the most flexible of all skeletal IF in the cells (Block et al., 2015). Importantly, each lamin isoform assembles into a distinct meshwork (Shimia et al., 2015; Xie et al., 2016). It is known that lamin B1 meshwork places closest to the INM, and this placing depends on correct farnesylation (Nmezi et al., 2019). Also, fluorescence correlation studies prove that A-type lamin meshworks are more dynamic than B-type lamins (Shimi et al., 2008), and that the loss of one type of lamin in the cell affects the organization of the other isoform meshworks, but for the loss of lamin B2 (Kittisopikul et al., 2021; Shimia et al., 2015). This indicates that different lamin isoforms interact among them.

Regarding NL interactions with other elements, both A- and B-type lamins have shown interactions with chromatin, via chromatin Lamina Associated Domains (LADs) (Buchwalter et al., 2019). LADs represent a third of the genome in human and mouse, and correspond mostly with non-coding regions (Karoutas & Akhtar, 2021; Kind et al., 2015). In the case of A-type, it interacts with both euchromatic and heterochromatic regions (Gesson et al., 2016), which restrict chromatin mobility inside the nucleus (Bronshtein et al., 2015). B-type lamins have proven to be essential for mouse genome organisation during the epithelial to mesenchymal transition (Pascual-Reguant et al., 2018).

The nuclear lamina also interacts with the LINC complex, which permits the force transmission from the cytoskeleton. SUN proteins interact strongly with Lamin A, but also with Lamin B (Crisp et al., 2006; Haque et al., 2006). As an example of their importance, MEF deficient in Lamin A show significant changes in the perinuclear cytoskeleton, e.g. an altered distribution of vimentin (Broers et al., 2004; Houben et al., 2009), a separation between the microtubule organizing centre and the nucleus that impedes cell polarization and correct wound healing (J. S. H. Lee et al., 2007), impaired anchorage of transmembrane actin-associated nuclear lines (Luxton et al., 2010), and the alteration of actin caps on the ventral surface of the nuclei (D. H. Kim et al., 2013).

As proof of NL importance, mutations in lamin A/C gene (*LMNA*) can cause a broad spectrum of diseases termed laminopathies (Gruenbaum et al., 2005; Stewart & Stewart, 2002) (see http://www.umd.be/LMNA/). These diseases include dilated cardiomyopathy (Fatkin et al., 1999), Emery-Dreifuss muscular dystrophy (EDMD) (Bonne et al., 1999), Dunnigan-type partial lipodystrophy (Cao & Hegele, 2000), mandibuloacral dysplasia (Novelli et al., 2002), Charcot-Marie-tooth syndrome type 2B1 (De Sandre-Giovannoli et al., 2002), limb girdle muscular dystrophy 1B (Muchir et al., 2003), Hutchinson-Gilford progeria (Eriksson et al., 2003; L. Mounkes et al., 2003), and atypical progeroid syndromes (Csoka et al., 2004). Mutations in B type lamins affect more in the embryogenesis process, most of the times having lethal consequences (Coffinier et al., 2010, 2011; Y. Kim et al., 2011; Vergnes et al., 2004).

1.2.5. Chromatin

Chromatin is the complex formed of DNA and proteins, which primary function is to compact DNA in dense structures. Considering that the human genome can reach 2 m long if extended (Piovesan et al., 2019), packing it in a nucleus of 10-20 µm of diameter needs a high level of condensation.

Stretches of 146 bp of DNA wrap around an octamer of the core histones H2A, H2B, H3, and H4 to form a nucleosome. Then, these nucleosomes are connected like in a pearl necklace-like structure (Yoshikawa et al., 2001). This structure then compacts into a 30-nm chromatin fibre that folds itself into higher-order chromosomal structures. Depending on the level of condensation, chromatin can be in a more condensed state (heterochromatin, which is related to low transcription profiles) or a less condensed state (euchromatin, which is related to highly transcribed regions). Histone and DNA modifications, including acetylation, citrullination, and methylation, alter the level of chromatin packing. How this level of packing regulates chromatin and, in turn, nucleus mechanics and vice versa has been the object of research recently (Stephens et al., 2019; Stephens, Banigan, et al., 2018). As described before, chromatin can interact with the NPC, the nuclear lamina and the LINC complex affecting the mechanical response of the nucleus.

1.3.Transport trough NPC

I find important to explain how the molecule transport through the NPC happens, regarding that working on both aim 1 amd aim 2 involves the transport through the nucleopores.

The first known function of NPC was the exchange of molecules between the nucleus and the cytoplasm. Its structure and function are highly conserved among species, which proves its essential role for the correct functioning of the eukaryotic cell. Molecules traversing the NPC include ions, proteins alone and in complexes, and mRNAs packed with messenger ribonucleoproteins. These variety of molecules transported, makes the NPC very different from other channels like ion pumps, porins, or metabolic transporters, which are highly specialized in one type of molecules.

An essential characteristic is that this molecule exchange is tightly regulated, and that NPCs are not freely diffusing channels for most macromolecules. As explained before, NPCs contain FG-nups in their central channel which form the non-solid structure that filters molecule passage. The main characteristics of FG-nups is that they contain Phenylalanine and Glycine residues, which create intrinsically disordered regions and have hydrophobic properties. They behave as conventional

polymers in many aspects (Ando et al., 2014; Lemke, 2016; R. van der Lee et al., 2014; Vovk et al., 2016). These characteristics determine molecule passage and allow passage in both ways, and also implies that the NPC is not a gate with an open or closed state but rather a specific filter. As a basic rule of thumb, it allows for molecules smaller than 40-60 kDa/5-9 nm and molecules bound to nuclear transport receptors (NTRs) to quickly traverse the pore. These two types of transport are named passive diffusion and facilitated diffusion (also known as active transport). Up to date there is not a clear explanation on how FG-nups form this barrier; but two models have the biggest acceptance in the field to explain the behaviour of transport through the NPC: selective phase model and virtual gate model.

The virtual gate model proposed by Michael Rout in 2003 (Rout et al., 2003) assumes that FG-nups are freely moving, being highly dynamic and interacting shortly with other FG-nups. This characteristic implies that many conformations are possible and there is a high conformational entropy inside the NPC channel. When a molecule tries to go through the channel, it reduces the space for the FG-nups, their available conformations, and therefore their entropy. If the molecule is big enough, the change in entropy is not negligible, which translates in big molecules not traversing the barrier. However, if this big molecule is attached to an NTR, which is able to interact with FG-nups, the loss of entropy is compensated by NTR - FG-nup binding. This explains size and NTR-dependent selectivity.

The selective phase model was proposed by Katharina Ribbeck and Dirk Görlich in 2001 (K. Ribbeck & Görlich, 2001). This model assumes that FG-nups are cross-linked and form a meshwork in the central channel. This stable meshwork opposes resistance to molecules wanting to go through it, as if it was polymer hydrogel. Molecules smaller than the mesh size would be able to travers it, and molecules binding NTR would be using the ability of NTR to bind FG-nups with their hydrophobic pockets. This way the NTR would be constantly modifying the links as it passed through the mesh.

1.3.1. Passive diffusion

We consider passive transport the passage of molecules through the NPC channel without direct interaction with NTR or FG-nups. First studies of the passive permeability barrier involved PEGylated gold nanoparticles, that were micro-injected into living cells, separately in the nucleoplasm and in the cytoplasm (Carl M. Feldherr & Akin, 1997). Images with electron microscopy demonstrated a size dependence on NPC passage, and big particles did not pass through even after long times. Later in time, a study used an *ex vivo* system in *Xenopus laevis,* where the NE was extended over a porous membrane, and determined size exclusion by using fluorescently labelled dextran cargoes. They determined that the flux through the pores stopped when the sizes reached 40 kDa or around 5 nm in diameter (Keminer & Peters, 1999). However, further studies using protein cargoes of different sizes has proven that there is no such of a sharp molecular weight cut-off, but rather a slow decay of passage rates depending on molecular size (Mohr et al., 2009; Timney et al., 2016). The cohesiveness of the barrier created by the FG-nups can be altered by mutating them to less cohesive variants, which alters protein density and intermolecular interactions and increase the flux of passive cargoes (Popken et al., 2015; Timney et al., 2016).

Not only size, but also molecular surface properties and protein stability affect the translocation through the NPC. Negative, hydrophobic and aromatic residues promote transport, while positive

residues impede it (Colwell et al., 2010; Frey et al., 2018; Goryaynov & Yang, 2014). This is explained by the cation – π and π – π interactions with the FG-nups. Regarding protein stability, it has been seen that proteins with lower unfolding forces can go through the nuclear pore at higher fluxes (Elosegui-Artola et al., 2017; Infante et al., 2019); unfolded molecules pay a lower entropy toll, and probably expose their hydrophobic residues when going through the FG-nups, which eases their passage.

Thanks to single molecules studies, we know that passive transport through the nucleopore is a stochastic process where translocations can be either successful or abortive. Plus, translocation times follow an exponential distribution with a characteristic decay time of several milliseconds (Dange et al., 2008; Kubitscheck et al., 2005; W. Yang et al., 2004; W. Yang & Musser, 2006).

1.3.2. Facilitated diffusion

Facilitated diffusion is the type of transport across the NPC that uses the binding to nuclear transport receptors (NTRs) to translocate. The principles that apply for passive diffusion are of general applicability in facilitated diffusion: molecules need to go through the same FG-nup barrier, but this time with the help of NTRs.

Most of the transport of macromolecules, especially of proteins, is mediated by the protein family of Karyopherin-β (Kaps). These proteins vary in number depending on the organism but are mostly identifiable and conserved across eukaryotes, which suggest a conservation of function (O'Reilly et al., 2011). This conservation is also related to their essential role in the cells and their contribution to diseases in case of disruption. Transporters are classified depending on the direction of transport: importins (into the nucleoplasm), exportins (out of the nucleoplasm), and biportins (in both directions) (Matsuura, 2016; Wing et al., 2022). In human cells there are 20 Kaps identified: 10 importins, 5 exportins, 3 biportins and 2 remain unknown (Wing et al., 2022).

The way Kaps work is:

1. they bind their cargo in their originating compartment, normally via linear elements such as Nuclear Localization Signals (NLSs) or Nuclear Export Signals (NESs), or folded domains that bind specific Kaps;
2. the Kap-cargo complex goes through the NPC binding FG-nups;
3. the cargo needs to be released in the destination compartment.

The energy and directionality of transport are obtained by a RAN-GTP/RAN-GDP gradient across the NE. In the nucleoplasmic side, the predominant form is RAN-GTP, because RCC1 is bound to chromatin and exchanges GDP for GTP nucleotides. In the cytoplasmic side, RANGAP and RANBP1 activate GTP hydrolysis to keep RAN-GDP concentration higher. It is when importins or biportins bound to their cargo translocate to the nucleoplasm and bind RAN-GTP that they release their cargo. Exportins and biportins form ternary complexes with cargo and RAN-GTP at the nucleoplasm, and when they translocate to the cytoplasm hydrolyzation of RAN-GTP happens, and complexes disassemble. In the case of importins, there is an added layer of complexity. Most cargos binding importins bind importin α proteins, which in turn bind importin β, and then the importin β – importin α – cargo complex translocates to the nucleoplasm.

An important characteristic of the system, which names facilitated diffusion, is that the passage through the NPC is completely passive and all steps but RAN-GTP hydrolysis are thermodynamically reversible (Görlich et al., 2003; Hoogenboom et al., 2021; Jovanovic-Talisman & Zilman, 2017; Kopito & Elbaum, 2007). What creates a favourable cargo gradient is the active asymmetric release of the molecules in one of the compartments and their slower passage back without an NTR bound. See Figure 3. By their affinity to FG-nups, NTRs tend to accumulate inside of the NPC channels (that would host tens or possibly hundreds) (Lowe et al., 2015), this crowding would ease the binding for molecules meant to bind and, in turn, reinforce the permeability barrier of FG-nups towards neutrals cargoes (Jovanovic-Talisman et al., 2009; Kapinos et al., 2017; Lowe et al., 2015).

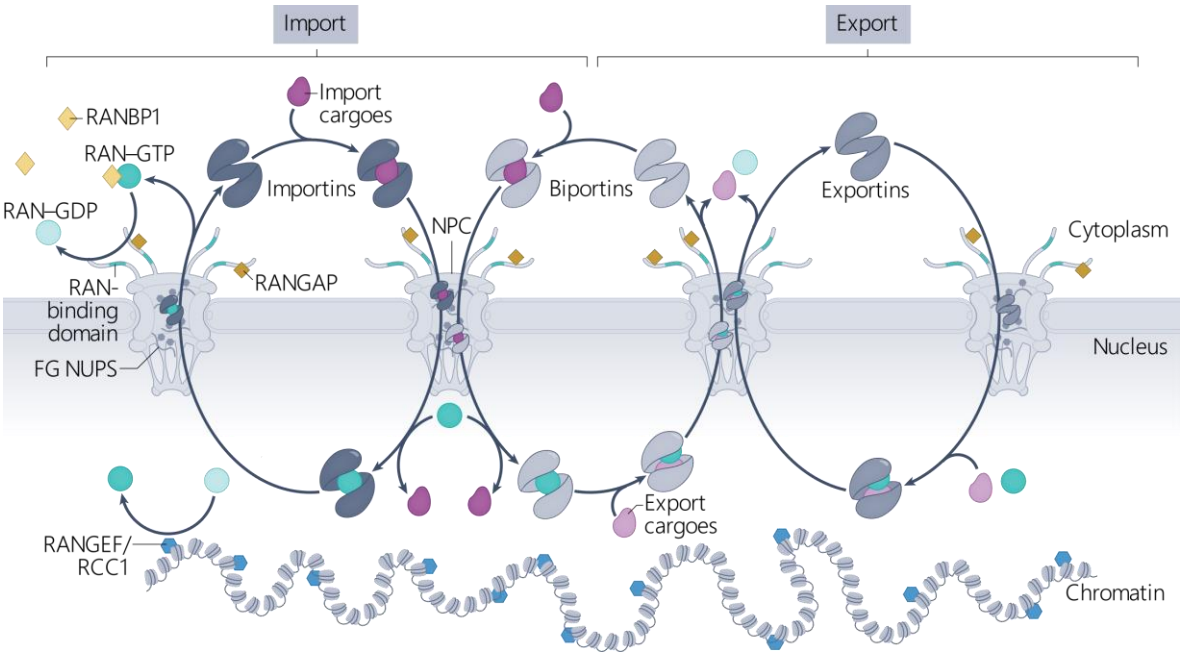

Figure 3 Karyopherin-mediated nucleocytoplasmic transport (extracted from Wing et al., 2022)

1.3.2.1. Transport signals

In order to bind Kaps, many proteins have signals with affinity to a certain Kap. Most known and studied signals are Nuclear Localization Signals (NLSs), that bind importins and translocate the protein to the nucleoplasm, and Nuclear Export Signals (NES), that bind exportins and translocate the protein to the cytoplasm. There is a wide variability in NLS length and features (Görlich, 1997; Hodel et al., 2001; Lange et al., 2007), but almost all have short stretches with a common consensus of basic amino acids K-(K/R)-X-(K/R). If they only have one stretch they are considered *monopartite*, and if they have two stretches (generally separated by 9 to 12 residues) they are considered *bipartite* (Bickmore, 2002; Görlich & Kutay, 1999). Nonetheless, we can even find *tripartite* NLSs where the distance between stretches is bigger (Qinying Liu et al., 2010). And NLS with completely different consensus also exist (B. J. Lee et al., 2006). In the case of NESs, common sequences contain three to four hydrophobic amino acids (often leucine) and there are proposals for a consensus sequence (Güttler et al., 2010).

1.4. Nuclear mechanics and mechanotransduction

Now, with a clear view of the nuclear structure, we can take a deeper look onto the mechanics and the unravelled mechanotransduction events in this organelle up to date. Mechanotransduction is defined as the process that happens when mechanical stimuli are converted into biochemical signals that lead to specific cellular responses. It has been studied in cellular structures like the plasma membrane (Murthy et al., 2017), cell-matrix (Elosegui-Artola et al., 2018) and cell-cell adhesions (Ladoux et al., 2015), and to a minor extent at the nucleus.

Even if the nucleus is connected to other elements in the cell, it is a mechanically differentiated body with distinct physical properties, i.e., it is 5- to 10-fold stiffer than the cytoplasm (Maniotis et al., 1997). Its mechanical behaviour is nonlinear (Stephens et al., 2017), anisotropic (Haase et al., 2016), and viscoelastic (Lele et al., 2018), and it is primarily directed by the lamina and chromatin and indirectly influenced by the cytoskeleton (Stephens et al., 2019). The cytoskeleton protects the nucleus with two elements: an actin cap (Khatau et al. 2009; Haase et al. 2016; Kim et al. 2018) and a perinuclear vimentin cage (Neelam et al., 2015; Patteson et al., 2019; Rosso et al., 2019). In the nucleus is primarily Lamin A/C the major mechanical constituent, as proven by AFM, constricted migration, micropipette aspiration, micromanipulation and other techniques (Dahl et al., 2004, 2005; Lammerding et al., 2004, 2006; Lee et al., 2007; Pajerowski et al., 2007; Schape et al., 2009; Swift et al., 2013; Hanson et al., 2015; Neelam et al., 2015; Stephens et al., 2017). However, the other elements constituting the nucleus also receive mechanical inputs, and all of them may behave as mechanoSensors that can convert mechanical signals into biochemical signals (Kirby & Lammerding, 2018).

In this section, I will introduce mechanical characteristics of the different elements that form the nucleus and their known mechanotransducing events.

1.4.1. Nuclear envelope mechanics and mechanosensing

As described before, the NE (nuclear envelope) is a double lipid bilayer. Lipids composing the membranes stick together showing their polar heads to the polar solvent and hiding aliphatic chains in the membrane. This translates to a basic characteristic of cell lipid membranes: they have bending elasticity but have very low extensibility before breakage, at around 5-10% (Hallett et al., 1993; Needham & Nunn, 1990).

Then during nuclear swelling or compressing, NE area fluctuations and nuclear invaginations disappear, and the area of the NE increases considerably (Dahl et al., 2004; Enyedi et al., 2016; Lomakin et al., 2020; Venturini et al., 2020). However, membrane elasticity cannot be the source of the considerable areal increase during nuclear swelling or compressing, due to its low extensibility.

NE stretch can be a consequence of osmotic pressure or compression and depending on the origin of the change yields differences in duration and amplitude. For example, osmotic-induced stretch is regulated by regulatory volume decrease mechanisms, such as increases in the net efflux of Cl^-, K^+, and organic osmolytes (E. K. Hoffmann et al., 2009). This mechanism can bring back cells to their original size within a minute (Enyedi et al., 2016). The most likely sources for surface increase are thermal undulations and the nucleoplasmic reticulum (Niethammer, 2021). As another source for increasing the NE surface, the equilibrium of tension between the INM and the ONM depends on

the lipid lateral flow at the NPC site (Chizmadzhev et al., 1999; Lamparter & Galic, 2020). Therefore, some integral membrane proteins bound to the NL, chromatin or the NPCs could work as valves for lipid flow at these spots. Once the reservoirs are depleted, the membranes are in tension.

INM stretch sensing has been demonstrated for two lipid enzymes: cytoplasmic phospholipase A_2 (cPLA) and 5-lipoxygenase, which may detect lipid packing defects on the membrane via their membrane attaching domains (Enyedi et al., 2013, 2016). Lipid packing defects happen when the membrane stretches, loosens lipid contacts, and exposes the hydrophobic core to the solvent (Y. L. Zhang et al., 2006). Which in turn promotes the interaction with hydrophobic residues of proteins (Janmey & Kinnunen, 2006), such as cPLA and 5-lipoxygenase. The activation of cPLA leads to cytoplasmic blebbing produced by actin, which can be seen as a mechanism for cells to crawl out of small spaces when nuclear integrity is compromised because the nucleus is compressed (Lomakin et al., 2020; Venturini et al., 2020).

Regarding ONM, a study from 2003 observed not only ion channels, but mechanosensitive calcium channels in the ONM with the same surface density than in the PM of cardiac myocytes. Perinuclear calcium ion release affected transcription from a calcium-regulated transcription factor (Itano et al., 2003), also INM calcium channels have been predicted to be necessary to provoke differentiated reactions at both sides of the NE (Capoen et al., 2011; Martins et al., 2016). Calcium release could potentially affect the activation of calmodulin-dependent kinase IV (Enslen et al., 1994), other multiple ways of gene transcription, apoptosis, protein import (Malviya & Rogue, 1998) and NPC structure (Erickson et al., 2006). However, not much research has been devoted to this topic, and there are hypotheses of stretch activated channels at the NE (Donnaloja et al., 2019). A recent study proves that calcium stretch-activated channel Piezo1 affects chromatin condensation, but instead of the NE, these are placed in the endoplasmic reticulum (Nava et al., 2020). If there are stretch activated channels in the NE is still a matter open for study.

1.4.2. LINC mechanics and mechanosensing

The LINC complex is embedded in the NE, and as the PM, the NE responds to mechanical stress despite their differences in composition and structure. Both membrane systems host transmembrane proteins bearing load, and membrane mechanosensitivity could have coevolved together (Aureille et al., 2017; Baum & Baum, 2014).

This is best exemplified by LINC complex remodelling in response to tension. Gundersen's group showed in 2010 that LINC complexes can arrange in linear fashion forming Transmembrane Actin-Associated Nuclear (TAN) lines (Luxton et al., 2010) similarly to what happens in the PM with integrins (Chrzanowska-Wodnicka & Burridge, 1996). The same team showed later that the interaction of FHOD1 protein with Nesprin-2G mediated the formation of the TAN lines, and involved a reinforcement by providing an extra actin binding domain (Kutscheidt et al., 2014).

At the same time, an independent team demonstrated that the application of tension to Nesprin-1 in isolated nuclei triggered an emerin-dependent LINC rearrangement to resist the applied tension, involving an increased association of lamin to the LINC complex (Guilluy et al., 2014).

1.4.3. Nuclear Pore Complex mechanics and mechanosensing

The NPC interacts both with the lamina in the nucleoplasm and with the cytoskeleton in the cytoplasm (see 1.2.3). In NPCs, as mentioned before, the meshwork of FG Nup proteins that conforms the permeability barrier is supported by the NPC inner ring, which is formed by 8 symmetric spokes (Kosinski et al., 2016; Lin et al., 2016). Spokes have limited interactions with each other through flexible linker proteins (Petrovic et al., 2022). This allows NPCs to dilate or constrict by changing the distance between spokes, as was proposed by Hoelz et al. and Wolf and Mofrad a decade ago in a mode where dilation occurred when cargoes traverse the NPC (Hoelz et al., 2011; Wolf & Mofrad, 2013).

Following this prediction, Alberto Elósegui Artola in our laboratory saw an increase in apparent pore size in cells seeded on top of stiff substrates, where the nucleus is more stretched (Elosegui-Artola et al., 2017). Results in the same direction have been published recently: using cryo-electron tomography in a human and yeast cells (Schuller et al., 2021; Zimmerli et al., 2021). Such dilation and constriction indeed can occur in response to energy depletion or to changes in osmotic pressure, likely due to changes in nuclear membrane tension (Zimmerli et al., 2021). And dilation and constriction have been also proposed to happen in response to calcium signalling in the NE (Erickson et al., 2006). These changes in diameter of the NPC in humans can go from around 40nm to 66nm, which changes the space for the central channel and for molecule exchange between the cytoplasm and the nucleoplasm (Matsuda & Mofrad, 2022; Schuller et al., 2021). The two states are associated with changes in the inner ring radial contraction and expansion, since the general structure of the outer ring remains mostly constant (Schuller et al., 2021; Zimmerli et al., 2021).

The changes in the inner diameter of the NPCs could have direct effects on the translocation of molecules between the cytoplasm and the nucleoplasm. As it was proposed by Elósegui-Artola et al. and Donnaloja et al. (Donnaloja et al., 2019; Elosegui-Artola et al., 2017). A widening of the central channel of the NPC, as it has been seen in human cells (Mahamid et al., 2016; Zila et al., 2021), MEFs (Schuller et al., 2021) and yeast (Allegretti et al., 2020; Zimmerli et al., 2021), has implications in the maximal size of soluble and membrane-bound cargos, but also affects the density of FG-nups in the transport channel (Frey et al., 2006), that would affect transport rates (Frey & Görlich, 2007). The reason for that would be that the permeability barrier created by the FG-nups in the channel depends on their density, and decreasing its density would ease the passage of molecules, as explained in 1.3 Transport trough NPC.

Apart from the dilation in the inner ring, the nuclear basket has also been proposed to be able to respond to mechanical signals (Donnaloja et al., 2019; García-González et al., 2018), as it has been proven to open or close the distal ring depending on calcium concentration (Sakiyama et al., 2017; Stoffler et al., 1999) and it is directly connected via Nup153 to SUN1 (P. Li & Noegel, 2015).

1.4.4. Nuclear Lamina mechanics and mechanosensing

Lamins are an important determinant of nuclear stiffness. In 2004 it was shown that null *Lmna* mutant mouse cells showed lower stiffness than the control cells (Broers et al., 2004; Lammerding et al., 2004). Different lamin proteins have different roles in the stiffness, as observed by a proteomics analysis. Lamin A to Lamin B stoichiometry correlates inversely to tissue microelasticity,

that is the higher the proportion of Lamin A, the stiffer the tissue (Swift et al., 2013). Also, lamina stiffness determines the ability of cells to migrate in 3D environment (Harada et al., 2014). Lamin A is responsible for the nuclear rigidity while Lamin B plays an important role in nuclear integrity (Lammerding et al., 2006). Lamina-dependent nuclear stiffness has proven to be essential for mechanosensing processes involving Ca^{2+} release (Lomakin et al., 2020; Nava et al., 2020), the softer the lamina the higher the threshold for triggering this effect and vice versa. Nava, Miroshnikova et al. propose that this effect may be due to the fact that stiffer nuclei deform less upon stretch, and more stretch is withstood by the ER membranes where tension-dependent Ca^{2+} channel Piezo1 is located, or that there is a higher force transmission to the cytoskeleton via the LINC complex as proposed by Cho and colleagues (Cho et al., 2017).

In cells seeded on soft substrates, Lamin A/C phosphorylation increases (Buxboim et al., 2014; Swift et al., 2013), which leads to a higher mobility and turnover (Buxboim et al., 2014; Kochin et al., 2014). When direct forces to the lamins come into play, shear stress induces partial unfolding of the Lamin A immunoglobulin domain (Swift et al., 2013), and enriches Lamin A/C at the vicinity of the NE (Philip & Dahl, 2008). Cells seeded in stiff 2D substrates can present regions with differential unfolding of the immunoglobulin domain due to different cytoskeletal tensions reaching the lamina, showing a localized effect (Ihalainen et al., 2015). Forces reaching the nucleus *in vivo*, such as myosin-generated contractility, induce lamin A/C dephosphorylation at Ser22, which then promotes its stabilization and stiffens the nucleus (Buxboim et al., 2014) and forces applied directly on isolated nuclei via nesprin-1 recruit Lamin A/C to the nuclear periphery and stiffen the nucleus (Guilluy et al., 2014). However, the exact mechanism by which forces alter phosphorylation of lamins is still unclear, it could involve alteration of kinase activity or substrate accessibility to the enzymes. Nuclear surface area stretches only at big deformations, that is when lamins exert resistance, as stated by Hobson and colleagues in 2020 (Hobson et al., 2020). This means that even if lamins are essential for cell function, their mechanical role comes into play in processes such as migration or joint compression when macroscopic and whole-cell deformations happen.

1.4.5. Chromatin mechanics and mechanosensing

Until very recently the physical properties of lamin and chromatin were not clearly distinguished, but a series of studies have come up with interesting results decoupling the role of these two elements (Hobson et al., 2020; Stephens et al., 2019; Stephens, Banigan, et al., 2018; Stephens, Liu, et al., 2018).

Chromatin compaction is the main parameter that determines its stiffness: the more compact chromatin is, the stiffer, and vice versa (Dahl et al., 2005; Erdel et al., 2015; Krause et al., 2013; Mazumder et al., 2008; Neubert et al., 2018; Pajerowski et al., 2007; Schreiner et al., 2015; Shimamoto et al., 2017; Stephens et al., 2017; Stephens, Liu, et al., 2018). Studies in chromatin fibres have shown that braided chromatin fibres are torsionally stiffer than single fibres (T. T. Le et al., 2019).

Chromatin dominates small extensions (at around 3 µm), as compared to Lamin A/C that respond in larger extensions (Stephens et al., 2017), as proven by decompacting chromatin and depleting lamins expression in isolated nuclei of different mammalian cell types. A posterior study with AFM on different mammalian cells yielded similar results: two regimes of deformation, the 1st at low

levels of indentation where only changes in nuclear volume were observed, the 2nd at higher indentations showed changes in volume plus changes in surface area of the nucleus (Hobson et al., 2020). When depleting histone-histone interactions, chromatin exerted less resistance to changes in nuclear volume but not in nuclear surface area; the inverse happened with the lamina, depleting lamin A/C, lamina exerted less resistance against changes in nuclear surface area (Hobson et al., 2020). The authors also state that strain-stiffening of the nucleus is more related to nuclear geometry and the type of deformation than the relative stiffnesses linked to the volume of the surface area, which is also supported by previous results with micromanipulation studies (Banigan et al., 2017). Up to date, we know about chromatin and lamina contributions to nuclear mechanics, but still few is known about their interactions from a mechanical perspective.

Another example of mechanosensing is the study published in 2020 by Wickström's team. When stretching the cells, and the nucleus which is coupled to the cytoskeleton, the nucleus counteracts via calcium-dependent nuclear softening. The process is provoked by the loss of H3K9me3-marked heterochromatin (Nava et al., 2020), which is the cellular reaction to isolate chromatin and protect it from possible damage due to chromatin tension. As a lead for future research, the state of condensation of chromatin may alter stretch activated transcription of native genes, as indicated by activation transcription of a heterologous gene by twisting fibronectin-coated beads at the cell surface (Tajik et al., 2016) which is most likely activated by stresses in the lamina (Enyedi & Niethammer, 2017).

1.4.6. Mechanosensing in transcription regulators

Transcription regulators (TRs) are proteins involved in DNA transcription to RNA at the cell nucleus. To perform their function as regulators, they need to be at the nucleus in direct or indirect contact with the regulated DNA regions. Cells can control their localization as way to control their activity. And their localization responds to biochemical cues, but there are also some TRs that also respond to mechanical stimuli in the cells, and specifically in the nucleus (Kassianidou et al., 2019). This has been proven for MRTF-A localization that depends on the NL (Ho et al., 2013) and translocates to the nucleus after force application in integrins (Xiao Han Zhao et al., 2007). These previous results led to the discovery of the fact that MRTF-A cellular localization is regulated by the levels of cytoplasmic and nuclear globular-actin (G-actin) (Mouilleron et al., 2011). G-actin can bind MRTF-A and makes inaccessible its bipartite NLS. When the cell is experiencing and exerting low forces, there is high cytoplasmic G-actin concentration, which sequesters MRTF-A and prevents MRTF-A from shuttling to the nucleoplasm. As an extra layer of regulation, XPO1 (an exportin) shuttles MRTF-A out of the nucleus only when it is bound to G-actin (Mouilleron et al., 2011).

β-catenin is also mechanosensitive (Fernandez-Sanchez et al., 2015; Gayrard et al., 2018), and it is regulated by its binding to α-catenin in a protein complex in cell-cell junctions (Shapiro & Weis, 2009). When Wnt signaling pathway turns on, this complex is dismantled and β-catenin can translocate to the nucleus and alter transcription (Lecarpentier et al., 2017). This kind of regulation processes have been described for YAP (Aragona et al., 2020; Chang et al., 2018; Ege et al., 2018), or Twist (Wei et al., 2015).

Alternatively, not only sequestering procedures can regulate localization but also the nucleocytoplasmic transport system. This was proposed for the nuclear translocation of YAP

(Elosegui-Artola et al., 2017) and MyoD21 (Jacchetti et al., 2021). Elósegui-Artola et al. (2017) work proved that the mechanical coupling between the ECM (extra cellular matrix) and the nucleus, via the LINC complex, translocated YAP to the nucleus in response to substrate rigidity. Also, force application to the nucleus was enough for YAP nuclear translocation (by-passing the LINC complex), and that this force increased YAP nuclear import by opening NPCs and reducing mechanical restriction for passage through NPC, which would increase the passive diffusion rates.

As an important remark, this last work proposed a lowering of the NPC permeability barrier causing an increase in the passive diffusion rates through the NPCs. However, changes in passive diffusion do not have any directionality, because transport increases both inwards and outwards.

1.5. Nuclear mechanosensing in cell layers

Introducing the state of the art in nuclear mechanosensing in cell layers is essential because the second aim of this work involves the use of cell layers as a system to study mechanotransduction in a multicellular level. Epithelial tissues form layers of cells with many functions, intended to work as a barrier. Regarding their physical characteristics, these tissues are load-bearing elements that suffer large-scale and force-driven deformations (Anlaş & Nelson, 2018; Jor et al., 2013). Healthy epithelial sheets can withstand big deformations and mechanical stress without rupturing (Latorre et al., 2018; H. Q. Le et al., 2016). However, when some cancer cells are deformed, undergo nuclear rupture and DNA damaging processes (Denais et al., 2016; Raab et al., 2016; Xia et al., 2018). Also, epidermis stem/progenitor cells are exposed to large-scale, dynamic mechanical forces in vivo (Maiti et al., 2016; Obropta & Newman, 2016), and must have robust mechanisms of genome mechanoprotection.

Nava and Miroshnikova, et al. (2020) submitted EPC (epidermal stem/progenitor cells) monolayers to increasing amplitudes of physiologically relevant cyclic, uniaxial mechanical stretch to study “how mechanical stress is dissipated within the nucleus, and how chromatin responds to and is protected against mechanical stress” (Nava et al., 2020). Uniaxial cyclic stretch triggered heterochromatin-mediated mechanosensing via nuclear deformation that in-turn activated Piezo1-mediated calcium release from the ER. This produced a decrease in lamina-associated heterochromatin and subsequent nuclear softening.

In a different study focusing in curvature sensing by monolayers, cells were seeded in corrugated hydrogels to understand nuclear mechanoadaptation in large-scale curvatures (Luciano et al., 2021). Nuclear deformations produced by the adaption to curvature affected the expression of Lamin A/C and Lamin B, with higher abundance of Lamin B1 in convex nuclei and Lamin A/C in concave nuclei. Furthermore, in the presence of cell thickness variability, nuclei positioned in the thickest regions to avoid their deformation.

Regarding nuclear heights in cell monolayers, there is evidence pointing to the fact that: (a) the z-dimensions of the nuclei are uniform compared to isolated nuclei and depend on lamin A/C, (b) the apical surface of the nuclei is flat in the monolayers and curved in isolated cells, cells with abolished cell-cell adhesions or disrupted LINC complex (Neelam et al., 2016). In the case disruption of LINC complex in individual cells, not only the cell with the disrupted complex presented a taller nucleus,

but also adjacent cells. In the same study, myosin activity is presumed to affect nuclear morphology only when affecting cell shape.

2. Aims

From the evidence presented in the Introduction, regarding the facts that (1) the molecular structures that form the nucleus respond to forces in different and specific ways, and that (2) some transcription regulators change their localization when forces reach the nucleus, we hypothesized that nucleocytoplasmic transport is mechanosensitive per se, independently of any specific signalling pathway. This would enable a general mechanism by which nuclear force could control the nuclear localization of proteins, and thereby transcription. However, mere changes in passive diffusion can provide neither directionality nor molecular specificity. Therefore, active transport (also termed facilitated diffusion) needs to have an essential role in this regulation.

In the case the hypothesis proved true, and nucleocytoplasmic transport is regulated by force both in the active and the passive components, a door opens to create *ad hoc* mechanosensitive molecules that shuttle between nucleoplasm and cytoplasm. These molecules would have differential locations depending on the forces reaching the nucleus.

2.1. General aim

The aim of this project is to understand how forces in the cell nucleus affect the nucleocytoplasmic shuttling of molecules. This involves two aspects: first, a fundamental understanding of mechanosensitive nucleocytoplasmic shuttling in simple and complex cellular contexts, from single cells to multicellular environments. Second, the application of this knowledge to create mechanosensitive molecules that shuttle between both compartments and can be used as Sensors of nuclear force.

2.2. Specific aims

1. To unveil the mechanisms by which nucleocytoplasmic transport is regulated by forces in the nucleus.
    - 1.1. To study separately passive and active transport.
    - 1.2. To study how molecular size affects the shuttling in both transport types.
    - 1.3. To study how transcriptional regulator localization is directed by this mechanism.
    - 1.4. To create a fluorescent protein with mechanosensitive localization to be used as a sensor of nuclear force.
2. To study how the mechanical regulation of nucleocytoplasmic transport applies in multicellular systems.
    - 2.1. To use the sensor fluorescent protein to study the effects of forces in the nucleus in multicellular systems.
    - 2.2. To study nuclear shape parameters to unveil how nuclear transport is mechanosensitive in multicellular systems.

3. Material and Methods

3.1. Cell culture and reagents

Mouse embryonic fibroblasts (MEFs) were cultured as previously described (Roca-Cusachs et al., 2013), using Dulbecco's modified eagle medium (DMEM, Thermofischer Scientific, 41965-039) supplemented with 10% v/v FBS (Thermofischer Scientific, 10270-106), 1% v/v penicillin-streptomycin (Thermofischer Scientific, 10378-016), and 1.5% v/v HEPES 1M (Sigma Aldrich, H0887). Cell cultures were routinely checked for mycoplasma. CO_2-independent media was prepared by using CO_2-independent DMEM (Thermofischer Scientific, 18045 -054) supplemented with 10% v/v FBS, 1% v/v penicillin-streptomycin, 1.5% v/v HEPES 1M, and 2% v/v L-Glutamine (Thermofischer Scientific, 25030-024). Media for AFM experiments was supplemented with Rutin (ThermoFischer Scientific, 132391000) 10 mg/l right before the experiment. Importazole (Sigma Aldrich) was used at 40 µM concentration for 1 h (Soderholm et al., 2011). Cells were transfected the day before the experiment using Neon transfection device (ThermoFischer Scientific) according to manufacturer's instructions. Cells were seeded ~4 h before the experiment.

MCF-7 and C-26 cells were cultured in Dulbecco's modified Eagle medium (DMEM) supplemented with foetal bovine serum (FBS, 10% aq.), L-glutamine (2 mM), penicillin (100 U/mL) and streptomycin (100 µg/mL) in a humidified atmosphere with 5% CO2 at 37 °C in humidified atmosphere. For the creation of stable cell lines expressing the Sensor, pLentiPGK coding for SV40A4-EGFP-2PrA was cloned using these primers to excise it from the parental plasmid: Infusion_SV40A4-EGFP-2PrA_Fwd cgg tac cgc ggg ccc atg ggc cca aaa aag gc; Infusion_SV40A4-EGFP-2PrA_Rev gaa agc tgg gtc tag acc act ttg tac aag aaa gct ggg tcg g. The plasmid was then used for viral production in HEK293T (ATCC® CRL-1573™) of low passage in media IMDM supplemented with 10% heat-inactivated FCS, 1% pen/strep. Reagents used were: 2.5 M CaCl2, 0.1x TE buffer,2x HBS pH 7.12 (fresh)

Virus production procedure was as following: Day 1 Plating. 1) 293T cells in 15 cm dishes, 7 million cells per plate (one plate per unconcentrated virus, 2 plates per concentrated virus). 2)Incubate cells at 37°C for 24 hours. Day 2 Transfection. 3) Prepare fresh 2x HBS. 4) Prepare CaCl2 and TE/H2O if needed (those can be stored at -20 and used several times). 4) Measure concentrations of packaging plasmids and plasmid DNA to be transfected by nanodrop. 5) Prepare a master mix of the packaging plasmids with the following amounts per reaction: pMDL 12.5 µg, REV 6.25 µg, VSV-G 9 µg. 6) Pipet the amount of packaging mix needed per reaction in a 15 ml tube (separate tube per reaction). 7) Add 32 µg of plasmid DNA from construct to be transfected. 8) Resuspend plasmid mix in 1 ml 0.1x TE/H2O buffer per reaction. 9) Add 125 µl 2.5 M CaCl2 per reaction and resuspend well. 10) Incubate the mix at RT for 5-10 min. 11) Add 1.25 ml of 2x HBS buffer dropwise to the mix whilst vortexing at maximum speed, pipet mix up and down whilst blowing in oxygen when releasing the volume from the pipet and add the mixture dropwise to the 293T cells immediately (Confluence between 60-70%). 11) Incubate the cells with the precipitated plasmid DNA at 37°C for 16 hours (O/N). Day 3 Refresh medium. 12) Refresh the media by carefully removing the supernatant and adding 16 ml of fresh medium. 13) Transport the cells to the lentivirus lab and incubate at 37°C for 30 hours. Day 4

Virus collection. 14) 30 hours after the medium change, cell supernatant can be collected. 15) Filter supernatant with 0.22 µm filters. 16) Store virus at -80°C or concentrate. Concentration for in vivo work: 17) Transfer filtered cell supernatant to ultracentrifuge tubes (make sure corresponding tubes hold same volume) . 18) Ultracentrifuge supernatant for 2 hours at 20,000 rpm at 7°C. 19) Carefully discard supernatant by inverting the tube and keep tube upside down to dry on paper. 20) Remove leftover supernatant at rim of tube with paper (before inverting tube back). 21) Resuspend virus pellet (not visible) in 150-200 µl PBS. Pipet several times. 22) Incubate at RT for 5-10 min. 23) Collect PBS in Eppi and wash tube with additional 150-200 µl PBS, add to collected virus. 24) Aliquot virus if preferred. 25) Store virus at -80°C.

Transduction of Cell lines was done as follows: 1) Grow three plates (two if no selection marker is needed) of cells in equal numbers in appropriate medium and under usual growth conditions up to around 60% confluence (cells should be stably growing but still not cluster together). 2) On day of transduction: thaw virus on ice.3) Mix polybrene (Sigma H9268 suspended at 4mg/ml in sterile water) with virus in 15 ml tube (1:1000; adjusted to final volume of culture dish). Virus amounts for 6 well plate and 10 cm dish, respectively: Unconcentrated virus 1-2 ml, 2 ml; Concentrated virus 20 µL, 40 µL. 4) Add medium, adjusted to total volume in plate (3 ml in 6 well plate, 10 ml in 10 cm dish) 5) Aspirate old medium off cells to be infected. 6) Carefully pipet polybrene-virus mix on top of cells. 7) Keep the remaining (two) plate(s) as control(s). 8) Incubate cells at 37°C for 24 hours. 9) If applicable: exchange medium for medium supplemented with selection marker 24 hours after transduction for transduced cells and one of the control plates (selection control). Here it's hygromycin that I add on cells at 200ug/ml. 10) Selection is complete when all cells in selection control plate are dead. Refresh the selection medium after 3-4 days if needed. 11) Let expand your population of interest and then just do a FACS sorting based on the GFP expression and made the gating strategy based on the same cell line but not transduce.

3.2.Antibodies and compounds

For primary antibodies, we used Anti Twist antibody (Twist2C1A, Santa cruz, sc-81417, RRID:AB_1130910) 1:200, Mouse monoclonal antibody to SNAIL + SLUG - N-terminal (clone number: CL3700; abcam, ab224731) 1:200, rabbit polyclonal anti SMAD3 (Cell Signaling, 9513, RRID:AB_2286450) 1:40, Rabbit polyclonal antibody to GATA2 (Abcam, ab153820) 1:200, rabbit polyclonal Anti-NF-kB p65 antibody (abcam, ab16502, RRID:AB_443394) 1:200, KPNA4 / Importin alpha 3 (NBP1-31260 Novus Biologicals, RRID:AB_2133841) 1:200, KPNA2 / Importin alpha 1 (MAB6207 Bio-techne, Clone number: 682239) 1:200, KPNB1 / Importin Beta 1 (ab2811 Abcam, RRID:AB_2133989) 1:200. The secondary antibodies used were Alexa Fluor 488 anti-mouse (A-11029; Thermo Fischer Scientific, RRID:AB_2534088) and Alexa Fluor 555 anti-rabbit (A-21429; Thermo Fischer Scientific, RRID:AB_2535850) diluted 1:200. YAP mouse monoclonal antibody (Cat# sc101199; RRID: AB_1131430) diluted 1:400, was used with Alexa Fluor-647 (ThermoFisher goat anti-mouse A-21236, RRID:AB_2535805) was used 1:200.

3.3. Plasmids

If not specified otherwise, plasmids were constructed via standard molecular biology methods, including well-known Gibson Assembly method and a simpler, cheaper and easier version of assembly developed by Liu and Naismith (H. Liu & Naismith, 2008). **LEXY plasmids:** NLS-mCherry-LEXY (pDN122) was a gift from Barbara Di Ventura & Roland Eils (Addgene plasmid # 72655 ; http://n2t.net/addgene:72655 ; RRID:Addgene_72655) (Niopek et al., 2016). **Nuclear transport plasmids:** NLS, NES, or nought combinations with different molecular weight modules were designed as following: Localization signal plus GGGGS linker, EGFP, and different repeats of Protein A (PrA) from *Staphylococcus aureus* modules. Nuclear Localization Signal sequences were extracted from Hodel *et al.* (2001). Nuclear Export Signal sequences were extracted from Kanwal *et al.* (2004). Protein A domain sequences were used originally in Timney *et al.* (2016) and were kindly provided by M. Rout. NLS and NES insertions were performed following Liu and Naismith protocol(H. Liu & Naismith, 2008). PrA insertions plasmid were constructed via Gibson Assembly protocol, as well as BFP plasmid from IG062. For more detailed information see Table 1 and Table 2. **DN-KASH DN-RAN:** DN (Dominant Negative)-KASH was described previously as EGFP-Nesprin1-KASH (Quiping Zhang et al., 2001). DN (Dominant Negative)-RAN (Addgene plasmid # 30309, described as pmCherry-C1-RanQ69L) was a gift from Jay Brenman (Kazgan et al., 2010). **Twist mutants:** pBABE-puro-mTwist was a gift from Bob Weinberg (Addgene plasmid # 1783 ; http://n2t.net/addgene:1783 ; RRID:Addgene_1783) (J. Yang et al., 2004). mTwist was cloned into a pEGFP-C3 backbone and a V5 tag was included at the N-terminal. The different mutants were constructed by adding the corresponding NLS sequences and/or changing the indicated codons. For more detailed information see Table 1.

Table 1 List of designed constructs

Name	Description	Code
Diffusive 27kDa (EGFP)	EGFP	IG062/P522
Diffusive 34kDa	EGFP-1PrA	IG024/P277
Diffusive 41kDa	EGFP-2PrA	IG025/P278
Diffusive 47kDa	EGFP-3PrA	IG026/P279
Diffusive 54kDa	EGFP-4PrA	IG027/P280
Diffusive 67kDa	EGFP-6PrA	IG028/P281
L_NLS 27kDa	SV40A4-EGFP	IG065/P525
L_NLS 34kDa	SV40A4-EGFP-1PrA	IG058/P311
L_NLS 41kDa	SV40A4-EGFP-2PrA	IG032/P285
L_NLS 47kDa	SV40A4-EGFP-3PrA	IG059/P312
L_NLS 54kDa	SV40A4-EGFP-4PrA	IG060/P313
L_NLS 67kDa	SV40A4-EGFP-6PrA	IG061/P314
M_NLS 27kDa	SV40A5-EGFP	IG064/P524
M_NLS 34kDa	SV40A5-EGFP-1PrA	IG029/P282

M_NLS 41kDa	SV40A5-EGFP-2PrA	IG031/P284
M_NLS 47kDa	SV40A5-EGFP-3PrA	IG033/P286
M_NLS 54kDa	SV40A5-EGFP-4PrA	IG034/P287
M_NLS 67kDa	SV40A5-EGFP-6PrA	IG044/P297
H_NLS 27kDa	SV40-EGFP	IG063/P523
H_NLS 34kDa	SV40-EGFP-1PrA	IG070/P530
H_NLS 41kDa	SV40-EGFP-2PrA	IG030/P283
H_NLS 47kDa	SV40-EGFP-3PrA	IG071/P531
H_NLS 54kDa	SV40-EGFP-4PrA	IG072/P532
H_NLS 67kDa	SV40-EGFP-6PrA	IG073/P533
L_NES 27kDa	Adeno_NES-EGFP	IG068/P528
L_NES 34kDa	Adeno_NES-EGFP-1PrA	IG046/P299
L_NES 41kDa	Adeno_NES-EGFP-2PrA	IG040/P293
L_NES 47kDa	Adeno_NES-EGFP-3PrA	IG049/P302
L_NES 54kDa	Adeno_NES-EGFP-4PrA	IG050/P303
L_NES 67kDa	Adeno_NES-EGFP-6PrA	IG052/P305
M_NES 27kDa	MAPK_NES-EGFP	IG066/P526
M_NES 34kDa	MAPK_NES-EGFP-1PrA	IG074/P534
M_NES 41kDa	MAPK_NES-EGFP-2PrA	IG038/P291
M_NES 47kDa	MAPK_NES-EGFP-3PrA	IG075/P535
M_NES 54kDa	MAPK_NES-EGFP-4PrA	IG077/P537
M_NES 67kDa	MAPK_NES-EGFP-6PrA	IG051/P304
H_NES 27kDa	HIV_NES-EGFP	IG067/P527
H_NES 34kDa	HIV_NES-EGFP-1PrA	IG045/P298
H_NES 41kDa	HIV_NES-EGFP-2PrA	IG039/P292
H_NES 47kDa	HIV_NES-EGFP-3PrA	IG041/P294
H_NES 54kDa	HIV_NES-EGFP-4PrA	IG042/P295
H_NES 67kDa	HIV_NES-EGFP-6PrA	IG043/P296
Control V5-Twist	V5-Twist	IG106/P641
mut GBP2 V5-Twist	V5-Twist Y107E	IG110/P645
H_NLS-mutNLS V5-Twist	SV40-V5-mTwist K38R K73R	IG115/P669
M_NLS-mutNLS V5-Twist	SV40A5-V5-mTwist K38R K73R	IG116/P670
mutNLS V5-Twist	V5-mTwist K38R K73R	IG117/P677
L_NLS-mutNLS V5-Twist	SV40A4-V5-mTwist K38R K73R	IG118/P678
UL_NLS-mutNLS V5-Twist	SV40A3-V5-mTwist K38R K73R	IG119/P679
BFP	BFP	IG123/P701

Table 2 Sequences of NLS and NES sequences used (Hodel et al., 2001; Kanwal et al., 2004)

Localization Sequence	Protein sequence	DNA sequence
H_NLS	MGPKKKRKV	ATGGGCCCAAAAAAGAAAAGAAAAGTT
M_NLS	MGPKKKAKV	ATGGGCCCAAAAAAGAAAGCCAAAGTT
L_NLS	MGPKKARKV	ATGGGCCCAAAAAAGGCCAGAAAAGTT
UL_NLS	MGPKAKRKV	ATGGGCCCAAAAGCCAAAAGAAAAGTT
H_NES	MLQLPPLERLTL	ATGCTTCAACTTCCTCCTCTTGAGAGACTTACTCTT
M_NES	MLQKKLEELEL	ATGCTTCAAAAAAAACTTGAAGAACTTGAACTT
L_NES	MLYPERLRRILT	ATGCTTTATCCTGAGAGACTTAGAAGAATTCTTACT

3.4. Polyacrylamide gels

Polyacrylamide gels were prepared as previously described (Oria et al., 2017), and coated using a protocol adapted from the literature (Lakins et al., 2012). Gels were prepared by mixing acrylamide (5.5% or 12% v/v for 1.5 or 30 kPa gels, respectively) and Bis-acrylamide (0.04% or 0.15% v/v for 1.5 or 30 kPa gels, respectively) with 2% v/v 200-nm-diameter dark red fluorescence carboxylate-modified beads (Fluospheres, ThermoFischer Scientific), 0.5% v/v ammonium persulphate (APS, Sigma Aldrich), and 0.05% tetramethylethylenediamine (TEMED, Sigma Aldrich), in PBS 1X. A drop of 22 µl was placed on top of a glass bottom well and then sandwiched with an 18 mm diameter coverslip. Gels where then let for 45 min at room temperature to polymerize. Finally, gels were covered in PBS 1X and the top coverslip was removed. To coat gels, we first prepared a mixture containing HEPES (0.5M, pH 6, 10% v/v), Acrylamide and Bis-Acrylamide (BioRad), N-hydroxysuccinimide (NHS, 0.3% v/v from an initial solution of 10 mg/ml in dimethyl sulfoxide, Sigma Aldrich), Irgacure 2959 (1% v/v, BASF), and Di(trimethylolpropane)tetra-acrylate (0.0012% v/v, Sigma Aldrich), in milliQ water. This mixture was placed on top of gels, and gels were then illuminated with UV light for 10 minutes. After exposure, gels were washed once with HEPES 25mM Ph 6 and once with PBS. Gels were then incubated with 10 µg/ml of fibronectin in PBS overnight at 4ºC, UV treated in the hood for 10 minutes, washed once with PBS and immediately used. The rigidity (Young's modulus) of the gels was measured as previously described (Elosegui-Artola et al., 2014) using a Nanowizard 4 AFM (JPK). Silicon nitride pyramidal tips with an effective half angle θ of 20º and a nominal spring constant of k=0.01 N/m were used (MLCT, Bruker). The spring constant of the cantilevers was calibrated by thermal tuning using the simple harmonic oscillator model. Force-displacement curves with a peak-to-peak amplitude of 6 µm and a frequency of 1 Hz were acquired. 64 points near the gel centre were selected in each gel, separated 5 µm from each other. Eight gels produced in two batches were measured for each stiffness. To compute the Young´s modulus (E), the Hertz model equation for pyramidal tips was fitted to the force-displacement curves, using the JPK software (JPK Data Processing Version 6.1.79). The equation was fitted for an effective indentation of 500 nm.

3.5. Immunostaining for Chapter 1

Immunostainings were performed as previously described (Elosegui-Artola et al., 2017). Cells were fixed with 4% v/v paraformaldehyde for 10 minutes, permeabilized with 0.1% v/v Triton X-100 for 40 minutes, blocked with 2% v/v Fish-Gelatin in PBS 1X for 40 minutes, incubated with primary antibody for 1 hour, washed 3 times with Fish-Gelatin-PBS for 5 minutes, incubated with secondary antibody for 1 hour, washed with Fish-Gelatin-PBS 3X for 5 minutes, and mounted using ProLong Gold Antifade Mountant (ThermoFischer Scientific).

3.6. Real-time PCR experiments

Real-time PCR experiments were performed according to the manufacturer's instructions (Applied Biosystems). Total mRNA was extracted from cells in the different conditions using the Qiagen RNeasy Micro Kit. Concentration of the obtained mRNA was measured with a Nanodrop ND-1000 Spectrophotometer. Equal amounts of RNA samples were reverse-transcribed into cDNA using the iScript™ cDNA Synthesis Kit. SYBR Green (Applied Biosystems 4385612) RT-qPCRs were performed in triplicates with a StepOnePlus System (Applied Biosystems) under standard conditions. The $2^{-\Delta\Delta Ct}$ method was used to calculate relative gene expression. All $\Delta\Delta Ct$ values were normalized to the housekeeping gene *GAPDH*. Primer sequences for the different measured genes are detailed in Table 3.

Table 3 qPCR primer sequences

Gene	Forward sequence	Reverse sequence
Twist1	GGACAAGCTGAGCAAGATTCA	CGGAGAAGGCGTAGCTGAG
Ankrd1	AGTAGAGGAGCTGGTAACAGG	TTGGCCGGAAGTGTCTTCAGGT
Ctgf	AGGAGTGGGTGTGTGACGA	CCAGGCAGTTGGCTCGCATC
Cd63	GAAGCAGGCCATTACCCATGA	TGACTTCACCTGGTCTCTAAACA
Snai2	ATGCCCAGTCTAGGAAATCG	CAGTGAGGGCAAGAGAAAGG
Bmp4	TGTGAGGAGTTTCCATCACGA	CAGGAACCATTTCTGCTGGGG
Il1r1	GTGCTACTGGGGCTCATTTGT	GGAGTAAGAGGACACTTGCGAAT
Gapdh	CAGTGAGGGCAAGAGAAAGG	GGGCCATCCACAGTCTTCTG

3.7. Steady state image acquisition and analysis for Chapter 1

For experiments in Chapter 1, cells were imaged with a Nikon Eclipse Ti inverted confocal microscope with Micromanager (version 1.4.22), using a 60x water immersion objective 1.2 NA. Microscopy images were acquired by using Zeiss ZEN2.3 SP1 FP3 (black, version 14.0.24.201) or Micromanager (version 1.4.22). N/C ratios were quantified manually by segmenting the nucleus using Hoechst (immunostaining) or taking advantage of the GFP tagged construct (live cells) by the following formula:

$$\frac{N}{C} = \frac{I_{nucleus} - I_{background}}{I_{cytoplasm} - I_{background}}$$

Where $I_{nucleus}$ and $I_{cytoplasm}$ are the mean fluorescence intensity of the nucleus and the cytoplasm respectively. ROIs in the nucleus an in the cytoplasm were selected manually next to each other, close to the nuclear membrane. $I_{background}$ is the mean intensity of the background far from the cell.

Mechanosensitivity was calculated once for each of the experimental repeats using the following formula:

$$mechanosensitivity = \frac{[{}^{N}/_{C}\ stiff\ substrate]}{[{}^{N}/_{C}\ soft\ substrate]}$$

Where *[N/C stiff substrate]* and *[N/C stiff substrate]* are the average N/C ratios on stiff/soft substrates for all cells within the experimental repeat. These quantifications were done by using ImageJ software (version 1.53e).

3.8. Live cell AFM experiments

Live cell AFM experiments were carried out as previously described (Elosegui-Artola et al., 2017). AFM experiments were carried out in a Nanowizard 4 AFM (JPK) mounted on top of a Nikon Ti Eclipse microscope, using the JPK software (JPK Data Processing Version 6.1.79). Polystyrene beads of 20 µm were attached using a non-fluorescent adhesive (NOA63, Norland Products) to the end of tipless MLCT cantilevers (Veeco). The spring constant of the cantilevers was calibrated by thermal tuning using the simple harmonic oscillator model. Experiments were carried out on cells previously transfected with the different constructs indicated in figures, incubated with Hoechst 33342 (Invitrogen), and seeded on 1.5 kPa gels. For each cell, the nucleus was identified by using the Hoechst fluorescence signal, and a force of 1.5 nN was applied to the nucleus. Once the maximum force was reached, the indentation was kept constant under force control, adjusting the z height by feedback control. An image was acquired every 10s by an Orca ER camera (Hamamatsu) and a 60X (NA = 1.2) objective.

3.9. Photoactivation experiment and quantification

Photoactivation experiments were done with a Zeiss LSM880 inverted confocal microscope using a 63X 1.46 NA oil immersion objective and using using Zeiss ZEN2.3 SP1 FP3 (black, version 14.0.24.201). An argon laser was used with 561 nm wavelength for acquisition and 488 nm laser for stimulation. For experiments, 4 images were obtained before stimulation, followed by 19 images during stimulation, and 18 images during recovery. All images were acquired every 30 s. During the stimulation period, the 488 nm laser was irradiated to the whole field of view also every 30 s, during 1 s at 100% laser power.

To obtain the entry and exit coefficient a single exponential equation was fitted to the N/C ratio of each cell:

$$n/c(t) = (n/c)_0 e^{-kt}$$

Where $(n/c)_0$ is the initial ratio of the stimulation or recovery phase, *t* is time, and *k* is the entry or exit coefficient. The curve was fitted to the whole stimulation or recovery phase.

3.10. FRAP Data Acquisition and Analysis

Estimation of mobile fraction of proteins was done using fluorescence recovery after photobleaching (FRAP) experiments. FRAP involves bleaching a region of interest (ROI) and then tracing the recovery of fluorescence in that region with respect to time. Image acquisition was done with a Zeiss LSM880 inverted confocal microscope objective and using using Zeiss ZEN2.3 SP1 FP3 (black, version 14.0.24.201), using a 63X 1.46 NA oil immersion objective and a 488nm wavelength argon laser at 100% laser power. We acquired images every 60 ms, before and after bleaching. We use two regions of interest (ROIs) for our experiments: first, the circular 14-pixel diameter (~6.9 μm^2) region being bleached (ROIF). Second, the cell area segmented manually (ROIC). The data for ROIs consist of the fluorescence integrated density as a function of time from images acquired before and after photobleaching. For further analysis, we normalize the fluorescence intensities of ROIs using the double normalization method (Rapsomaniki et al., 2012). Double normalization corrects for photobleaching during the post bleach imaging and normalizes recovery fluorescence with a pre bleach signal. Double normalized intensity (I) for recovery signal can be calculated by using following formula.

$$I = \frac{F}{F_0} \times \frac{C_0}{C}$$

where F and C are the fluorescence integrated densities of ROIF and ROIC respectively for post bleach imaging, and F_0 and C_0 correspond to pre bleach imaging. The mobile fraction mf represents the fraction of molecules that are free to diffuse. It is estimated by using the first timepoint after bleaching (I_0) and the median of the last twenty timepoints (I_f) in the following expression:

$$mf = \frac{I_f - I_0}{1 - I_0}$$

3.11. FLIP Model

Fluorescence loss in photobleaching (FLIP) is used to assess influx and efflux rates of the different constructs. FLIP experiments involve continually bleaching of a region of interest (ROIb) and tracking signal loss from different regions. Quantification of these curves yields the transport dynamics between nucleus and cytoplasm. We set up experiments and analysis motivated from[20] for determining the rates of nuclear influx and efflux.

To model the FLIP data, we developed a system of Ordinary Differential Equations (ODEs) describing the change in protein concentration between two compartments i.e., the nucleus and the cytoplasm. These two compartments are linked with boundary fluxes going in (Q_i) and out (Q_e) of the nucleus (Fig S1).

We assume that the proteins remain in unbound and mobile state in each compartment. During steady state cells maintain a constant ratio (α) of protein concentration between nucleus (n) and cytoplasm (c), and the flux between both compartments is equal.

$$\alpha = \frac{n}{c}$$

$$Q_e = Q_i$$

During photobleaching the transport equations for the number of unbleached molecules in nucleus (*N*) and cytoplasm (*C*) can be described as follows, where (Q_b) is the number of molecules being bleached per unit time.

$$\frac{dN}{dt} = -Q_e + Q_i$$
$$\frac{dC}{dt} = +Q_e - Q_i - Q_b$$

The fluxes are proportional to the concentration of the compartment, times a rate coefficient. Here, k_e', k_i' are efflux and influx rate coefficients respectively and η' is the bleaching rate:

$$Q_e = k_e' n \quad Q_i = k_i' c \quad Q_b = \eta' c$$

Because these rates (in units of volume per unit time) will depend on the size of the compartment, we define normalized rates as $k_e = k_e'/V_n$, $k_i = k_i'/V_n$, $\eta = \eta'/V_n$, where V_n is the volume of the nucleus. Note that we normalize both k_e and k_i by the same volume (that of the nucleus, V_n) so that the values remain comparable, and that equal k_e and k_i correspond to equal concentrations in nucleus and cytoplasm. Thus:

$$Q_e = V_n k_e n \quad Q_i = V_n k_i c \quad Q_b = V_n \eta c$$

This enables us to rewrite transport equations in terms of concentration.

During bleaching,

$$V_n \frac{dn}{dt} = -V_n k_e n + V_n k_i c$$
$$V_c \frac{dc}{dt} = +V_n k_e n - V_n k_i c - V_n \eta c$$

Where V_c is cytoplasm volume. During steady state,

$$V_n k_e n = V_n k_i c$$
$$k_e \frac{n}{c} = k_i$$
$$k_e = \frac{k_i}{\alpha}$$

One can further simplify these by using ratio of nuclear volume to cytoplasm volume $\beta = \frac{V_n}{V_c}$

$$\frac{dn}{dt} = -k_e n + k_i c$$
$$\frac{1}{\beta}\frac{dc}{dt} = +k_e n - k_i c - \eta c$$

By substituting k_i, we get following equations to solve ultimately:

$$\frac{dn}{dt} = -(\boldsymbol{k_e})n + (\boldsymbol{k_e}\alpha)c \qquad \textit{(eq. 1)}$$

$$\frac{dc}{dt} = +(\beta \boldsymbol{k_e})n - (\beta \boldsymbol{k_e}\alpha + \beta \boldsymbol{\eta})c \qquad \textit{(eq. 2)}$$

We then solve these equations numerically using MATLAB function ode15s, and fit them to the experimental data to get influx/efflux rates and bleaching rates. Variables in bold are the unknowns to be fitted with fminsearch function in MATLAB (R2020b).

3.12. FLIP Imaging and Analysis

For quantification of FLIP (Fluorescent Loss In Photobleaching) experiments, we followed the fluorescence intensities of three different regions, segmented manually: nucleus, cell, and background. Image acquisition was done with a Zeiss LSM880 inverted confocal microscope objective and using using Zeiss ZEN2.3 SP1 FP3 (black, version 14.0.24.201), using a 63X 1.46 NA oil immersion objective and a 488nm wavelength argon laser. We used a bleaching ROI of 17 x 17 (~12.9 μm^2) pixels. 10 baseline images were acquired every 3 seconds before photobleaching. Then, every 3 seconds (during a total of 120 seconds) the ROI was photobleached, and an image of 512 x 512 pixels was acquired. The power of the laser used to bleach was adjusted to result in the same bleaching rate η. Due to differences in cell morphology, this corresponded to 60% power for cells on 1.5 kPa substrates, and 100% power for cells on 30 kPa substrates. This difference occurred because cells were more rounded on soft gels and therefore thicker in the z axis, leading to a taller column of cytoplasm affected by photobleaching. Cells with beaching rates above 0.12 were discarded. We note that differences in obtained rates between 1.5/30 kPa substrates were reproduced when comparing cells at 30 kPa with/without DN KASH overexpression, where cell morphologies and bleaching laser power was not altered. In the mathematical model, the transport between nucleus and cytoplasm is modelled as transport between two compartments, where the cytoplasm is continuously bleached. We assume that the concentration of protein is uniform in each compartment and that during steady state (before photobleaching) the ratio (α) between nucleus and cytoplasm's protein concentration is constant. The ROIs identified for nucleus and cytoplasm were narrow rings around the nucleus, either inside or outside of the nucleus. The average fluorescence intensity of these regions was used as a proxy for nuclear concentration (n) and cytoplasmic concentration (c). The intensities were corrected for background noise, and normalized by the total integrated cell intensity. Experimental data for n and c was used to solve equations 1 and 2, as explained above. The ratio of concentrations at steady state (α) was taken as n/c at the initial timepoint (before photobleaching). To calculate the ratio of nuclear-to-cytoplasmic volume (β), we first took confocal stacks of cells with a nuclear fluorescent label (DAPI) and whole cell fluorescent label (GFP), seeded on both 1.5 kPa and 30 kPa gels. In those cells, we noted an excellent correlation between the nuclear/cytoplasmic ratio volume ratio β, and the nuclear/cytosolic area ratio, calculated with nuclear and cytosolic areas at a representative central slice of the cell (**Figure 6**). Thus, in FLIP experiments we measured area ratios from images, and converted this to volume ratios using the experimental correlation.

To solve for unknown variables, we used a curve fitting technique with a weighted least square method. The experimental data for concentrations (n,c) is fitted to a solution of the ODEs (n_f, c_f). The objective function f is then formulated as the sum of squares of residuals of model and experimental data as:

$$f = \sum_t w_n\left(n - n_f\right)^2 + w_c\left(c - c_f\right)^2$$

Where w_n and w_c are used to weigh the function by time and compartment concentration to avoid bias in the fitting:

$$w_n = \frac{1}{(t+\epsilon)\sum_t n} \qquad w_c = \frac{1}{(t+\epsilon)\sum_t c}$$

Here, w_n, w_c, n, c, and n_f, c_f are all a function of time t and ϵ is an arbitrary scalar constant (set to 10) used simply to prevent the denominator of w_n and w_c from reaching zero. We use the fminsearch function of MATLAB to minimize f as a function of ODE parameters k_e and η (equations 1 and 2). For each iteration, n_f, c_f is calculated as a function of k_e and η using the Matlab ode15s solver. We note that resulting fitted rates showed more variability for conditions with fast rates (corresponding to small molecular weight constructs) than conditions with slow rates (see Figure 5e,f). This is likely caused by a higher experimental error in measuring fast rates: in cells with faster rates, photobleaching occurs faster, and therefore the important part of the fluorescence intensity curves is compressed in a shorter interval (less frames). This makes the subsequent fitting more susceptible to noise.

3.13. Cell layer seeding for Chapter 2

Mattek, glass-bottom dishes were incubated with 10 µg/mL of fibronectin in PBS for 2 hours at room temperature. Magnetic PDMS gaskets (Rodriguez-Franco et al., 2017) sized 4mm times 8mm at the inner side, were treated water and soap, washed in EtOH, washed in MiliQ, incubated in Pluronic® F-127 (20g/L) 1h room temperature, washed twice in PBS, and air dried. Both matteks and gaskets were UV sterilized before seeding. For cell seeding, gaskets were put in the center of the matteks dishes, and the dishes were placed on top of a holder including a magnet to keep them in place. Around 60k cells were seeded in every gasket. Cells were incubated for 4h, and then some washes with medium were performed to retrieve non-attached cells, and add enough medium to cover the gaskets completely. Cells were then incubated for 242h with the gasket. The gasket was then retrieved, and cells were incubated O/N before imaging started.

3.14. Cell layer imaging for Chapter 2

Image acquisition was done with a Zeiss LSM880 inverted confocal microscope objective and using using Zeiss ZEN2.3 SP1 FP3 (black, version 14.0.24.201), using a 63X 1.46 NA oil immersion objective and a 403, 488, 561 and 633nm wavelength lasers, in the Fast Airyscan mode. Image size was set to 1504 pixels in xy and a variable number of slices depending on the cell layer thickness, to include minimum the two lowest layers of cells. Voxel size was of 0.1413 µm for xy and z-step of 0.4. Image positioning was automatically set to fit a tile positioning with an 15% image overlap. In the case of YAP immune stainings for MCF-7 cell layers, only properly permeabilized regions were imaged. To recognise the properly permeabilized regions a control staining of the Sensor was performed (not shown).

3.15. Image processing for Chapter 2

Images were processed to .czi with Zeiss ZEN2.3 SP1 FP3 (black, version 14.0.24.201). Then they were binned in xy by a factor of 4 calculating the mean using Fiji (Schindelin et al., 2012), leaving the voxel size in xy at 0.5652. Tiles were stitched using Fiji's plugin *Grid/Collection stitching*, with the linear interpolation option and default values for the rest. Once stitched, images were separated by channels, and the nuclei staining was segmented in 3D using Cellpose (Stringer et al., 2021) and the following settings: *python -m cellpose --dir* Directory *--do_3D --cellprob_threshold=0.0 --batch_size*

2 --pretrained_model nuclei --chan 1 --diameter 34. --save_tif --no_npy --use_gpu; changing directory by the actual directory containing the images to be segmented. Once the nuclei mask was created MATLAB was used for the following computation procedures, code structure will be described in *11 Appendix C: Data processing for Chapter 2*.

3.15.1. Density measurements

To measure the cell density a cell is placed in, for the n^{th} cell the algorithm counts the number of nuclei placed in a square (200 pixels/112 µm per side) centred in the n^{th} cell nucleus. The algorithm does not discern the z-dimension because it only considers the xy centres of the nuclei.

3.15.2. Ratio measurements

For ratio measurements the algorithm uses the segmentation mask of the n^{th} cell nucleus to select the xy plane where the area is the biggest. From that plane, it creates a 2-pixel-wide ring around to measure the cytoplasmic signal and a 1-pixel eroded nuclear plane to extract the nuclear signal. In all the cases, the outer ring is prevented from measuring any other close nucleus. Quality measurements are made by computing the Standard Deviation of this areas, since inside one cell both Sensor and YAP are homogeneously distributed inside of the same compartment. Therefore, high variability means that the created region-of-interest (ROI) is measuring out of the cell or measuring another cell.

3.15.3. Sensor-YAP correaltion

Live cell to fixed cell correlation was performed by: first, imaging the same spots before and after immune staining; second, registering the nuclei images to be in the same position; third, since cell masks are overlapping after the registration, we manually correlated the cells creating a two-columns table of cell identifiers. The table includes for every row the nucleus number in the live imaging mask and the nucleus number in the staining mask. This table is then used to create a subsequent table including Sensor and yap ratios for the very same cells.

3.16. Immunostaining for chapter 2

Immunostainings were performed as previously described (Elosegui-Artola et al., 2017). Cells were fixed with 4% v/v paraformaldehyde for 10 minutes, permeabilized and blocked with 0.1% (MCF-7) and 1% (C-26) v/v Triton X-100 and with 2% v/v Fish-Gelatin in PBS 1X for 45 minutes, incubated with primary antibody for 1 hour (MCF-7) and O/N (C-26), washed 3 times with Fish-Gelatin-PBS for 5 minutes, incubated with secondary antibody for 1 hour, washed with Fish-Gelatin-PBS 3X for 5 minutes, and mounted using ProLong Gold Antifade Mountant (ThermoFischer Scientific).

The discrepancies between MCF-7 and C-26 in the staining protocols are due to time restrictions in the presentation of this work. C-26 staining performs better and data will be reproduced with that protocol for MCF-7 for any subsequent publication.

3.17. Statistics and plotting for Chapter 2

Figures in Chapter 2 show Spearman r values and p-values corresponding to the correlation of the raw data points, that have been then used for binning and plotting. The statistical tests were performed with GraphPad Prism 9.4.1.

For binned graphs in chapter 2, the averaged data point is plotted at the left/lower side of the bin. Bins with n<5 point have not been plotted for.

4. Results. Chapter 1: Mechanical force application to the nucleus regulates nucleocytoplasmic transport

Cells sense and respond to mechanical stimuli from their environment by a process known as mechanosensing, which drives important processes in health and disease (Broders-Bondon et al., 2018; Hamant & Saunders, 2020; Humphrey et al., 2015). Growing evidence shows that the cell nucleus is directly submitted to force (Arsenovic et al., 2016; Elosegui-Artola et al., 2017; Lombardi et al., 2011), and can act as a mechanoSensory (Kirby & Lammerding, 2018). Force applied to the nucleus (henceforth termed nuclear force for simplicity) can affect chromatin architecture (Nava et al., 2020), the accessibility of the transcription machinery (Tajik et al., 2016), the conformation of nucleoskeletal proteins such as lamins (Swift et al., 2013), or cell contractility (Lomakin et al., 2020; Venturini et al., 2020). Further, forces transmitted to cells, and specifically nuclei, affect the nucleocytoplasmic localization of transcriptional regulators involved in different signalling pathways (Kassianidou et al., 2019). As proposed for MRTF-A (Ho et al., 2013; X H Zhao et al., 2007), β-catenin (Fernandez-Sanchez et al., 2015; Gayrard et al., 2018), or YAP (Aragona et al., 2020; Chang et al., 2018; Ege et al., 2018), this can be due to a retention mechanism, in which force controls the localization of proteins by regulating their affinity for binding partners in the nucleus or cytoplasm. Alternatively, the nuclear translocation of YAP (Elosegui-Artola et al., 2017) and MyoD (Jacchetti et al., 2021) has been associated to a force-induced increase in passive diffusion across nuclear pore complexes (NPCs).

As it has been explained in the introduction, nucleocytoplasmic transport takes place through NPCs in two main ways, passive and facilitated diffusion (Beck & Hurt, 2017; Wente & Rout, 2010). Passive diffusion is rapid for small proteins, but is progressively impaired as the molecular weight (MW) of the protein increases (Mohr et al., 2009; Paine & Feldherr, 1972; Timney et al., 2016). This impairment is caused by a meshwork of disordered proteins within NPCs called phenylalanine-glycine (FG) Nups, commonly termed the NPC permeability barrier (Denning et al., 2003). Facilitated diffusion of larger proteins is mediated by nuclear transport receptors (NTRs) (Nachury & Weis, 1999; Yuh & Blobel, 2001), which interact specifically with both the cargo molecules and FG Nups to overcome the NPC permeability barrier. They are divided between importins (mediating active nuclear import) and exportins (mediating active nuclear export) (Cautain et al., 2015). Both classes interact with cargoes by binding to specific sequences (Kalderon et al., 1984) termed nuclear localisation signals (NLS) or nuclear export signals (NES) for proteins binding to importins or exportins, respectively (Görlich, 1998; Wente & Rout, 2010). The directionality of facilitated transport in either the import or export direction is enabled by the coupling of binding/unbinding events to the phosphorylation status of the small GTPase Ran (either GTP, predominant in the nucleus, or GDP, predominant in the cytoplasm) (Nachury & Weis, 1999). For example, in the canonical import, a complex is formed between importin β (which interacts with FG Nups), importin α (which binds importin β), and the cargo (which binds importin α through an NLS). The complex then diffuses through the NPC and finally dissociates in the nucleus in a RanGTP-dependent manner (Cautain et al., 2015; Kalderon et al., 1984).

Considering all this knowledge and the hypothesis on which this work is based, Chapter 1 is devoted to fulfilling aim 1 of this thesis and its sub aims. These are: unveiling the regulation and mechanisms by which nucleocytoplasmic transport is regulated by forces in the nucleus, study separately passive and active transport, study how molecular size affects the shuttling in both transport types, study how transcriptional regulator localization is directed by this mechanism, and create a fluorescent protein with mechanosensitive localization to be used as a Sensor of nuclear force.

4.1. Nucleocytoplasmic transport is mechanosensitive.

To assess if and how mechanical force affects nucleocytoplasmic transport, we studied different artificial constructs undergoing both passive and facilitated diffusion, transfected in mouse embryonic fibroblasts (MEFs). First, we used a light-inducible nuclear export construct (LEXY) (Niopek et al., 2016) (Figure 4a). The construct presents a mild NLS fused to mCherry, plus a stronger NES that is only functional upon light excitation. To control the mechanical environment, cells were seeded on soft or stiff fibronectin-coated polyacrylamide gels (Young's modulus of 1.5 and 30 kPa, respectively). Increasing substrate stiffness leads to the growth of focal adhesions, increasing the transmission of actomyosin-generated forces between cells and the substrate (Elosegui-Artola et al., 2016; Schiller et al., 2013). In turn, these forces reach and deform the nucleus through the Linker of Nucleus and Cytoskeleton (LINC) complex (Elosegui-Artola et al., 2017; Lombardi et al., 2011), which connects actin fibres to the nuclear lamina. Before photoactivation (t=0), with only the NLS active, the N/C ratio was higher for cells on stiff substrates (Figure 4b,c). Upon excitation by light, the construct exited the nucleus to similar final N/C ratios in both conditions, although the rate of N/C change was higher for the stiff substrate (Figure 4b-d). Once light excitation stopped, the reverse process occurred, with N/C ratios increasing faster for the stiff substrate, until restoring original values (Figure 4e). We then co-transfected cells with DN-KASH, a dominant-negative domain of nesprin that disrupts the LINC complex (Lombardi et al., 2011) and prevents force transmission to the nucleus (Elosegui-Artola et al., 2017). DN-KASH overexpression led cells on stiff substrates to behave like those on soft substrates (Figure 4b-e), demonstrating that the effect of stiffness was mediated by nuclear force.

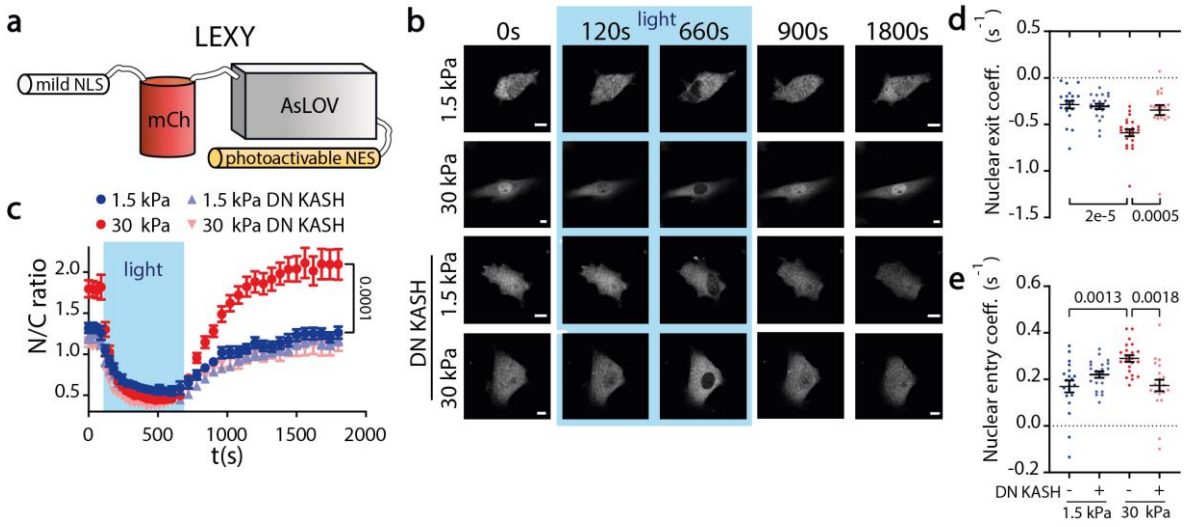

Figure 4 Nucleocytoplasmic transport is mechanosensitive. a) Cartoon of light-activated nucleocytoplasmic shuttling construct. Mild NLS is always active, NES is activated only upon light excitation. **b)** Time sequences of construct fluorescence before, during, and after excitation for cells seeded on 1.5/30 kPa substrates, with or without DN KASH overexpression. Scale bars, 20 µm. **c-e)** Corresponding quantifications of N/C ratios, and coefficients of exit and subsequent re-entry of constructs into the nucleus (in units of s^{-1}, obtained by fitting an exponential to the curves, see methods). (N=20, 22, 21, 21 cells per condition (1.5 kPa, 30 kPa, 1.5 kPa DN KASH, and 30 kPa DN KASH, respectively) from 3 independent experiments, data are presented as mean values +/- SEM.In c) the bar indicates the statistical significance between the last timepoint of 1.5kPa and 30kPa values. In d-e, p-values calculated with 2-way ANOVA Šídák's multiple comparisons test.

4.2. Passive diffusion is mechanosensitive for small MWs.

Our results strongly suggest that nucleocytoplasmic transport is generally affected by nuclear force, but do not clarify the contributions of passive and facilitated diffusion (the ~45 KDa LEXY construct is likely sufficiently small to diffuse passively). To dissect the different contributions, we first used constructs undergoing only passive diffusion, and regulated their diffusivity through their MW. These constructs were composed of a Green Fluorescent Protein (GFP), attached through a short linker to between zero and six repeats of the 7 kDa bacterial Protein A (PrA) (Figure 5a). PrA is inert and purely diffusive in eukaryotic cells, as shown previously (Timney et al., 2016) and also confirmed by the complete fluorescence recovery of the constructs after photobleaching (Figure 6e). When we transfected the constructs in cells, the N/C ratios of all proteins were ≈ 1 regardless of MW and substrate stiffness (Figure 5b,c).

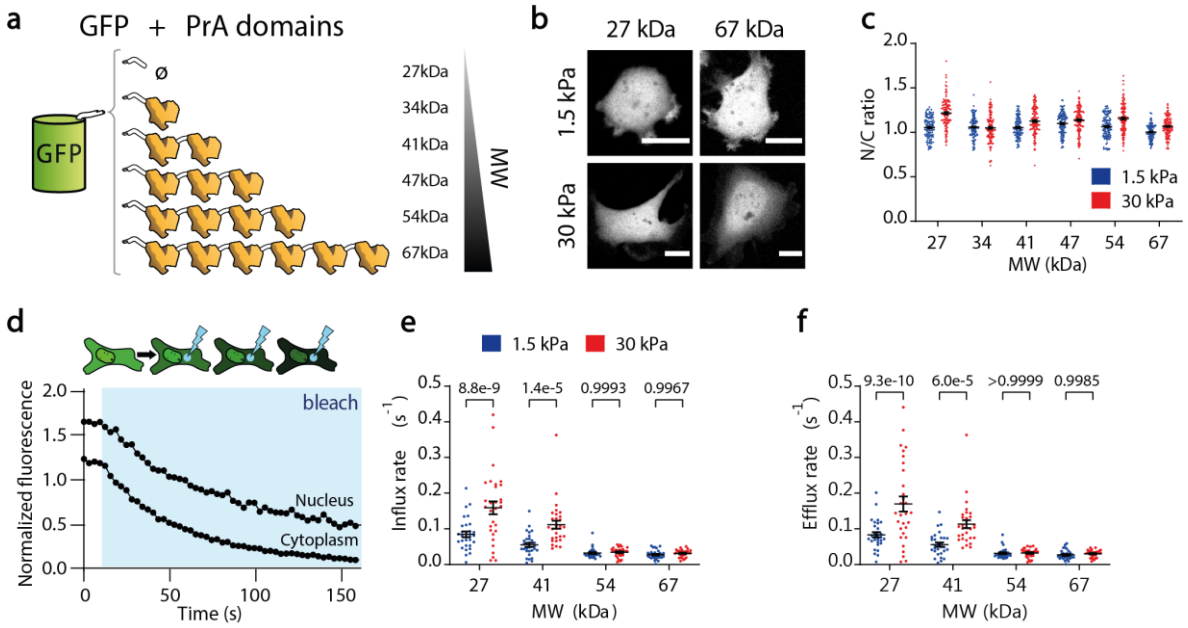

Figure 5 Passive diffusion through NPCs is mechanosensitive for small MWs. **a)** Cartoon of constructs with EGFP and different amount of repeats of PrA domains. **b)** Images showing fluorescence of indicated constructs on 1.5/30 kPa substrates. **c)** N/C ratios of constructs on 1.5/30 kPa substrates as a function of MW. N=120 cells from 3 independent experiments. Significant effects of stiffness and MW were observed (p <1e-15 and p <1e-15; computed via 2-way ANOVA). **d)** Example of a FLIP experiment: a laser photobleaches a region of the cell cytoplasm, and fluorescence intensities are recorded over time in nucleus and cytoplasm. Resulting curves are fitted to a kinetic model to obtain influx and efflux rates (see methods). **e,f)** Influx and efflux rates on 1.5 and 30 kPa substrates as a function of MW of the constructs. N=30 cells from 3 independent experiments. The effects of both substrate stiffness and MW were significant in both e,f). p-values e) 2.9e-8, <1e-15, f) 4.0e-8, <1e-15, computed via 2-way ANOVA. Scale bars, 20 µm. Data are mean ±SEM.

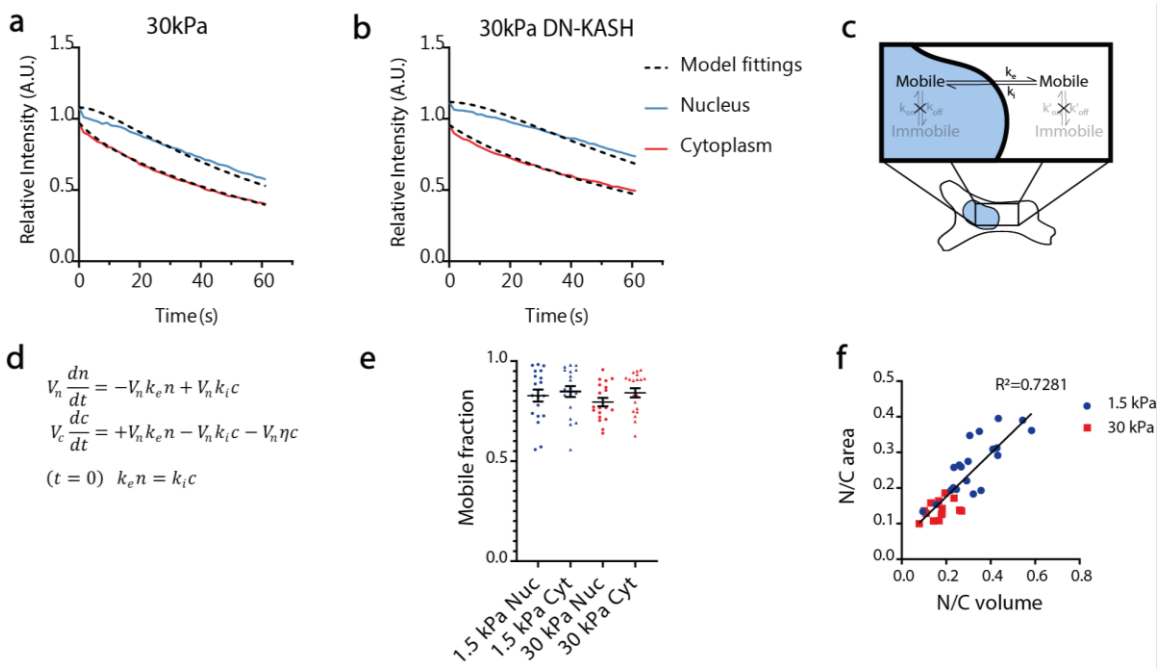

Figure 6 Fluorescence Loss In Photobleaching (FLIP) technique. a,b) Examples of curves showing fluorescence intensity as a function of time in the nucleus and cytoplasm in FLIP experiments on two example cells transfected with the diffusive 41kDa construct and seeded on a) 30 kPa in control condition and b) 30kPa with DN-KASH overexpression. Data represent the mean fluorescence intensity of the compartments (nucleus/cytoplasm), normalized with the mean of the whole cell before the beginning of photobleaching, and corrected for background signal. Each curve depicts a representative experiment of one cell each. **c,d)** Cartoon and equations describing the model used for fitting curves as in A,B, and calculating influx and efflux rates. The model considers the molecules to freely diffuse inside the nuclear and cytoplasmic compartments (see methods). **e**) Mobile fraction of the L_NLS 41kDa construct in the nucleus (Nuc) and cytoplasm (Cyt) of cells seeded on 1.5/30 kPa gels measured by FRAP. N=19 cells from 3 independent experiments, lines show mean ±SEM **f**) For cells seeded on 1.5 and 30 kPa gels, correlation between nuclear to cytosolic ratios of volume, and of areas as measured in confocal slices used for FLIP measurements; regression equation *y = 0,6075 x + 0,05375*. N=20 (1.5kPa) and N=14 (30kPa) cells from 2 independent experiments. Black line shows the linear regression.

This result shows that concentrations of passively diffusing proteins were not mechanosensitive (where mechanosensitivity is defined as the fold change in a given magnitude in stiff versus soft substrates). However, this does not provide information on diffusion kinetics. To quantify this, we adapted a previously described method and model (Ege et al., 2018) based on Fluorescence Loss in Photobleaching (FLIP, Figure 5d), which allowed us to measure nuclear influx and efflux rates (see methods and Figure 6). These rates quantify overall transport into and out of the nucleus, regardless of whether it is passive or mediated by active import/export. As expected, both influx and efflux rates decreased with MW (Figure 5e,f). Interestingly, rates increased with substrate stiffness, and this effect decreased for increasing MW (Figure 5e,f). Confirming that this was mediated by nuclear force, DN-KASH overexpression had the same effect as reducing substrate stiffness (Figure 7). Thus,

nuclear force weakens the permeability barrier of NPCs (i.e., increases diffusion), and the effect is more pronounced for molecules with low MW (high diffusivity). Nevertheless, and because diffusion is non-directional, this does not affect the steady state nucleocytoplasmic distribution of molecules, which remains uniform.

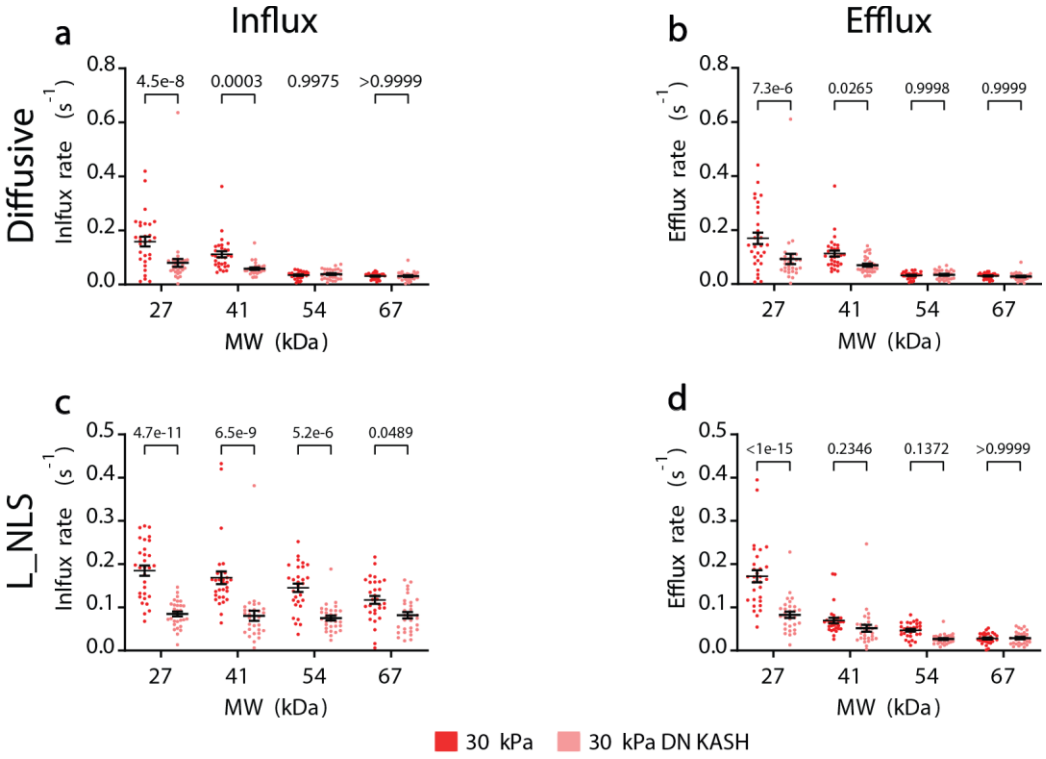

Figure 7 Blocking nuclear to cytoskeletal force transmission with DN-KASH recapitulates the effects of substrate stiffness on transport rates. a,b) Influx and efflux rates of diffusive constructs for cells seeded on 30 kPa gels, with or without DN-KASH overexpression. In a, both MW (p<1e-15) and DN KASH (p=1e-6) effects tested significant. In b, both MW (p<1e-15) and DN KASH (p=0,0002) effects tested significant. **c,d)** Influx and efflux rates of constructs containing L_NLS for cells seeded on 30 kPa gels, with or without DN-KASH overexpression. In c, both MW (p=0,0025) and DN KASH (p<1e-15) effects tested significant. In d, both MW (p<1e-15) and DN KASH (p=3.4e-10) effects tested significant. In all panels, N= 30 cells from 3 independent experiments. Two-way ANOVA, Šídák's multiple comparisons test was used to obtain p-values between conditions. Data are mean ±SEM.

4.3. Mechanosensitivity of facilitated vs passive diffusion.

Next, we assessed how substrate stiffness affected facilitated transport. We first assessed the protein directly interacting with FG Nups, importin β. As expected, transfected importin β-GFP localized at the nuclear membrane (Figure 8a). Due to this localization and the diffraction limit, our FLIP measurements could not capture the likely very fast kinetics taking place in the immediate vicinity of the nuclear membrane. However, we did measure the kinetics of importin β molecules released in the bulk of either the nucleus or cytoplasm. Influx and efflux rates of importin β showed a high mechanosensitivity (Figure 8b,c), similarly to that of highly diffusive passive molecules (Figure

5e,f). Because importin β exhibits facilitated diffusion both in the influx and efflux direction, influx and efflux rates were largely symmetrical, leading to uniform concentrations inside and outside the nucleus regardless of substrate stiffness (Figure 8d).

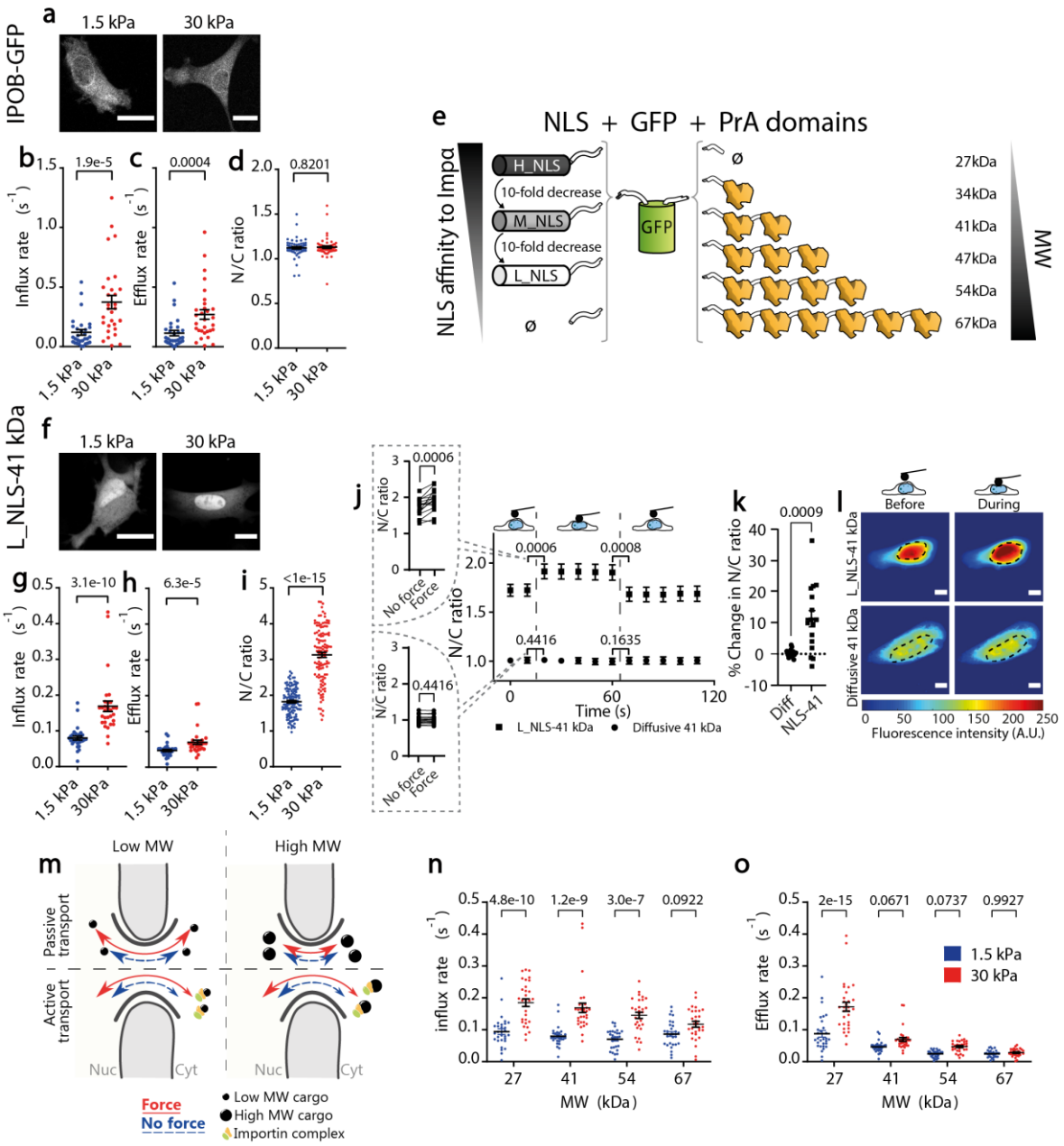

Figure 8 Differential mechanosensitivity of facilitated import versus passive diffusion explains force-induced nuclear translocation. a) Example importin β-GFP images for cells on 1.5/30 kPa substrates. **b-d)** Corresponding importin β-GFP influx rates (b), efflux rates (c), and resulting N/C ratios (d). N=30, 30, and 60 cells from 3 independent experiments. p-values calculated with two-tailed Mann-Whitney test. **e)** Cartoon of constructs with EGFP, different number of repeats of PrA domains, and NLS of different affinities to importin α. **f)** Example images of L_NLS-41 kDa construct for cells on 1.5 and 30 kPa substrates. **g-i)** Corresponding Influx rates (g), efflux rates (h), and resulting N/C ratios (i) of L_NLS-

41 kDa construct. N=30, N=30, N=120 cells from 3 independent experiments respectively each. p-values calculated with two-tailed Mann-Whitney test. j) N/C ratios of L_NLS-41 kDa or diffusive 41 kDa constructs in cells seeded on 1.5 kPa gels before, during, and after nuclear deformation with AFM. Graphs on the left show paired dot plots of the time points right before and after force application. p-values were calculated with two-tailed paired t-test. k) Corresponding % change in N/C ratios right after force application for both constructs. p-value was calculated with a two-tailed unpaired t-test with Welch's correction. In j,k, N= 16 cells from 3 independent experiments, traces of all cells are shown in Figure 9. l) Corresponding images of constructs before and during force application, dotted line marks nucleus outline. Scale bars 20µm. Data are mean ±SEM in all panels. m) Cartoon summarizing the effects of nuclear force and MW on active and passive transport. Passive transport decreases with MW, and depends on force only for low MW molecules. Active transport does not depend on MW, and depends on force regardless of MW. Note that active transport arrows also show a small arrow in the export direction, as discussed in the text. n) Influx rates (mediated by facilitated transport) of L_NLS constructs with different molecular weights. The effect of substrate stiffness and MW tested p<1e-15 and p=0.0004. o) Efflux rates of L_NLS constructs (mediated by passive transport) with different molecular weights. The effect of substrate stiffness and MW tested p=3,5e-11 and p<1e-15. In n), o), N= 30 cells from 3 independent experiments. Two-way ANOVA, Šídák's multiple comparisons test was used to obtain p-values between conditions. Data are mean ±SEM.

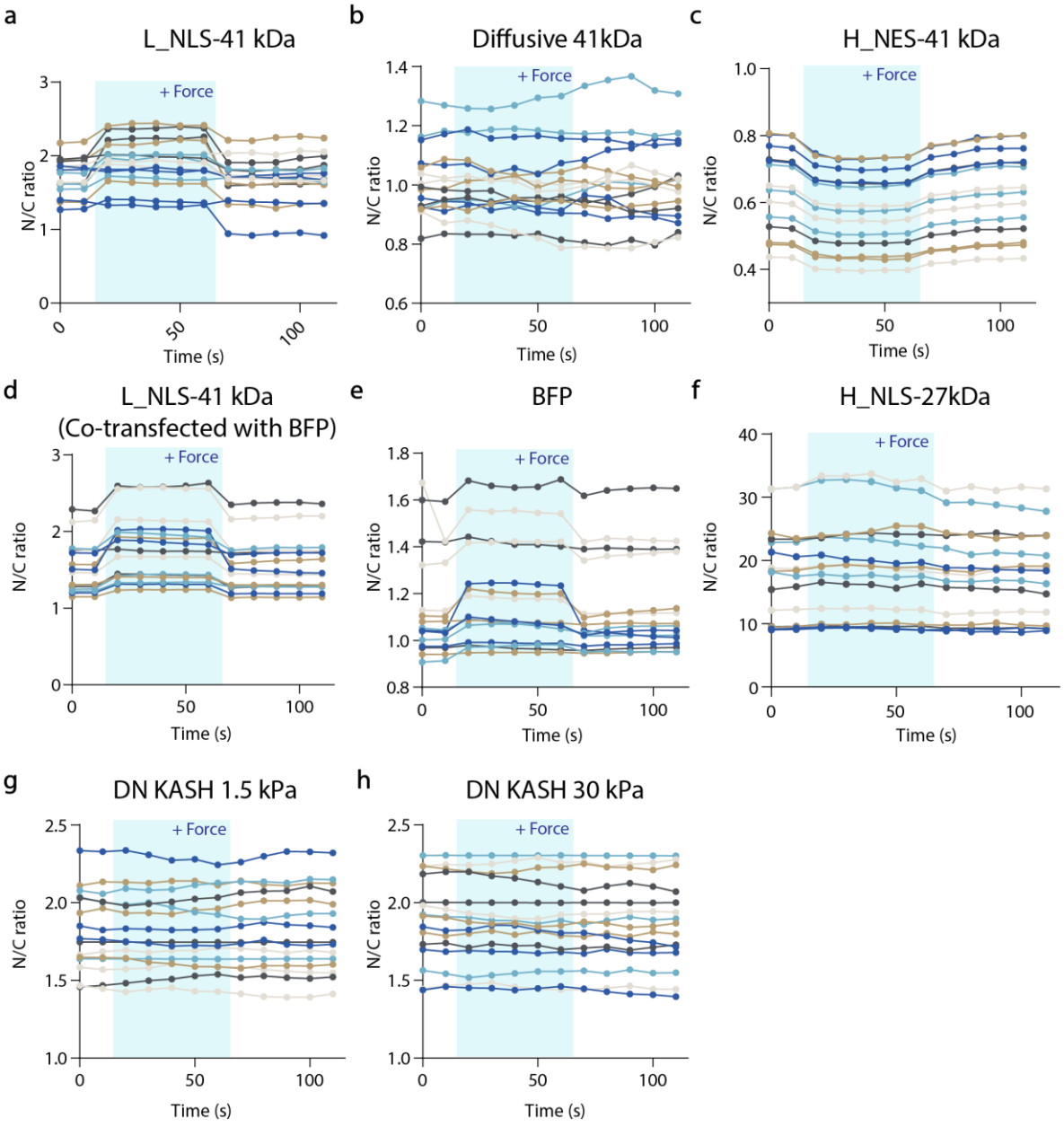

Figure 9 Cell-by-cell fluorescence curves of all AFM experiments. Plots showing the evolution with time of N/C ratios before, during and after force application to the cell nucleus for all cells measured. **a-b)** AFM experiments reported in Figure 8, **c)** Figure 14, and **d-h)** Figure 10.

Then, we studied cargo proteins undergoing facilitated diffusion by adding NLS sequences to the GFP-PrA constructs (Figure 8e). To regulate facilitated diffusion, we used NLS sequences with point mutations resulting in varying levels of affinity for importin α (Hodel et al., 2001). We termed them H_NLS, M_NLS, and L_NLS, for high, medium, and low affinity, respectively (see Table 2). The mechanosensitivity of such constructs can be predicted from the behaviour of passively diffusing molecules (Figure 5e,f) and importin β (Figure 8b,c). Indeed, a cargo molecule with an NLS should have a high mechanosensitivity in the influx direction (because it enters the nucleus with importin

β), but a low mechanosensitivity in the efflux direction if its MW is above ~ 40 kDa (because it exits the nucleus through passive diffusion, which loses mechanosensitivity as MW increases).

By taking L_NLS-EGFP-2PrA (41 kDa) as a starting point, we confirmed this prediction: this molecule had a higher mechanosensitivity in influx than efflux rates, leading to an increase in N/C ratios with stiffness (Figure 8f-i). We then carried out several controls to confirm that this was caused by nuclear force. First, we checked that the same effects on rates were observed when comparing cells with and without DN-KASH overexpression (Figure 7). Second, we assessed stiffness-mediated changes in importin concentrations. Concentrations of importin β did not change with stiffness, but the two types of importin α binding to our NLS constructs (importin α3 and importin α1) respectively showed a ~50% increase or ~40% decrease with stiffness (Figure 10a-e). The N/C ratios of all importins remained close to 1 in all cases, with only a ~10-30% increase with stiffness that if anything should impair, rather than promote, nuclear import of cargo (Figure 10f). Thus, changes in importin concentration may have an impact, but do not exhibit any consistent trend that could explain our results. Finally, we applied force to the nucleus of cells seeded on soft gels with an Atomic Force Microscope (AFM), and verified that this also led to an increase in N/C ratios only if the construct contained the L_NLS sequence (Figure 8j-l). Applying force to cells co-transfected with L_NLS-EGFP-2PrA and purely diffusive BFP also led to a nuclear enrichment of GFP versus BFP (Figure 10g-k,n). Response to AFM-applied force was also lost for cells overexpressing DN-KASH, showing that the effects of force require an intact LINC complex (Figure 10o-r).

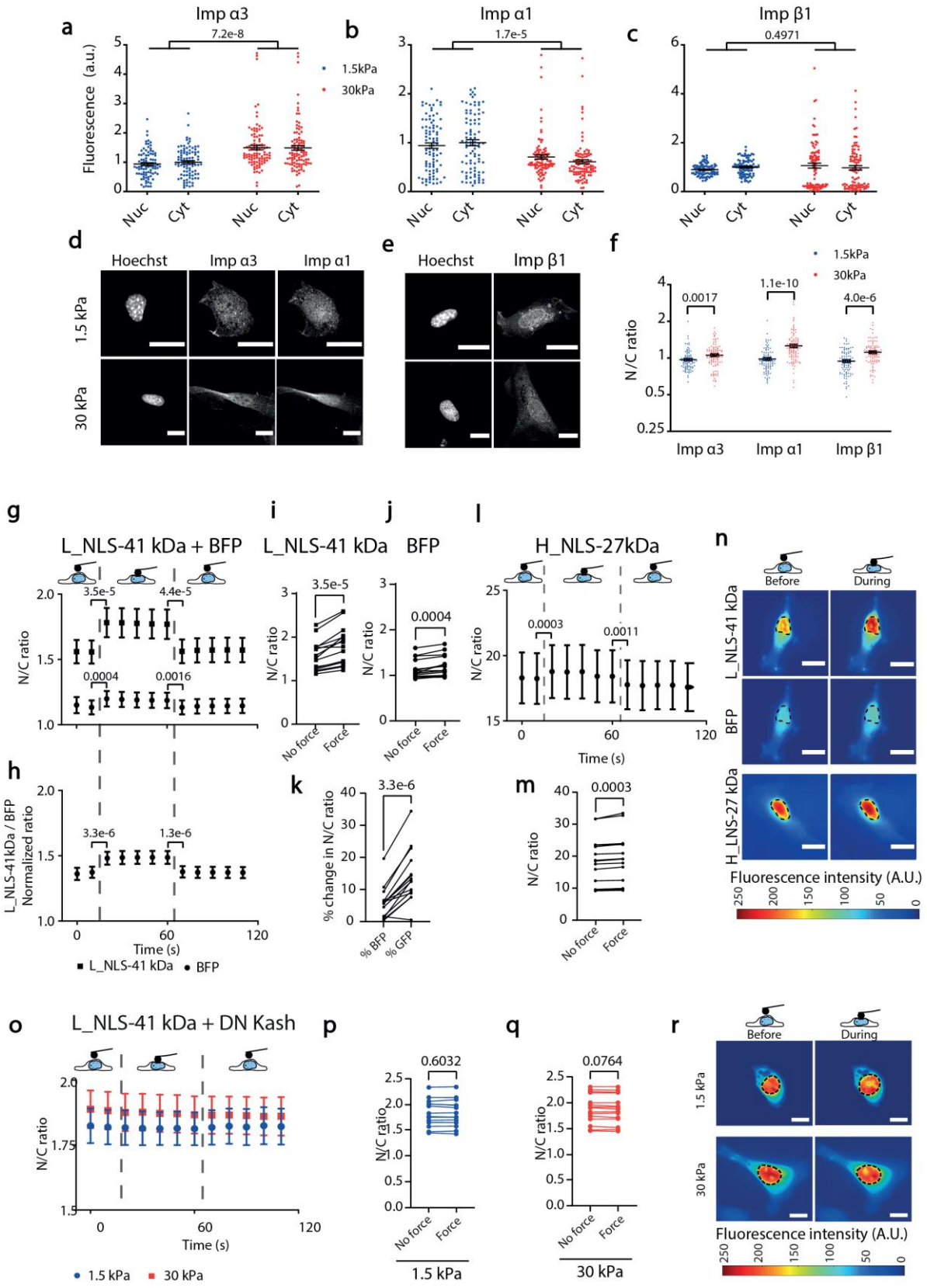

Figure 10 Control experiments on importins and AFM. a-c) Average fluorescence intensities of nuclear

and cytoplasmic areas of cells seeded on substrates of 1.5 or 30 kPa stiffness and immunostained for importin α3 (imp α3) importin α1 (imp α1), and importin β1 (imp β1). N= 90 cells from 3 independent experiments. The effect of substrate stiffness tested significant for importin α3 (p=7.2e-8) and importin α1 (p=1.7e-5), but not for importin β1 (p=0.4971). p-values from Two-way ANOVA **d-e)** Corresponding example images showing the nucleus (Hoechst) and the distribution of the different importins. **f)** Corresponding quantification of N/C ratio of importin localization. N= 91,98, 91, 98, 90, 90 cells (from left to right) from 3 independent experiments. p-values from independent two-tailed Mann-Whitney tests. **g)** N/C ratios of L_NLS-41 kDa or BFP constructs in cells seeded on 1.5 kPa gels before, during, and after nuclear deformation with AFM. **h)** L_NLS-41 kDa ratios normalized by BFP ratios, from panel g) paired measures. **i,j)** from g, corresponding paired dot plots of the time points right before and after force application. **k)** from g, corresponding % change in N/C ratios right after force application for both constructs. In g,h,i,j,k N= 15 cells from 3 independent experiments, p-values were calculated with a two-tailed paired t-test. **l)** N/C ratios of H_NLS-27 kDa construct in cells seeded on 1.5 kPa gels before, during, and after nuclear deformation with AFM. **m)** from l, corresponding paired dot plots of the time points right before and after force application. In l, m, N= 15 cells from 3 independent experiments. p-values were calculated with a two-tailed paired t-test. **n)** Corresponding images of constructs before and during force application, dotted line marks nucleus outline. **o)** N/C ratios of the L_NLS-41 kDa construct in cells co-transfected with DN-KASH and seeded on 1.5 or 30 kPa gels before, during, and after nuclear deformation with AFM. Data are mean ±SEM. **p,q)** from o, corresponding paired dot plots of the time points right before and after force application. In o,p,q, N= 15 cells from 3 independent experiments. p-values were calculated with a two-tailed paired t-test, traces of all cells are shown in Figure 9. **r)** Corresponding images of constructs before and during force application, dotted line marks nucleus outline. Scale bars, 20 µm. Note: in AFM experiments, non-mechanosensitive constructs (BFP and H_NLS) still show a small increase with force, likely due to lensing effects caused by changes in cell shape during indentation. This increase (~6% for BFP, ~2% for H_NLS) is much smaller than that of the mechanosensitive construct (L_NLS 41 kDa, ~14%), see panel k. Panel h in fact shows the response of the L_NLS construct after factoring out the response of BFP. Data are mean ±SEM in all panels.

For L_NLS-EGFP-2PrA, nuclear accumulation with force is explained by a higher mechanosensitivity of facilitated versus passive diffusion. This differential behaviour may arise from the role of MW. Indeed, passive diffusion is strongly impaired as MW increases (Timney et al., 2016) whereas facilitated diffusion can transport large molecules (Lowe et al., 2010; Lyman et al., 2002; Katharina Ribbeck & Görlich, 2002). Thus, one could expect a scheme (summarized in Figure 8m) in which passive diffusion decreases both in magnitude and in mechanosensitivity as MW increases (as measured in Figure 5e,f) whereas facilitated transport is not affected (or only mildly affected) by MW. To verify this hypothesis, we measured influx and efflux rates of constructs containing the L_NLS sequence and different MW (Figure 8n,o). Indeed, influx rates (dominated by active transport, Figure 8m) had a much milder dependence on MW than efflux rates (dominated by diffusion and with very similar behaviour to that of purely diffusive constructs, Figure 8o).

4.4. Molecular properties defining mechanosensitivity.

With these elements, we can generate an initial conceptual model of how nucleocytoplasmic transport should broadly depend on force, MW, and NLS affinity (see 9. Appendix A: Note from Chapter 1). To this end, we assume that N/C ratios are given by the ratio of influx and efflux rates, where efflux rates are purely passive and influx rates have additive contributions of both passive and facilitated diffusion. Then, we assume as experimentally verified that **i)** passive influx and efflux rates (which are equal) decrease as MW increases, **ii)** passive influx and efflux rates increase when nuclear force is applied, but this effect disappears as MW increases, **iii)** facilitated influx rates increase with nuclear force and with NLS sequence affinity, but do not depend on MW. We also assume that there is a limit to the efficiency of active facilitated transport, and therefore **iv)** N/C ratios saturate and cannot increase above a given level. In such a saturation regime, changes in influx and efflux rates can no longer behave differently and should be matched. The potential origin of this is discussed in the more detailed, kinetic model introduced later in the manuscript. With these assumptions, we can plot two simple diagrams showing how N/C ratios should depend on MW and NLS affinity before applying force to the nucleus (Figure 11a), and their fold change with force, i.e., their mechanosensitivity (Figure 11b). According to this framework, for low MW or a weak NLS, passive diffusion dominates over facilitated import, leading to N/C ratios close to 1 independently of nuclear force. For high MW or a strong NLS, facilitated import dominates over diffusion, leading to high, saturated N/C ratios, also independently of nuclear force. However, when passive and facilitated rates are comparable, they depend differently on force, leading to mechanosensitive N/C ratios. As MW decreases (and passive diffusion increases) a progressively higher facilitated influx is required to match passive diffusion, and thus the “mechanosensitive zone” is placed along a diagonal in Figure 11b.

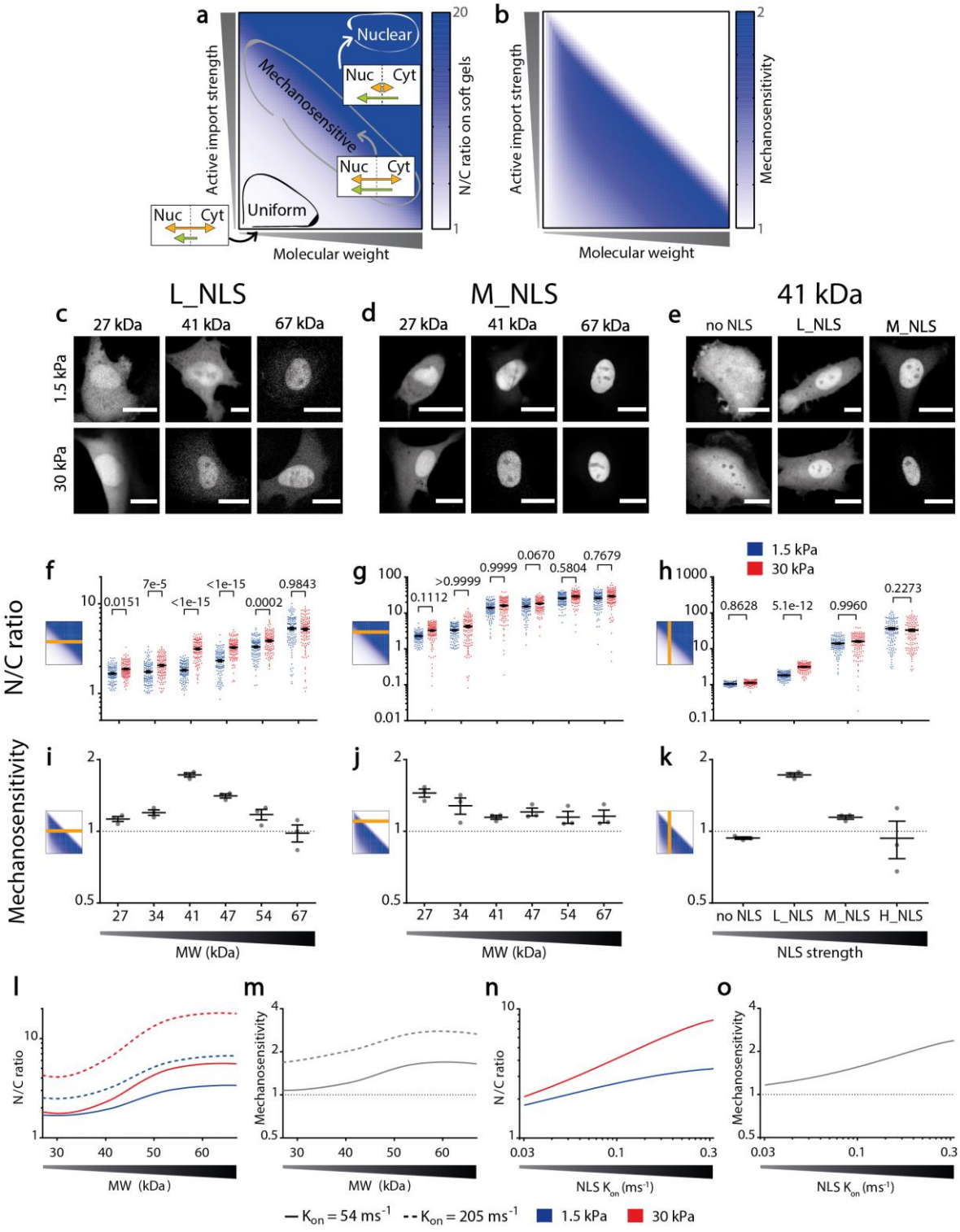

Figure 11 Balance between affinity to importins and MW defines the mechanosensitivity of nuclear localization. a,b) Qualitative prediction from conceptual model of how MW and affinity to importins should affect N/C ratios (a) on soft substrates and their mechanosensitivity (b) (see methods). Mechanosensitivity is defined as $(N/C)_{stiff}/(N/C)_{soft}$. **c-e)** Representative examples of construct distribution in cells seeded in substrates of 1.5kPa or 30kPa, for L_NLS constructs at different MW,

M_NLS constructs at different MW, and 41kDa constructs at different NLS strengths. **f-h)** N/C ratios corresponding to the same conditions as C-E. **i-k)** Mechanosensitivity corresponding to the same conditions as C-E. **l-m)** Kinetic model predictions of N/C ratios (l) and mechanosensitivities (m) for NLS of different affinities for importin α (modelled through the binding rates k_{on} between the NLS and importin α, with values of 54 and 205 ms^{-1}) as a function of MW. **n-o)** Model predictions of N/C ratios (n) and mechanosensitivities (o) for 41kDa constructs, as a function of increasing NLS strength. Statistics: f) N= 120 cells from 3 independent experiments. Both MW (p<1e-15) and Stiffness (p<1e-15) effects tested significant. g) N= 120 cells from 3 independent experiments. Both MW (p<1e-15) and Stiffness (p=0,0015) effects tested significant. h) N= 120 cells from 3 independent experiments. Both NLS strength (p<1e-15) and Stiffness (p=0,0012) effects tested significant. Two-way ANOVA, Šídák's multiple comparisons test was used to obtain p-values between conditions. Scale bars: 20 µm. Data are mean ±SEM.

We then verified the different predictions of the conceptual model by using the different constructs. First, for proteins with a fixed NLS sequence (L_NLS), N/C ratios increased with MW monotonically, but mechanosensitivity peaked at an intermediate MW between the high passive diffusion regime (low MW) and the saturated regime (high MW) (Figure 11c,f,i). Of note, increasing N/C ratios also led to increased variability in measurements, due to the increased noise caused by the low cytoplasmic signal (Figure 12). Second, increasing MW in proteins with a fixed NLS sequence of higher affinity (M_NLS) moved the point of maximum mechanosensitivity to a lower MW (Figure 11d,g,j). Finally, increasing NLS affinity in proteins with a fixed MW (41 kDa) also increased N/C ratios monotonically, but affected mechanosensitivity in a biphasic manner (Figure 11e,h,k). For this last set of constructs, we also used the highly nuclear and not mechanosensitive H_NLS construct to verify that force application with AFM did not lead to the same response as in mechanosensitive constructs (Figure 10l-n).

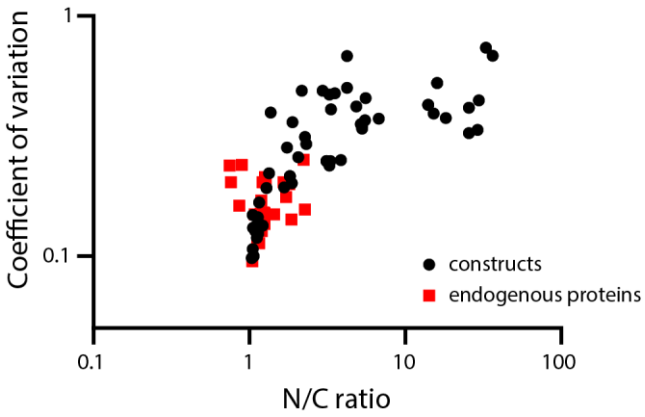

Figure 12 Noise levels in N/C ratio measurements. Relationship between mean N/C ratio as reported in figures, and corresponding coefficient of variation (standard deviation divided by the mean). The different points show all different constructs and conditions reported in the manuscript. Black dots indicate values of overexpressed engineered constructs, red squares indicate values of stained endogenous proteins.

Our conceptual model thus provides a useful framework to interpret our results, but it does not consider important elements of nucleocytoplasmic transport, such as the Ran cycle, or the fact that facilitated transport is reversible and can operate in both directions (Kopito & Elbaum, 2009). To address this, we developed a more elaborate kinetic mathematical model, which follows a canonical description of importin-mediated nucleocytoplasmic transport. This includes docking, undocking, and bidirectional translocation of importins in different intermediate forms, competitive binding of cargo and RanGTP to importins, the Ran cycle, and passive diffusion of unbound cargo molecules (see 9. Appendix A: Note from Chapter 1) (Cautain et al., 2015; Görlich et al., 2003; Jovanovic-Talisman & Zilman, 2017; S. Kim & Elbaum, 2013a). To model the effect of force on passive diffusion, we used the experimentally measured passive diffusion rates as a function of force and MW from Figure 5e,f. For facilitated diffusion, we simply assumed that force reduces the mean time required for importin-cargo complexes to cross NPCs (in a MW-independent way), without changing any other parameter.

The kinetic model correctly predicted the increase of N/C ratios, and of their mechanosensitivity, with MW and NLS affinity (Figure 11l-o). Interestingly, as NLS affinities increase, the model predicted an increase not only in influx rates but to a lesser degree also efflux rates, something which we confirmed experimentally (Figure 13). This occurs because as NLS affinity increases, cargo molecules can compete with Ran-GTP for binding importins, limiting the ability of Ran-GTP to disassemble the cargo-importin complex. This leads to the facilitated diffusion of importin-cargo complexes out of (and not only into) the nucleus. Eventually and for very high NLS affinities, the model predicted that N/C ratios would first saturate and then collapse, as cargo becomes so tightly bound to importins that it diffuses with it out of the nucleus regardless of Ran-GTP (Figure 13). This was not observed in experiments, and likely corresponds to non-physiological high affinities. The only experimental feature that the kinetic model did not capture was the fact that high MWs or NLS affinities decreased mechanosensitivity (Figure 11i-k). Instead, the model predicted that mechanosensitivity should be maintained even in this regime (Figure 11m,o). Potentially, this could be because the model underestimated the effect of NLS affinity on efflux rates (Figure 13). If efflux rates are mediated by facilitated rather than passive diffusion, then their dependency on force is the same as that of influx rates, and the overall effect on N/C ratios cancels out.

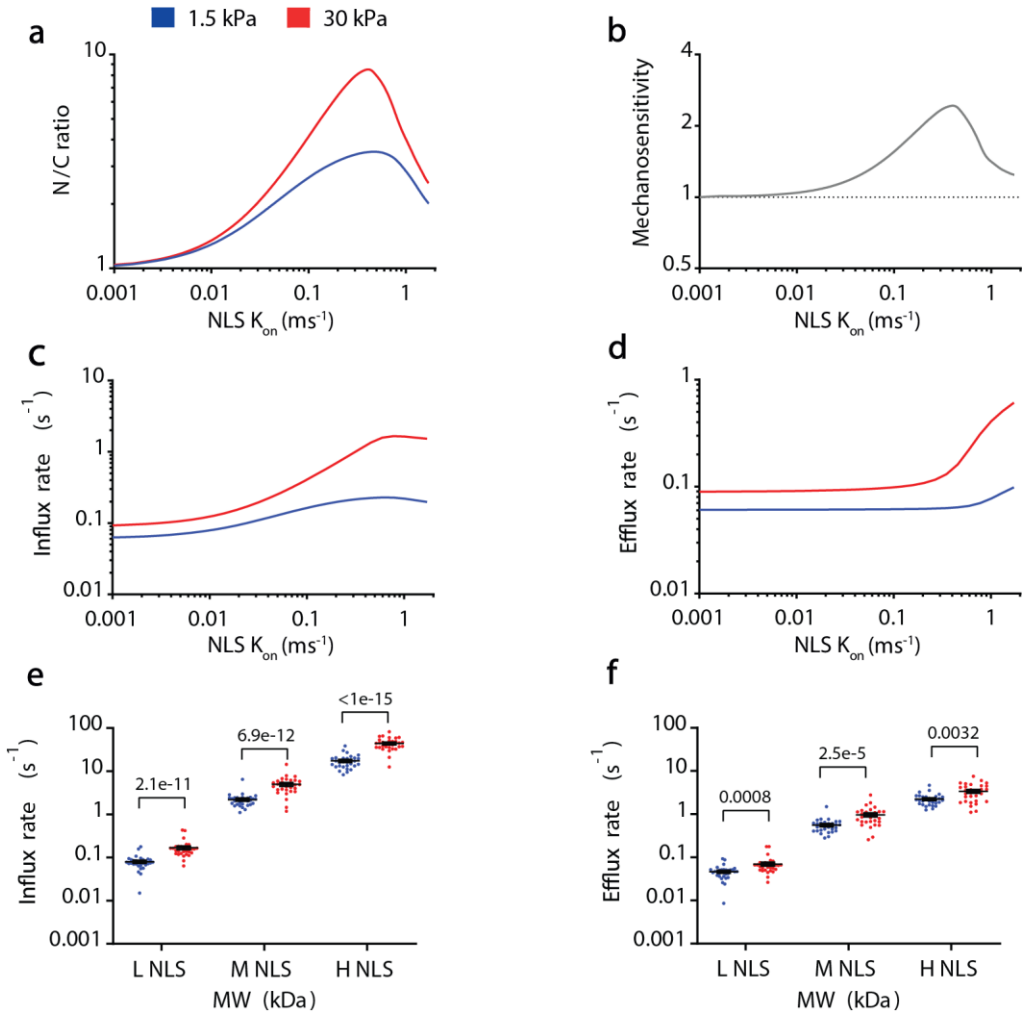

Figure 13 Effect of the affinity of the NLS signal in influx and efflux rates. a-d) Model predictions for N/C ratios (a), mechanosensitivities (b), influx rates (c) and efflux rates (d) for 41kDa constructs as a function of NLS affinity (modelled by the binding rate k_{on} between the NLS and importin α). **e-f)** Experimental Influx and efflux rates of 41 kDa constructs containing NLS signals of different affinity for importin β. In both cases (e,f), NLS strength and substrate stiffness effects tested significant (respectively: e) p<1e-15, p<1e-15, f) p<1e-15, p=2.4e-10). N= 30 cells from 3 independent experiments. p-values from Two-way ANOVA. Data are mean ±SEM. Mechanosensitivity of facilitated export.

Given the observed mechanosensitivity of active nuclear import, one might expect a similar (but reversed) behaviour for active export. To test this, we developed constructs by combining PrA repeats with different NES signals of different strength (Kanwal et al., 2004) (see Table 2). N/C ratios changed as expected with MW and NES strength (by following the opposite trends than NLS constructs, Figure 14a-i). The mechanosensitivity of the constructs also behaved in the opposite way, with constructs leaving (rather than entering) the nucleus with force (Figure 14g-i). Consistently, influx and efflux rates of NES constructs also had opposite trends with MW than NLS constructs: efflux rates were largely independent of MW, whereas influx rates showed a strong

dependence, mimicking diffusive constructs (Figure 13a,b). Confirming the effect of force, applying force to the nucleus with AFM to the most mechanosensitive NES construct (H_NES-EGFP-2PrA 41 kDa) led to a reduction of N/C ratios (Figure 14j-l). Interestingly, mechanosensitivity of the NES constructs was systematically milder than that of the NLS constructs. This is consistent with the behaviour of the light inducible construct (Figure 4b), which had a stiffness-dependent localization when controlled by active import (no light excitation) but not when controlled by active export (under light excitation). This lower mechanosensitivity of active export as compared to import may be related to the many differences between the transport cycles in both directions, and particularly the fact that NES-mediated export, unlike NLS-mediated import, is directly coupled to the hydrolysis of Ran-GTP (Cautain et al., 2015; S. Kim & Elbaum, 2013a, 2013b). However, another potential intuitive explanation could be that a concentration gradient is more easily generated by accumulating proteins in a small compartment (the nucleus) than a large one (the cytoplasm). In line with this hypothesis, model predictions obtained by inverting nuclear and cytoplasmic volumes led to lower N/C ratios and mechanosensitivity (Figure 15).

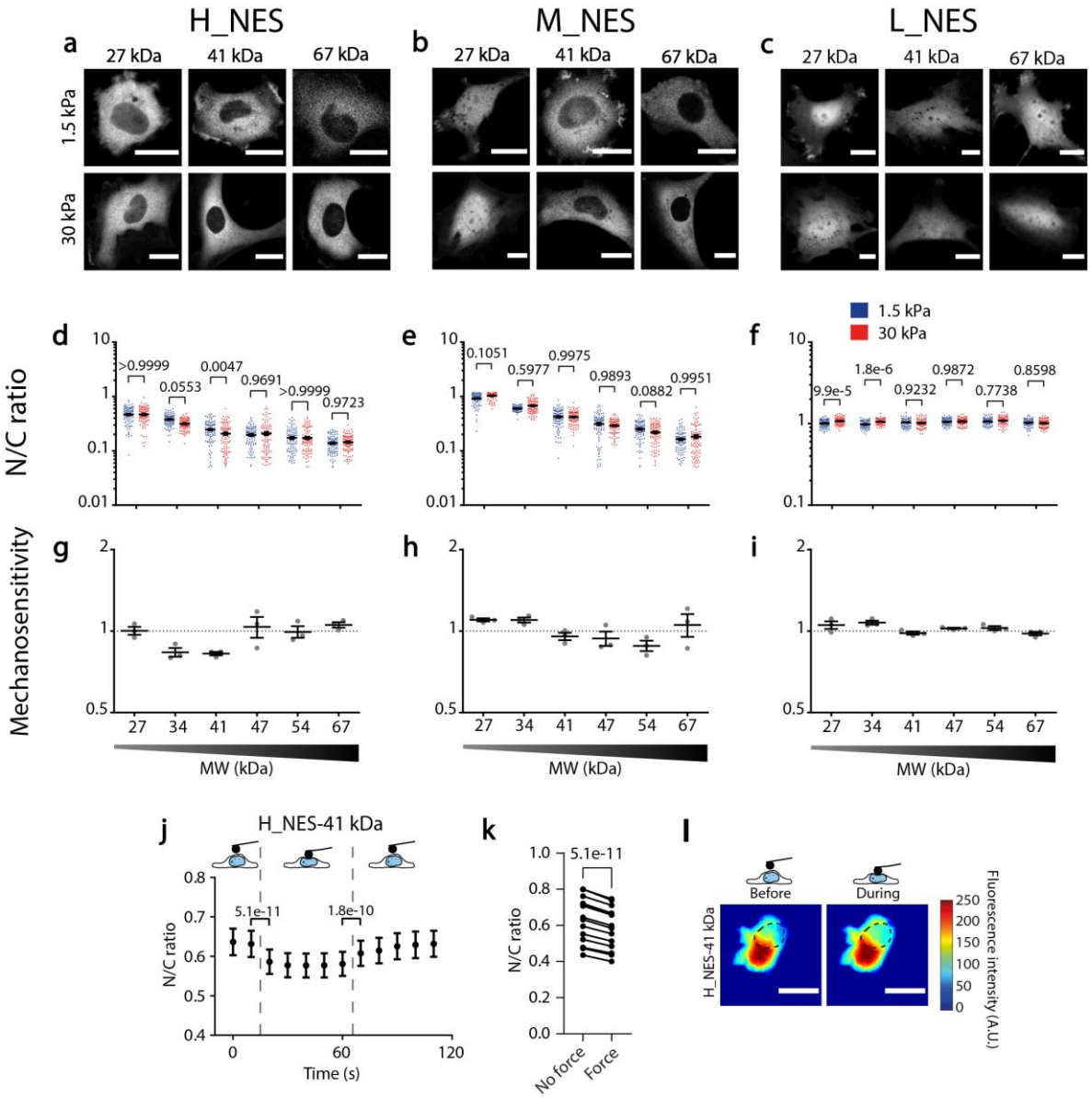

Figure 14 Balance between affinity to Exportin1 and MW defines the mechanosensitivity of nuclear localization in constructs containing NES signals. **a-c)** Representative examples of construct distribution in cells seeded in substrates of 1.5kPa or 30kPa, for H_NES constructs at different MW, M_NES constructs at different MW, and L_NES constructs at different MW. **d-f)** N/C ratios corresponding to the same conditions as A-C. d) N= 90 cells from 3 independent experiments. Both MW (p<1e-15) and Stiffness (p=0,0162) effects tested significant. e) N= 120 cells from 3 independent experiments. Only MW effects tested significant (p<1e-15). f) N= 90 cells from 3 independent experiments. Both MW (p<1e-15) and Stiffness (p=0,0001) effects tested significant. Two-way ANOVA, Šídák's multiple comparisons test was used to obtain p-values between conditions. **g-i**) Mechanosensitivity corresponding to the same conditions as A-C. Mechanosensitivity is defined as $(N/C)_{stiff}/(N/C)_{soft}$ (n=3 experiments). **j)** N/C ratios of H_NES 41 kDa construct in cells seeded on 1.5 kPa gels before, during, and after nuclear deformation with AFM. **k)** From data in j, paired dot plots of the time points right before and after force application. In j and k, N= 15 cells from 3 independent

experiments. p-values were calculated with a two-tailed paired t-test, traces of all cells are shown in Figure 9. **I)** Corresponding images of constructs before and during force application, dotted line marks nucleus outline. Scale bars 20µm. Data are mean ±SEM.

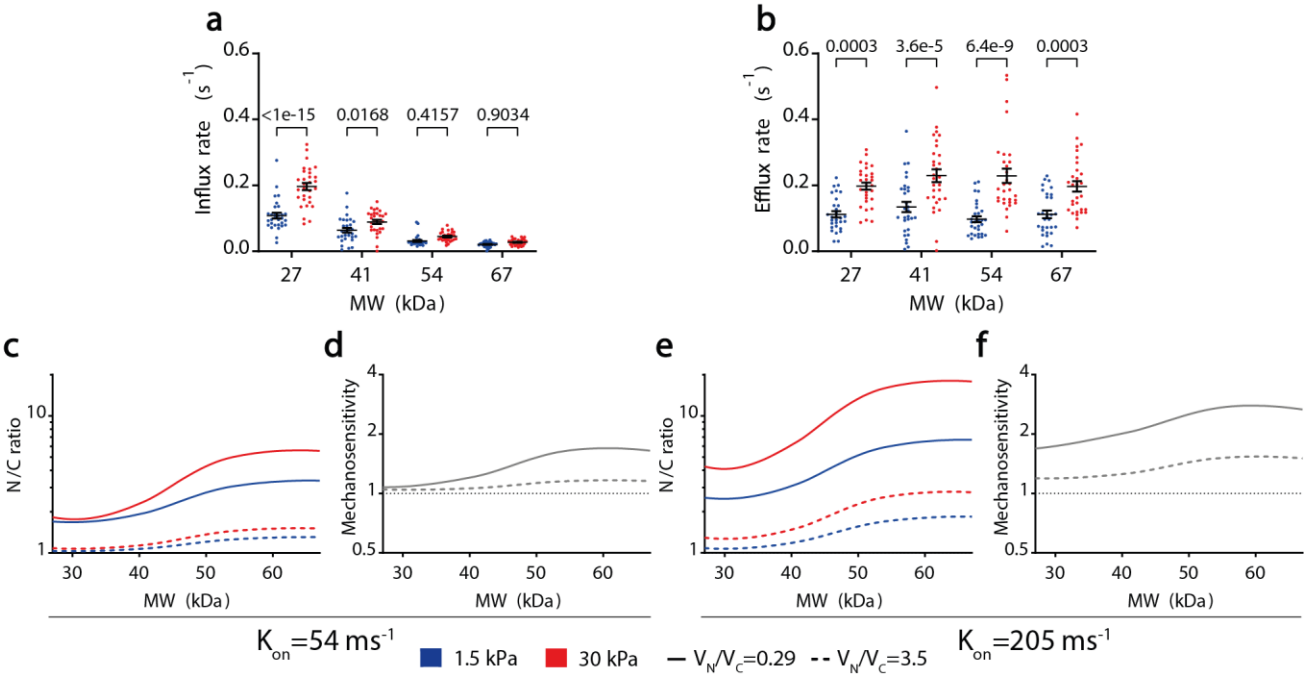

Figure 15 Further experiments and modelling results regarding NES constructs. a-b) For M_NES constructs, influx rates (mediated by passive transport) and efflux rates (mediated by facilitated transport) as a function of molecular weight. N= 30 cells from 3 independent experiments. Substrate stiffness effects tested significative in both cases (a) p=5.1e-13; b) p<1e-15); MW only tested significative for influx, a) p<1e-15; b) p=0.2138). Two-way ANOVA, Šídák's multiple comparisons test was used to obtain p-values between conditions. Data presented as mean ±SEM. **c-d)** Model predictions of N/C ratios (c) and mechanosensitivities (d) for an NLS with a binding rate k_{on} of 54 ms^{-1} as a function of MW. Data are shown for experimentally measured N/C volume ratios (0.29) and for inverted volume ratios (3.5). **e-f)** Same predictions as in c,d for an NLS with a binding rate k_{on} of 205 ms^{-1}. Note that these predictions simply evaluate the role of N/C volumes on import, they do not explicitly model the export cycle (and hence mechanosensitivities are above and not below 1).

4.5. Mechanosensitivity of transcriptional regulators.

Finally, we evaluated whether nucleocytoplasmic transport can explain the reported mechanosensitivity of different transcriptional regulators. Different transcriptional regulators localize to the nucleus with force in different contexts, including YAP (Dupont et al., 2011; Elosegui-Artola et al., 2017), twist1 (Wei et al., 2015), snail (K. Zhang et al., 2016), SMAD3 (Furumatsu et al., 2012), GATA2 (Mammoto et al., 2009), and NFκβ (Ishihara et al., 2013). If their mechanosensitivity is explained by regulation of nucleocytoplasmic transport with nuclear force, then it should be abolished by preventing either force transmission to the nucleus (by overexpressing DN-KASH) or nucleocytoplasmic transport (by overexpressing either DN-Ran, a dominant-negative version of Ran

(Bischoff et al., 1994), or by treatment with importazole, a drug which blocks active import by importin β (Soderholm et al., 2011). For the case of YAP, we previously showed that its mechanosensitivity is abrogated by both factors (Elosegui-Artola et al., 2017). Regarding the rest, GATA2 and NFκβ exhibited a very low mechanosensitivity in our system (Figure 16), but SMAD3, Snail, and Twist1 showed a clear response (Figure 16 and Figure 17a,b). In all cases, mechanosensitivity was abrogated by DN-KASH, DN-Ran, or importazole (Figure 16 and Figure 17a,b). Interestingly and consistent with our finding that NLS constructs were more mechanosensitive than NES constructs, SMAD3 mechanosensitivity was higher for cells treated with TGFβ (which induces SMAD3 nuclear import) than with lapatinib (which induces SMAD3 nuclear export) (Huang et al., 2018).

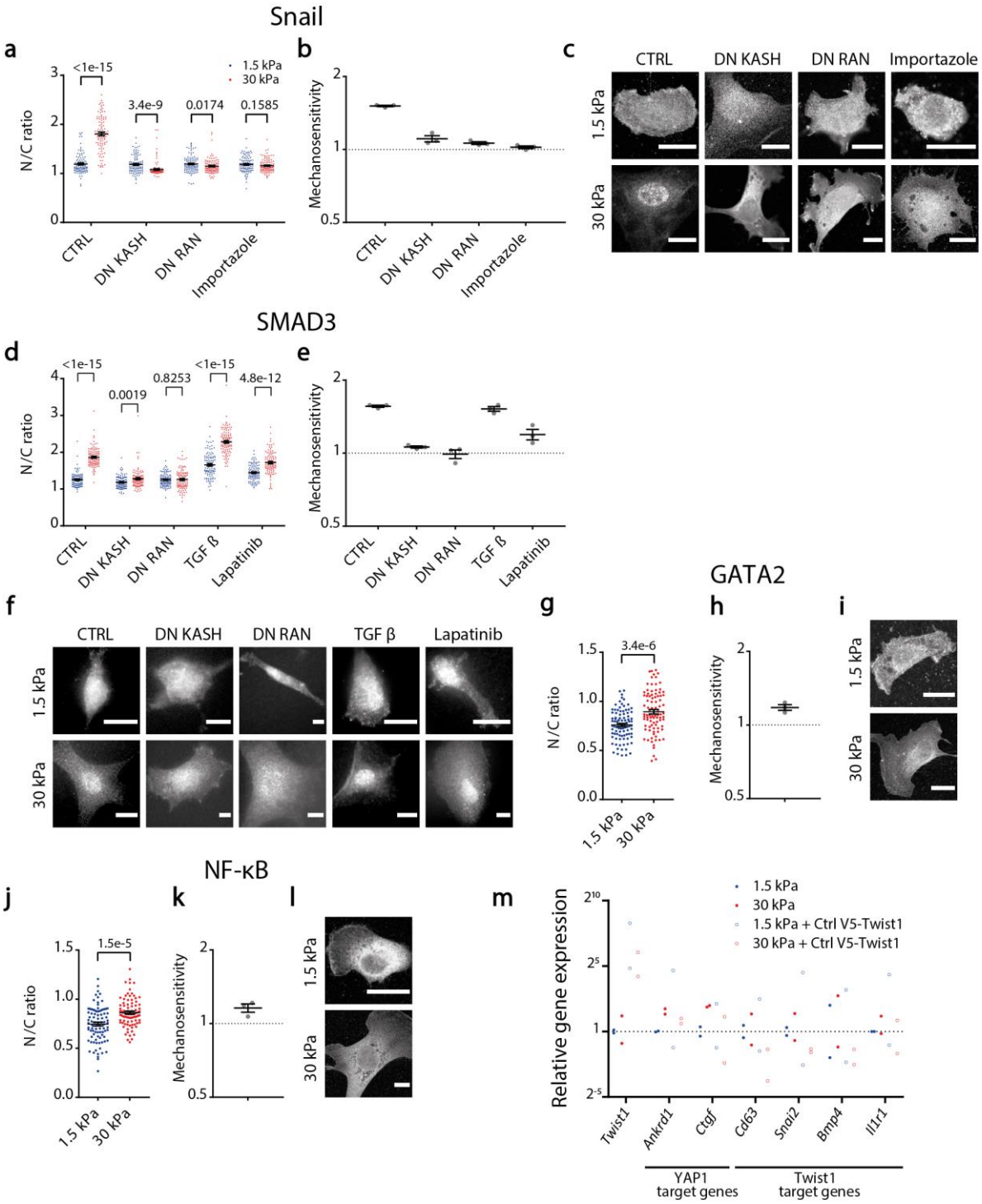

Figure 16 a-c) For Snail stainings at different conditions, quantifications of N/C ratios on 1.5/30 kPa substrates (a , N= 100 cells from 3 independent repeats), corresponding mechanosensitivities for the 3 different repeats (b), and representative images (c). d-f) For SMAD3 stainings at different conditions, quantifications of N/C ratios on 1.5/30 kPa substrates (d, N= 100 cells from 3 different repeats), corresponding mechanosensitivities for the 3 different repeats (e), and representative images (f). g-i) For GATA2 stainings at different conditions, quantifications of N/C ratios on 1.5/30 kPa

substrates (g, N= 90 cells from 3 independent repeats), Corresponding mechanosensitivities for the 3 different repeats (h), and representative images (i). **j-l)** For NF-κβ stainings at different conditions, quantifications of N/C ratios on 1.5/30 kPa substrates, (j, N= 90 cells from 3 independent repeats), corresponding mechanosensitivities for the 3 different repeats (k), and representative images (l). For a-l, data are presented as mean ±SEM, scale bars correspond to 20 µm, and p-values from corrected multiple two-tailed Mann-Whitney (a,d) and two-tailed Mann-Whitney (g,j) tests. **m)** Relative gene expression of different genes as assessed with qPCR. Conditions are cells seeded on 1.5 or 30 kPa substrates, overexpressing or not a WT twist1 construct (Ctrl V5-twist1). Gene expression is shown relative to the 1.5 kPa condition without overexpression. n=2 independent experimental repeats.

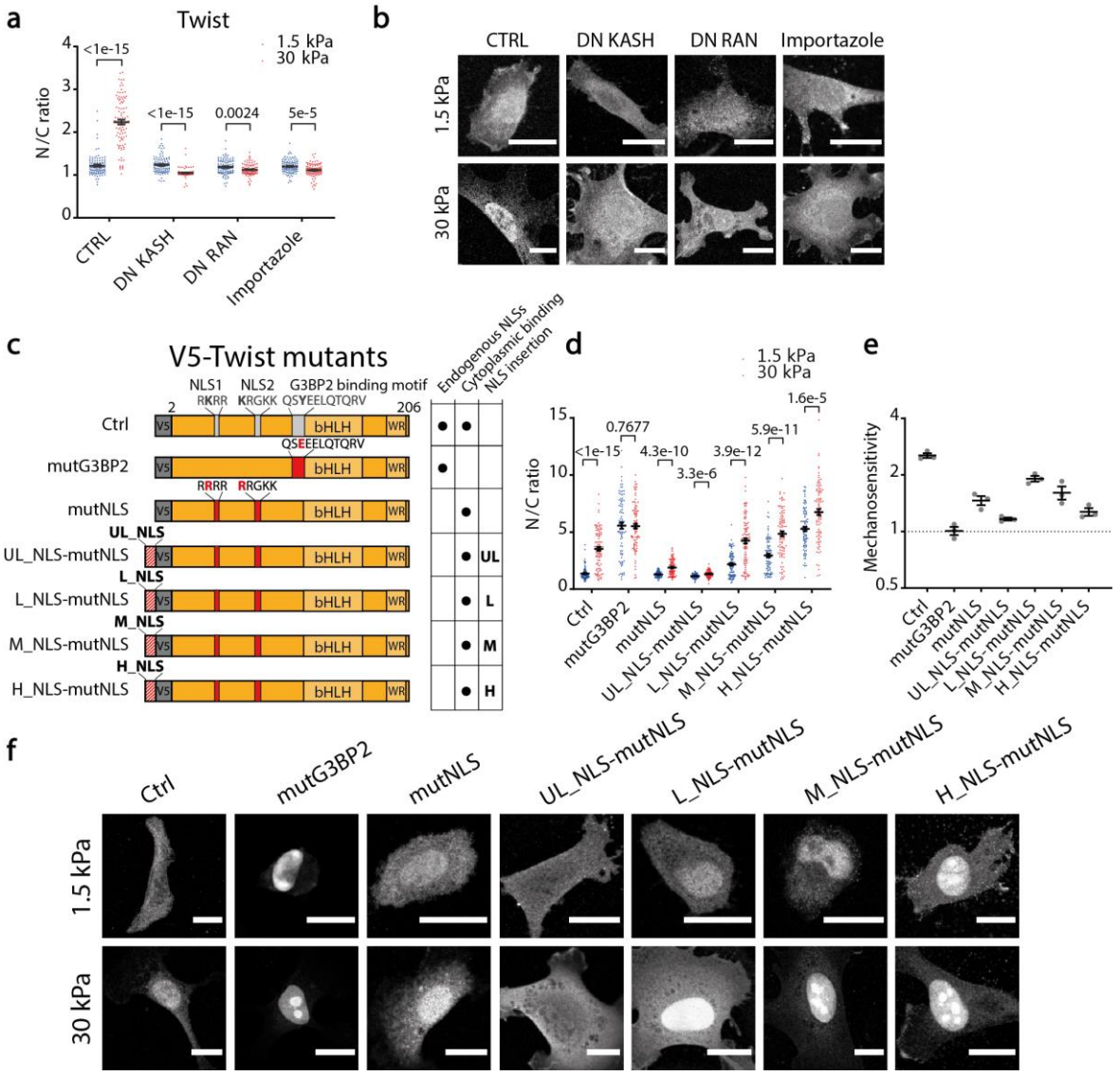

Figure 17 The mechanosensitivity of twist1 can be re-engineered with exogenous NLS sequences. a) N/C ratios of endogenous twist1 for cells on 1.5/30 kPa substrates, and under indicated treatments. N= 100 cells from 3 independent experiments. p-values from two-tailed Mann-Whitney tests,

corrected for multiple tests in the intracondition comparisons with the two-stage step-up method of Benjamini, Krieger and Yekuteili. **b)** Corresponding images of twist1 distribution. **c)** Scheme of different twist1 mutants. Mutations inactivating both NLS sequences and the G3BP2 binding motif are indicated in red. **d)** N/C ratios of transfected twist1 mutants for cells on 1.5/30 kPa substrates. N= 90 cells from 3 independent experiments. p-values from two-tailed Mann-Whitney tests, corrected for multiple tests with the two-stage step-up method of Benjamini, Krieger and Yekuteili. **e)** Corresponding construct mechanosensitivities, defined as $(N/C)_{stiff}/(N/C)_{soft}$ (N= 3 experiments). **f)** Corresponding images showing the distribution of the different mutants. Scale bars, 20 µm, data are mean ±SEM.

Thus, the mechanosensitivity of several transcriptional regulators is controlled by force-induced effects in nucleocytoplasmic transport. Our proposed mechanism also has the stronger implication that mechanosensitivity can be engineered simply by selecting the appropriate levels of affinity to importins. To verify this, we took twist1 as a convenient model, since its NLS sequences are known, and their function can be abolished with point mutations (Singh & Gramolini, 2009). Further, its mechanosensitivity depends on its binding to G3BP2, which retains twist1 in the cytoplasm (K. Zhang et al., 2016). We first overexpressed wild-type twist1 in cells, which retained the mechanosensitivity of endogenous twist1 (Figure 17c-f). Of note, changes in twist1 caused by either stiffness or overexpression did not consistently increase the expression of twist1 target genes (Figure 16). Thus, twist1 serves as a model for protein localization but not transcription. Then, we overexpressed a G3BP2 binding deficient mutant, mutG3BP2. As expected, this led to high N/C ratios on both soft and stiff substrates, thereby losing mechanosensitivity. Confirming the role of nucleocytoplasmic transport, the NLS dead mutant (mutNLS, still under the control of G3BP2), lost the nuclear localization in both soft and stiff substrates, thereby also losing mechanosensitivity (although not completely, Figure 17c-f). We then assessed whether we could restore twist1 mechanosensitivity by rescuing twist mutNLS not with its endogenous NLS, but by exogenously adding our different characterized NLS sequences (plus an additional ultra-low affinity sequence, UL_NLS). Adding NLS sequences of different strength mimicked the effects seen in Figure 11: as the NLS strength increased, nuclear localization progressively increased, and mechanosensitivity was highest at a low strength (L_NLS), where it was almost as high as in the endogenous case. Thus, simply substituting the endogenous twist1 NLS with an exogenous one of the appropriate strength, not regulated by any twist-1 related signalling mechanism, recapitulates its mechanosensitivity.

5. Results. Chapter 2: Study of the mechanical regulation of nucleocytoplasmic transport in multicellular systems

As we have proven in the results from Chapter 1, nucleocytoplasmic transport is mechanosensitive and forces affect differentially active and passive transport (Andreu, Granero-Moya, et al., 2022). This fact affects protein shuttling between both compartments, controlling their steady state localization. We have studied this mechanotransduction process in single cells. However, in most biological environments cells are surrounded by other cells, some of them establishing cell-to-cell contacts. Despite the multicellular knowledge presented in section *1.5 Nuclear mechanosensing in cell layers*, it is unknown how forces reach the nucleus and nuclear mechanotransduction happens in multicellular systems. Does force-induced increase in nucleocytoplasmic transport in multicellular systems work the same way as in single cells? Do cell-cell contacts add another layer of complexity in nuclear mechanotransduction? Do all eukaryotic cells respond the same way to nuclear membrane stretch?

For the study in Chapter 1, we have created a battery of proteins that have different passage rates in terms of active and passive transport (Figure 8e and Table 1). These proteins present mechanosensitive shuttling rates, meaning that shuttling rates are higher when cells are seeded on stiff substrates and the nucleus is under higher tension. And some show a mechanosensitive localization, meaning that the nuclear-to-cytoplasmic ratio (N/C ratio) changes if the forces reaching the nucleus change. For being mechanosensitive, these latter have the accurate combination of affinity to importin α and diffusion rate. Among those artificial constructs, there is a protein that presents the biggest changes in mechanosensitive localization: L_NLS-41 kDa (Figure 8f-i). L_NLS-41 kDa is an innocuous protein that only interacts with the active transport machinery at the NPC. Apart from those contacts, its diffusion rates in the cytoplasm and the nucleoplasm indicate that it is a freely diffusing molecule (Figure 6e). Therefore, it is a suitable molecule to be used a as Sensor of nuclear force-related changes in nucleocytoplasmic transport, which fulfills Aim 1.4. Henceforth it will be referred as (the) *Sensor*.

Taking all this into account, Chapter 2 is focused on how forces to the nucleus affect nucleocytoplasmic transport in multicellular systems. And it is devoted to Aim 2, which involves using the Sensor to study nuclear mechanotransduction in cell layers.

5.1. Multicellular system characterization

To investigate how forces in the nucleus produce changes in nucleocytoplasmic transport, we have used MCF-7 and C-26 stable cell lines expressing the Sensor. These cell lines have been created in collaboration with Jaccko van Rheenen's group at NKI (Netherlands Cancer Institute).

MCF-7 are epithelial cells isolated from metastatic adenorcarcioma of a human breast tumour and are used for breast cancer research and many mechanobiological studies. Due to their epithelial phenotype, which makes them have strong cell-cell adhesions, they are an interesting model to study how forces to the nucleus are transmitted in a multicellular system, and are suitable for future studies involving cancer research. C-26 is murine colon adenocarcinoma cell line (also named MCA-26, CT-26, and Colo-26) (Corbett et al., 1975). It has a mesenchymal phenotype, therefore its behavior in cell-cell contacts differs from MCF-7 which is an epithelial cell line (Ahlstrom & Erickson,

2007). Working with epithelial and mesenchymal cell lines allows us to produce information on the two ends (or phenotypes) of EMT (Epithelial-to-Mesenchymal Transition), a very important process during development, wound healing, fibrosis or metastasis (J. Yang & Weinberg, 2008).

To study how these cells respond when the nucleus is under force loads, we use a system of gaskets to: a) control seeding density, b) create an edge in the monolayer when the gasket is retrieved; see Figure 18. By controlling cell density, we can control cell packing and crowding, which in turn affects the forces that the cytoskeleton applies to the nucleus. With the gaskets in place, increasing the cell density reduces the available space cells have to spread, to the point that, over a certain threshold, cells form a multilayer with the tendency to form cell aggregates. Retrieving the gasket before imaging allows the cells to migrate out of the confined space and extend the cell layer. This creates different cell densities within very close regions, allowing us to compare nuclei submitted to very different mechanical forces in the exact same condition and same imaging process.

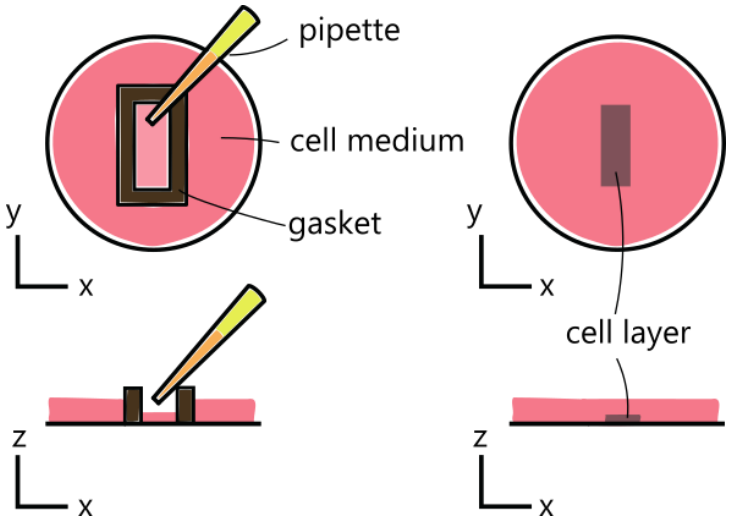

Figure 18 Cell layer seeding with a gasket

For the setup, we have used live optical confocal microscopy to acquire 3D images of the cell layer that is expressing the Sensor and with stained nuclei. The 3D images have been used to segment and measure nuclear morphology and the Sensor N/C ratio. First, the nuclei channel has been processed via Cellpose (Stringer et al., 2021) to obtain the nuclear mask, then this mask has been used in MATLAB to fit an ellipsoid and measure nuclear morphology, Sensor N/C ratio and shape parameters (Figure 19).

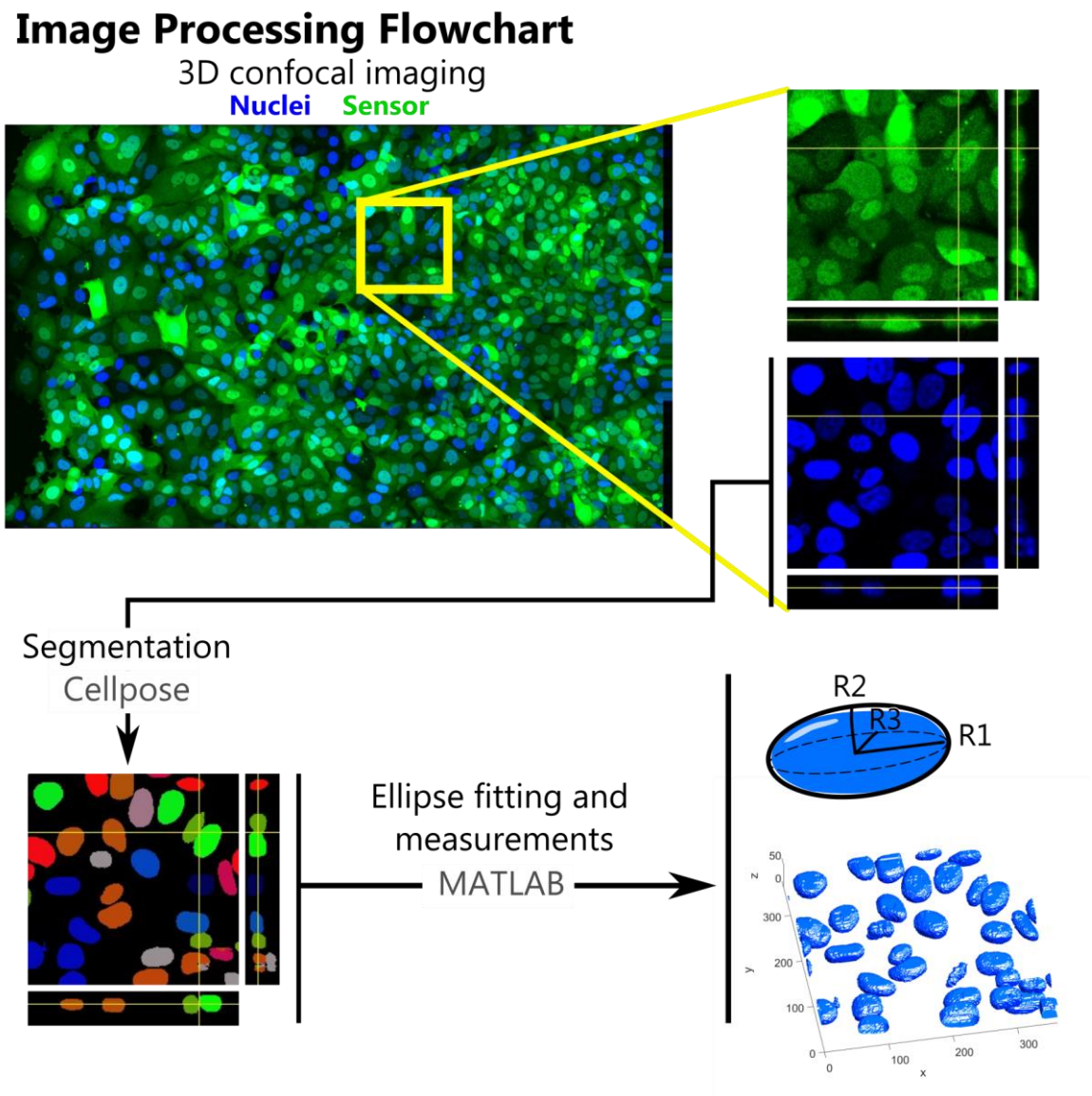

Figure 19 Image processing flowchart. Example live image of a MCF-7 monolayer, whose nuclear staining channel is then segmented and processed for nuclei feature data extraction.

5.1.1. Cell density

We have performed different repeats to study the MCF-7 and the C-26 cell lines expressing the Sensor and using the gasket setup. For MCF-7, this has produced a dataset of around 10k cells (computed as nuclei), that yields 6k cells after a process of data curation to assure their quality and avoid data artifacts. For C-26, we have a dataset of 9k cells, and 6k cells after curing. Data curation involves checking steps to filter bad segmented nuclei, nuclei at the edges of the images, or, for example, discarding particles that are too small to be cell nuclei, like condensed chromosomes or nuclei after apoptosis.

To characterize the setup, the first analysis we made is to compare cell density to the distance of cells to the edge, where the gasket has been retrieved. As expected, cell density increases with the distance to the edge of the cell layer both in MCF-7 and C-26 cell lines (Figure 20 and Figure 21). When observing the sample in a bright field microscope, we can see differences in cell density at the centre of the gasket, probably due to slight changes in the way of seeding, the gasket shape, and the procedure of washing unattached cells. This is not a problem in a system where cell density is precisely measured, in fact, it allows for analysing the whole density spectrum; see *3.15.1 Density measurements*.

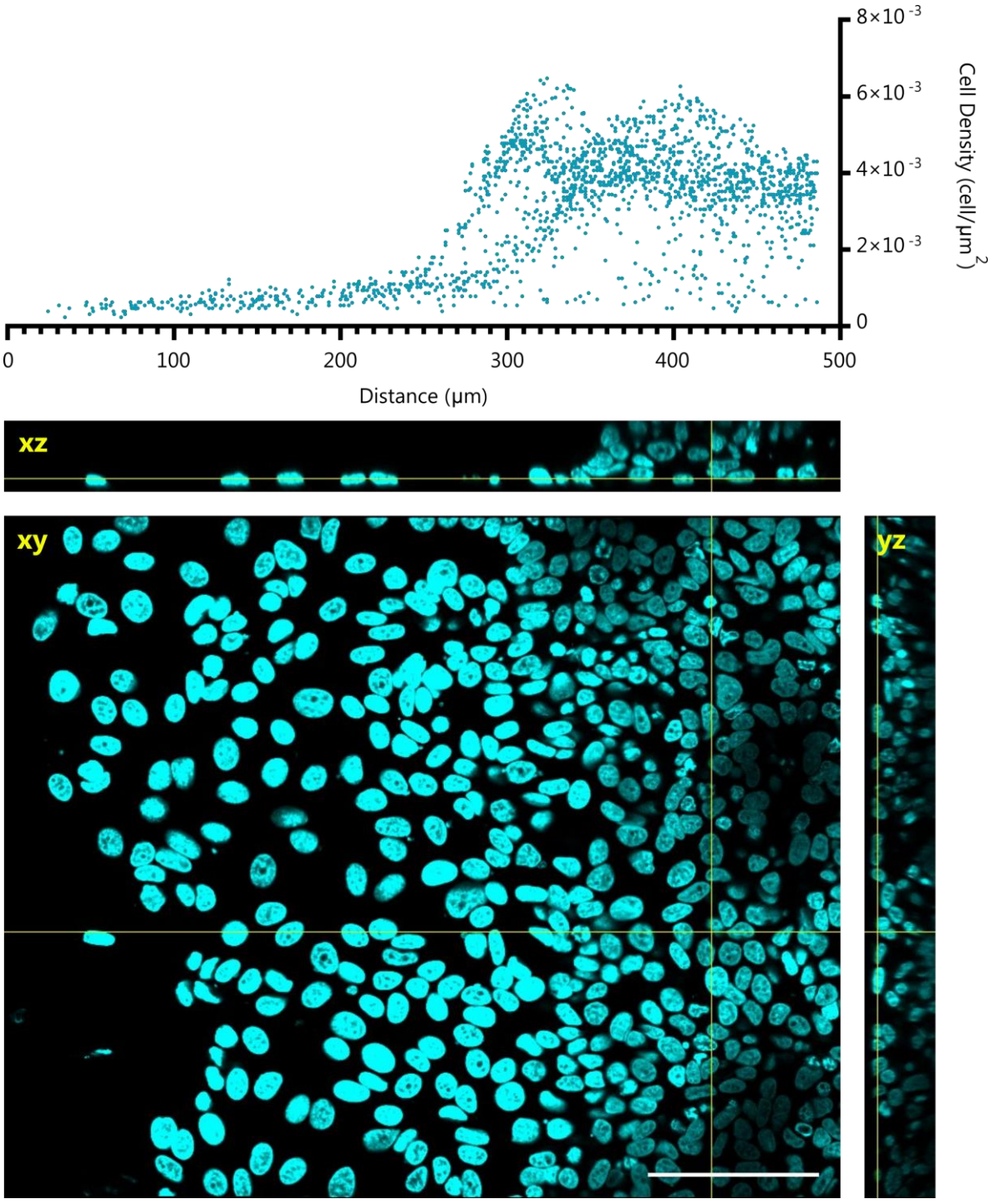

Figure 20 MCF-7 Density versus distance to the edge. *Every dot represents a cell. Image from cells fixed and stained with Hoechst. Data from a single repeat, which is depicted in the image with the orthogonal views. Scale bar: 100 µm.*

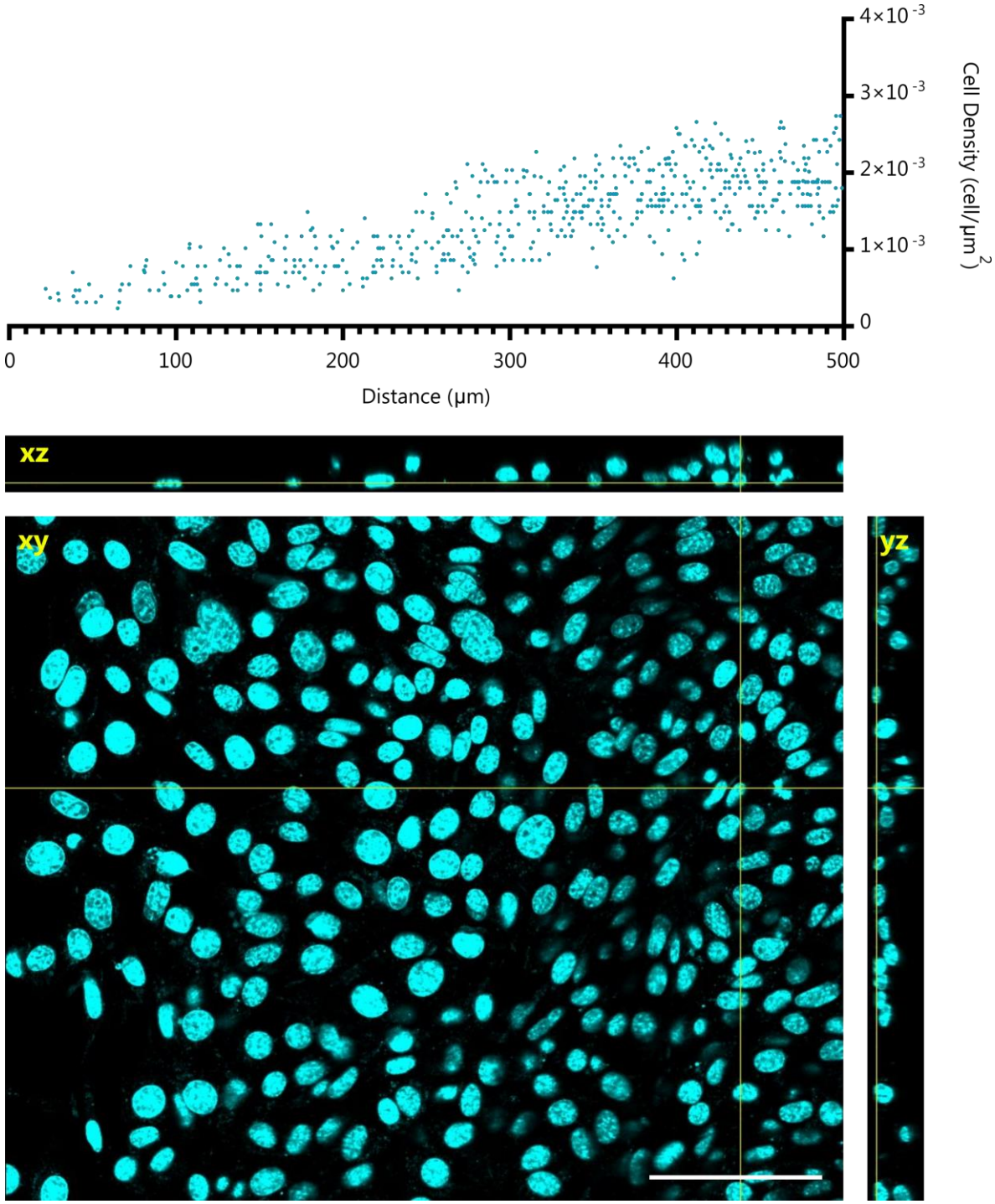

Figure 21 C-26 Density versus distance to the edge. *Every dot represents a cell. Image from cells fixed and stained with Hoechst. Data from a single repeat, which is depicted in the image with the orthogonal views. Scale bar: 100 µm.*

For an epithelial cell line as MCF-7, increasing cell density is a good strategy to change cell and nuclear shape and submit them to different forces, however, monolayer density has an upper limit. When the cell density threshold is crossed, cells start stacking and forming a multilayer, as can be

seen by plotting cell thickness and cell layer thickness versus density in Figure 22a. Over 1E-3 cell/µm^2, cell thickness and cell layer thickness start diverging, which means that cells start stacking up. At around 2E-3 cell/µm^2, the cell layer is already a multi-layer, and cells may have other cells over and/or under. Over that threshold, nuclear projected area in xy and nuclear volume reach their lowest values and increasing cell density only increases the cell layer thickness.

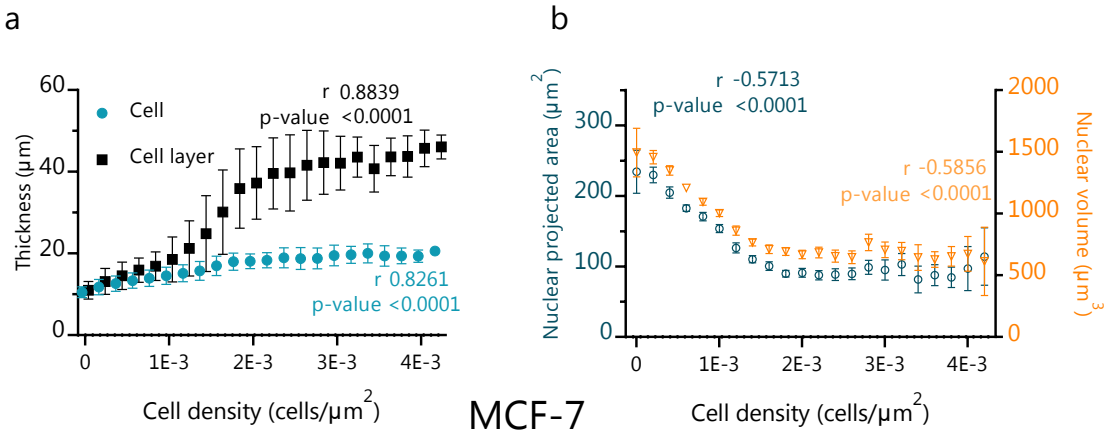

Figure 22 MCF-7 cell and cell layer morphology compared to cell density. a) *Cell and cell layer thickness. b) Nuclear projected area and Nuclear volume. Error bars depict 95% confidence interval. For all, N=5689, from 6 independent experiments.*

For a mesenchymal cell line as C-26, we can see differences compared to MCF-7. C-26 does not show a cell density region where density increases, and cells do not stack up to keep a monolayer topology (Figure 23). As soon as cells start touching the neighbors they start stacking up. This difference can be explained by the cell type and the presence or absence of specific cell-cell interactions.

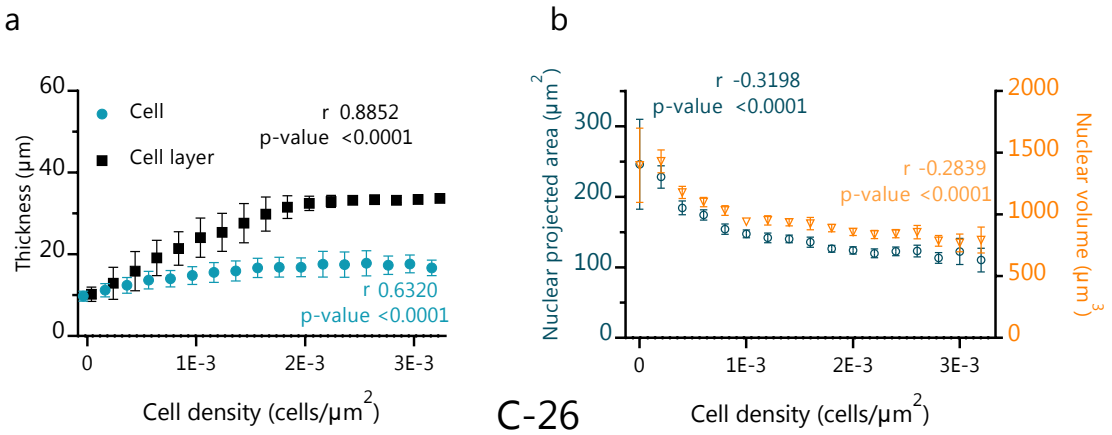

Figure 23 C-26 cell and cell layer morphology compared to cell density. a) *Cell and cell layer thickness. b) Nuclear projected area and Nuclear volume. Error bars depict 95% confidence interval. For all, N=5932, from 3 independent experiments.*

5.1.2. Nuclear morphology

The nucleus as a physical body inside of the cell has a certain viscoelasticity and can be considered active matter since it has its own (nucleo)skeleton, which reorganizes under tension. Our way to estimate how the nucleus is under different mechanical conditions is by its shape and its dimensions (area and volume), parameters that have been linked to nuclear mechanics in literature. The shape of the nucleus is a readout of the forces that it has undergone, and have deformed it, plus the ones that are still taking place, which make the nucleus store elastic energy.

Therefore, to further understand the mechanical state of the nuclei and how cells undergo nuclear mechanotransduction nucleocytoplasmic transport, we have analysed nuclear shape and dimension features. We have fitted an ellipsoid to every nucleus to obtain the length of the 3 axes that define this regular shape, and their orientation in the xyz space. This allows us to measure parameters such as the Oblateness, Prolateness, Nuclear Shape index, and Verticality of the nuclear shortest axis; we also calculate its Sphericity and Solidity (see Figure 24 for graphical examples).

Oblateness measures how an ellipsoidal shape approximates to a disk shape. A value of oblateness=1 would be the most disk-like shape possible: a circle. 2 radii are equal and the third one is equal to 0. Prolateness is analogous to oblateness, but in this case measures how the shape approximates to a rod shape. A long and thin bar would have a prolateness close to 1. Nuclear Shape index indicates how close is the fitted shape to a sphere. It doesn't have any specificity for oblate or prolate shapes; 1 would be a sphere, and 0 either a circle or a long bar. Nuclear Shape index is a precise way of measuring 3D shape and it is very similar to the flattening parameter used in previous works of our group (Elosegui-Artola et al., 2017).

Verticality of the nuclear shortest axis (R_3) indicates what is the z component of the shortest axis of the ellipsoid. Meaning that if R_3 is pointing upwards (parallel to the z dimension) the value will be one. If there is a deviation from the vertical of θ degrees, the value of verticality will be cos(θ). Sphericity indicates how much extra surface area there is for a certain amount of volume. A sphere is the 3D shape with the lowest surface area-to-volume ratio, therefore changing any of its radii and keeping the volume constant will necessarily increase its surface area. For two shapes with the same volume, one being spherical and the other being ellipsoidal, the first one would have Sphericity =1 and the second Sphericity <<1. Solidity, on the other hand, also takes into account the volume of the 3D shape but compares it with the convex hull volume. The convex hull volume is the volume of the shape plus the volume of the concave fold in it. Solidity is a measure for how smooth/convex or folded/concave is the shape.

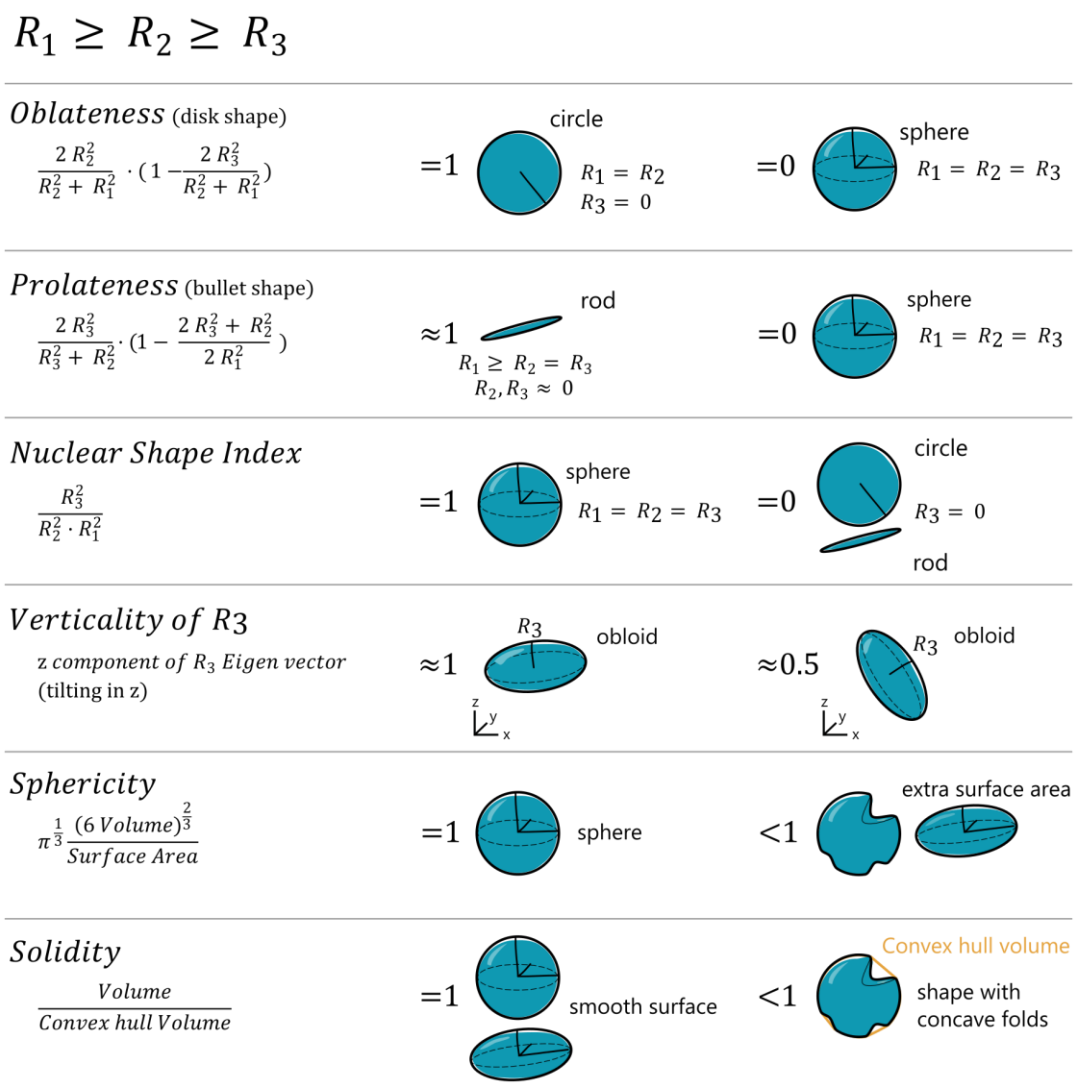

Figure 24 3D Shape parameters. *Formulae and graphical explanation on Oblateness, Prolateness, Nuclear Shape index, Verticality or R_3 (shortest axis), Sphericity, and Solidity*.

For MCF-7, cells at low densities have nuclei with discoidal shapes, which can be seen in Figure 20 and in the shape parameters. Oblateness is >0.5 at lowest densities and ≈0.4 at high densities (Figure 25a). Also, nuclei tend to be more prolate at higher densities (>0.4), mirroring the oblateness graph. At lower densities, the nuclear shape is the furthest from being a sphere, therefore Nuclear Shape index value is the lowest (≈0.35).

Verticality of R_3 indicates if the shortest dimension of the nucleus has any preferential orientation in the z-axis; in Figure 25b we can see that at low densities this verticality is maximal, while at higher densities cells have no preferential orientation in the z-axis. This is because a nucleus with an oblate shape placed in a region of low density has the shortest axis almost parallel to the z-axis and more

irregular or rounded shapes can have this shortest axis pointing in directions non-parallel to the z-axis.

Nuclei in lowest density zones tend to be discoidal and very smooth, which translates in high Solidity values, but far from being a sphere (Figure 25c). When cell density increases to 1E-3 cells/µm^2, nuclei are around 0.02 less solid, but have the highest Sphericity possible, because they are not so stretched, but still have space to their sides in the xy plane. When density increases up to 2E-3 cells/µm^2, Solidity drops to the minimum as well as Sphericity. Briefly, for MCF-7 shape goes from discoidal, to more spherical, to laterally compressed nuclei, as density increases.

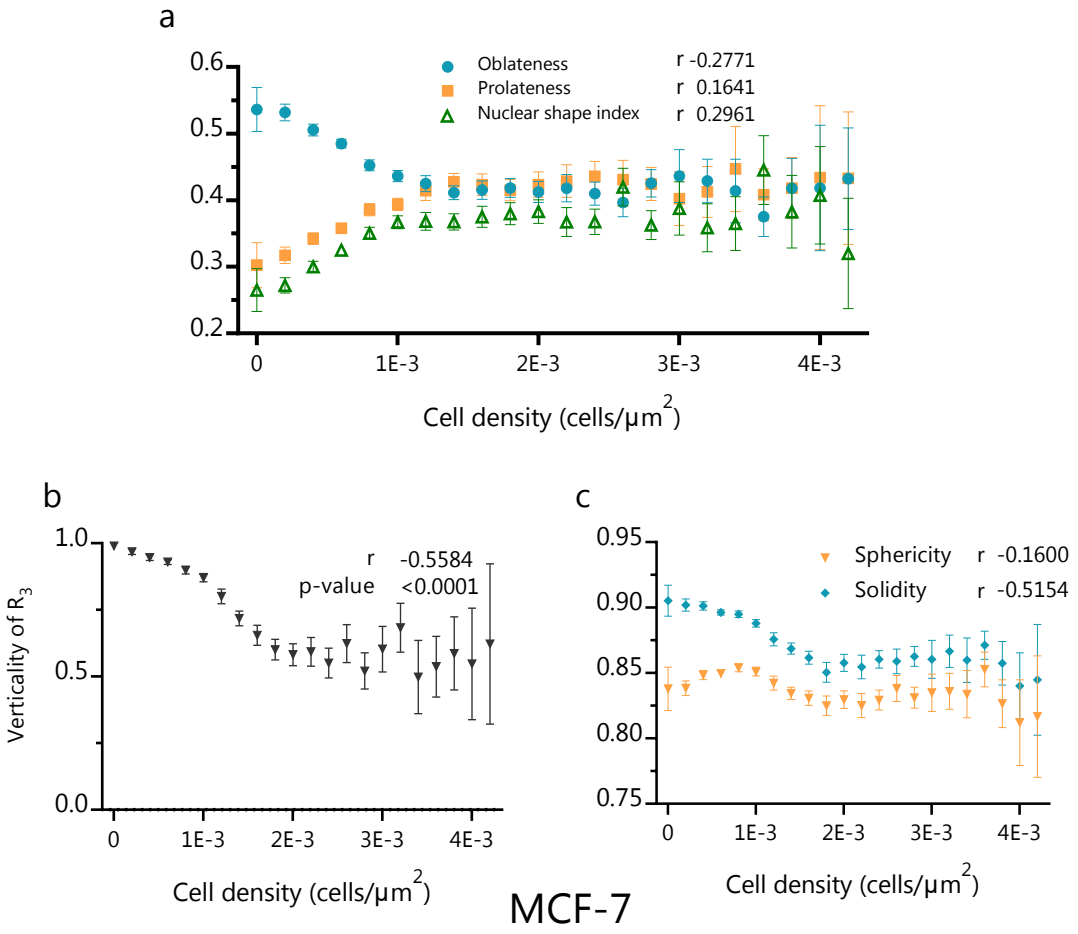

Figure 25 MCF-7 nuclear morphology parameters versus cell density. a*) Oblateness, Prolateness, Nuclear Shape index, b) Verticality of the shortest axis, c) Sphericity and Solidity. Error bars depict 95% confidence interval. In a) and c) all five correlations tested significative, p-value <0.0001. For all, N=5689, from 6 independent experiments.*

For C-26, we can see similar nuclear shape relationships with cell density (Figure 26). Nuclei are discoidal at the lowest densities and at high densities they are more prolate than oblate (Figure 26a). Verticality of R_3, the shortest axis of the ellipsoid, is maximal at low densities and decreases with increasing density. This means that at low densities discoidal nuclei have their shortest axis almost

parallel to the z-axis, and with increasing density nuclei become more roundish and bullet-shaped, which deviates the shortest axis from verticality. However, the decrease is milder than in the case of MCF-7 because cells can crawl on top of each other, their nuclei do not experience such lateral compression which makes the shortest axis deviate from verticality in MCF-7 (Figure 26b). In terms of Sphericity, there is more variability in C-26 than in MCF-7, but the biggest changes are placed from 0 to 1E-3 cells/µm^2, where Sphericity values stabilize (Figure 26c). In the case of Solidity, though, there is a mild but constant decrease (Figure 26c), compared to the steep decrease and flattening of MCF-7 (Figure 25c)

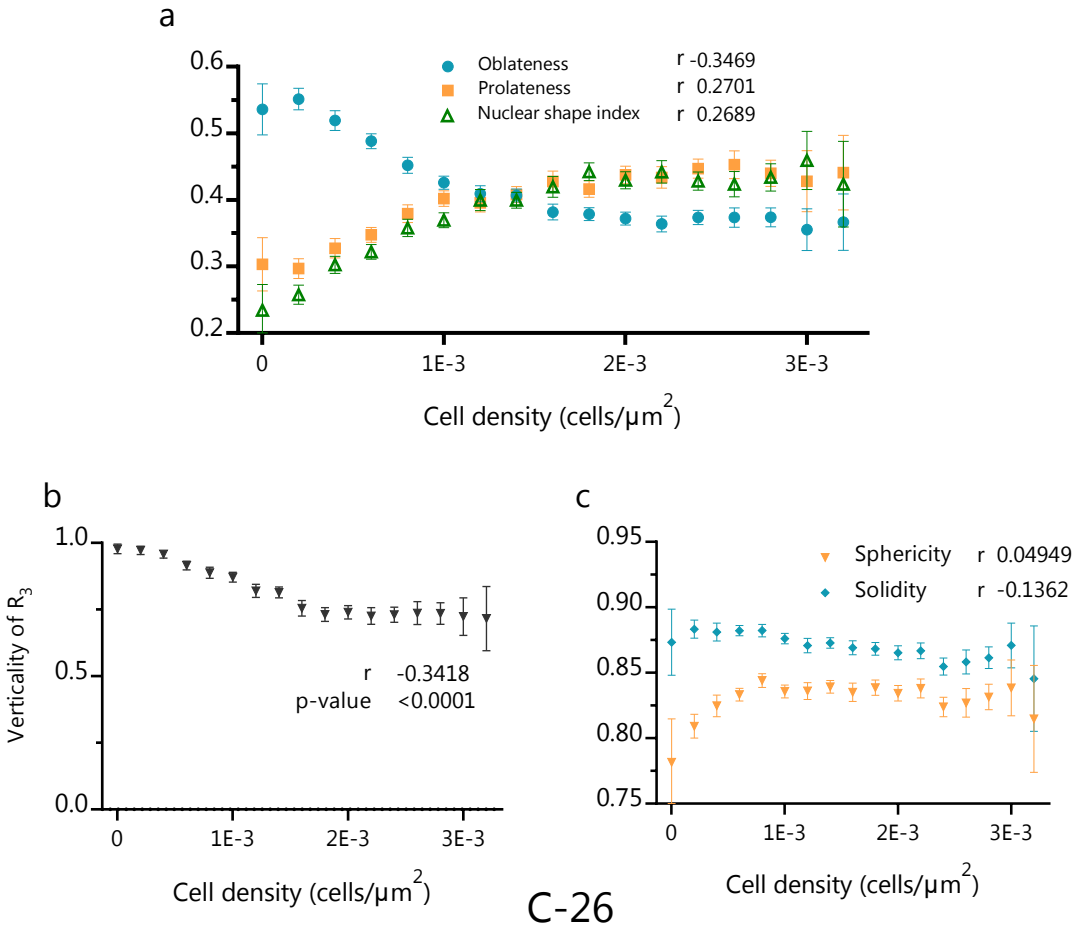

Figure 26 C-26 nuclear morphology parameters versus cell density. a) Oblateness, Prolateness, Nuclear Shape index, b) Verticality of the shortest axis, c) Sphericity and Solidity. Error bars depict 95% confidence interval. In a) and c) all five correlations tested significative, p-value <0.0001. For all, N=5932, from 3 independent experiments.

5.2. Mechanosensitive regulation of nucleocytoplasmic transport in the multicellular system

Nucleocytoplasmic transport is mechanosensitive and depends on forces to the nucleus. And the direction and magnitude of cytoskeletal and external forces that reach the cell nuclei are different in single cell and in multicellular systems. We have set up a system where cell density changes the forces that reach the nuclei and affects cell and nuclear morphology (Figure 19 and Figure 25). Then nuclear shapes are finely measured and the Sensor N/C ratio can be precisely measured. After analysing how nuclear characteristics change depending on cell density, we have analysed how the N/C ratio of the Sensor changes with respect to all these nuclear characteristics, for both MCF-7 and C-26. We have always measured N/C ratio, but in Chapter 1 they are expressed linearly, whereas here, in Chapter 2, we express them in logarithmic scale of base 2 to account better for YAP N/C ratio variability. A value of 0 means no preferential location in the cell, positive values correspond to relative nuclear localization, and negative values to cytoplasmic nuclear localization.

For MCF-7, in Figure 27a, we can see how Sensor N/C ratio does not have any statistically significant correlation with cell density. In Figure 27b-c Sensor ratio correlates with nuclear projected area and nuclear volume.

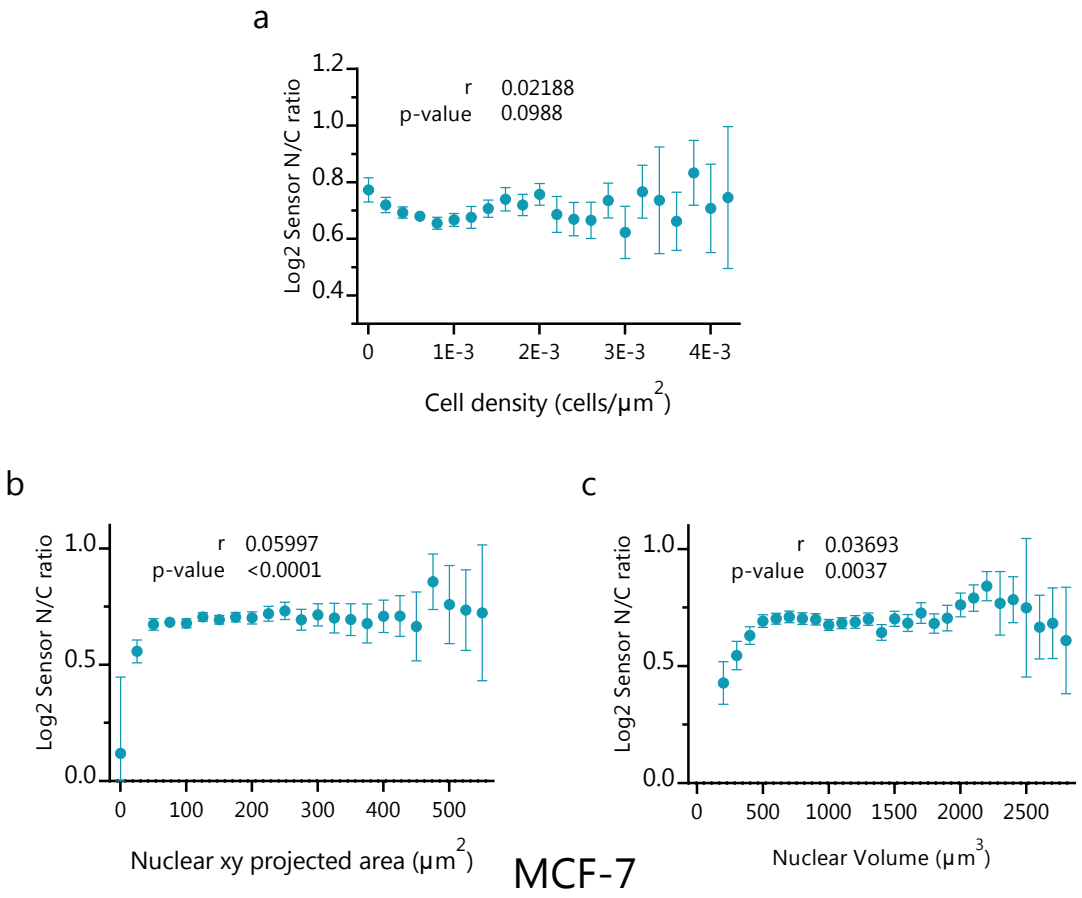

Figure 27 MCF-7 Changes of Sensor ratio depending on a) cell density, b) nuclear projected area, and c) nuclear volume. Error bars show 95% confidence intervals. Data binned from N=5689, 6161, 6162 points, from 6 independent experiments.

In C-26, there is also not any statistically significant correlation between cell density and Sensor ratio (Figure 28a). And mirroring MCF-7, there is a positive correlation between Sensor ratio and both Nuclear Projected Area and Nuclear Volume, but it is an effect coming from the subset of cells with low nuclear volume (Figure 28b-c); >87% of the cells have a nuclear projected area over 75µm^2, and >91% of the cells have nuclear volume over 500µm^3. These cells could be dying cells or could have just undergone mitosis, which would be in concordance with recent data linking the activation of the nuclear active transport machinery to nuclear volume via osmotic pressure after cell division (Pennacchio et al., 2022). Apart from this, recent data relate nuclear volume and NPC diameter in yeast (Zimmerli et al., 2021), which could be linked to the drop in Sensor ratio at lowest volumes.

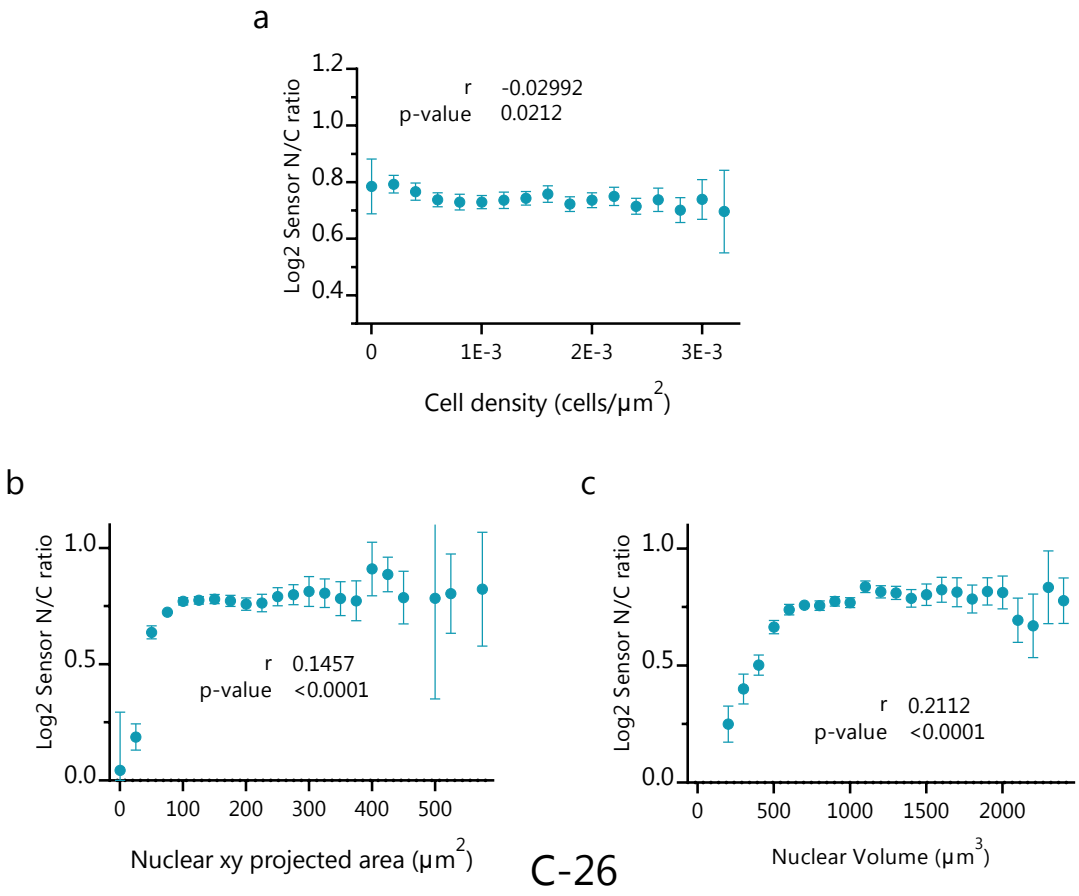

Figure 28 C-26 Changes of Sensor ratio depending on a) cell density, b) nuclear projected area, and c) nuclear volume. Error bars show 95% confidence intervals. Data binned from N= 5932, 5917, 5902 points, from 3 independent experiments.

Then, we have checked Sensor N/C ratio versus the shape parameters introduced in Figure 24: Oblateness, Prolateness, Nuclear Shape index, Verticality of R_3, Sphericity and Solidity. We have different and interesting results when comparing MCF-7 and C-26, epithelial and mesenchymal cell types, respectively.

For MCF-7, Oblateness correlates positively with Sensor ratio as well as Verticality of R_3, and Solidity (Figure 29a,d,f). Nuclear Shape index negatively correlates with Sensor ratio (Figure *29*c), which is not surprising considering that it behaves opposite to Oblateness when changing density (Figure *25*a). Out of all the compared parameters, Solidity is the parameter that provokes the widest changes to Sensor ratio, but Nuclear Shape index is the one with the highest correlation with Sensor ratio.

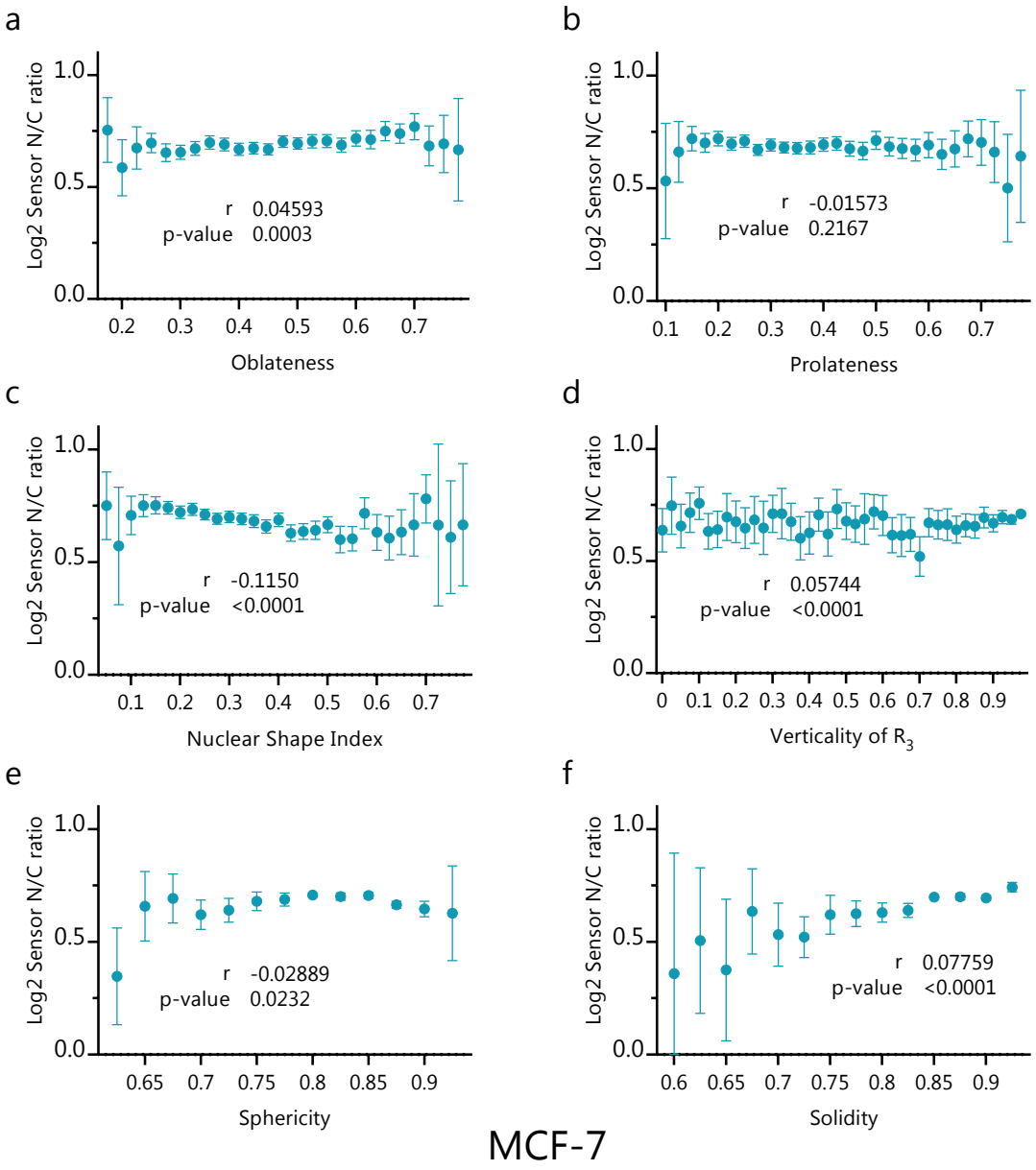

Figure 29 MCF-7 Changes in Sensor N/C ratio depending on nuclear shape parameters. a) Oblateness, b) Prolateness, c) Nuclear Shape index, d) Verticality of R_3, e) Sphericity, f) Solidity. Error bars show 95% confidence intervals. Data binned from N= 6159, 6161, 6166, 6173, 6161, 6163 points, from 6 independent experiments.

Regarding shape parameters for C-26, we see a clear difference between these results and MCF-7 results. First there are some inverted correlations: Oblateness and Nuclear Shape index correlate with an inverted sign to the one they have for MCF-7 (Figure 30a,c). Prolateness stays non-significant (Figure 30b), and Verticality of R_3 proves significant but with a very mild slope (Figure 30d). Most interesting results come up when comparing Sphericity and Solidity. Sphericity positively correlates with Sensor ratio (Figure 30e), whereas in MCF-7 it does not. In C-26, this is in agreement with

Oblateness and Nuclear Shape index results, that have higher correlation in C-26 than in MCF-7. Finally, for C-26 the strongest correlating parameter and also the one that shows the highest dynamic range is Solidity (Figure 30f).

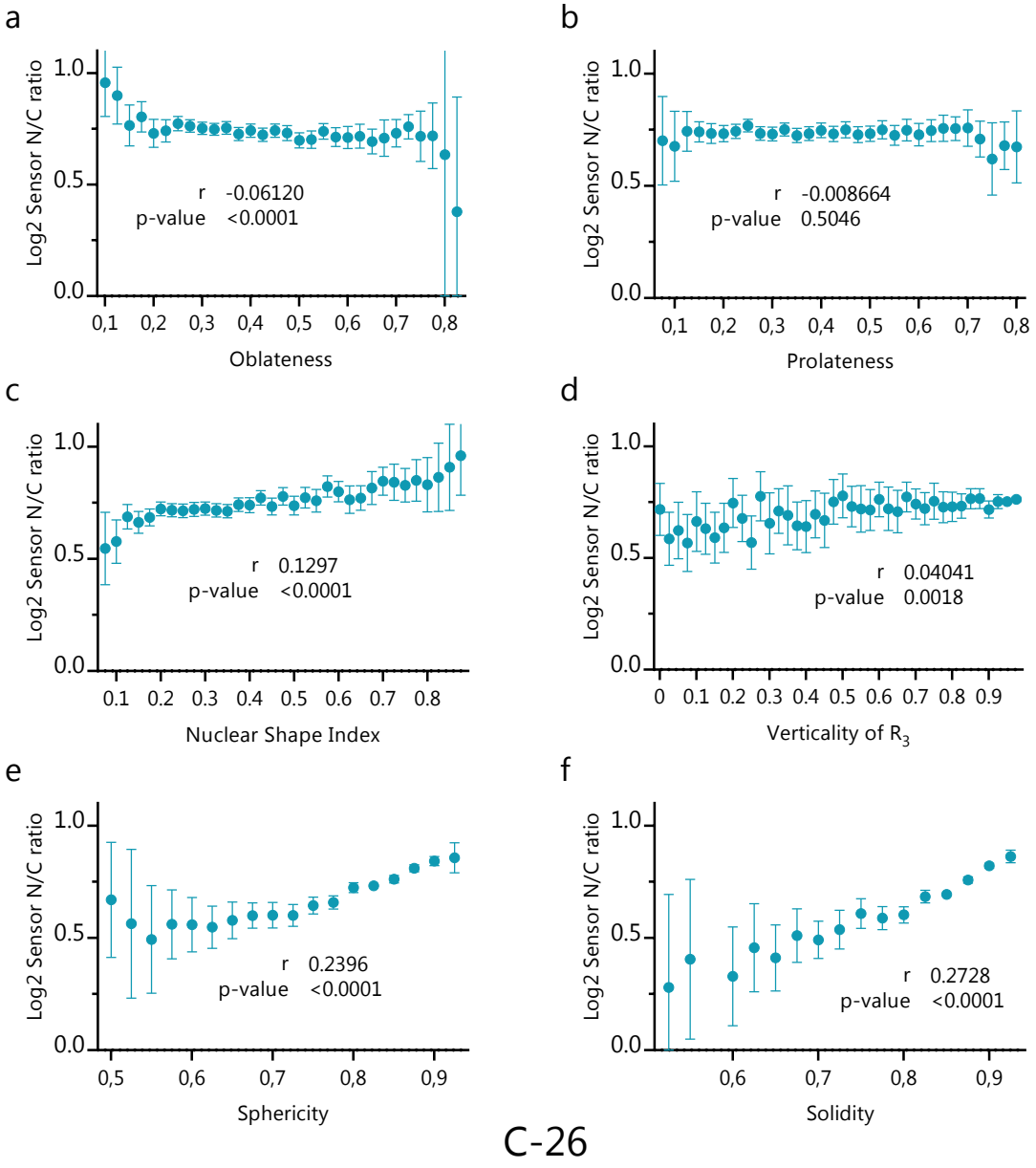

Figure 30 C-26 Changes in Sensor nuclear-to-cytoplasmic ratio depending on nuclear shape parameters. a) Oblateness, b) Prolateness, c) Nuclear Shape index, d) Verticality of R_3, e) Sphericity, f) Solidity. Error bars show 95% confidence intervals. Data binned from N= 5926, 5926, 5922, 5933, 5925, 5923 points, from 3 independent experiments.

5.3. Mechanosensitive regulation of YAP ratio in the multicellular system

Having established the link between Sensor ratio and shape parameters, we immunostained with anti-YAP antibody the same regions we imaged live for the Sensor. YAP is an important mechanosensitive transcription regulator involved in cancer and other diseases (Moroishi et al., 2015; Plouffe et al., 2015; Zanconato et al., 2016), organ size control (B. Zhao et al., 2010), and development (Porazinski et al., 2015; Varelas, 2014). It has also previously been proven that YAP needs nucleocytoplasmic transport for its regulation (Elosegui-Artola et al., 2017). Thus, staining for YAP allows us to compare the Sensor N/C ratio to a well-studied and relevant transcription regulator involved in mechanosensing.

The Sensor needs to be imaged live because fixing alters localization (data not shown), and YAP is analysed by immunostaining. Two steps of data analysis can be done for the images of YAP immune staining: first, analyze the images the same way it was done for the Sensor data; second, correlate the data in a cell by cell manner to obtain a direct relation between Sensor and YAP data (*Methods 3.15.3 Sensor-YAP correaltion*).

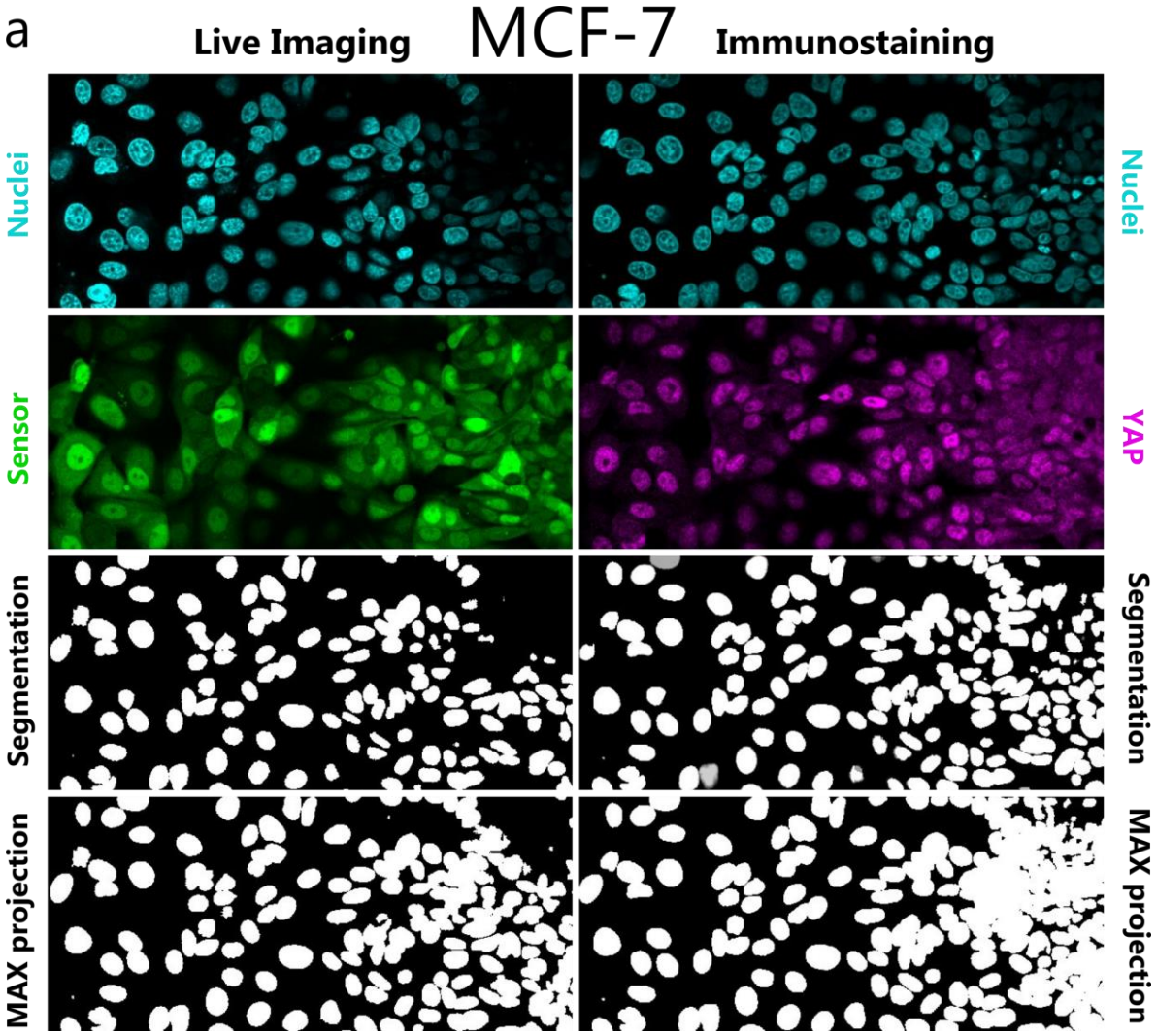

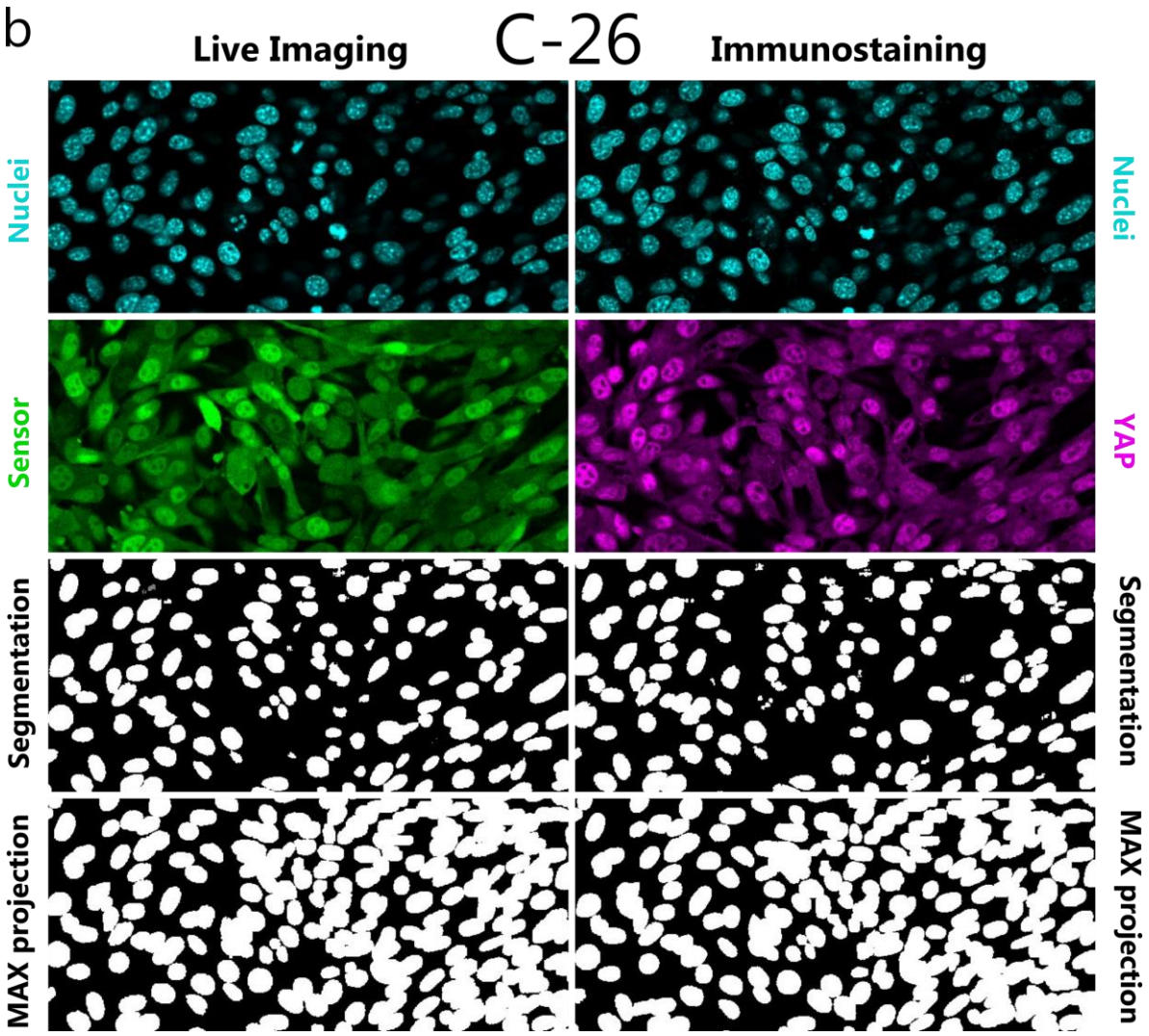

Figure 31 Significative z-slice image of live imaging and YAP immuno staining of the same location of the cell layer. High density zones placed on the right side. a) MCF-7, b) C-26. Hoechst staining, Sensor or YAP, nuclear segmentation, and maximal projection of nuclear segmentation. Scale bar: 100µm.

In the sample image of the YAP immunostainings of the cell layers (Figure 31), at the left side there are the zones of low density with nuclear localization of YAP, and at the right side a high-density zone can be seen forming a multi-cell layer, with less nuclear YAP distribution. The analysis was performed in the same way as for the Sensor, with the same imaged wells (as can be seen by comparing left and right columns), and with the identical nuclei segmentation pipeline. This process was performed again because the cells move from the live imaging to the staining imaging, due to the time taken for the imaging, the fixing and staining processes.

The first parameter to analyze is cell density; it has been described that YAP N/C ratio depends on cell density (Aragona et al., 2013; B. Zhao et al., 2007). We reproduce those results for both cell lines with very clear negative correlations (Figure 32a and Figure 33a). In the cases of Nuclear Projected Area and Nuclear Volume, we can see that under a certain threshold (around 150µm^2 and 800µm^3 for MCF-7 and 1000µm^3 for C-26) YAP ratio depends on them, but over the threshold it saturates

(Figure 32b-c and Figure 33b-c). This is a curious result when we compare it with the Sensor N/C ratio behavior with those parameters, because the threshold is lower (around 50µm^2 and around 500µm^3; (Figure 27b-c and Figure 28b-c). A hypothesis on why this happens is that for the Sensor the drop at very low volumes is due to very small nuclei of dying cells or that have just undergone mitosis, as mentioned before, whereas with YAP the differences happen in ranges where cells are alive and proliferative, and their volume is smaller due to the space constraint.

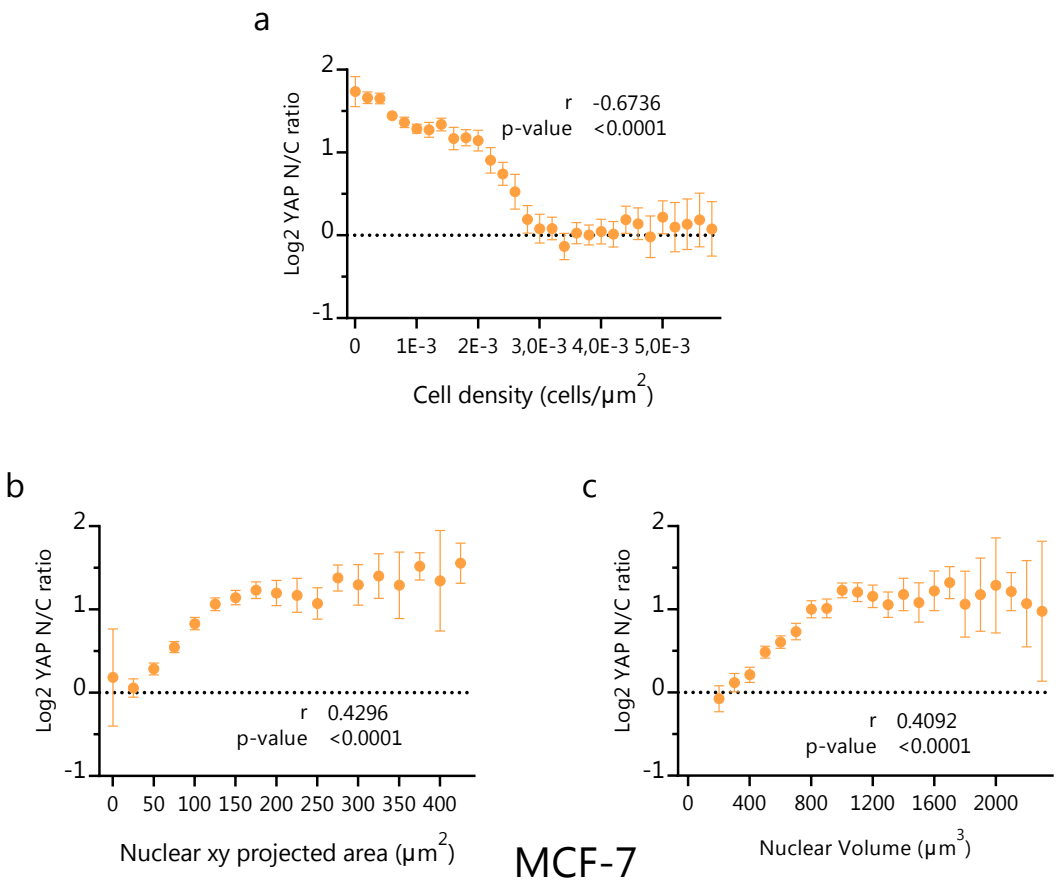

Figure 32 MCF-7 changes of YAP ratio depending on cell density, nuclear projected area, and nuclear volume. *Error bars show 95% confidence intervals. Data binned from N= 4605, 4598, 4601 points, from 3 independent experiments.*

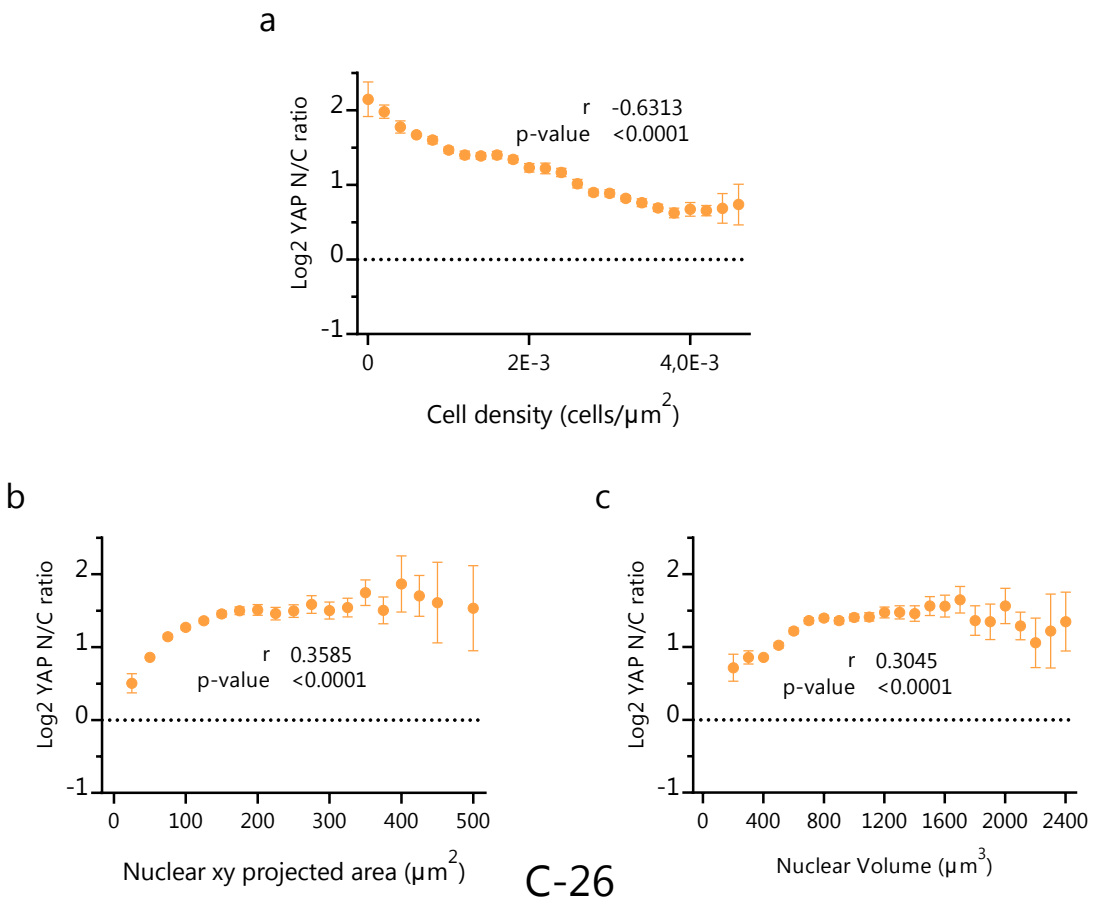

Figure 33 C-26 changes of YAP ratio depending on cell density, nuclear projected area, and nuclear volume. *Error bars show 95% confidence intervals. Data binned from N= 5584, 5573, 5568 points, from 3 independent experiments.*

Then we have also correlated YAP N/C ratio with shape parameters (Figure 34 and Figure 35), which shows interesting results. In the case of MCF-7 cell line, statistically significant correlations appear for all the parameters, but the clearest include Oblateness and Nuclear Shape index (Figure 34a,c), which have opposite correlation sign, and that is expected by their mathematical definition. Also, the Verticality of R_3 is correlated because discoidal nuclei touching the bottom glass have higher YAP N/C ratios (Figure 34d), but the strongest correlation corresponds to Solidity (Figure 34f). This dependence on Solidity and Nuclear Shape index was also seen with the Sensor ratios (Figure 29f).

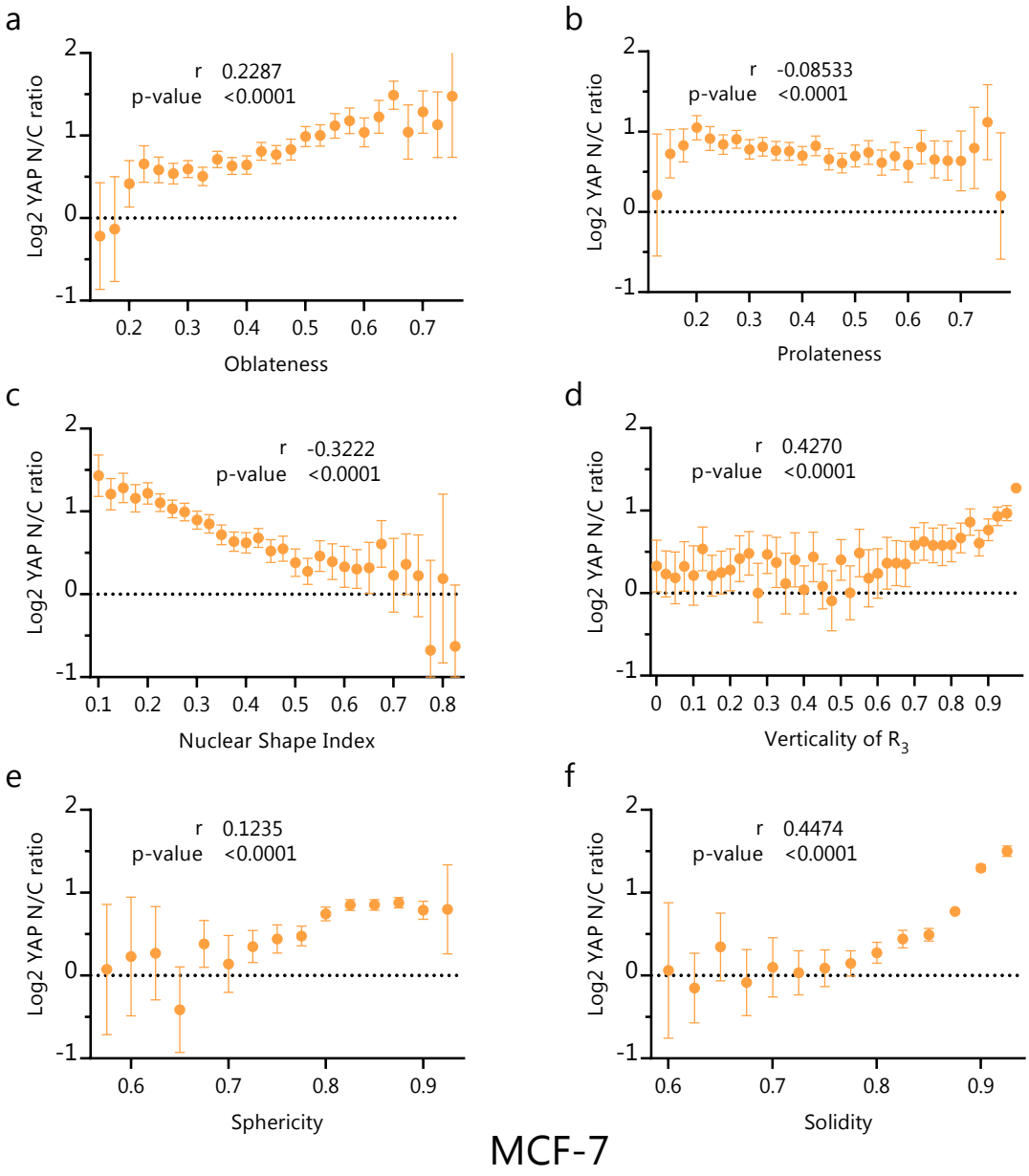

Figure 34 MCF-7 changes in YAP nuclear-to-cytoplasmic ratio depending on nuclear shape parameters. a) Oblateness, b) Prolateness, c) Nuclear Shape index, d) Verticality of R_3, e) Sphericity, f) Solidity. Error bars show 95% confidence intervals. N= 4603, 4605, 4604, 4613, 4597, 4600 points, from 3 independent experiments.

The C-26 YAP N/C ratio correlation with nuclear shape parameters yield similar results to MCF-7 cell line (Figure 35). There are mild differences in correlation levels, but correlation signs (positive or negative correlation) stay the same. Of note, Solidity correlation level is smaller, but correlation seems more linear for C-26 than for MCF-7 (Figure 34f and Figure 35f). An interesting remark for C-26 is that Oblateness and Nuclear Shape index correlations versus YAP N/C ratio have an inverted

sign if compared to Sensor N/C ratio, whereas this doesn't happen for MCF-7, where Sensor and YAP correlate similarly to shape parameters.

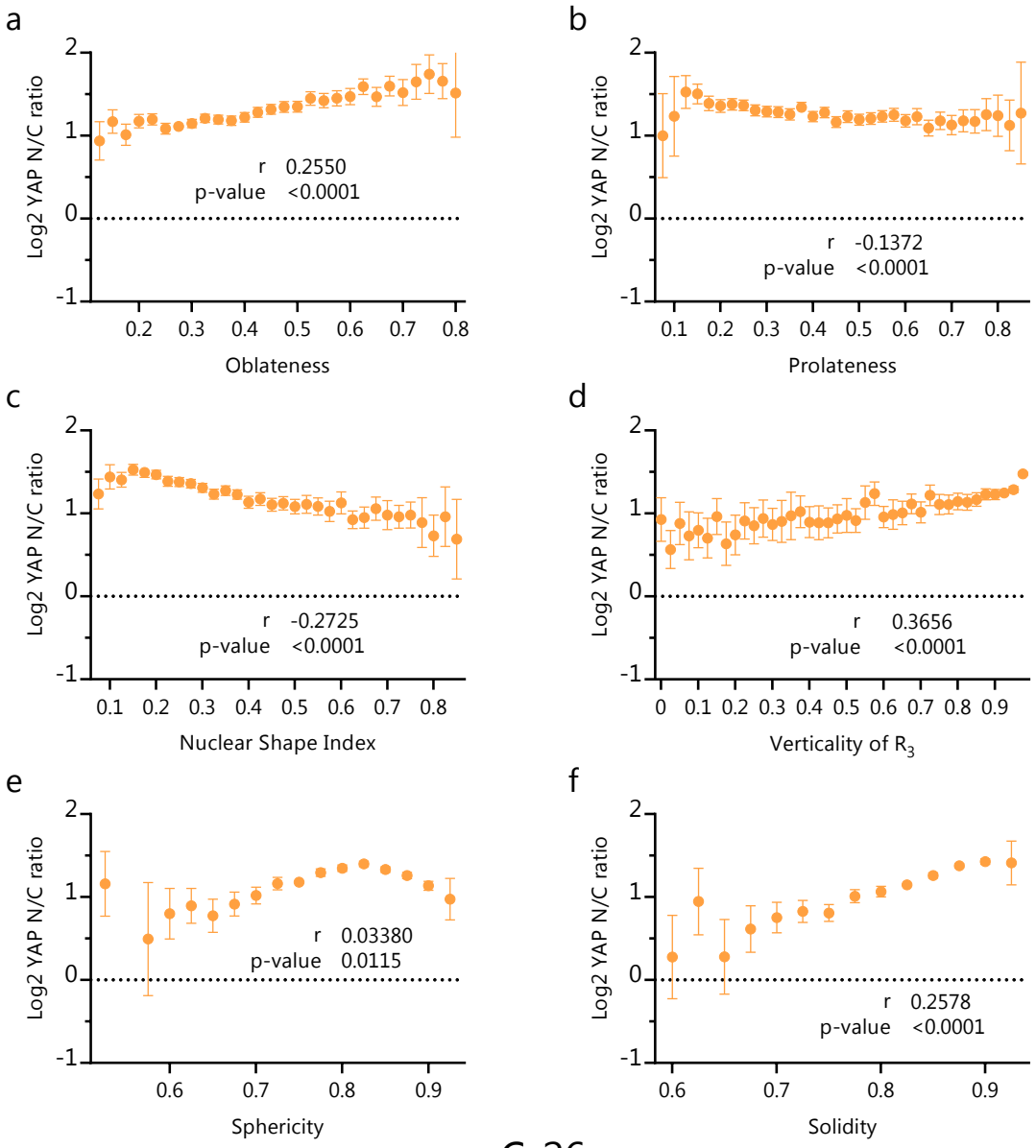

Figure 35 C-26 changes in YAP nuclear-to-cytoplasmic ratio depending on nuclear shape parameters. a) Oblateness, b) Prolateness, c) Nuclear Shape index, d) Verticality of R_3, e) Sphericity, f) Solidity. Error bars show 95% confidence intervals. N= 5577, 5584, 5584, 5587, 5578, 5576 points, from 3 independent experiments.

Finally, we have manually correlated cells from the live imaging of the Sensor to the YAP immunostaining, to be able to compare both N/C ratios in a cell-by-cell basis. Remarkably, YAP and

Sensor N/C ratios positively correlate for both cell lines, but with a stronger correlation for MCF-7 (Figure 36 and Figure **37**).

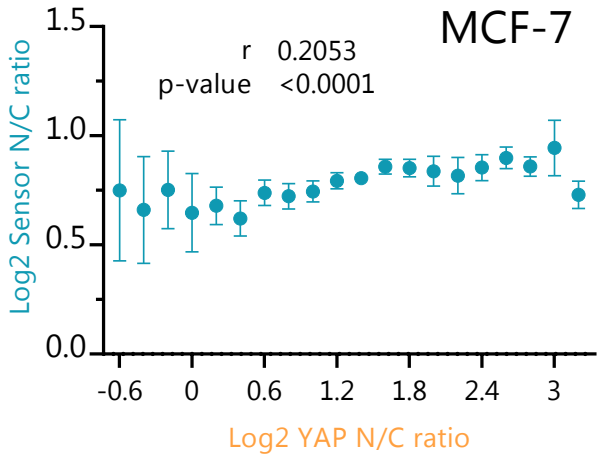

Figure 36 MCF-7 Log2 Sensor N/C ratio versus Log2 YAP N/C ratio. Error bars show 95% confidence intervals. Data binned from 1180 points, from 3 independent experiments.

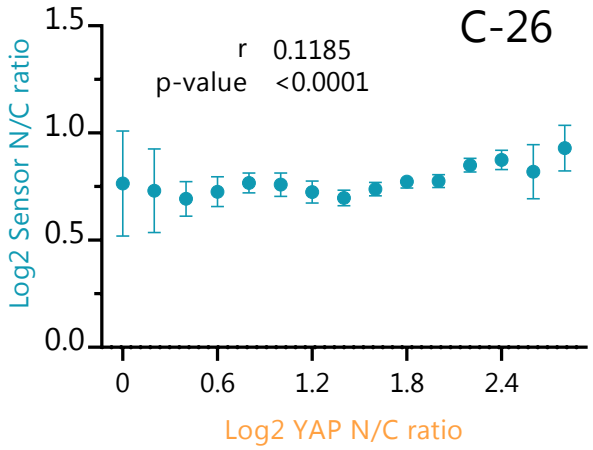

Figure 37 C-26 Log2 Sensor N/C ratio versus Log2 YAP N/C ratio. Error bars show 95% confidence intervals. Data binned from 1552 points, from 3 independent experiments.

In summary, in Chapter 2 we have developed a system to analyze images and measure nuclear shapes, nuclear volume, cell density and N/C ratios of the Sensor and YAP cell-by-cell. Then, we have

been able to correlate all this data to understand the effect of mechanical forces on the nucleo-cytoplasmic transport system.

6. Discussion

In Chapter 1, this work shows that force regulates nucleocytoplasmic transport by weakening the permeability barrier of NPCs, affecting both passive and facilitated diffusion; which is directly related to Aim 1. Because MW affects more passive than facilitated diffusion, this generates a differential effect on both types of transport that enables force-induced nuclear (or cytosolic) localization of cargo. The mechanical weakening of the permeability barrier is most likely the consequence of NPC deformation, as previous work reported increased apparent NPC diameters for cells on stiff versus soft substrates (Elosegui-Artola et al., 2017). Further, recent structural evidence has confirmed the deformability of NPCs (Schuller et al., 2021; Zimmerli et al., 2021). In NPCs, the meshwork of FG Nup proteins that conforms the permeability barrier is supported by the NPC inner ring, which is formed by 8 symmetric spokes (Kosinski et al., 2016; Lin et al., 2016). These spokes have limited interactions with each other through flexible linker proteins (Petrovic et al., 2022). This allows NPCs to dilate or constrict by changing the distance between spokes, as proposed a decade ago (Hoelz et al., 2011) and as verified very recently (Petrovic et al., 2022; Schuller et al., 2021; Zimmerli et al., 2021). Such dilation and constriction indeed occur in response to energy depletion or to changes in osmotic pressure (Zimmerli et al., 2021). This proposed direct regulation of NPC permeability with force is strongly supported by the immediate response observed in AFM experiments (Figure 8), the effects observed in passive diffusion, and the dependency on MW (Figure 5). On top of this mechanism, indirect effects mediated for instance by changes in importin α levels (Figure 10) or by competition between cargoes for importin binding (as recently demonstrated between YAP and importin 7 (García-García et al., 2022)) may play a role in different contexts.

Three important open questions emerge from our findings. First, how mechanical deformation of NPCs weakens the permeability barrier of FG Nups in both passive and facilitated diffusion, remains to be understood. The LINC complex may play an important role, as suggested by the fact that responses to stiffness (in which cells apply force to the nucleus through the cytoskeleton and the LINC complex) are larger than responses to more unspecific force application with an AFM. This is further supported by the abrogation of AFM responses upon DN-KASH overexpression and the overexpression of DN-KASH in gels of different stiffness. Second, the exact set of properties that confer mechanosensitivity to transcriptional regulators or other proteins remains to be fully explored. The different transcriptional regulators discussed here range in size from over 20 kDa (for twist) to over 60 kDa (for YAP), thereby encompassing almost the full range of weights analysed with our designed constructs. However, diffusivity through NPCs depends not only on MW and their diameter, but also on surface charges (Frey et al., 2018) and protein mechanical properties (Infante et al., 2019), which could play major roles. Finally, why facilitated export is less affected than facilitated import may be related to the different volumes of nucleus and cytoplasm (as suggested by modelling in Figure 15), to the different interactions between importins and exportins with FG-nups (Aramburu & Lemke, 2017) or to the asymmetric manner in which NPCs deform (Zimmerli et al., 2021).

Chapter 1 demonstrates a general mechanism of mechanosensitivity, with incorporated specificity through molecular properties such as the NLS sequence and MW. Although other complementary

mechanisms (such as differential binding to nuclear or cytosolic proteins) can generate mechanosensitive nuclear translocation (Fernandez-Sanchez et al., 2015; X H Zhao et al., 2007), our mechanism is consistent with the behaviour of several transcriptional regulators and has potential general applicability. Our findings suggest that interfering with nucleocytoplasmic transport may be an avenue to regulate or abrogate mechanically-induced transcription in several pathological conditions. Perhaps, they open the door to design artificial mechanosensitive transcription factors, to enable mechanical control of transcriptional programs at will.

To achieve the results in Chapter 1, we measured the mechanosensitivity for every construct out of the 84 presented in this work, plus some others that were discarded on the way (Figure 8e and Table 1). This information has been essential for choosing L_NLS-41 kDa, which is the most mechanosensitive construct among all (Figure 8f-i). Its defined relation between NLS affinity to importin α and MW, regulate independently facilitated diffusion (active transport) rate and passive diffusion (passive transport) rate through the NPC. Then, it is a mechanosensitive molecule because relative nuclear-to-cytoplasmic concentration (N/C ratio) is highly sensitive to changes in nucleocytoplasmic shuttling rates: small changes in facilitated or passive diffusion affect its accumulation levels in the nucleus. In our studies, these shuttling rates change depending on how the forces reach and affect the nucleus and the nuclear transport system. Therefore, we have used the term “Sensor” to name L_NLS-41 kDa.

Regarding L_NLS-41 kDa (Sensor) widespread use in all cell types, we can say that its utility in a certain cell line depends on the level of active transport versus passive transport of that cell line itself, its mechanosensitivity, and the environment where the cells are. For instance, if the active transport machinery is too strong, the Sensor will have a very nuclear localization and will be out of the mechanosensitive region in the active transport-passive transport space (Figure 11b), therefore, we would need to choose construct with a lower MW to move back to the mechanosensitive zones. Also, not all cells are mechanosensitive or respond the same way to forces, for example, cells seeded on top of laminin have keratins shielding the nucleus from mechanical deformations and subsequent signaling (Kechagia et al., 2022). If for any reason a cell type is not mechanosensitive, we would observe no changes in Sensor N/C ratio after force application.

For Chapter 2, we have used the Sensor as a tool to study how the mechanical regulation of nucleocytoplasmic transport applies in multicellular systems (Aim 2). And more specifically to use the Sensor to study the effects of forces in the nucleus in multicellular systems (Aim 2.1) and to study nuclear shape parameters to unveil how nuclear transport is mechanosensitive in multicellular systems (Aim 2.2). To do so we have established a system to image cell layers in 3D, segment the cells’ nuclei, and measure nuclear volume, cell density, shape parameters, as well as Sensor and YAP N/C ratio. The setup is suitable to relate nuclear shapes or dimensions to any other cell characteristic measurable by confocal fluorescence imaging.

By analyzing MCF-7 and C-26 cell layers with this setup, we have been able to analyze thousands of cells with different nuclear shapes, in different cell density levels, with their Sensor N/C ratio and YAP N/C ratio. Thus, we have discerned the shape parameters that affect the most the nuclear shuttling of the Sensor and YAP: an artificial construct and a very well-studied TR, respectively. This

nuclear shape information is a very comfortable “base camp” from which we are now able to hypothesize what are the next steps to approach the mechanism and the molecular basis for the phenomenon observed in Chapter 1.

Regarding Chapter 2 data, we can extract some important features. But first, we need to keep in mind that YAP is an endogenous protein. Thus, it is a very well-regulated TR, with sequestering and binding mechanisms both in the nucleoplasm (B. Zhao et al., 2008) and the cytoplasm (M. Kim et al., 2013; C. Wang et al., 2016), which allows for a big dynamic range of N/C ratios. Whereas our Sensor, is a protein that freely diffuses inside each compartment (Figure 6e), and contains an NLS that makes its nuclear concentration to be always higher than the cytoplasmic, when the active transport system is working.

Regarding the differences in cell layer organization between cell lines (MCF-7, epithelial and C-26, mesenchymal), when density increases, MCF-7 cell layer thickness shows a clear transition between monolayer organization to multilayer organization over a certain density threshold (Figure 22a), but C-26 does not show such a transition, rather a smooth increase (Figure 23a). This can be explained by the tendency of epithelial cells to form a monolayer and maintain lateral cell-cell contacts, while mesenchymal cells tend to stack one on top of the other without creating strong cell-cell contacts. For shape parameters, both cell types have oblate (discoidal) nuclei when cells are at low densities; these nuclei at low cell density are also flattened in the xy plane (therefore, parallel to the glass) and have a high Solidity (Figure 25, Figure 26).

Density changes nuclear shapes, but we need to understand the effect of density itself for both Sensor and YAP N/C ratios. We can consider that the Sensor does not respond to density (Figure 27a, Figure 28a), but YAP clearly does (Figure 32a , Figure 33a), and in fact, it is the strongest correlation of all the data analysis. This coincides with the literature describing cell-cell contact inhibition of YAP nuclear localization that involves many layers of regulation (Aragona et al., 2013; B. Zhao et al., 2007, 2008). These differences indicate that it is not density *per se* what is changing nucleocytoplasmic transport. Instead, the Sensor does not respond to density and changes in YAP N/C ratio come from independent and well-described cell-cell contact effects.

We have then compared Sensor and YAP with the specific shape parameters presented in Figure 24. Oblateness does not have a big effect on Sensor ratio (Figure 29a, Figure 30a), but it positively correlates with YAP Sensor ratio (Figure 34a, Figure 35a). This correlation could be explained due to the fact that Oblateness is correlated with cell density (Figure 25, Figure 26), and cell density to YAP ratio (Figure 32, Figure 33), this would not imply a direct effect of Oblateness on YAP N/C ratio.

The Nuclear Shape index measures how much smaller is the smallest axis of the nucleus compared to the other two, in other words how much the shape deviates from a sphere. Nuclear Shape index has a higher correlation than Oblateness in all four cases (both cell lines, and both Sensor and YAP) (Figure 29c, Figure 30c, Figure 34c, Figure 35c). However, it correlates negatively with YAP ratios in both cell lines and with Sensor ratios in MCF-7, but it correlates positively in the case of Sensor N/C ratios in C-26. Therefore, in the case of Sensor ratios in C-26, the more spherical the higher the ratio. A different way to get to the same conclusion is by looking at Sphericity values (Figure 29e, Figure

30e, Figure 34e, Figure 35e). C-26 Sensor ratio versus Sphericity presents a monophasic increase, and by far the highest correlation of all four comparisons. Briefly, the difference between Sphericity and Nuclear Shape index resides in the fact that the Nuclear Shape index considers the three axes of the ellipsoid fitted to the nuclear shape, while Sphericity accounts for how spherical a shape is in terms of area to volume ratio. For any given volume, the lowest surface area will always be achieved if the shape is spherical. We do not have an explanation for the different results correlating Sensor N/C ratio and Nuclear Shape index in the different cell lines, however, they have low correlation levels, so they are not very informative parameters.

As a last shape parameter, we have Solidity, which is a measure of ruffling of the nucleus. In general, it is the best correlating factor with both YAP and Sensor ratios in both cell lines (Figure 29f, Figure 30f, Figure 34f, Figure 35f). Finally, we have correlated in a cell-by-cell manner Sensor N/C ratios and YAP ratios (Figure 36, Figure 37). For both cell lines Sensor and YAP relative concentrations correlate significantly, more in MCF-7 than in C-26. However, the correlation values are low at the level of YAP and Sensor, indicating that both parameters are not molecularly tied and that even if they are caused by similar factors the different layers of YAP regulation may be reducing the correlations.

These results, mainly Solidity, lead us to think that it is Nuclear Membrane tension what could be driving this effect. This could be affecting NPC channel size, as has been previously proposed (Donnaloja et al., 2019; Elosegui-Artola et al., 2017) and happens in other physiological conditions (Schuller et al., 2021; Zimmerli et al., 2021). It could also be affecting any other type of membrane tension protein effectors, such as Piezo1 transmembrane channel (Murthy et al., 2017). Piezo1is both placed in the ER, which is contiguous to the NM, and in the cell membrane (Coste et al., 2010). It has been proven to be essential for ER Calcium release after nuclear stretch and the subsequent mechanoresponse (Nava et al., 2020). Also, Piezo1 activation is higher in cells with stiffer nuclei, which have higher levels of Lamin A. Apart from Piezo1, other Calcium channels have been detected in the nuclear envelope by pipette aspiration (Itano et al., 2003). Once Calcium has been released, new effectors come into play. With high cytoplasmic Calcium levels, $cPLA_2$ can attach to the INM under nuclear membrane stretch conditions, leading to activation of contractility (Lomakin et al., 2020; Venturini et al., 2020). However, sufficiently high Lamin A levels are needed for $cPLA_2$ response after nuclear confinement (Lomakin et al., 2020), which indicates that different cell types with different nuclear mechanic characteristics may respond differently.

To test if any of these elements are key molecular parameters in the nuclear force-dependent increase of nucleocytoplasmic transport, we have several options to be attempted in further work. First, we need to observe the level of nuclear folding in higher definition. For so, we will need to optimize Lap2β (INM integral protein) transfections in our cell lines. So far, we have segmented the nuclei with the signal coming from Hoechst staining, which is very convenient to image a high number of cells, but has lower ruffle definition compared to LAP2β (Figure 19). Second, we will need to alter the stretch level of the nuclear membrane, either (a) by altering the forces reaching the nucleus, or (b) by altering nuclear mechanical characteristics; mechanical characteristics have proven to depend on the cell type and on the environmental conditions and can modulate cell responses to mechanical stimuli.

a) To alter the forces reaching the nucleus we have several options. For instance, hypotonic shocks have already proven useful to alter nuclear shape (and putatively membrane stretch) in a short time scale (Elosegui-Artola et al., 2017; Venturini et al., 2020). To alter nuclear forces reaching the nucleus in a longer time scale, a well-known alteration is transfecting DN-KASH to abolish the LINC complex. We have already used it in Figure 7, but in a single cell environment and not extracting any nuclear shape information.
b) To alter nuclear mechanical characteristics, typical conditions are depleting nuclear lamins (Lomakin et al., 2020; Stephens et al., 2017) or by compaction or decompaction of chromatin (Stephens et al., 2017).

Finally, we will need to check on molecular effectors such as the NPC, $cPLA_2$ or Piezo1 to understand the basis of the increase of nuclear force-dependent in nucleocytoplasmic transport, which is the driver for the location of the Sensor. Furthermore, it would be interesting to understand the generality of the mechanism, by measuring changes in N/C ratio of a freely diffusing TR mutant, for example a YAP mutant that does not bind any element in the nucleus or in the cytoplasm.

7. Conclusions

1. Nucleocytoplasmic transport is mechanosensitive.
2. Force regulates nucleocytoplasmic transport by weakening the permeability barrier of NPCs, affecting both passive and facilitated diffusion.
3. Passive diffusion through NPCs is mechanosensitive for small MWs.
4. MW affects passive diffusion more than facilitated diffusion, which generates differential mechanosensitivity on both types of transport, that enables force-induced nucleoplasmic (or cytoplasmic) localization of cargo.
5. The balance between affinity to importins and MW defines the mechanosensitivity of nuclear localization in constructs containing NLS signals.
6. The balance between affinity to exportin 1 and MW defines the mechanosensitivity of nuclear localization in constructs containing NES signals.
7. Facilitated export is less affected by nuclear force than facilitated import.
8. Blocking nuclear to cytoskeletal force transmission with DN-KASH recapitulates the effects of substrate stiffness on transport rates.
9. The effect of forces to the nucleus can be seen via changing substrate stiffness and equivalently via direct AFM pressure to the nucleus.
10. L_NLS-EGFP-2PrA (Sensor) accumulates in the nucleus with force. Which is explained by a higher mechanosensitivity of facilitated versus passive diffusion.
11. The mechanosensitivity of several transcriptional regulators is controlled by force-induced effects in nucleocytoplasmic transport.
12. The mechanosensitivity of twist1 can be re-engineered with exogenous NLS sequences.
13. We have developed a system to analyse nuclear shape parameters, nuclear volume, and cell density in high throughput number.
14. Cell density defines cell layer thickness in MCF-7 and C-26 cell lines.
15. Cell density strongly affects nuclear shapes by impeding cells to flatten their nuclei and reducing their nuclear volume.
16. As described in the literature, cell density strongly correlates with YAP N/C ratios.
17. Nuclear Solidity significantly correlates with Sensor and YAP N/C ratios.
18. Sensor and YAP N/C ratios significantly correlate for both MCF-7 and C-26 cell lines.

8. References

Aaronson, R. P., & Blobel, G. (1974). On the attachment of the nuclear pore complex. *Journal of Cell Biology*, *62*(3), 746–754. https://doi.org/10.1083/jcb.62.3.746

Aaronson, R. P., & Blobel, G. (1975). Isolation of nuclear pore complexes in association with a lamina. *Proceedings of the National Academy of Sciences of the United States of America*, *72*(3), 1007–1011. https://doi.org/10.1073/pnas.72.3.1007

Adam, S. A. (2017). The nucleoskeleton. *Cold Spring Harbor Perspectives in Biology*, *9*(2), a023556. https://doi.org/10.1101/cshperspect.a023556

Agrawal, A., & Lele, T. P. (2019). Mechanics of nuclear membranes. *Journal of Cell Science*, *132*(14), 1–8. https://doi.org/10.1242/JCS.229245

Ahlstrom, J. D., & Erickson, C. A. (2007). Organization of cells into higher-ordered structures. *Principles of Tissue Engineering*, 67–79. https://doi.org/10.1016/B978-012370615-7/50010-X

Ahn, J., Jo, I., Kang, S. mi, Hong, S., Kim, S., Jeong, S., Kim, Y. H., Park, B. J., & Ha, N. C. (2019). Structural basis for lamin assembly at the molecular level. *Nature Communications*, *10*(1). https://doi.org/10.1038/s41467-019-11684-x

Akey, C. W., Singh, D., Ouch, C., Echeverria, I., Nudelman, I., Varberg, J. M., Yu, Z., Fang, F., Shi, Y., Wang, J., Salzberg, D., Song, K., Xu, C., Gumbart, J. C., Suslov, S., Unruh, J., Jaspersen, S. L., Chait, B. T., Sali, A., … Rout, M. P. (2022). Comprehensive structure and functional adaptations of the yeast nuclear pore complex. *Cell*, *185*(2), 361-378.e25. https://doi.org/10.1016/j.cell.2021.12.015

Alam, S. G., Lovett, D., Kim, D. I., Roux, K. J., Dickinson, R. B., & Lele, T. P. (2015). The nucleus is an intracellular propagator of tensile forces in NIH 3T3 fibroblasts. *Journal of Cell Science*, *128*(10), 1901–1911. https://doi.org/10.1242/jcs.161703

Allegretti, M., Zimmerli, C. E., Rantos, V., Wilfling, F., Ronchi, P., Fung, H. K. H., Lee, C. W., Hagen, W., Turoňová, B., Karius, K., Börmel, M., Zhang, X., Müller, C. W., Schwab, Y., Mahamid, J., Pfander, B., Kosinski, J., & Beck, M. (2020). In-cell architecture of the nuclear pore and snapshots of its turnover. *Nature*, *586*(7831), 796–800. https://doi.org/10.1038/s41586-020-2670-5

Alvarado-Kristensson, M., & Rosselló, C. A. (2019). The biology of the nuclear envelope and its implications in cancer biology. *International Journal of Molecular Sciences*, *20*(10). https://doi.org/10.3390/ijms20102586

Ando, D., Zandi, R., Kim, Y. W., Colvin, M., Rexach, M., & Gopinathan, A. (2014). Nuclear Pore Complex Protein Sequences Determine Overall Copolymer Brush Structure and Function. *Biophysical Journal*, *106*(9), 1997–2007. https://doi.org/10.1016/j.bpj.2014.03.021

Andreu, I., Granero-Moya, I., Chahare, N. R., Clein, K., Jordàn, M. M., Beedle, A. E. M., Elosegui-Artola, A., Abenza, J. F., Rossetti, L., Trepat, X., Raveh, B., & Roca-Cusachs, P. (2022). Mechanical force application to the nucleus regulates nucleocytoplasmic transport. *Nature Cell Biology*, In press. https://doi.org/10.1038/s41556-022-00927-7

Andreu, I., Granero-Moya, I., Garcia-Manyes, S., & Roca-Cusachs, P. (2022). Understanding the role of mechanics in nucleocytoplasmic transport. *APL Bioengineering*, *6*(2), 020901.

https://doi.org/10.1063/5.0076034

Anlaş, A. A., & Nelson, C. M. (2018). Tissue mechanics regulates form, function, and dysfunction. *Current Opinion in Cell Biology*, *54*, 98–105. https://doi.org/10.1016/j.ceb.2018.05.012

Aragona, M., Panciera, T., Manfrin, A., Giulitti, S., Michielin, F., Elvassore, N., Dupont, S., & Piccolo, S. (2013). A mechanical checkpoint controls multicellular growth through YAP/TAZ regulation by actin-processing factors. *Cell*, *154*(5), 1047–1059. https://doi.org/10.1016/j.cell.2013.07.042

Aragona, M., Sifrim, A., Malfait, M., Song, Y., Van Herck, J., Dekoninck, S., Gargouri, S., Lapouge, G., Swedlund, B., Dubois, C., Baatsen, P., Vints, K., Han, S., Tissir, F., Voet, T., Simons, B. D., & Blanpain, C. (2020). Mechanisms of stretch-mediated skin expansion at single-cell resolution. In *Nature* (Vol. 584, Issue 7820). Springer US. https://doi.org/10.1038/s41586-020-2555-7

Aramburu, I. V., & Lemke, E. A. (2017). Floppy but not sloppy: Interaction mechanism of FG-nucleoporins and nuclear transport receptors. In *Seminars in Cell and Developmental Biology* (Vol. 68, pp. 34–41). Elsevier Ltd. https://doi.org/10.1016/j.semcdb.2017.06.026

Arsenovic, P. T., Ramachandran, I., Bathula, K., Zhu, R., Narang, J. D., Noll, N. A., Lemmon, C. A., Gundersen, G. G., & Conway, D. E. (2016). Nesprin-2G, a Component of the Nuclear LINC Complex, Is Subject to Myosin-Dependent Tension. *Biophysical Journal*, *110*(1), 34–43. https://doi.org/10.1016/j.bpj.2015.11.014

Aureille, J., Belaadi, N., & Guilluy, C. (2017). Mechanotransduction via the nuclear envelope: a distant reflection of the cell surface. *Current Opinion in Cell Biology*, *44*, 59–67. https://doi.org/10.1016/j.ceb.2016.10.003

Bahmanyar, S., & Schlieker, C. (2020). Lipid and protein dynamics that shape nuclear envelope identity. *Molecular Biology of the Cell*, *31*(13), 1315–1323. https://doi.org/10.1091/MBC.E18-10-0636

Banigan, E. J., Stephens, A. D., & Marko, J. F. (2017). Mechanics and Buckling of Biopolymeric Shells and Cell Nuclei. *Biophysical Journal*, *113*(8), 1654–1663. https://doi.org/10.1016/j.bpj.2017.08.034

Baum, D. A., & Baum, B. (2014). An inside-out origin for the eukaryotic cell. *BMC Biology*, *12*(1), 76. https://doi.org/10.1186/s12915-014-0076-2

Beck, M., & Hurt, E. (2017). The nuclear pore complex: Understanding its function through structural insight. *Nature Reviews Molecular Cell Biology*, *18*(2), 73–89. https://doi.org/10.1038/nrm.2016.147

Berret, J. F. (2016). Local viscoelasticity of living cells measured by rotational magnetic spectroscopy. *Nature Communications*, *7*. https://doi.org/10.1038/ncomms10134

Bickmore, W. A. (2002). Addressing protein localization within the nucleus. *The EMBO Journal*, *21*(10), 2507-a-2507. https://doi.org/10.1093/emboj/21.10.2507-a

Bigay, J., & Antonny, B. (2012). Curvature, Lipid Packing, and Electrostatics of Membrane Organelles: Defining Cellular Territories in Determining Specificity. *Developmental Cell*, *23*(5), 886–895. https://doi.org/10.1016/j.devcel.2012.10.009

Bischoff, F. R., Klebe, C., Kretschmer, J., Wittinghofer, A., & Ponstingl, H. (1994). RanGAP1 induces

GTPase activity of nuclear Ras-related Ran. *Proceedings of the National Academy of Sciences of the United States of America*, *91*(7), 2587–2591. https://doi.org/10.1073/pnas.91.7.2587

Blobel, G. (1985). Gene gating: A hypothesis. *Proceedings of the National Academy of Sciences of the United States of America*, *82*(24), 8527–8529. https://doi.org/10.1073/pnas.82.24.8527

Block, J., Schroeder, V., Pawelzyk, P., Willenbacher, N., & Köster, S. (2015). Physical properties of cytoplasmic intermediate filaments. *Biochimica et Biophysica Acta - Molecular Cell Research*, *1853*(11), 3053–3064. https://doi.org/10.1016/j.bbamcr.2015.05.009

Bonne, G., Di Barletta, M. R., Varnous, S., Bécane, H. M., Hammouda, E. H., Merlini, L., Muntoni, F., Greenberg, C. R., Gary, F., Urtizberea, J. A., Duboc, D., Fardeau, M., Toniolo, D., & Schwartz, K. (1999). Mutations in the gene encoding lamin A/C cause autosomal dominant Emery- Dreifuss muscular dystrophy. *Nature Genetics*, *21*(3), 285–288. https://doi.org/10.1038/6799

Broders-Bondon, F., Ho-Bouldoires, T. H. N., Fernandez-Sanchez, M. E., & Farge, E. (2018). Mechanotransduction in tumor progression: The dark side of the force. In *Journal of Cell Biology* (Vol. 217, Issue 5, pp. 1571–1587). Rockefeller University Press. https://doi.org/10.1083/jcb.201701039

Broers, J. L. V., Peeters, E. A. G., Kuijpers, H. J. H., Endert, J., Bouten, C. V. C., Oomens, C. W. J., Baaijens, F. P. T., & Ramaekers, F. C. S. (2004). Decreased mechanical stiffness in LMNA-/- cells is caused by defective nucleo-cytoskeletal integrity: Implications for the development of laminopathies. *Human Molecular Genetics*, *13*(21), 2567–2580. https://doi.org/10.1093/hmg/ddh295

Bronshtein, I., Kepten, E., Kanter, I., Berezin, S., Lindner, M., Redwood, A. B., Mai, S., Gonzalo, S., Foisner, R., Shav-Tal, Y., & Garini, Y. (2015). Loss of lamin A function increases chromatin dynamics in the nuclear interior. *Nature Communications*, *6*. https://doi.org/10.1038/ncomms9044

Buchwalter, A., Kaneshiro, J. M., & Hetzer, M. W. (2019). Coaching from the sidelines: the nuclear periphery in genome regulation. *Nature Reviews Genetics*, *20*(1), 39–50. https://doi.org/10.1038/s41576-018-0063-5

Bui, K. H., Von Appen, A., Diguilio, A. L., Ori, A., Sparks, L., Mackmull, M. T., Bock, T., Hagen, W., Andrés-Pons, A., Glavy, J. S., & Beck, M. (2013). XIntegrated structural analysis of the human nuclear pore complex scaffold. *Cell*, *155*(6), 1233–1243. https://doi.org/10.1016/j.cell.2013.10.055

Burke, B., & Stewart, C. L. (2014). Functional architecture of the cell's nucleus in development, aging, and disease. In *Current Topics in Developmental Biology* (1st ed., Vol. 109). Elsevier Inc. https://doi.org/10.1016/B978-0-12-397920-9.00006-8

Buxboim, A., Swift, J., Irianto, J., Spinler, K. R., Dingal, P. C. D. P., Athirasala, A., Kao, Y. R. C., Cho, S., Harada, T., Shin, J. W., & Discher, D. E. (2014). Matrix elasticity regulates lamin-A,C phosphorylation and turnover with feedback to actomyosin. *Current Biology*, *24*(16), 1909–1917. https://doi.org/10.1016/j.cub.2014.07.001

Caille, N., Thoumine, O., Tardy, Y., & Meister, J. J. (2002). Contribution of the nucleus to the mechanical properties of endothelial cells. *Journal of Biomechanics*, *35*(2), 177–187. https://doi.org/10.1016/S0021-9290(01)00201-9

Cain, N. E., Tapley, E. C., McDonald, K. L., Cain, B. M., & Starr, D. A. (2014). The SUN protein UNC-84 is required only in force-bearing cells to maintain nuclear envelope architecture. *Journal of Cell Biology*, *206*(2), 163–172. https://doi.org/10.1083/jcb.201405081

Cao, H., & Hegele, R. A. (2000). Nuclear lamin A/C R482Q mutation in Canadian kindreds with Dunnigan-type familial partial lipodystrophy. *Human Molecular Genetics*, *9*(1), 109–112. https://doi.org/10.1093/hmg/9.1.109

Capelson, M., Liang, Y., Schulte, R., Mair, W., Wagner, U., & Hetzer, M. W. (2010). Chromatin-Bound Nuclear Pore Components Regulate Gene Expression in Higher Eukaryotes. *Cell*, *140*(3), 372–383. https://doi.org/10.1016/j.cell.2009.12.054

Capoen, W., Sun, J., Wysham, D., Otegui, M. S., Venkateshwaran, M., Hirsch, S., Miwa, H., Downie, J. A., Morris, R. J., Ané, J. M., & Oldroyd, G. E. D. (2011). Nuclear membranes control symbiotic calcium signaling of legumes. *Proceedings of the National Academy of Sciences of the United States of America*, *108*(34), 14348–14353. https://doi.org/10.1073/pnas.1107912108

Casolari, J. M., Brown, C. R., Komili, S., West, J., Hieronymus, H., & Silver, P. A. (2004). Genome-wide localization of the nuclear transport machinery couples transcriptional status and nuclear organization. *Cell*, *117*(4), 427–439. https://doi.org/10.1016/S0092-8674(04)00448-9

Cautain, B., Hill, R., De Pedro, N., & Link, W. (2015). Components and regulation of nuclear transport processes. In *FEBS Journal* (Vol. 282, Issue 3, pp. 445–462). Blackwell Publishing Ltd. https://doi.org/10.1111/febs.13163

Chan, C. J., Li, W., Cojoc, G., & Guck, J. (2017). Volume Transitions of Isolated Cell Nuclei Induced by Rapid Temperature Increase. *Biophysical Journal*, *112*(6), 1063–1076. https://doi.org/10.1016/j.bpj.2017.01.022

Chancellory, T. J., Lee, J., Thodeti, C. K., & Lele, T. (2010). Actomyosin tension exerted on the nucleus through nesprin-1 connections influences endothelial cell adhesion, migration, and cyclic strain-induced reorientation. *Biophysical Journal*, *99*(1), 115–123. https://doi.org/10.1016/j.bpj.2010.04.011

Chang, L., Azzolin, L., Di Biagio, D., Zanconato, F., Battilana, G., Lucon Xiccato, R., Aragona, M., Giulitti, S., Panciera, T., Gandin, A., Sigismondo, G., Krijgsveld, J., Fassan, M., Brusatin, G., Cordenonsi, M., & Piccolo, S. (2018). The SWI/SNF complex is a mechanoregulated inhibitor of YAP and TAZ. In *Nature* (Vol. 563, Issue 7730, pp. 265–269). https://doi.org/10.1038/s41586-018-0658-1

Chen, B., Co, C., & Ho, C. C. (2015). Cell shape dependent regulation of nuclear morphology. *Biomaterials*, *67*, 129–136. https://doi.org/10.1016/j.biomaterials.2015.07.017

Chi, Y. H., Haller, K., Peloponese, J. M., & Jeang, K. T. (2007). Histone acetyltransferase hALP and nuclear membrane protein hsSUN1 function in de-condensation of mitotic chromosomes. *Journal of Biological Chemistry*, *282*(37), 27447–27458. https://doi.org/10.1074/jbc.M703098200

Chizmadzhev, Y. A., Kumenko, D. A., Kuzmin, P. I., Chernomordik, L. V., Zimmerberg, J., & Cohen, F. S. (1999). Lipid flow through fusion pores connecting membranes of different tensions. *Biophysical Journal*, *76*(6), 2951–2965. https://doi.org/10.1016/S0006-3495(99)77450-3

Cho, S., Irianto, J., & Discher, D. E. (2017). Mechanosensing by the nucleus: From pathways to scaling

relationships. *Journal of Cell Biology*, *216*(2), 305–315. https://doi.org/10.1083/jcb.201610042

Chrzanowska-Wodnicka, M., & Burridge, K. (1996). Rho-stimulated contractility drives the formation of stress fibers and focal adhesions. *Journal of Cell Biology*, *133*(6), 1403–1415. https://doi.org/10.1083/jcb.133.6.1403

Coffinier, C., Chang, S. Y., Nobumori, C., Tu, Y., Farber, E. A., Toth, J. I., Fong, L. G., & Young, S. G. (2010). Abnormal development of the cerebral cortex and cerebellum in the setting of lamin B2 deficiency. *Proceedings of the National Academy of Sciences of the United States of America*, *107*(11), 5076–5081. https://doi.org/10.1073/pnas.0908790107

Coffinier, C., Jung, H. J., Nobumori, C., Chang, S., Tu, Y., Barnes, R. H., Yoshinaga, Y., De Jong, P. J., Vergnes, L., Reue, K., Fong, L. G., & Young, S. G. (2011). Deficiencies in lamin B1 and lamin B2 cause neurodevelopmental defects and distinct nuclear shape abnormalities in neurons. *Molecular Biology of the Cell*, *22*(23), 4683–4693. https://doi.org/10.1091/mbc.E11-06-0504

Colwell, L. J., Brenner, M. P., & Ribbeck, K. (2010). Charge as a selection criterion for translocation through the nuclear pore complex. *PLoS Computational Biology*, *6*(4). https://doi.org/10.1371/journal.pcbi.1000747

Corbett, T. H., Griswold, D. P., Roberts, B. J., Peckham, J. C., & Schabel, F. M. (1975). Tumor Induction Relationships in Development of Transplantable Cancers of the Colon in Mice for Chemotherapy Assays, with a Note on Carcinogen Structure. *Cancer Research*, *35*(9), 2434–2439.

Coste, B., Mathur, J., Schmidt, M., Earley, T. J., Ranade, S., Petrus, M. J., Dubin, A. E., & Patapoutian, A. (2010). Piezo1 and Piezo2 are essential components of distinct mechanically activated cation channels. *Science*, *330*(6000), 55–60. https://doi.org/10.1126/science.1193270

Crick, F. H. (1958). On protein synthesis. *Symposia of the Society for Experimental Biology*, *12*, 138–163.

Crisp, M., Liu, Q., Roux, K., Rattner, J. B., Shanahan, C., Burke, B., Stahl, P. D., & Hodzic, D. (2006). Coupling of the nucleus and cytoplasm: Role of the LINC complex. *Journal of Cell Biology*, *172*(1), 41–53. https://doi.org/10.1083/jcb.200509124

Cruz, V. E., Esra Demircioglu, F., & Schwartz, T. U. (2020). Structural Analysis of Different LINC Complexes Reveals Distinct Binding Modes. *Journal of Molecular Biology*, *432*(23), 6028–6041. https://doi.org/10.1016/j.jmb.2020.09.019

Csoka, A. B., Cao, H., Sammak, P. J., Constantinescu, D., Schatten, G. P., & Hegele, R. A. (2004). Novel lamin A/C gene (LMNA) mutations in atypical progeroid syndromes. *Journal of Medical Genetics*, *41*(4), 304–308. https://doi.org/10.1136/jmg.2003.015651

Dahl, K. N., Engler, A. J., Pajerowski, J. D., & Discher, D. E. (2005). Power-law rheology of isolated nuclei with deformation mapping of nuclear substructures. *Biophysical Journal*, *89*(4), 2855–2864. https://doi.org/10.1529/biophysj.105.062554

Dahl, K. N., Kahn, S. M., Wilson, K. L., & Discher, D. E. (2004). The nuclear envelope lamina network has elasticity and a compressibility limit suggestive of a molecular shock absorber. *Journal of Cell Science*, *117*(20), 4779–4786. https://doi.org/10.1242/jcs.01357

Dahl, K. N., Ribeiro, A. J. S., & Lammerding, J. (2008). Nuclear shape, mechanics, and

mechanotransduction. *Circulation Research*, *102*(11), 1307–1318. https://doi.org/10.1161/CIRCRESAHA.108.173989

Daigle, N., Beaudouin, J., Hartnell, L., Imreh, G., Hallberg, E., Lippincott-Schwartz, J., & Ellenberg, J. (2001). Nuclear pore complexes form immobile networks and have a very low turnover in live mammalian cells. *Journal of Cell Biology*, *154*(1), 71–84. https://doi.org/10.1083/jcb.200101089

Dange, T., Grünwald, D., Grünwald, A., Peters, R., & Kubitscheck, U. (2008). Autonomy and robustness of translocation through the nuclear pore complex: A single-molecule study. *Journal of Cell Biology*, *183*(1), 77–86. https://doi.org/10.1083/jcb.200806173

Davidson, P. M., Sliz, J., Isermann, P., Denais, C., & Lammerding, J. (2015). Design of a microfluidic device to quantify dynamic intra-nuclear deformation during cell migration through confining environments. *Integrative Biology (United Kingdom)*, *7*(12), 1534–1546. https://doi.org/10.1039/c5ib00200a

Dazzoni, R., Grélard, A., Morvan, E., Bouter, A., Applebee, C. J., Loquet, A., Larijani, B., & Dufourc, E. J. (2020). The unprecedented membrane deformation of the human nuclear envelope, in a magnetic field, indicates formation of nuclear membrane invaginations. *Scientific Reports*, *10*(1). https://doi.org/10.1038/s41598-020-61746-0

de Leeuw, R., Gruenbaum, Y., & Medalia, O. (2018). Nuclear Lamins: Thin Filaments with Major Functions. *Trends in Cell Biology*, *28*(1), 34–45. https://doi.org/10.1016/j.tcb.2017.08.004

De Sandre-Giovannoli, A., Chaouch, M., Kozlov, S., Vallat, J. M., Tazir, M., Kassouri, N., Szepetowski, P., Hammadouche, T., Vandenberghe, A., Stewart, C. L., Grid, D., & Lévy, N. (2002). Homozygous defects in LMNA, encoding lamin A/C nuclear-envelope proteins, cause autosomal recessive axonal neuropathy in human (Charcot-Marie-Tooth disorder type 2) and mouse. *American Journal of Human Genetics*, *70*(3), 726–736. https://doi.org/10.1086/339274

Dechat, T., Gesson, K., & Foisner, R. (2010). Lamina-independent lamins in the nuclear interior serve important functions. *Cold Spring Harbor Symposia on Quantitative Biology*, *75*, 533–543. https://doi.org/10.1101/sqb.2010.75.018

Denais, C. M., Gilbert, R. M., Isermann, P., McGregor, A. L., Te Lindert, M., Weigelin, B., Davidson, P. M., Friedl, P., Wolf, K., & Lammerding, J. (2016). Nuclear envelope rupture and repair during cancer cell migration. *Science*, *352*(6283), 353–358. https://doi.org/10.1126/science.aad7297

Denning, D. P., Patel, S. S., Uversky, V., Fink, A. L., & Rexach, M. (2003). Disorder in the nuclear pore complex: The FG repeat regions of nucleoporins are natively unfolded. *Proceedings of the National Academy of Sciences of the United States of America*, *100*(5), 2450–2455. https://doi.org/10.1073/pnas.0437902100

Denning, D. P., & Rexach, M. F. (2007). Rapid evolution exposes the boundaries of domain structure and function in natively unfolded FG nucleoporins. *Molecular and Cellular Proteomics*, *6*(2), 272–282. https://doi.org/10.1074/mcp.M600309-MCP200

Dey, P. (2005). Chromatin pattern alteration in malignant cells: An enigma. *Diagnostic Cytopathology*, *32*(1), 25–30. https://doi.org/10.1002/dc.20187

Dey, P. (2010). Cancer nucleus: Morphology and beyond. *Diagnostic Cytopathology*, *38*(5), 382–390. https://doi.org/10.1002/dc.21234

Dickinson, R. B., Katiyar, A., Dubell, C. R., & Lele, T. P. (2022). Viscous shaping of the compliant cell nucleus. *APL Bioengineering*, *6*(1). https://doi.org/10.1063/5.0071652

Ding, X., Xu, R., Yu, J., Xu, T., Zhuang, Y., & Han, M. (2007). SUN1 Is Required for Telomere Attachment to Nuclear Envelope and Gametogenesis in Mice. *Developmental Cell*, *12*(6), 863–872. https://doi.org/10.1016/j.devcel.2007.03.018

Donnaloja, F., Jacchetti, E., Soncini, M., & Raimondi, M. T. (2019). Mechanosensing at the nuclear envelope by nuclear pore complex stretch activation and its effect in physiology and pathology. *Frontiers in Physiology*, *10*(JUL). https://doi.org/10.3389/fphys.2019.00896

Dougherty, E. C. (1957). Abstracts. *The Journal of Protozoology*, *4*, 5–24. https://doi.org/10.1111/j.1550-7408.1957.tb02521.x

Drin, G., Casella, J. F., Gautier, R., Boehmer, T., Schwartz, T. U., & Antonny, B. (2007). A general amphipathic α-helical motif for sensing membrane curvature. *Nature Structural and Molecular Biology*, *14*(2), 138–146. https://doi.org/10.1038/nsmb1194

Dupont, S., Morsut, L., Aragona, M., Enzo, E., Giulitti, S., Cordenonsi, M., Zanconato, F., Le Digabel, J., Forcato, M., Bicciato, S., Elvassore, N., & Piccolo, S. (2011). Role of YAP/TAZ in mechanotransduction. *Nature*, *474*(7350), 179–183. https://doi.org/10.1038/nature10137

Dwyer, N., & Blobel, G. (1976). A modified procedure for the isolation of a pore complex-lamina fraction from rat liver nuclei. *Journal of Cell Biology*, *70*(3), 581–591. https://doi.org/10.1083/jcb.70.3.581

Echevarria, W., Leite, M. F., Guerra, M. T., Zipfel, W. R., & Nathanson, M. H. (2003). Regulation of calcium signals in the nucleus by a nucleoplasmic reticulum. *Nature Cell Biology*, *5*(5), 440–446. https://doi.org/10.1038/ncb980

Ege, N., Dowbaj, A. M., Jiang, M., Howell, M., Hooper, S., Foster, C., Jenkins, R. P., & Sahai, E. (2018). Quantitative Analysis Reveals that Actin and Src-Family Kinases Regulate Nuclear YAP1 and Its Export. *Cell Systems*, *6*(6), 692-708.e13. https://doi.org/10.1016/j.cels.2018.05.006

Elosegui-Artola, A., Andreu, I., Beedle, A. E. M. M., Lezamiz, A., Uroz, M., Kosmalska, A. J., Oria, R., Kechagia, J. Z., Rico-Lastres, P., Le Roux, A.-L. L., Shanahan, C. M., Trepat, X., Navajas, D., Garcia-Manyes, S., & Roca-Cusachs, P. (2017). Force Triggers YAP Nuclear Entry by Regulating Transport across Nuclear Pores. *Cell*, *171*(6), 1397-1410.e14. https://doi.org/10.1016/j.cell.2017.10.008

Elosegui-Artola, A., Bazellières, E., Allen, M. D., Andreu, I., Oria, R., Sunyer, R., Gomm, J. J., Marshall, J. F., Jones, J. L., Trepat, X., & Roca-Cusachs, P. (2014). Rigidity sensing and adaptation through regulation of integrin types. *Nature Materials*, *13*(6), 631–637. https://doi.org/10.1038/nmat3960

Elosegui-Artola, A., Oria, R., Chen, Y., Kosmalska, A., Pérez-González, C., Castro, N., Zhu, C., Trepat, X., & Roca-Cusachs, P. (2016). Mechanical regulation of a molecular clutch defines force transmission and transduction in response to matrix rigidity. *Nature Cell Biology*, *18*(5), 540–548. https://doi.org/10.1038/ncb3336

Elosegui-Artola, A., Trepat, X., & Roca-Cusachs, P. (2018). Control of Mechanotransduction by Molecular Clutch Dynamics. *Trends in Cell Biology*, *28*(5), 356–367. https://doi.org/10.1016/j.tcb.2018.01.008

Enslen, H., Sun, P., Brickey, D., Soderling, S. H., Klamo, E., & Soderling, T. R. (1994). Characterization of Ca2+/calmodulin-dependent protein kinase IV. Role in transcriptional regulation. *Journal of Biological Chemistry*, *269*(22), 15520–15527. https://doi.org/10.1016/s0021-9258(17)40710-1

Enyedi, B., Jelcic, M., & Niethammer, P. (2016). The Cell Nucleus Serves as a Mechanotransducer of Tissue Damage-Induced Inflammation. *Cell*, *165*(5), 1160–1170. https://doi.org/10.1016/j.cell.2016.04.016

Enyedi, B., Kala, S., Nikolich-Zugich, T., & Niethammer, P. (2013). Tissue damage detection by osmotic surveillance. *Nature Cell Biology*, *15*(9), 1123–1130. https://doi.org/10.1038/ncb2818

Enyedi, B., & Niethammer, P. (2017). Nuclear membrane stretch and its role in mechanotransduction. *Nucleus*, *8*(2), 156–161. https://doi.org/10.1080/19491034.2016.1263411

Erdel, F., Baum, M., & Rippe, K. (2015). The viscoelastic properties of chromatin and the nucleoplasm revealed by scale-dependent protein mobility. *Journal of Physics Condensed Matter*, *27*(6). https://doi.org/10.1088/0953-8984/27/6/064115

Erickson, E. S., Mooren, O. L., Moore, D., Krogmeier, J. R., & Dunn, R. C. (2006). The role of nuclear envelope calcium in modifying nuclear pore complex structure. *Canadian Journal of Physiology and Pharmacology*, *84*(3–4), 309–318. https://doi.org/10.1139/Y05-109

Eriksson, M., Brown, W. T., Gordon, L. B., Glynn, M. W., Singer, J., Scott, L., Erdos, M. R., Robbins, C. M., Moses, T. Y., Berglund, P., Dutra, A., Pak, E., Durkin, S., Csoka, A. B., Boehnke, M., Glover, T. W., & Collins, F. S. (2003). Recurrent de novo point mutations in lamin A cause Hutchinson-Gilford progeria syndrome. *Nature*, *423*(6937), 293–298. https://doi.org/10.1038/nature01629

Fatkin, D., MacRae, C., Sasaki, T., Wolff, M. R., Porcu, M., Frenneaux, M., Atherton, J., Vidaillet, H. J., Spudich, S., De Girolami, U., Seidman, J. G., Muntoni, F., Müehle, G., Johnson, W., McDonough, B., & Seidman, C. E. (1999). Missense Mutations in the Rod Domain of the Lamin A/C Gene as Causes of Dilated Cardiomyopathy and Conduction-System Disease. *New England Journal of Medicine*, *341*(23), 1715–1724. https://doi.org/10.1056/nejm199912023412302

Feldherr, C. M., & Akin, D. (1990). The permeability of the nuclear envelope in dividing and nondividing cell cultures. *Journal of Cell Biology*, *111*(1), 1–8. https://doi.org/10.1083/jcb.111.1.1

Feldherr, Carl M., & Akin, D. (1997). The location of the transport gate in the nuclear pore complex. *Journal of Cell Science*, *110*(24), 3065–3070. https://doi.org/10.1242/jcs.110.24.3065

Fernandez-Martinez, J., Kim, S. J., Shi, Y., Upla, P., Pellarin, R., Gagnon, M., Chemmama, I. E., Wang, J., Nudelman, I., Zhang, W., Williams, R., Rice, W. J., Stokes, D. L., Zenklusen, D., Chait, B. T., Sali, A., & Rout, M. P. (2016). Structure and Function of the Nuclear Pore Complex Cytoplasmic mRNA Export Platform. *Cell*, *167*(5), 1215-1228.e25. https://doi.org/10.1016/j.cell.2016.10.028

Fernandez-Martinez, J., Phillips, J., Sekedat, M. D., Diaz-Avalos, R., Velazquez-Muriel, J., Franke, J. D., Williams, R., Stokes, D. L., Chait, B. T., Sali, A., & Rout, M. P. (2012). Structure-function mapping of a heptameric module in the nuclear pore complex. *Journal of Cell Biology*, *196*(4),

419–434. https://doi.org/10.1083/jcb.201109008

Fernandez-Martinez, J., & Rout, M. P. (2021). One Ring to Rule them All? Structural and Functional Diversity in the Nuclear Pore Complex. *Trends in Biochemical Sciences*, *46*(7), 595–607. https://doi.org/10.1016/j.tibs.2021.01.003

Fernandez-Sanchez, M. E., Barbier, S., Whitehead, J., Bealle, G., Michel, A., Latorre-Ossa, H., Rey, C., Fouassier, L., Claperon, A., Brulle, L., Girard, E., Servant, N., Rio-Frio, T., Marie, H., Lesieur, S., Housset, C., Gennisson, J.-L., Tanter, M., Menager, C., … Farge, E. (2015). Mechanical induction of the tumorigenic [bgr]-catenin pathway by tumour growth pressure. *Nature*, *523*(7558), 92–95. https://doi.org/10.1038/nature14329http://www.nature.com/nature/journal/v523/n7558/abs/nature14329.html#supplementary-information

Fichtman, B., Ramos, C., Rasala, B., Harel, A., & Forbes, D. J. (2010). Inner/outer nuclear membrane fusion in nuclear pore assembly: Biochemical demonstration and molecular analysis. *Molecular Biology of the Cell*, *21*(23), 4197–4211. https://doi.org/10.1091/mbc.E10-04-0309

Fidorra, J., Mielke, T., Booz, J., & Feinendegen, L. E. (1981). Cellular and nuclear volume of human cells during the cell cycle. *Radiation and Environmental Biophysics*, *19*(3), 205–214. https://doi.org/10.1007/BF01324188

Finan, J. D., Chalut, K. J., Wax, A., & Guilak, F. (2009). Nonlinear osmotic properties of the cell nucleus. *Proceedings of the ASME Summer Bioengineering Conference 2009, SBC2009*, *PART A*, 93–94. https://doi.org/10.1115/SBC2009-206197

Finan, J. D., & Guilak, F. (2010). The effects of osmotic stress on the structure and function of the cell nucleus. In *Journal of Cellular Biochemistry* (Vol. 109, Issue 3, pp. 460–467). https://doi.org/10.1002/jcb.22437

Finan, J. D., Leddy, H. A., & Guilak, F. (2011). Osmotic stress alters chromatin condensation and nucleocytoplasmic transport. *Biochemical and Biophysical Research Communications*, *408*(2), 230–235. https://doi.org/10.1016/j.bbrc.2011.03.131

Fischer-Vize, J. A., & Mosley, K. L. (1994). marbles mutants: Uncoupling cell determination and nuclear migration in the developing Drosophila eye. *Development*, *120*(9), 2609–2618. https://doi.org/10.1242/dev.120.9.2609

Fischer, A. H., Zhao, C., Li, Q. K., Gustafson, K. S., Eltoum, I. E., Tambouret, R., Benstein, B., Savaloja, L. C., & Kulesza, P. (2010). The cytologic criteria of malignancy. *Journal of Cellular Biochemistry*, *110*(4), 795–811. https://doi.org/10.1002/jcb.22585

Fiserova, J., & Goldberg, M. W. (2010). Relationships at the nuclear envelope: Lamins and nuclear pore complexes in animals and plants. *Biochemical Society Transactions*, *38*(3), 829–831. https://doi.org/10.1042/BST0380829

Franke, W. W., Scheer, U., Krohne, G., & Jarasch, E. D. (1981). The nuclear envelope and the architecture of the nuclear periphery. *Journal of Cell Biology*, *91*(3 II). https://doi.org/10.1083/jcb.91.3.39s

Franz, C., Walczak, R., Yavuz, S., Santarella, R., Gentzel, M., Askjaer, P., Galy, V., Hetzer, M., Mattaj, I. W., & Antonin, W. (2007). MEL-28/ELYS is required for the recruitment of nucleoporins to chromatin and postmitotic nuclear pore complex assembly. *EMBO Reports*, *8*(2), 165–172.

https://doi.org/10.1038/sj.embor.7400889

Frey, S., & Görlich, D. (2007). A Saturated FG-Repeat Hydrogel Can Reproduce the Permeability Properties of Nuclear Pore Complexes. *Cell*, *130*(3), 512–523. https://doi.org/10.1016/j.cell.2007.06.024

Frey, S., Rees, R., Schünemann, J., Ng, S. C., Fünfgeld, K., Huyton, T., & Görlich, D. (2018). Surface Properties Determining Passage Rates of Proteins through Nuclear Pores. *Cell*, *174*(1), 202-217.e9. https://doi.org/10.1016/j.cell.2018.05.045

Frey, S., Richter, R. P., & Görlich, D. (2006). FG-rich repeats of nuclear pore proteins form a three-dimensional meshwork with hydrogel-like properties. *Science*, *314*(5800), 815–817. https://doi.org/10.1126/science.1132516

Frosst, P., Guan, T., Subauste, C., Hahn, K., & Gerace, L. (2002). Tpr is localized within the nuclear basket of the pore complex and has a role in nuclear protein export. *Journal of Cell Biology*, *156*(4), 617–630. https://doi.org/10.1083/jcb.200106046

Funakoshi, T., Clever, M., Watanabe, A., & Imamoto, N. (2011). Localization of Pom121 to the inner nuclear membrane is required for an early step of interphase nuclear pore complex assembly. *Molecular Biology of the Cell*, *22*(7), 1058–1069. https://doi.org/10.1091/mbc.E10-07-0641

Furumatsu, T., Kanazawa, T., Miyake, Y., Kubota, S., Takigawa, M., & Ozaki, T. (2012). Mechanical stretch increases Smad3-dependent CCN2 expression in inner meniscus cells. *Journal of Orthopaedic Research*, *30*(11), 1738–1745. https://doi.org/10.1002/jor.22142

Gant, T. M., & Wilson, K. L. (1997). Nuclear assembly. *Annual Review of Cell and Developmental Biology*, *13*(1), 669–695. https://doi.org/10.1146/annurev.cellbio.13.1.669

García-García, M., Sánchez-Perales, S., Jarabo, P., Calvo, E., Huyton, T., Fu, L., Ng, S. C., Sotodosos-Alonso, L., Vázquez, J., Casas-Tintó, S., Görlich, D., Echarri, A., & Del Pozo, M. A. (2022). Mechanical control of nuclear import by Importin-7 is regulated by its dominant cargo YAP. *Nature Communications*, *13*(1). https://doi.org/10.1038/s41467-022-28693-y

García-González, A., Jacchetti, E., Marotta, R., Tunesi, M., Matas, J. F. R., & Raimondi, M. T. (2018). The effect of cell morphology on the permeability of the nuclear envelope to diffusive factors. *Frontiers in Physiology*, *9*(JUL). https://doi.org/10.3389/fphys.2018.00925

Garcia-Segura, L. M., Lafarga, M., Berciano, M. T., Hernandez, P., & Andres, M. A. (1989). Distribution of nuclear pores and chromatin organization in neurons and glial cells of the rat cerebellar cortex. *Journal of Comparative Neurology*, *290*(3), 440–450. https://doi.org/10.1002/cne.902900311

Gayrard, C., Bernaudin, C., Déjardin, T., Seiler, C., & Borghi, N. (2018). Src- and confinement-dependent FAK activation causes E-cadherin relaxation and β-catenin activity. *Journal of Cell Biology*, *217*(3), 1063–1077. https://doi.org/10.1083/jcb.201706013

Gerace, L., Comeau, C., & Benson, M. (1984). Organization and modulation of nuclear lamina structure. *Journal of Cell Science*, *SUPPL. 1*(Supplement_1), 137–160. https://doi.org/10.1242/jcs.1984.supplement_1.10

Gesson, K., Rescheneder, P., Skoruppa, M. P., Von Haeseler, A., Dechat, T., & Foisner, R. (2016). A-type Lamins bind both hetero- and euchromatin, the latter being regulated by lamina-

associated polypeptide 2 alpha. *Genome Research*, *26*(4), 462–473. https://doi.org/10.1101/gr.196220.115

Goldberg, M. W. (2017). Nuclear pore complex tethers to the cytoskeleton. *Seminars in Cell and Developmental Biology*, *68*, 52–58. https://doi.org/10.1016/j.semcdb.2017.06.017

Goldberg, M. W., & Allen, T. D. (1996). The nuclear pore complex and lamina: Three-dimensional structures and interactions determined by field emission in-lens scanning electron microscopy. *Journal of Molecular Biology*, *257*(4), 848–865. https://doi.org/10.1006/jmbi.1996.0206

Goldman, R. D., Shumaker, D. K., Erdos, M. R., Eriksson, M., Goldman, A. E., Gordon, L. B., Gruenbaum, Y., Khuon, S., Mendez, M., Varga, R., & Collins, F. S. (2004). Accumulation of mutant lamin A progressive changes in nuclear architecture in Hutchinson-Gilford progeria syndrome. *Proceedings of the National Academy of Sciences of the United States of America*, *101*(24), 8963–8968. https://doi.org/10.1073/pnas.0402943101

Görlich, D. (1997). Nuclear protein import. *Current Opinion in Cell Biology*, *9*(3), 412–419. https://doi.org/10.1016/S0955-0674(97)80015-4

Görlich, D. (1998). Transport into and out of the cell nucleus. *EMBO Journal*, *17*(10), 2721–2727. https://doi.org/10.1093/emboj/17.10.2721

Görlich, D., & Kutay, U. (1999). Transport between the cell nucleus and the cytoplasm. *Annual Review of Cell and Developmental Biology*, *15*(1), 607–660.

Görlich, D., Seewald, M. J., & Ribbeck, K. (2003). Characterization of Ran-driven cargo transport and the RanGTPase system by kinetic measurements and computer simulation. *EMBO Journal*, *22*(5), 1088–1100. https://doi.org/10.1093/emboj/cdg113

Goryaynov, A., & Yang, W. (2014). Role of molecular charge in nucleocytoplasmic transport. *PLoS ONE*, *9*(2). https://doi.org/10.1371/journal.pone.0088792

Griffis, E. R., Craige, B., Dimaano, C., Ullman, K. S., & Powers, M. A. (2004). Distinct Functions Domains within Nucleoporins Nup153 and Nup98 Mediate Transcription-dependent Mobility. *Molecular Biology of the Cell*, *15*(4), 1991–2002. https://doi.org/10.1091/mbc.E03-10-0743

Gruenbaum, Y., & Foisner, R. (2015). Lamins: Nuclear intermediate filament proteins with fundamental functions in nuclear mechanics and genome regulation. *Annual Review of Biochemistry*, *84*(1), 131–164. https://doi.org/10.1146/annurev-biochem-060614-034115

Gruenbaum, Y., Goldman, R. D., Meyuhas, R., Mills, E., Margalit, A., Fridkin, A., Dayani, Y., Prokocimer, M., & Enosh, A. (2003). The nuclear lamina and its functions in the nucleus. *International Review of Cytology*, *226*, 1–62. https://doi.org/10.1016/S0074-7696(03)01001-5

Gruenbaum, Y., Margalit, A., Goldman, R. D., Shumaker, D. K., & Wilson, K. L. (2005). The nuclear lamina comes of age. *Nature Reviews Molecular Cell Biology*, *6*(1), 21–31. https://doi.org/10.1038/nrm1550

Guilak, F. (1995). Compression-induced changes in the shape and volume of the chondrocyte nucleus. *Journal of Biomechanics*, *28*(12), 1529–1541. https://doi.org/10.1016/0021-9290(95)00100-X

Guilak, F., Tedrow, J. R., & Burgkart, R. (2000). Viscoelastic properties of the cell nucleus. *Biochemical and Biophysical Research Communications*, *269*(3), 781–786.

https://doi.org/10.1006/bbrc.2000.2360

Guilluy, C., Osborne, L. D., Van Landeghem, L., Sharek, L., Superfine, R., Garcia-Mata, R., & Burridge, K. (2014). Isolated nuclei adapt to force and reveal a mechanotransduction pathway in the nucleus. *Nature Cell Biology*, *16*(4), 376–381. https://doi.org/10.1038/ncb2927

Guo, M., Pegoraro, A. F., Mao, A., Zhou, E. H., Arany, P. R., Han, Y., Burnette, D. T., Jensen, M. H., Kasza, K. E., Moore, J. R., Mackintosh, F. C., Fredberg, J. J., Mooney, D. J., Lippincott-Schwartz, J., & Weitz, D. A. (2017). Cell volume change through water efflux impacts cell stiffness and stem cell fate. *Proceedings of the National Academy of Sciences of the United States of America*, *114*(41), E8618–E8627. https://doi.org/10.1073/pnas.1705179114

Guo, Y., Kim, Y., Shimi, T., Goldman, R. D., & Zheng, Y. (2014). Concentration-dependent lamin assembly and its roles in the localization of other nuclear proteins. *Molecular Biology of the Cell*, *25*(8), 1287–1297. https://doi.org/10.1091/mbc.E13-11-0644

Gurusaran, M., & Davies, O. R. (2021). A molecular mechanism for LINC complex branching by structurally diverse SUN-KASH 6:6 assemblies. *ELife*, *10*, 1–25. https://doi.org/10.7554/ELIFE.60175

Güttler, T., Madl, T., Neumann, P., Deichsel, D., Corsini, L., Monecke, T., Ficner, R., Sattler, M., & Görlich, D. (2010). NES consensus redefined by structures of PKI-type and Rev-type nuclear export signals bound to CRM1. *Nature Structural and Molecular Biology*, *17*(11), 1367–1376. https://doi.org/10.1038/nsmb.1931

Haase, K., MacAdangdang, J. K. L., Edrington, C. H., Cuerrier, C. M., Hadjiantoniou, S., Harden, J. L., Skerjanc, I. S., & Pelling, A. E. (2016). Extracellular Forces Cause the Nucleus to Deform in a Highly Controlled Anisotropic Manner. *Scientific Reports*, *6*. https://doi.org/10.1038/srep21300

Hallett, F. R., Marsh, J., Nickel, B. G., & Wood, J. M. (1993). Mechanical properties of vesicles. II. A model for osmotic swelling and lysis. *Biophysical Journal*, *64*(2), 435–442. https://doi.org/10.1016/S0006-3495(93)81384-5

Hamant, O., & Saunders, T. E. (2020). Shaping Organs: Shared Structural Principles Across Kingdoms. *Annual Review of Cell and Developmental Biology*, *36*(1), null. https://doi.org/10.1146/annurev-cellbio-012820-103850

Hanso, B. (2016). 済無No Title No Title No Title. *Medycyna, Czasopismo Tygodniowe Dla Lekarzy*, *4*(45), 1–23.

Hao, Q., Zhang, B., Yuan, K., Shi, H., & Blobel, G. (2018). Electron microscopy of Chaetomium pom152 shows the assembly of ten-bead string. *Cell Discovery*, *4*(1). https://doi.org/10.1038/s41421-018-0057-7

Haque, F., Lloyd, D. J., Smallwood, D. T., Dent, C. L., Shanahan, C. M., Fry, A. M., Trembath, R. C., & Shackleton, S. (2006). SUN1 Interacts with Nuclear Lamin A and Cytoplasmic Nesprins To Provide a Physical Connection between the Nuclear Lamina and the Cytoskeleton. *Molecular and Cellular Biology*, *26*(10), 3738–3751. https://doi.org/10.1128/mcb.26.10.3738-3751.2006

Haque, F., Mazzeo, D., Patel, J. T., Smallwood, D. T., Ellis, J. A., Shanahan, C. M., & Shackleton, S. (2010). Mammalian SUN protein interaction networks at the inner nuclear membrane and

their role in laminopathy disease processes. *Journal of Biological Chemistry*, *285*(5), 3487–3498. https://doi.org/10.1074/jbc.M109.071910

Harada, T., Swift, J., Irianto, J., Shin, J. W., Spinler, K. R., Athirasala, A., Diegmiller, R., Dingal, P. C. D. P., Ivanovska, I. L., & Discher, D. E. (2014). Nuclear lamin stiffness is a barrier to 3D migration, but softness can limit survival. *Journal of Cell Biology*, *204*(5), 669–682. https://doi.org/10.1083/jcb.201308029

Herrmann, H., & Aebi, U. (2016). Intermediate filaments: Structure and assembly. *Cold Spring Harbor Perspectives in Biology*, *8*(11). https://doi.org/10.1101/cshperspect.a018242

Ho, C. Y., Jaalouk, D. E., Vartiainen, M. K., & Lammerding, J. (2013). Lamin A/C and emerin regulate MKL1-SRF activity by modulating actin dynamics. *Nature*, *497*(7450), 507–513. https://doi.org/10.1038/nature12105

Hobson, C. M., Kern, M., O'Brien, E. T., Stephens, A. D., Falvo, M. R., & Superfine, R. (2020). Correlating nuclear morphology and external force with combined atomic force microscopy and light sheet imaging separates roles of chromatin and lamin A/C in nuclear mechanics. *Molecular Biology of the Cell*, *31*(16), 1788–1801. https://doi.org/10.1091/mbc.E20-01-0073

Hodel, M. R., Corbett, A. H., & Hodel, A. E. (2001). Dissection of a nuclear localization signal. *Journal of Biological Chemistry*, *276*(2), 1317–1325. https://doi.org/10.1074/jbc.M008522200

Hoelz, A., Debler, E. W., & Blobel, G. (2011). The Structure of the nuclear pore complex. *Annual Review of Biochemistry*, *80*, 613–643. https://doi.org/10.1146/annurev-biochem-060109-151030

Hoffmann, E. K., Lambert, I. H., & Pedersen, S. F. (2009). Physiology of cell volume regulation in vertebrates. *Physiological Reviews*, *89*(1), 193–277. https://doi.org/10.1152/physrev.00037.2007

Hoffmann, K., Dreger, C. K., Olins, A. L., Olins, D. E., Shultz, L. D., Lucke, B., Karl, H., Kaps, R., Müller, D., Vayá, A., Aznar, J., Ware, R. E., Sotelo Cruz, N., Lindner, T. H., Herrmann, H., Reis, A., & Sperling, K. (2002). Mutations in the gene encoding the lamin B receptor produce an altered nuclear morphology in granulocytes (Pelger-Huët anomaly). *Nature Genetics*, *31*(4), 410–414. https://doi.org/10.1038/ng925

Hoffmann, K., Sperling, K., Olins, A. L., & Olins, D. E. (2007). The granulocyte nucleus and lamin B receptor: Avoiding the ovoid. *Chromosoma*, *116*(3), 227–235. https://doi.org/10.1007/s00412-007-0094-8

Holthuis, J. C. M., & Levine, T. P. (2005). Lipid traffic: Floppy drives and a superhighway. *Nature Reviews Molecular Cell Biology*, *6*(3), 209–220. https://doi.org/10.1038/nrm1591

Hoogenboom, B. W., Hough, L. E., Lemke, E. A., Lim, R. Y. H., Onck, P. R., & Zilman, A. (2021). Physics of the nuclear pore complex: Theory, modeling and experiment. *Physics Reports*, *921*, 1–53. https://doi.org/10.1016/j.physrep.2021.03.003

Houben, F., Willems, C. H. M. P., Declercq, I. L. J., Hochstenbach, K., Kamps, M. A., Snoeckx, L. H. E. H., Ramaekers, F. C. S., & Broers, J. L. V. (2009). Disturbed nuclear orientation and cellular migration in A-type lamin deficient cells. *Biochimica et Biophysica Acta - Molecular Cell Research*, *1793*(2), 312–324. https://doi.org/10.1016/j.bbamcr.2008.10.003

Huang, F., Shi, Q., Li, Y., Xu, L., Xu, C., Chen, F., Wang, H., Liao, H., Chang, Z., Liu, F., Zhang, X. H.-F., Feng, X.-H., Han, J.-D. J., Luo, S., & Chen, Y.-G. (2018). HER2/EGFR–AKT Signaling Switches TGFβ from Inhibiting Cell Proliferation to Promoting Cell Migration in Breast Cancer. *Cancer Research*, *78*(21), 6073–6085. https://doi.org/10.1158/0008-5472.CAN-18-0136

Humphrey, J. D., Schwartz, M. A., Tellides, G., & Milewicz, D. M. (2015). Role of mechanotransduction in vascular biology: focus on thoracic aortic aneurysms and dissections. *Circ Res*, *116*(8), 1448–1461. https://doi.org/10.1161/CIRCRESAHA.114.304936

Hutchison, C. J. (2002). Lamins: Building blocks or regulators of gene expression? *Nature Reviews Molecular Cell Biology*, *3*(11), 848–858. https://doi.org/10.1038/nrm950

Ihalainen, T. O., Aires, L., Herzog, F. A., Schwartlander, R., Moeller, J., & Vogel, V. (2015). Differential basal-to-apical accessibility of lamin A/C epitopes in the nuclear lamina regulated by changes in cytoskeletal tension. *Nature Materials*, *14*(12), 1252–1261. https://doi.org/10.1038/nmat4389

Infante, E., Stannard, A., Board, S. J., Rico-Lastres, P., Rostkova, E., Beedle, A. E. M., Lezamiz, A., Wang, Y. J., Gulaidi Breen, S., Panagaki, F., Sundar Rajan, V., Shanahan, C., Roca-Cusachs, P., & Garcia-Manyes, S. (2019). The mechanical stability of proteins regulates their translocation rate into the cell nucleus. *Nature Physics*, *15*(9), 973–981. https://doi.org/10.1038/s41567-019-0551-3

Ishihara, S., Yasuda, M., Harada, I., Mizutani, T., Kawabata, K., & Haga, H. (2013). Substrate stiffness regulates temporary NF-κB activation via actomyosin contractions. *Experimental Cell Research*, *319*(19), 2916–2927. https://doi.org/10.1016/j.yexcr.2013.09.018

Itano, N., Okamoto, S. ichi, Zhang, D., Lipton, S. A., & Ruoslahti, E. (2003). Cell spreading controls endoplasmic and nuclear calcium: A physical gene regulation pathway from the cell surface to the nucleus. *Proceedings of the National Academy of Sciences of the United States of America*, *100*(9), 5181–5186. https://doi.org/10.1073/pnas.0531397100

Jacchetti, E., Nasehi, R., Boeri, L., Parodi, V., Negro, A., Albani, D., Osellame, R., Cerullo, G., Matas, J. F. R., & Raimondi, M. T. (2021). The nuclear import of the transcription factor MyoD is reduced in mesenchymal stem cells grown in a 3D micro-engineered niche. *Scientific Reports*, *11*(1). https://doi.org/10.1038/s41598-021-81920-2

Jacinto, F. V., Benner, C., & Hetzer, M. W. (2015). The nucleoporin Nup153 regulates embryonic stem cell pluripotency through gene silencing. *Genes and Development*, *29*(12), 1224–1238. https://doi.org/10.1101/gad.260919.115

Jacobelli, J., Estin Matthews, M., Chen, S., & Krummel, M. F. (2013). Activated T Cell Trans-Endothelial Migration Relies on Myosin-IIA Contractility for Squeezing the Cell Nucleus through Endothelial Cell Barriers. *PLoS ONE*, *8*(9). https://doi.org/10.1371/journal.pone.0075151

Jahed, Z., Soheilypour, M., Peyro, M., & Mofrad, M. R. K. (2016). The LINC and NPC relationship - it's complicated! *Journal of Cell Science*, *129*(17), 3219–3229. https://doi.org/10.1242/jcs.184184

Janmey, P. A., & Kinnunen, P. K. J. (2006). Biophysical properties of lipids and dynamic membranes. *Trends in Cell Biology*, *16*(10), 538–546. https://doi.org/10.1016/j.tcb.2006.08.009

Jor, J. W. Y., Parker, M. D., Taberner, A. J., Nash, M. P., & Nielsen, P. M. F. (2013). Computational and experimental characterization of skin mechanics: Identifying current challenges and future

directions. *Wiley Interdisciplinary Reviews: Systems Biology and Medicine*, *5*(5), 539–556. https://doi.org/10.1002/wsbm.1228

Jorgensen, P., Nicholas P. Edgington, Brandt L. Schneider, Ivan Rupes, Mike Tyers, B. F., Edgington, N. P., Schneider, B. L., Rupes, I., Tyers, M., & Futcher, B. (2007). The Size of the Nucleus Increases as Yeast Cells Grow. *Molecular Biology of the Cell*, *18*(December), 986–994.

Joseph, J., & Dasso, M. (2008). The nucleoporin Nup358 associates with and regulates interphase microtubules. *FEBS Letters*, *582*(2), 190–196. https://doi.org/10.1016/j.febslet.2007.11.087

Jovanovic-Talisman, T., Tetenbaum-Novatt, J., McKenney, A. S., Zilman, A., Peters, R., Rout, M. P., & Chait, B. T. (2009). Artificial nanopores that mimic the transport selectivity of the nuclear pore complex. *Nature*, *457*(7232), 1023–1027. https://doi.org/10.1038/nature07600

Jovanovic-Talisman, T., & Zilman, A. (2017). Protein Transport by the Nuclear Pore Complex: Simple Biophysics of a Complex Biomachine. *Biophysical Journal*, *113*(1), 6–14. https://doi.org/10.1016/j.bpj.2017.05.024

Kadota, S., Ou, J., Shi, Y., Lee, J. T., Sun, J., & Yildirim, E. (2020). Nucleoporin 153 links nuclear pore complex to chromatin architecture by mediating CTCF and cohesin binding. *Nature Communications*, *11*(1). https://doi.org/10.1038/s41467-020-16394-3

Kalderon, D., Roberts, B. L., Richardson, W. D., & Smith, A. E. (1984). A short amino acid sequence able to specify nuclear location. *Cell*, *39*(3 PART 2), 499–509. https://doi.org/10.1016/0092-8674(84)90457-4

Kalverda, B., & Fornerod, M. (2010). Characterization of genome-nucleoporin interactions in Drosophila links chromatin insulators to the nuclear pore complex. *Cell Cycle*, *9*(24), 4812–4817. https://doi.org/10.4161/cc.9.24.14328

Kanwal, C., Mu, S., Kern, S. E., & Lim, C. S. (2004). Bidirectional on/off switch for controlled targeting of proteins to subcellular compartments. *Journal of Controlled Release*, *98*(3), 379–393. https://doi.org/10.1016/j.jconrel.2004.05.008

Kapinos, L. E., Huang, B., Rencurel, C., & Lim, R. Y. H. (2017). Karyopherins regulate nuclear pore complex barrier and transport function. *Journal of Cell Biology*, *216*(11), 3609–3624. https://doi.org/10.1083/jcb.201702092

Karoutas, A., & Akhtar, A. (2021). Functional mechanisms and abnormalities of the nuclear lamina. *Nature Cell Biology*, *23*(2), 116–126. https://doi.org/10.1038/s41556-020-00630-5

Kassianidou, E., Kalita, J., & Lim, R. Y. H. (2019). The role of nucleocytoplasmic transport in mechanotransduction. *Experimental Cell Research*, *377*(1–2), 86–93. https://doi.org/10.1016/j.yexcr.2019.02.009

Katiyar, A., Tocco, V. J., Li, Y., Aggarwal, V., Tamashunas, A. C., Dickinson, R. B., & Lele, T. P. (2019). Nuclear size changes caused by local motion of cell boundaries unfold the nuclear lamina and dilate chromatin and intranuclear bodies. *Soft Matter*, *15*(45), 9310–9317. https://doi.org/10.1039/c9sm01666j

Kazgan, N., Williams, T., Forsberg, L. J., & Brenman, J. E. (2010). Identification of a nuclear export signal in the catalytic subunit of AMP-activated protein kinase. *Molecular Biology of the Cell*, *21*(19), 3433–3442. https://doi.org/10.1091/mbc.E10-04-0347

Kechagia, Z., Sáez, P., Gómez-González, M., Zamarbide, M., Andreu, I., Koorman, T., Beedle, A. E. M., Derksen, P. W. B., Trepat, X., Arroyo, M., & Roca-Cusachs, P. (2022). The laminin-keratin link shields the nucleus from mechanical deformation and signalling. *BioRxiv*, 2022.03.01.482474. https://www.biorxiv.org/content/10.1101/2022.03.01.482474v1%0Ahttps://www.biorxiv.org/content/10.1101/2022.03.01.482474v1.abstract

Keminer, O., & Peters, R. (1999). Permeability of single nuclear pores. *Biophysical Journal*, *77*(1), 217–228. https://doi.org/10.1016/S0006-3495(99)76883-9

Ketema, M., Wilhelmsen, K., Kuikman, I., Janssen, H., Hodzic, D., & Sonnenberg, A. (2007). Requirements for the localization of nesprin-3 at the nuclear envelope and its interaction with plectin. *Journal of Cell Science*, *120*(19), 3384–3394. https://doi.org/10.1242/jcs.014191

Khandwala, A. S., & Kasper, C. B. (1971). The fatty acid composition of individual phospholipids from rat liver nuclear membrane and nuclei. *Journal of Biological Chemistry*, *246*(20), 6242–6246. https://doi.org/10.1016/s0021-9258(18)61781-8

Kim, D. H., Chambliss, A. B., & Wirtz, D. (2013). The multi-faceted role of the actin cap in cellular mechanosensation and mechanotransduction. *Soft Matter*, *9*(23), 5516–5523. https://doi.org/10.1039/c3sm50798j

Kim, M., Kim, M., Lee, S., Kuninaka, S., Saya, H., Lee, H., Lee, S., & Lim, D. S. (2013). CAMP/PKA signalling reinforces the LATS-YAP pathway to fully suppress YAP in response to actin cytoskeletal changes. *EMBO Journal*, *32*(11), 1543–1555. https://doi.org/10.1038/emboj.2013.102

Kim, S., & Elbaum, M. (2013a). A simple kinetic model with explicit predictions for nuclear transport. *Biophysical Journal*, *105*(3), 565–569. https://doi.org/10.1016/j.bpj.2013.04.025

Kim, S., & Elbaum, M. (2013b). Enzymatically driven transport: A kinetic theory for nuclear export. *Biophysical Journal*, *105*(9), 1997–2005. https://doi.org/10.1016/j.bpj.2013.09.011

Kim, S. J., Fernandez-Martinez, J., Nudelman, I., Shi, Y., Zhang, W., Raveh, B., Herricks, T., Slaughter, B. D., Hogan, J. A., Upla, P., Chemmama, I. E., Pellarin, R., Echeverria, I., Shivaraju, M., Chaudhury, A. S., Wang, J., Williams, R., Unruh, J. R., Greenberg, C. H., … Rout, M. P. (2018). Integrative structure and functional anatomy of a nuclear pore complex. *Nature*, *555*(7697), 475–482. https://doi.org/10.1038/nature26003

Kim, Y., Sharov, A. A., McDole, K., Cheng, M., Hao, H., Fan, C. M., Gaiano, N., Ko, M. S. H., & Zheng, Y. (2011). Mouse B-type lamins are required for proper organogenesis but not by embryonic stem cells. *Science*, *334*(6063), 1706–1710. https://doi.org/10.1126/science.1211222

Kind, J., Pagie, L., De Vries, S. S., Nahidiazar, L., Dey, S. S., Bienko, M., Zhan, Y., Lajoie, B., De Graaf, C. A., Amendola, M., Fudenberg, G., Imakaev, M., Mirny, L. A., Jalink, K., Dekker, J., Van Oudenaarden, A., & Van Steensel, B. (2015). Genome-wide Maps of Nuclear Lamina Interactions in Single Human Cells. *Cell*, *163*(1), 134–147. https://doi.org/10.1016/j.cell.2015.08.040

Kirby, T. J., & Lammerding, J. (2018). Emerging views of the nucleus as a cellular mechanosensor. In *Nature Cell Biology* (Vol. 20, Issue 4, pp. 373–381). Nature Publishing Group. https://doi.org/10.1038/s41556-018-0038-y

Kittisopikul, M., Shimi, T., Tatli, M., Tran, J. R., Zheng, Y., Medalia, O., Jaqaman, K., Adam, S. A., &

Goldman, R. D. (2021). Computational analyses reveal spatial relationships between nuclear pore complexes and specific lamins. *Journal of Cell Biology*, *220*(4). https://doi.org/10.1083/JCB.202007082

Kochin, V., Shimi, T., Torvaldson, E., Adam, S. A., Goldman, A., Pack, C. G., Melo-Cardenas, J., Imanishi, S. Y., Goldman, R. D., & Eriksson, J. E. (2014). Interphase phosphorylation of lamin A. *Journal of Cell Science*, *127*(12), 2683–2696. https://doi.org/10.1242/jcs.141820

Köhler, A., & Hurt, E. (2010). Gene Regulation by Nucleoporins and Links to Cancer. *Molecular Cell*, *38*(1), 6–15. https://doi.org/10.1016/j.molcel.2010.01.040

Kopito, R. B., & Elbaum, M. (2007). Reversibility in nucleocytoplasmic transport. *Proceedings of the National Academy of Sciences of the United States of America*, *104*(31), 12743–12748. https://doi.org/10.1073/pnas.0702690104

Kopito, R. B., & Elbaum, M. (2009). Nucleocytoplasmic transport: A thermodynamic mechanism. *HFSP Journal*, *3*(2), 130–141. https://doi.org/10.2976/1.3080807

Kosinski, J., Mosalaganti, S., Von Appen, A., Teimer, R., Diguilio, A. L., Wan, W., Bui, K. H., Hagen, W. J. H., Briggs, J. A. G., Glavy, J. S., Hurt, E., & Beck, M. (2016). Molecular architecture of the inner ring scaffold of the human nuclear pore complex. *Science*, *352*(6283), 363–365. https://doi.org/10.1126/science.aaf0643

Krause, M., Te Riet, J., & Wolf, K. (2013). Probing the compressibility of tumor cell nuclei by combined atomic force-confocal microscopy. *Physical Biology*, *10*(6). https://doi.org/10.1088/1478-3975/10/6/065002

Krull, S., Thyberg, J., Björkroth, B., Rackwitz, H. R., & Cordes, V. C. (2004). Nucleoporins as components of the nuclear pore complex core structure and Tpr as the architectural element of the nuclear basket. *Molecular Biology of the Cell*, *15*(9), 4261–4277. https://doi.org/10.1091/mbc.E04-03-0165

Kubitscheck, U., Grünwald, D., Hoekstra, A., Rohleder, D., Kues, T., Siebrasse, J. P., & Peters, R. (2005). Nuclear transport of single molecules: Dwell times at the nuclear pore complex. *Journal of Cell Biology*, *168*(2), 233–243. https://doi.org/10.1083/jcb.200411005

Kuhn, T. M., & Capelson, M. (2019). Nuclear pore proteins in regulation of chromatin state. *Cells*, *8*(11). https://doi.org/10.3390/cells8111414

Kutscheidt, S., Zhu, R., Antoku, S., Luxton, G. W. G., Stagljar, I., Fackler, O. T., & Gundersen, G. G. (2014). FHOD1 interaction with nesprin-2G mediates TAN line formation and nuclear movement. *Nature Cell Biology*, *16*(7), 708–715. https://doi.org/10.1038/ncb2981

Ladoux, B., Nelson, W. J., Yan, J., & Mège, R. M. (2015). The mechanotransduction machinery at work at adherens junctions. *Integrative Biology*, *7*(10), 1109–1119. https://doi.org/10.1039/c5ib00070j

Lakins, J. N., Chin, A. R., & Weaver, V. M. (2012). Exploring the link between human embryonic stem cell organization and fate using tension-calibrated extracellular matrix functionalized polyacrylamide gels. In *Methods in Molecular Biology* (Vol. 916, Issue June 2014, pp. 317–350). https://doi.org/10.1007/978-1-61779-980-8_24

Lammerding, J., Fong, L. G., Ji, J. Y., Reue, K., Stewart, C. L., Young, S. G., & Lee, R. T. (2006). Lamins

a and C but not lamin B1 regulate nuclear mechanics. *Journal of Biological Chemistry*, *281*(35), 25768–25780. https://doi.org/10.1074/jbc.M513511200

Lammerding, J., & Lee, R. T. (2008). Mechanical properties of interphase nuclei probed by cellular strain application. *Methods in Molecular Biology*, *464*, 13–26. https://doi.org/10.1007/978-1-60327-461-6_2

Lammerding, J., Schulze, P. C., Takahashi, T., Kozlov, S., Sullivan, T., Kamm, R. D., Stewart, C. L., & Lee, R. T. (2004). Lamin A/C deficiency causes defective nuclear mechanics and mechanotransduction. *Journal of Clinical Investigation*, *113*(3), 370–378. https://doi.org/10.1172/JCI200419670

Lämmermann, T., Bader, B. L., Monkley, S. J., Worbs, T., Wedlich-Söldner, R., Hirsch, K., Keller, M., Förster, R., Critchley, D. R., Fässler, R., & Sixt, M. (2008). Rapid leukocyte migration by integrin-independent flowing and squeezing. *Nature*, *453*(7191), 51–55. https://doi.org/10.1038/nature06887

Lamparter, L., & Galic, M. (2020). Cellular Membranes, a Versatile Adaptive Composite Material. *Frontiers in Cell and Developmental Biology*, *8*. https://doi.org/10.3389/fcell.2020.00684

Lange, A., Mills, R. E., Lange, C. J., Stewart, M., Devine, S. E., & Corbett, A. H. (2007). Classical nuclear localization signals: Definition, function, and interaction with importin α. *Journal of Biological Chemistry*, *282*(8), 5101–5105. https://doi.org/10.1074/jbc.R600026200

Langen, P., & Hucho, F. (2008). Karl Lohmann und die Entdeckung des ATP. *Angewandte Chemie*, *120*(10), 1848–1851. https://doi.org/10.1002/ange.200702929

Latorre, E., Kale, S., Casares, L., Gómez-González, M., Uroz, M., Valon, L., Nair, R. V., Garreta, E., Montserrat, N., del Campo, A., Ladoux, B., Arroyo, M., & Trepat, X. (2018). Active superelasticity in three-dimensional epithelia of controlled shape. *Nature*, *563*(7730), 203–208. https://doi.org/10.1038/s41586-018-0671-4

Le, H. Q., Ghatak, S., Yeung, C. Y. C., Tellkamp, F., Günschmann, C., Dieterich, C., Yeroslaviz, A., Habermann, B., Pombo, A., Niessen, C. M., & Wickström, S. A. (2016). Mechanical regulation of transcription controls Polycomb-mediated gene silencing during lineage commitment. *Nature Cell Biology*, *18*(8), 864–875. https://doi.org/10.1038/ncb3387

Le, T. T., Gao, X., Park, S. ha, Lee, J., Inman, J. T., Lee, J. H., Killian, J. L., Badman, R. P., Berger, J. M., & Wang, M. D. (2019). Synergistic Coordination of Chromatin Torsional Mechanics and Topoisomerase Activity. *Cell*, *179*(3), 619-631.e15. https://doi.org/10.1016/j.cell.2019.09.034

Lecarpentier, Y., Claes, V., Vallée, A., & Hébert, J. (2017). Thermodynamics in cancers: opposing interactions between PPAR gamma and the canonical WNT/beta-catenin pathway. *Clinical and Translational Medicine*, *6*(1). https://doi.org/10.1186/s40169-017-0144-7

Lee, B. J., Cansizoglu, A. E., Süel, K. E., Louis, T. H., Zhang, Z., & Chook, Y. M. (2006). Rules for Nuclear Localization Sequence Recognition by Karyopherinβ2. *Cell*, *126*(3), 543–558. https://doi.org/10.1016/j.cell.2006.05.049

Lee, J. S. H., Hale, C. M., Panorchan, P., Khatau, S. B., George, J. P., Tseng, Y., Stewart, C. L., Hodzic, D., & Wirtz, D. (2007). Nuclear lamin A/C deficiency induces defects in cell mechanics, polarization, and migration. *Biophysical Journal*, *93*(7), 2542–2552. https://doi.org/10.1529/biophysj.106.102426

Leeuwenhoek, A. van. (1719). *Opera omnia, seu arcana naturae ope exactissimorum microscopiorum detecta, experimentis variis comprobata*. 728. http://books.google.fr/books?id=hfoTAAAAQAAJ

Leggett, S. E., Sim, J. Y., Rubins, J. E., Neronha, Z. J., Williams, E. K., & Wong, I. Y. (2016). Morphological single cell profiling of the epithelial-mesenchymal transition. *Integrative Biology (United Kingdom)*, *8*(11), 1133–1144. https://doi.org/10.1039/c6ib00139d

Lele, T. P., Dickinson, R. B., & Gundersen, G. G. (2018). Mechanical principles of nuclear shaping and positioning. *Journal of Cell Biology*, *217*(10), 3330–3342. https://doi.org/10.1083/JCB.201804052

Lemke, E. A. (2016). The Multiple Faces of Disordered Nucleoporins. *Journal of Molecular Biology*, *428*(10), 2011–2024. https://doi.org/10.1016/j.jmb.2016.01.002

Levy, D. L., & Heald, R. (2010). Nuclear Size Is Regulated by Importin α and Ntf2 in Xenopus. *Cell*, *143*(2), 288–298. https://doi.org/10.1016/j.cell.2010.09.012

Li, P., & Noegel, A. A. (2015). Inner nuclear envelope protein SUN1 plays a prominent role in mammalian mRNA export. *Nucleic Acids Research*, *43*(20), 9874–9888. https://doi.org/10.1093/nar/gkv1058

Li, Y., Lovett, D., Zhang, Q., Neelam, S., Kuchibhotla, R. A., Zhu, R., Gundersen, G. G., Lele, T. P., & Dickinson, R. B. (2015). Moving Cell Boundaries Drive Nuclear Shaping during Cell Spreading. *Biophysical Journal*, *109*(4), 670–686. https://doi.org/10.1016/j.bpj.2015.07.006

Liang, Y., Franks, T. M., Marchetto, M. C., Gage, F. H., & Hetzer, M. W. (2013). Dynamic Association of NUP98 with the Human Genome. *PLoS Genetics*, *9*(2). https://doi.org/10.1371/journal.pgen.1003308

Lin, D. H., Stuwe, T., Schilbach, S., Rundlet, E. J., Perriches, T., Mobbs, G., Fan, Y., Thierbach, K., Huber, F. M., Collins, L. N., Davenport, A. M., Jeon, Y. E., & Hoelz, A. (2016). Architecture of the symmetric core of the nuclear pore. *Science*, *352*(6283). https://doi.org/10.1126/science.aaf1015

Liu, H., & Naismith, J. H. (2008). An efficient one-step site-directed deletion, insertion, single and multiple-site plasmid mutagenesis protocol. *BMC Biotechnology*, *8*(1), 91. https://doi.org/10.1186/1472-6750-8-91

Liu, Qian, Pante, N., Misteli, T., Elsagga, M., Crisp, M., Hodzic, D., Burke, B., & Roux, K. J. (2007). Functional association of Sun1 with nuclear pore complexes. *Journal of Cell Biology*, *178*(5), 785–798. https://doi.org/10.1083/jcb.200704108

Liu, Qinying, Yu, J., Zhuo, X., Jiang, Q., & Zhang, C. (2010). Pericentrin contains five NESs and an NLS essential for its nucleocytoplasmic trafficking during the cell cycle. *Cell Research*, *20*(8), 948–962. https://doi.org/10.1038/cr.2010.89

Lomakin, A. J., Cattin, C. J., Cuvelier, D., Alraies, Z., Molina, M., Nader, G. P. F. F., Srivastava, N., Sáez, P. J., Garcia-Arcos, J. M., Zhitnyak, I. Y., Bhargava, A., Driscoll, M. K., Welf, E. S., Fiolka, R., Petrie, R. J., de Silva, N. S., González-Granado, J. M., Manel, N., Lennon-Duménil, A. M., … Piel, M. (2020). The nucleus acts as a ruler tailoring cell responses to spatial constraints. *Science*, *370*(6514), 863514. https://doi.org/10.1126/science.aba2894

Lombardi, M. L., Jaalouk, D. E., Shanahan, C. M., Burke, B., Roux, K. J., & Lammerding, J. (2011). The interaction between nesprins and sun proteins at the nuclear envelope is critical for force transmission between the nucleus and cytoskeleton. *Journal of Biological Chemistry*, *286*(30), 26743–26753. https://doi.org/10.1074/jbc.M111.233700

Lombardi, M. L., & Lammerding, J. (2011). Keeping the LINC: The importance of nucleocytoskeletal coupling in intracellular force transmission and cellular function. *Biochemical Society Transactions*, *39*(6), 1729–1734. https://doi.org/10.1042/BST20110686

Lovett, D. B., Shekhar, N., Nickerson, J. A., Roux, K. J., & Lele, T. P. (2013). Modulation of nuclear shape by substrate rigidity. *Cellular and Molecular Bioengineering*, *6*(2), 230–238. https://doi.org/10.1007/s12195-013-0270-2

Lowe, A. R., Siegel, J. J., Kalab, P., Siu, M., Weis, K., & Liphardt, J. T. (2010). Selectivity mechanism of the nuclear pore complex characterized by single cargo tracking. *Nature*, *467*(7315), 600–603. https://doi.org/10.1038/nature09285

Lowe, A. R., Tang, J. H., Yassif, J., Graf, M., Huang, W. Y., Groves, J. T., Weis, K., & Liphardt, J. T. (2015). Importin-β modulates the permeability of the nuclear pore complex in a Ran-dependent manner. *ELife*, *4*. https://doi.org/10.7554/eLife.04052

Lu, W., Gotzmann, J., Sironi, L., Jaeger, V.-M., Schneider, M., Lüke, Y., Uhlén, M., Szigyarto, C. A.-K., Brachner, A., Ellenberg, J., Foisner, R., Noegel, A. A., & Karakesisoglou, I. (2008). Sun1 forms immobile macromolecular assemblies at the nuclear envelope. *Biochimica et Biophysica Acta (BBA) - Molecular Cell Research*, *1783*(12), 2415–2426. https://doi.org/10.1016/j.bbamcr.2008.09.001

Luciano, M., Xue, S. L., De Vos, W. H., Redondo-Morata, L., Surin, M., Lafont, F., Hannezo, E., & Gabriele, S. (2021). Cell monolayers sense curvature by exploiting active mechanics and nuclear mechanoadaptation. *Nature Physics*, *17*(12), 1382–1390. https://doi.org/10.1038/s41567-021-01374-1

Lutzmann, M., Kunze, R., Buerer, A., Aebi, U., & Hurt, E. (2002). Modular self-assembly of a Y-shaped multiprotein complex from seven nucleoporins. *EMBO Journal*, *21*(3), 387–397. https://doi.org/10.1093/emboj/21.3.387

Luxton, G. W. G., Gomes, E. R., Folker, E. S., Vintinner, E., & Gundersen, G. G. (2010). Linear arrays of nuclear envelope proteins harness retrograde actin flow for nuclear movement. *Science*, *329*(5994), 956–959. https://doi.org/10.1126/science.1189072

Lyman, S. K., Guan, T., Bednenko, J., Wodrich, H., & Gerace, L. (2002). Influence of cargo size on Ran and energy requirements for nuclear protein import. *Journal of Cell Biology*, *159*(1), 55–67. https://doi.org/10.1083/jcb.200204163

Maeshima, K., Yahata, K., Sasaki, Y., Nakatomi, R., Tachibana, T., Hashikawa, T., Imamoto, F., & Imamoto, N. (2006). Cell-cycle-dependent dynamics of nuclear pores: Pore-free islands and lamins. *Journal of Cell Science*, *119*(21), 4442–4451. https://doi.org/10.1242/jcs.03207

Mahamid, J., Pfeffer, S., Schaffer, M., Villa, E., Danev, R., Cuellar, L. K., Förster, F., Hyman, A. A., Plitzko, J. M., & Baumeister, W. (2016). Visualizing the molecular sociology at the HeLa cell nuclear periphery. *Science*, *351*(6276), 969–972. https://doi.org/10.1126/science.aad8857

Maiti, R., Gerhardt, L. C., Lee, Z. S., Byers, R. A., Woods, D., Sanz-Herrera, J. A., Franklin, S. E., Lewis,

R., Matcher, S. J., & Carré, M. J. (2016). In vivo measurement of skin surface strain and sub-surface layer deformation induced by natural tissue stretching. *Journal of the Mechanical Behavior of Biomedical Materials*, *62*, 556–569. https://doi.org/10.1016/j.jmbbm.2016.05.035

Malhas, A., Goulbourne, C., & Vaux, D. J. (2011). The nucleoplasmic reticulum: Form and function. *Trends in Cell Biology*, *21*(6), 362–373. https://doi.org/10.1016/j.tcb.2011.03.008

Malone, C. J., Fixsen, W. D., Horvitz, H. R., & Han, M. (1999). UNC-84 localizes to the nuclear envelope and is required for nuclear migration and anchoring during C. elegans development. *Development*, *126*(14), 3171–3181. https://doi.org/10.1242/dev.126.14.3171

Malviya, A. N., & Rogue, P. J. (1998). "Tell me where is calcium bred": Clarifying the roles of nuclear calcium. *Cell*, *92*(1), 17–23. https://doi.org/10.1016/S0092-8674(00)80895-8

Mammoto, A., Connor, K. M., Mammoto, T., Yung, C. W., Huh, D., Aderman, C. M., Mostoslavsky, G., Smith, L. E. H., & Ingber, D. E. (2009). A mechanosensitive transcriptional mechanism that controls angiogenesis. *Nature*, *457*(7233), 1103–1108. https://doi.org/10.1038/nature07765

Maniotis, A. J., Chen, C. S., & Ingber, D. E. (1997). Demonstration of mechanical connections between integrins, cytoskeletal filaments, and nucleoplasm that stabilize nuclear structure. *Proceedings of the National Academy of Sciences of the United States of America*, *94*(3), 849–854. https://doi.org/10.1073/pnas.94.3.849

Martins, T. V., Evans, M. J., Wysham, D. B., & Morris, R. J. (2016). Nuclear pores enable sustained perinuclear calcium oscillations. *BMC Systems Biology*, *10*(1). https://doi.org/10.1186/s12918-016-0289-9

Matsuda, A., & Mofrad, M. R. K. (2022). On the nuclear pore complex and its emerging role in cellular mechanotransduction. *APL Bioengineering*, *6*(1), 011504. https://doi.org/10.1063/5.0080480

Matsuura, Y. (2016). Mechanistic Insights from Structural Analyses of Ran-GTPase-Driven Nuclear Export of Proteins and RNAs. *Journal of Molecular Biology*, *428*(10), 2025–2039. https://doi.org/10.1016/j.jmb.2015.09.025

Maul, G. G., & Deaven, L. (1977). Quantitative determination of nuclear pore complexes in cycling cells with differing DNA content. *Journal of Cell Biology*, *73*(3), 748–760. https://doi.org/10.1083/jcb.73.3.748

Maul, G. G., Deaven, L. L., Freed, J. J., Campbell, G. L. M., & Beçak, W. (1980). Investigation of the determinants of nuclear pore number. *Cytogenetic and Genome Research*, *26*(2–4), 175–190. https://doi.org/10.1159/000131439

Maul, Gerd G., Price, J. W., & Lieberman, M. W. (1971). Formation and distribution of nuclear pore complexes in interphase. *Journal of Cell Biology*, *51*(2), 405–418. https://doi.org/10.1083/jcb.51.2.405

Mazumder, A., Roopa, T., Basu, A., Mahadevan, L., & Shivashankar, G. V. (2008). Dynamics of chromatin decondensation reveals the structural integrity of a mechanically prestressed nucleus. *Biophysical Journal*, *95*(6), 3028–3035. https://doi.org/10.1529/biophysj.108.132274

McGregor, A. L., Hsia, C. R., & Lammerding, J. (2016). Squish and squeeze - the nucleus as a physical barrier during migration in confined environments. *Current Opinion in Cell Biology*, *40*, 32–40. https://doi.org/10.1016/j.ceb.2016.01.011

Mendjan, S., Taipale, M., Kind, J., Holz, H., Gebhardt, P., Schelder, M., Vermeulen, M., Buscaino, A., Duncan, K., Mueller, J., Wilm, M., Stunnenberg, H. G., Saumweber, H., & Akhtar, A. (2006). Nuclear pore components are involved in the transcriptional regulation of dosage compensation in Drosophila. *Molecular Cell*, *21*(6), 811–823. https://doi.org/10.1016/j.molcel.2006.02.007

Mimura, Y., Takemoto, S., Tachibana, T., Ogawa, Y., Nishimura, M., Yokota, H., & Imamoto, N. (2017). A statistical image analysis framework for pore-free islands derived from heterogeneity distribution of nuclear pore complexes. *Scientific Reports*, *7*(1), 1–14. https://doi.org/10.1038/s41598-017-16386-2

Mofrad, M. R. K., & Kamm, R. D. (2006). Cytoskeletal mechanics: Models and measurements. *Cytoskeletal Mechanics: Models and Measurements*, *9780521846*, 1–244. https://doi.org/10.1017/CBO9780511607318

Mohl, H. (1837). Ueber die Vermehrung der Pflanzen-Zellen durch Theilung. *Flora; Oder Allgemeine Botanische Zeitung*, *20(1)*, 1–32.

Mohr, D., Frey, S., Fischer, T., Güttler, T., & Görlich, D. (2009). Characterisation of the passive permeability barrier of nuclear pore complexes. *EMBO Journal*, *28*(17), 2541–2553. https://doi.org/10.1038/emboj.2009.200

Moroishi, T., Hansen, C. G., & Guan, K. L. (2015). The emerging roles of YAP and TAZ in cancer. *Nature Reviews Cancer*, *15*(2), 73–79. https://doi.org/10.1038/nrc3876

Mosley-Bishop, K. L., Li, Q., Patterson, K., & Fischer, J. A. (1999). Molecular analysis of the klarsicht gene and its role in nuclear migration within differentiating cells of the Drosophila eye. *Current Biology*, *9*(21), 1211–1220. https://doi.org/10.1016/S0960-9822(99)80501-6

Mouilleron, S., Langer, C. A., Guettler, S., McDonald, N. Q., & Treisman, R. (2011). Structure of a pentavalent G-actin•MRTF-A complex reveals how G-actin controls nucleocytoplasmic shuttling of a transcriptional coactivator. *Science Signaling*, *4*(177). https://doi.org/10.1126/scisignal.2001750

Mounkes, L. C., Kozlov, S., Hernandez, L., Sullivan, T., & Stewart, C. L. (2003). A progeroid syndrome in mice is caused by defects in A-type lamins. *Nature*, *423*(6937), 298–301. https://doi.org/10.1038/nature01631

Mounkes, L., Kozlov, S., Burke, B., & Stewart, C. L. (2003). The laminopathies: Nuclear structure meets disease. *Current Opinion in Genetics and Development*, *13*(3), 223–230. https://doi.org/10.1016/S0959-437X(03)00058-3

Muchir, A., Van Engelen, B. G., Lammens, M., Mislow, J. M., McNally, E., Schwartz, K., & Bonne, G. (2003). Nuclear envelope alterations in fibroblasts from LGMD1B patients carrying nonsense Y259X heterozygous or homozygous mutation in lamin A/C gene. *Experimental Cell Research*, *291*(2), 352–362. https://doi.org/10.1016/j.yexcr.2003.07.002

Murthy, S. E., Dubin, A. E., & Patapoutian, A. (2017). Piezos thrive under pressure: Mechanically activated ion channels in health and disease. *Nature Reviews Molecular Cell Biology*, *18*(12), 771–783. https://doi.org/10.1038/nrm.2017.92

Nachury, M. V., & Weis, K. (1999). The direction of transport through the nuclear pore can be inverted. *Proceedings of the National Academy of Sciences of the United States of America*,

96(17), 9622–9627. https://doi.org/10.1073/pnas.96.17.9622

Nava, M. M., Miroshnikova, Y. A., Biggs, L. C., Whitefield, D. B., Metge, F., Boucas, J., Vihinen, H., Jokitalo, E., Li, X., García Arcos, J. M., Hoffmann, B., Merkel, R., Niessen, C. M., Dahl, K. N., & Wickström, S. A. (2020). Heterochromatin-Driven Nuclear Softening Protects the Genome against Mechanical Stress-Induced Damage. *Cell*, *181*(4), 800-817.e22. https://doi.org/10.1016/j.cell.2020.03.052

Needham, D., & Nunn, R. S. (1990). Elastic deformation and failure of lipid bilayer membranes containing cholesterol. *Biophysical Journal*, *58*(4), 997–1009. https://doi.org/10.1016/S0006-3495(90)82444-9

Neelam, S., Hayes, P. R., Zhang, Q., Dickinson, R. B., & Lele, T. P. (2016). Vertical uniformity of cells and nuclei in epithelial monolayers. *Scientific Reports*, *6*(1), 1–10. https://doi.org/10.1038/srep19689

Neubert, E., Meyer, D., Rocca, F., Günay, G., Kwaczala-Tessmann, A., Grandke, J., Senger-Sander, S., Geisler, C., Egner, A., Schön, M. P., Erpenbeck, L., & Kruss, S. (2018). Chromatin swelling drives neutrophil extracellular trap release. *Nature Communications*, *9*(1). https://doi.org/10.1038/s41467-018-06263-5

Neumann, F. R., & Nurse, P. (2007). Nuclear size control in fission yeast. *Journal of Cell Biology*, *179*(4), 593–600. https://doi.org/10.1083/jcb.200708054

Niethammer, P. (2021). Components and Mechanisms of Nuclear Mechanotransduction. *Annual Review of Cell and Developmental Biology*, *37*, 233–256. https://doi.org/10.1146/annurev-cellbio-120319-030049

Niopek, D., Wehler, P., Roensch, J., Eils, R., & Di Ventura, B. (2016). Optogenetic control of nuclear protein export. *Nature Communications*, *7*. https://doi.org/10.1038/ncomms10624

Nmezi, B., Xu, J., Fu, R., Armiger, T. J., Rodriguez-Bey, G., Powell, J. S., Ma, H., Sullivan, M., Tu, Y., Chen, N. Y., Young, S. G., Stolz, D. B., Dahl, K. N., Liu, Y., & Padiath, Q. S. (2019). Concentric organization of A- and B-type lamins predicts their distinct roles in the spatial organization and stability of the nuclear lamina. *Proceedings of the National Academy of Sciences of the United States of America*, *116*(10), 4307–4315. https://doi.org/10.1073/pnas.1810070116

Novelli, G., Muchir, A., Sangiuolo, F., Helbling-Leclerc, A., D'apice, M. R., Massart, C., Capon, F., Sbraccia, P., Federici, M., Lauro, R., Tudisco, C., Pallotta, R., Scarano, G., Dallapiccola, B., Merlini, L., & Bonne, G. (2002). Mandibuloacral dysplasia is caused by a mutation in LMNA-encoding lamin A/C. *American Journal of Human Genetics*, *71*(2), 426–431. https://doi.org/10.1086/341908

O'Reilly, A. J., Dacks, J. B., & Field, M. C. (2011). Evolution of the karyopherin-β family of nucleocytoplasmic transport factors; ancient origins and continued specialization. *PLoS ONE*, *6*(4). https://doi.org/10.1371/journal.pone.0019308

Obropta, E. W., & Newman, D. J. (2016). Skin strain fields at the shoulder joint for mechanical counter pressure space suit development. *IEEE Aerospace Conference Proceedings*, *2016-June*. https://doi.org/10.1109/AERO.2016.7500744

Ori, A., Andrés-Pons, A., & Beck, M. (2014). The use of targeted proteomics to determine the stoichiometry of large macromolecular assemblies. *Methods in Cell Biology*, *122*, 117–146.

https://doi.org/10.1016/B978-0-12-417160-2.00006-0

Ori, A., Banterle, N., Iskar, M., Andrés-Pons, A., Escher, C., Khanh Bui, H., Sparks, L., Solis-Mezarino, V., Rinner, O., Bork, P., Lemke, E. A., & Beck, M. (2013). Cell type-specific nuclear pores: A case in point for context-dependent stoichiometry of molecular machines. *Molecular Systems Biology*, *9*(1). https://doi.org/10.1038/msb.2013.4

Oria, R., Wiegand, T., Escribano, J., Elosegui-Artola, A., Uriarte, J. J., Moreno-Pulido, C., Platzman, I., Delcanale, P., Albertazzi, L., Navajas, D., Trepat, X., García-Aznar, J. M., Cavalcanti-Adam, E. A., & Roca-Cusachs, P. (2017). Force loading explains spatial sensing of ligands by cells. *Nature*, *552*(7684), 219–224. https://doi.org/10.1038/nature24662

Padmakumar, V. C., Libotte, T., Lu, W., Zaim, H., Abraham, S., Noegel, A. A., Gotzmann, J., Foisner, R., & Karakesisoglou, I. (2005). The inner nuclear membrane protein Sun1 mediates the anchorage of Nesprin-2 to the nuclear envelope. *Journal of Cell Science*, *118*(15), 3419–3430. https://doi.org/10.1242/jcs.02471

Paine, P. L., & Feldherr, C. M. (1972). Nucleocytoplasmic exchange of macromolecules. *Experimental Cell Research*, *74*(1), 81–98. https://doi.org/10.1016/0014-4827(72)90483-1

Pajerowski, J. D., Dahl, K. N., Zhong, F. L., Sammak, P. J., & Discher, D. E. (2007). Physical plasticity of the nucleus in stem cell differentiation. *Proceedings of the National Academy of Sciences of the United States of America*, *104*(40), 15619–15624. https://doi.org/10.1073/pnas.0702576104

Paradise, A., Levin, M. K., Korza, G., & Carson, J. H. (2007). Significant Proportions of Nuclear Transport Proteins with Reduced Intracellular Mobilities Resolved by Fluorescence Correlation Spectroscopy. *Journal of Molecular Biology*, *365*(1), 50–65. https://doi.org/10.1016/j.jmb.2006.09.089

Pascual-Garcia, P., Debo, B., Aleman, J. R., Talamas, J. A., Lan, Y., Nguyen, N. H., Won, K. J., & Capelson, M. (2017). Metazoan Nuclear Pores Provide a Scaffold for Poised Genes and Mediate Induced Enhancer-Promoter Contacts. *Molecular Cell*, *66*(1), 63-76.e6. https://doi.org/10.1016/j.molcel.2017.02.020

Pascual-Reguant, L., Blanco, E., Galan, S., Le Dily, F., Cuartero, Y., Serra-Bardenys, G., Di Carlo, V., Iturbide, A., Cebrià-Costa, J. P., Nonell, L., de Herreros, A. G., Di Croce, L., Marti-Renom, M. A., & Peiró, S. (2018). Lamin B1 mapping reveals the existence of dynamic and functional euchromatin lamin B1 domains. *Nature Communications*, *9*(1). https://doi.org/10.1038/s41467-018-05912-z

Pendás, A. M., Zhou, Z., Cadiñanos, J., Freije, J. M. P., Wang, J., Hultenby, K., Astudillo, A., Wernerson, A., Rodríguez, F., Tryggvason, K., & López-Otín, C. (2002). Defective prelamin A processing and muscular and adipocyte alterations in Zmpste24 metalloproteinase-deficient mice. *Nature Genetics*, *31*(1), 94–99. https://doi.org/10.1038/ng871

Pennacchio, F. A., Poli, A., Pramotton, F. M., Rancati, I., Cinquanta, M., Vorselen, D., Prina, E., Maria, O., Ferrari, A., Piel, M., Lagomarsino, M. C., & Maiuri, P. (2022). Force-biased nuclear import sets nuclear-cytoplasmic volumetric coupling by osmosis. *BioRxiv*. https://doi.org/https://doi.org/10.1101/2022.06.07.494975

Petrovic, S., Samanta, D., Perriches, T., Bley, C. J., Thierbach, K., Brown, B., Nie, S., Mobbs, G. W.,

Stevens, T. A., Liu, X., Tomaleri, G. P., Schaus, L., & Hoelz, A. (2022). Architecture of the linker-scaffold in the nuclear pore. *Science*, *376*(6598). https://doi.org/10.1126/science.abm9798

Philip, J. T., & Dahl, K. N. (2008). Nuclear mechanotransduction: Response of the lamina to extracellular stress with implications in aging. *Journal of Biomechanics*, *41*(15), 3164–3170. https://doi.org/10.1016/j.jbiomech.2008.08.024

Piovesan, A., Pelleri, M. C., Antonaros, F., Strippoli, P., Caracausi, M., & Vitale, L. (2019). On the length, weight and GC content of the human genome. *BMC Research Notes*, *12*(1). https://doi.org/10.1186/s13104-019-4137-z

Plouffe, S. W., Hong, A. W., & Guan, K. L. (2015). Disease implications of the Hippo/YAP pathway. *Trends in Molecular Medicine*, *21*(4), 212–222. https://doi.org/10.1016/j.molmed.2015.01.003

Poh, Y. C., Shevtsov, S. P., Chowdhury, F., Wu, D. C., Na, S., Dundr, M., & Wang, N. (2012). Dynamic force-induced direct dissociation of protein complexes in a nuclear body in living cells. *Nature Communications*, *3*. https://doi.org/10.1038/ncomms1873

Popken, P., Ghavami, A., Onck, P. R., Poolman, B., & Veenhoff, L. M. (2015). Size-dependent leak of soluble and membrane proteins through the yeast nuclear pore complex. *Molecular Biology of the Cell*, *26*(7), 1386–1394. https://doi.org/10.1091/mbc.E14-07-1175

Porazinski, S., Wang, H., Asaoka, Y., Behrndt, M., Miyamoto, T., Morita, H., Hata, S., Sasaki, T., Krens, S. F. G., Osada, Y., Asaka, S., Momoi, A., Linton, S., Miesfeld, J. B., Link, B. A., Senga, T., Castillo-Morales, A., Urrutia, A. O., Shimizu, N., … Furutani-Seiki, M. (2015). YAP is essential for tissue tension to ensure vertebrate 3D body shape. *Nature*, *521*(7551), 217–221. https://doi.org/10.1038/nature14215

Raab, M., Gentili, M., De Belly, H., Thiam, H. R., Vargas, P., Jimenez, A. J., Lautenschlaeger, F., Voituriez, R., Lennon-Duménil, A. M., Manel, N., & Piel, M. (2016). ESCRT III repairs nuclear envelope ruptures during cell migration to limit DNA damage and cell death. *Science*, *352*(6283), 359–362. https://doi.org/10.1126/science.aad7611

Rabut, G., Doye, V., & Ellenberg, J. (2004). Mapping the dynamic organization of the nuclear pore complex inside single living cells. *Nature Cell Biology*, *6*(11), 1114–1121. https://doi.org/10.1038/ncb1184

Raharjo, W. H., Enarson, P., Sullivan, T., Stewart, C. L., & Burke, B. (2001). Nuclear envelope defects associated with LMNA mutations cause dilated cardiomyopathy and Emery-Dreifuss muscular dystrophy. *Journal of Cell Science*, *114*(24), 4447–4457. https://doi.org/10.1242/jcs.114.24.4447

Rapsomaniki, M. A., Kotsantis, P., Symeonidou, I. E., Giakoumakis, N. N., Taraviras, S., & Lygerou, Z. (2012). EasyFRAP: An interactive, easy-to-use tool for qualitative and quantitative analysis of FRAP data. *Bioinformatics*, *28*(13), 1800–1801. https://doi.org/10.1093/bioinformatics/bts241

Renault, L., Kuhlmann, J., Henkel, A., & Wittinghofer, A. (2001). Structural basis for guanine nucleotide exchange on Ran by the regulator of chromosome condensation (RCC1). *Cell*, *105*(2), 245–255. https://doi.org/10.1016/S0092-8674(01)00315-4

Ribbeck, K., & Görlich, D. (2001). Kinetic analysis of translocation through nuclear pore complexes. *EMBO Journal*, *20*(6), 1320–1330. https://doi.org/10.1093/emboj/20.6.1320

Ribbeck, Katharina, & Görlich, D. (2002). The permeability barrier of nuclear pore complexes appears to operate via hydrophobic exclusion. *EMBO Journal*, *21*(11), 2664–2671. https://doi.org/10.1093/emboj/21.11.2664

Ribbeck, Katharina, Lipowsky, G., Kent, H. M., Stewart, M., & Görlich, D. (1998). NTF2 mediates nuclear import of Ran. *EMBO Journal*, *17*(22), 6587–6598. https://doi.org/10.1093/emboj/17.22.6587

Ris, H., & Malecki, M. (1993). High-resolution field emission scanning electron microscope imaging of internal cell structures after epon extraction from sections: A new approach to correlative ultrastructural and immunocytochemical studies. *Journal of Structural Biology*, *111*(2), 148–157. https://doi.org/10.1006/jsbi.1993.1045

Roca-Cusachs, P., Alcaraz, J., Sunyer, R., Samitier, J., Farré, R., & Navajas, D. (2008). Micropatterning of single endothelial cell shape reveals a tight coupling between nuclear volume in G1 and proliferation. *Biophysical Journal*, *94*(12), 4984–4995. https://doi.org/10.1529/biophysj.107.116863

Roca-Cusachs, P., Del Rio, A., Puklin-Faucher, E., Gauthier, N. C., Biais, N., & Sheetz, M. P. (2013). Integrin-dependent force transmission to the extracellular matrix by α-actinin triggers adhesion maturation. *Proceedings of the National Academy of Sciences of the United States of America*, *110*(15). https://doi.org/10.1073/pnas.1220723110

Rodriguez-Franco, P., Brugués, A., Marin-Llaurado, A., Conte, V., Solanas, G., Batlle, E., Fredberg, J. J., Roca-Cusachs, P., Sunyer, R., & Trepat, X. (2017). Long-lived force patterns and deformation waves at repulsive epithelial boundaries. *Nature Materials*, *16*(10), 1029–1036. https://doi.org/10.1038/NMAT4972

Roeder, R. G., & Rutter, W. J. (1969). Multiple forms of DNA-dependent RNA polymerase in eukaryotic organisms. *Nature*, *224*(5216), 234–237. https://doi.org/10.1038/224234a0

Rosińczuk, J., Taradaj, J., Dymarek, R., & Sopel, M. (2016). Mechanoregulation of Wound Healing and Skin Homeostasis. *BioMed Research International*, *2016*, 1–13. https://doi.org/10.1155/2016/3943481

Rothballer, A., Schwartz, T. U., & Kutay, U. (2013). LINCing complex functions at the nuclear envelope what the molecular architecture of the LINC complex can reveal about its function. *Nucleus (United States)*, *4*(1), 29–36. https://doi.org/10.4161/nucl.23387

Rout, M. P., Aitchison, J. D., Magnasco, M. O., & Chait, B. T. (2003). Virtual gating and nuclear transport: The hole picture. *Trends in Cell Biology*, *13*(12), 622–628. https://doi.org/10.1016/j.tcb.2003.10.007

Rout, M. P., Aitchison, J. D., Suprapto, A., Hjertaas, K., Zhao, Y., & Chait, B. T. (2000). The yeast nuclear pore complex: Composition, architecture, transport mechanism. *Journal of Cell Biology*, *148*(4), 635–651. https://doi.org/10.1083/jcb.148.4.635

Rout, M. P., & Wente, S. R. (1994). Pores for thought: nuclear pore complex proteins. *Trends in Cell Biology*, *4*(10), 357–365. https://doi.org/10.1016/0962-8924(94)90085-X

Roux, K. J., Kim, D. I., Raida, M., & Burke, B. (2012). A promiscuous biotin ligase fusion protein identifies proximal and interacting proteins in mammalian cells. *Journal of Cell Biology*, *196*(6), 801–810. https://doi.org/10.1083/jcb.201112098

Sakiyama, Y., Panatala, R., & Lim, R. Y. H. (2017). Structural dynamics of the nuclear pore complex. *Seminars in Cell and Developmental Biology*, *68*, 27–33. https://doi.org/10.1016/j.semcdb.2017.05.021

Scheer, U., Kartenbeck, J., Trendelenburg, M. F., Stadler, J., & Franke, W. W. (1976). Experimental disintegration of the nuclear envelope: Evidence for pore-connecting fibrils. *Journal of Cell Biology*, *69*(1), 1–18. https://doi.org/10.1083/jcb.69.1.1

Schiller, H. B., Hermann, M.-R., Polleux, J., Vignaud, T., Zanivan, S., Friedel, C. C., Sun, Z., Raducanu, A., Gottschalk, K.-E., Théry, M., Mann, M., & Fässler, R. (2013). β1- and αv-class integrins cooperate to regulate myosin II during rigidity sensing of fibronectin-based microenvironments. *Nature Cell Biology*, *15*(6), 625–636. https://doi.org/10.1038/ncb2747

Schindelin, J., Arganda-Carreras, I., Frise, E., Kaynig, V., Longair, M., Pietzsch, T., Preibisch, S., Rueden, C., Saalfeld, S., Schmid, B., Tinevez, J. Y., White, D. J., Hartenstein, V., Eliceiri, K., Tomancak, P., & Cardona, A. (2012). Fiji: An open-source platform for biological-image analysis. *Nature Methods*, *9*(7), 676–682. https://doi.org/10.1038/nmeth.2019

Schmitt, J., Benavente, R., Hodzic, D., Höög, C., Stewart, C. L., & Alsheimer, M. (2007). Transmembrane protein Sun2 is involved in tethering mammalian meiotic telomeres to the nuclear envelope. *Proceedings of the National Academy of Sciences of the United States of America*, *104*(18), 7426–7431. https://doi.org/10.1073/pnas.0609198104

Schreiner, S. M., Koo, P. K., Zhao, Y., Mochrie, S. G. J., & King, M. C. (2015). The tethering of chromatin to the nuclear envelope supports nuclear mechanics. *Nature Communications*, *6*. https://doi.org/10.1038/ncomms8159

Schuller, A. P., Wojtynek, M., Mankus, D., Tatli, M., Kronenberg-Tenga, R., Regmi, S. G., Dip, P. V., Lytton-Jean, A. K. R., Brignole, E. J., Dasso, M., Weis, K., Medalia, O., & Schwartz, T. U. (2021). The cellular environment shapes the nuclear pore complex architecture. *Nature*, *598*(7882), 667–671. https://doi.org/10.1038/s41586-021-03985-3

Shapiro, L., & Weis, W. I. (2009). Structure and biochemistry of cadherins and catenins. *Cold Spring Harbor Perspectives in Biology*, *1*(3). https://doi.org/10.1101/cshperspect.a003053

Shimamoto, Y., Tamura, S., Masumoto, H., & Maeshima, K. (2017). Nucleosome-nucleosome interactions via histone tails and linker DNA regulate nuclear rigidity. *Molecular Biology of the Cell*, *28*(11), 1580–1589. https://doi.org/10.1091/mbc.E16-11-0783

Shimi, T., Pfleghaar, K., Kojima, S. I., Pack, C. G., Solovei, I., Goldman, A. E., Adam, S. A., Shumaker, D. K., Kinjo, M., Cremer, T., & Goldman, R. D. (2008). The A- and B-type nuclear lamin networks: Microdomains involved in chromatin organization and transcription. *Genes and Development*, *22*(24), 3409–3421. https://doi.org/10.1101/gad.1735208

Shimia, T., Kittisopikul, M., Tran, J., Goldman, A. E., Adam, S. A., Zheng, Y., Jaqaman, K., & Goldman, R. D. (2015). Structural organization of nuclear lamins A, C, B1, and B2 revealed by superresolution microscopy. *Molecular Biology of the Cell*, *26*(22), 4075–4086. https://doi.org/10.1091/mbc.E15-07-0461

Sims, J. R., Karp, S., & Ingber, D. E. (1992). Altering the cellular mechanical force balance results in integrated changes in cell, cytoskeletal and nuclear shape. *Journal of Cell Science*, *103*(4), 1215–1222. https://doi.org/10.1242/jcs.103.4.1215

Singh, S., & Gramolini, A. O. (2009). Characterization of sequences in human TWIST required for nuclear localization. *BMC Cell Biology*, *10*. https://doi.org/10.1186/1471-2121-10-47

Siniossoglou, S., Lutzmann, M., Santos-Rosa, H., Leonard, K., Mueller, S., Aebi, U., & Hurt, E. (2000). Structure and assembly of the Nup84p complex. *Journal of Cell Biology*, *149*(1), 41–53. https://doi.org/10.1083/jcb.149.1.41

Skinner, B. M., & Johnson, E. E. P. (2017). Nuclear morphologies: their diversity and functional relevance. *Chromosoma*, *126*(2), 195–212. https://doi.org/10.1007/s00412-016-0614-5

Smith, A., Brownawell, A., & Macara, I. G. (1998). Nuclear import of Ran is mediated by the transport factor NTF2. *Current Biology*, *8*(25), 1403–1406. https://doi.org/10.1016/s0960-9822(98)00023-2

Smith, E. R., Meng, Y., Moore, R., Tse, J. D., Xu, A. G., & Xu, X. X. (2017). Nuclear envelope structural proteins facilitate nuclear shape changes accompanying embryonic differentiation and fidelity of gene expression. *BMC Cell Biology*, *18*(1). https://doi.org/10.1186/s12860-017-0125-0

Soderholm, J. F., Bird, S. L., Kalab, P., Sampathkumar, Y., Hasegawa, K., Uehara-Bingen, M., Weis, K., & Heald, R. (2011). Importazole, a small molecule inhibitor of the transport receptor importin-β. *ACS Chemical Biology*, *6*(7), 700–708. https://doi.org/10.1021/cb2000296

Sosa, B. A., Rothballer, A., Kutay, U., & Schwartz, T. U. (2012). LINC complexes form by binding of three KASH peptides to domain interfaces of trimeric SUN proteins. *Cell*, *149*(5), 1035–1047. https://doi.org/10.1016/j.cell.2012.03.046

Steen, H. B., & Lindmo, T. (1978). Cellular and Nuclear Volume During the Cell Cycle of Nhik 3025 Cells. *Cell Proliferation*, *11*(1), 69–81. https://doi.org/10.1111/j.1365-2184.1978.tb00876.x

Stephens, A. D., Banigan, E. J., Adam, S. A., Goldman, R. D., & Marko, J. F. (2017). Chromatin and lamin a determine two different mechanical response regimes of the cell nucleus. *Molecular Biology of the Cell*, *28*(14), 1984–1996. https://doi.org/10.1091/mbc.E16-09-0653

Stephens, A. D., Banigan, E. J., & Marko, J. F. (2018). Separate roles for chromatin and lamins in nuclear mechanics. *Nucleus*, *9*(1), 119–124. https://doi.org/10.1080/19491034.2017.1414118

Stephens, A. D., Banigan, E. J., & Marko, J. F. (2019). Chromatin's physical properties shape the nucleus and its functions. In *Current Opinion in Cell Biology* (Vol. 58, pp. 76–84). Elsevier Ltd. https://doi.org/10.1016/j.ceb.2019.02.006

Stephens, A. D., Liu, P. Z., Banigan, E. J., Almassalha, L. M., Backman, V., Adam, S. A., Goldman, R. D., & Marko, J. F. (2018). Chromatin histone modifications and rigidity affect nuclear morphology independent of lamins. *Molecular Biology of the Cell*, *29*(2), 220–233. https://doi.org/10.1091/mbc.E17-06-0410

Stewart, C. L., & Stewart, C. L. (2002). Life at the edge: The nuclear envelope and human disease. *Nature Reviews Molecular Cell Biology*, *3*(8), 575–585. https://doi.org/10.1038/nrm879

Stoffler, D., Goldie, K. N., Feja, B., & Aebi, U. (1999). Calcium-mediated structural changes of native nuclear pore complexes monitored by time-lapse atomic force microscopy. *Journal of Molecular Biology*, *287*(4), 741–752. https://doi.org/10.1006/jmbi.1999.2637

Stringer, C., Wang, T., Michaelos, M., & Pachitariu, M. (2021). Cellpose: a generalist algorithm for cellular segmentation. *Nature Methods*, *18*(1), 100–106. https://doi.org/10.1038/s41592-020-

01018-x

Swift, J., Ivanovska, I. L., Buxboim, A., Harada, T., Dingal, P. C. D. P., Pinter, J., Pajerowski, J. D., Spinler, K. R., Shin, J. W., Tewari, M., Rehfeldt, F., Speicher, D. W., & Discher, D. E. (2013). Nuclear lamin-A scales with tissue stiffness and enhances matrix-directed differentiation. *Science*, *341*(6149). https://doi.org/10.1126/science.1240104

Tajik, A., Zhang, Y., Wei, F., Sun, J., Jia, Q., Zhou, W., Singh, R., Khanna, N., Belmont, A. S., & Wang, N. (2016). Transcription upregulation via force-induced direct stretching of chromatin. *Nature Materials*, *15*(12), 1287–1296. https://doi.org/10.1038/nmat4729

Takaki, T., Montagner, M., Serres, M. P., Le Berre, M., Russell, M., Collinson, L., Szuhai, K., Howell, M., Boulton, S. J., Sahai, E., & Petronczki, M. (2017). Actomyosin drives cancer cell nuclear dysmorphia and threatens genome stability. *Nature Communications*, *8*. https://doi.org/10.1038/ncomms16013

Tamada, H., Van Thuan, N., Reed, P., Nelson, D., Katoku-Kikyo, N., Wudel, J., Wakayama, T., & Kikyo, N. (2007). Chromatin Decondensation and Nuclear Reprogramming by Nucleoplasmin. *Molecular and Cellular Biology*, *27*(18), 6580–6580. https://doi.org/10.1128/mcb.01302-07

Thiam, H. R., Vargas, P., Carpi, N., Crespo, C. L., Raab, M., Terriac, E., King, M. C., Jacobelli, J., Alberts, A. S., Stradal, T., Lennon-Dumenil, A. M., & Piel, M. (2016). Perinuclear Arp2/3-driven actin polymerization enables nuclear deformation to facilitate cell migration through complex environments. *Nature Communications*, *7*. https://doi.org/10.1038/ncomms10997

Timney, B. L., Raveh, B., Mironska, R., Trivedi, J. M., Kim, S. J., Russel, D., Wente, S. R., Sali, A., & Rout, M. P. (2016). Simple rules for passive diffusion through the nuclear pore complex. *Journal of Cell Biology*, *215*(1), 57–76. https://doi.org/10.1083/jcb.201601004

Tingey, M., Mudumbi, K. C., Schirmer, E. C., & Yang, W. (2019). Casting a wider net: Differentiating between inner nuclear envelope and outer nuclear envelope transmembrane proteins. In *International Journal of Molecular Sciences* (Vol. 20, Issue 21). https://doi.org/10.3390/ijms20215248

Tipoe, G. L., & White, F. H. (1998). Quantitative assessment of normal and potentially premalignant epithelium at different levels of human colorectal crypts. *Histology and Histopathology*, *13*(2), 395–404. https://doi.org/10.14670/HH-13.395

Tocco, V. J., Li, Y., Christopher, K. G., Matthews, J. H., Aggarwal, V., Paschall, L., Luesch, H., Licht, J. D., Dickinson, R. B., & Lele, T. P. (2018). The nucleus is irreversibly shaped by motion of cell boundaries in cancer and non-cancer cells. *Journal of Cellular Physiology*, *233*(2), 1446–1454. https://doi.org/10.1002/jcp.26031

Torbati, M., Lele, T. P., & Agrawal, A. (2016). Ultradonut topology of the nuclear envelope. *Proceedings of the National Academy of Sciences of the United States of America*, *113*(40), 11094–11099. https://doi.org/10.1073/pnas.1604777113

Torvaldson, E., Kochin, V., & Eriksson, J. E. (2015). Phosphorylation of lamins determine their structural properties and signaling functions. *Nucleus*, *6*(3), 166–171. https://doi.org/10.1080/19491034.2015.1017167

Turgay, Y., Eibauer, M., Goldman, A. E., Shimi, T., Khayat, M., Ben-Harush, K., Dubrovsky-Gaupp, A., Sapra, K. T., Goldman, R. D., & Medalia, O. (2017). The molecular architecture of lamins in

somatic cells. *Nature*, *543*(7644), 261–264. https://doi.org/10.1038/nature21382

Uhler, C., & Shivashankar, G. V. (2017). Regulation of genome organization and gene expression by nuclear mechanotransduction. In *Nature Reviews Molecular Cell Biology* (Vol. 18, Issue 12, pp. 717–727). Nature Publishing Group. https://doi.org/10.1038/nrm.2017.101

Upla, P., Kim, S. J., Sampathkumar, P., Dutta, K., Cahill, S. M., Chemmama, I. E., Williams, R., Bonanno, J. B., Rice, W. J., Stokes, D. L., Cowburn, D., Almo, S. C., Sali, A., Rout, M. P., & Fernandez-Martinez, J. (2017). Molecular Architecture of the Major Membrane Ring Component of the Nuclear Pore Complex. *Structure*, *25*(3), 434–445. https://doi.org/10.1016/j.str.2017.01.006

Vahabikashi, A., Adam, S. A., Medalia, O., & Goldman, R. D. (2022). Nuclear lamins: Structure and function in mechanobiology. In *APL Bioengineering* (Vol. 6, Issue 1, p. 11503). https://doi.org/10.1063/5.0082656

van der Lee, R., Buljan, M., Lang, B., Weatheritt, R. J., Daughdrill, G. W., Dunker, A. K., Fuxreiter, M., Gough, J., Gsponer, J., Jones, D. T., Kim, P. M., Kriwacki, R. W., Oldfield, C. J., Pappu, R. V., Tompa, P., Uversky, V. N., Wright, P. E., & Babu, M. M. (2014). Classification of Intrinsically Disordered Regions and Proteins. *Chemical Reviews*, *114*(13), 6589–6631. https://doi.org/10.1021/cr400525m

Van Meer, G., Voelker, D. R., & Feigenson, G. W. (2008). Membrane lipids: Where they are and how they behave. *Nature Reviews Molecular Cell Biology*, *9*(2), 112–124. https://doi.org/10.1038/nrm2330

Vaquerizas, J. M., Suyama, R., Kind, J., Miura, K., Luscombe, N. M., & Akhtar, A. (2010). Nuclear pore proteins Nup153 and megator define transcriptionally active regions in the Drosophila genome. *PLoS Genetics*, *6*(2). https://doi.org/10.1371/journal.pgen.1000846

Varberg, J. M., Unruh, J. R., Bestul, A. J., Khan, A. A., & Jaspersen, S. L. (2022). Quantitative analysis of nuclear pore complex organization in Schizosaccharomyces pombe . *Life Science Alliance*, *5*(7), e202201423. https://doi.org/10.26508/lsa.202201423

Varelas, X. (2014). The hippo pathway effectors TAZ and YAP in development, homeostasis and disease. *Development (Cambridge)*, *141*(8), 1614–1626. https://doi.org/10.1242/dev.102376

Venturini, V., Pezzano, F., Català Castro, F., Häkkinen, H.-M. M., Jiménez-Delgado, S., Colomer-Rosell, M., Marro, M., Tolosa-Ramon, Q., Paz-López, S., Valverde, M. A., Weghuber, J., Loza-Alvarez, P., Krieg, M., Wieser, S., Ruprecht, V., Castro, F. C., Häkkinen, H.-M. M., Jiménez-Delgado, S., Colomer-Rosell, M., … Ruprecht, V. (2020). The nucleus measures shape changes for cellular proprioception to control dynamic cell behavior. *Science*, *370*(6514), eaba2644. https://doi.org/10.1126/science.aba2644

Vergnes, L., Péterfy, M., Bergo, M. O., Young, S. G., & Reue, K. (2004). Lamin B1 is required for mouse development and nuclear integrity. *Proceedings of the National Academy of Sciences of the United States of America*, *101*(28), 10428–10433. https://doi.org/10.1073/pnas.0401424101

Vovk, A., Gu, C., Opferman, M. G., Kapinos, L. E., Lim, R. Y., Coalson, R. D., Jasnow, D., & Zilman, A. (2016). Simple biophysics underpins collective conformations of the intrinsically disordered proteins of the Nuclear Pore Complex. *ELife*, *5*. https://doi.org/10.7554/eLife.10785

Wallin, I. E. (1925). On the nature of mitochondria. IX. Demonstration of the bacterial nature of

mitochondria. *American Journal of Anatomy*, *36*(1), 131–149. https://doi.org/10.1002/aja.1000360106

Wang, C., Zhu, X., Feng, W., Yu, Y., Jeong, K., Guo, W., Lu, Y., & Mills, G. B. (2016). Verteporfin inhibits YAP function through up-regulating 14-3-3σ sequestering YAP in the cytoplasm. *American Journal of Cancer Research*, *6*(1), 27–37.

Wang, W., Shi, Z., Jiao, S., Chen, C., Wang, H., Liu, G., Wang, Q., Zhao, Y., Greene, M. I., & Zhou, Z. (2012). Structural insights into SUN-KASH complexes across the nuclear envelope. *Cell Research*, *22*(10), 1440–1452. https://doi.org/10.1038/cr.2012.126

Wei, S. C., Fattet, L., Tsai, J. H., Guo, Y., Pai, V. H., Majeski, H. E., Chen, A. C., Sah, R. L., Taylor, S. S., Engler, A. J., & Yang, J. (2015). Matrix stiffness drives epithelial-mesenchymal transition and tumour metastasis through a TWIST1-G3BP2 mechanotransduction pathway. *Nature Cell Biology*, *17*(5), 678–688. https://doi.org/10.1038/ncb3157

Wente, S. R., & Rout, M. P. (2010). The nuclear pore complex and nuclear transport. *Cold Spring Harbor Perspectives in Biology*, *2*(10), a000562. https://doi.org/10.1101/cshperspect.a000562

Wilhelmsen, K., Litjens, S. H. M., Kuikman, I., Tshimbalanga, N., Janssen, H., Van Bout, I. Den, Raymond, K., & Sonnenberg, A. (2005). Nesprin-3, a novel outer nuclear membrane protein, associates with the cytoskeletal linker protein plectin. *Journal of Cell Biology*, *171*(5), 799–810. https://doi.org/10.1083/jcb.200506083

Wing, C. E., Fung, H. Y. J., & Chook, Y. M. (2022). Karyopherin-mediated nucleocytoplasmic transport. *Nature Reviews Molecular Cell Biology*, *0123456789*. https://doi.org/10.1038/s41580-021-00446-7

Woese, C. R., Kandler, O., & Wheelis, M. L. (1990). Towards a natural system of organisms: Proposal for the domains Archaea, Bacteria, and Eucarya. *Proceedings of the National Academy of Sciences of the United States of America*, *87*(12), 4576–4579. https://doi.org/10.1073/pnas.87.12.4576

Wolf, C. B., & Mofrad, M. R. K. (2013). Mechanotransduction: Role of nuclear pore mechanics and nucleocytoplasmic transport. In M. R. K. Mofrad & R. D. Kamm (Eds.), *Cellular Mechanotransduction: Diverse Perspectives from Molecules to Tissues* (Vol. 9780521895, pp. 417–437). Cambridge University Press. https://doi.org/10.1017/CBO9781139195874.019

Worman, H. J. (2012). Nuclear lamins and laminopathies. *Journal of Pathology*, *226*(2), 316–325. https://doi.org/10.1002/path.2999

Xia, Y., Ivanovska, I. L., Zhu, K., Smith, L., Irianto, J., Pfeifer, C. R., Alvey, C. M., Ji, J., Liu, D., Cho, S., Bennett, R. R., Liu, A. J., Greenberg, R. A., & Discher, D. E. (2018). Nuclear rupture at sites of high curvature compromises retention of DNA repair factors. *Journal of Cell Biology*, *217*(11), 3796–3808. https://doi.org/10.1083/jcb.201711161

Xie, W., Chojnowski, A., Boudier, T., Lim, J. S. Y., Ahmed, S., Ser, Z., Stewart, C., & Burke, B. (2016). A-type Lamins Form Distinct Filamentous Networks with Differential Nuclear Pore Complex Associations. *Current Biology*, *26*(19), 2651–2658. https://doi.org/10.1016/j.cub.2016.07.049

Xiong, H., Rivero, F., Euteneuer, U., Mondal, S., Mana-Capelli, S., Larochelle, D., Vogel, A., Gassen, B., & Noegel, A. A. (2008). Dictyostelium Sun-1 connects the centrosome to chromatin and ensures genome stability. *Traffic*, *9*(5), 708–724. https://doi.org/10.1111/j.1600-

0854.2008.00721.x

Yamada, J., Phillips, J. L., Patel, S., Goldfien, G., Calestagne-Morelli, A., Huang, H., Reza, R., Acheson, J., Krishnan, V. V., Newsam, S., Gopinathan, A., Lau, E. Y., Colvin, M. E., Uversky, V. N., & Rexacha, M. F. (2010). A bimodal distribution of two distinct categories of intrinsically disordered structures with separate functions in FG nucleoporins. *Molecular and Cellular Proteomics*, *9*(10), 2205–2224. https://doi.org/10.1074/mcp.M000035-MCP201

Yang, J., Mani, S. A., Donaher, J. L., Ramaswamy, S., Itzykson, R. A., Come, C., Savagner, P., Gitelman, I., Richardson, A., & Weinberg, R. A. (2004). Twist, a master regulator of morphogenesis, plays an essential role in tumor metastasis. *Cell*, *117*(7), 927–939. https://doi.org/10.1016/j.cell.2004.06.006

Yang, J., & Weinberg, R. A. (2008). Epithelial-Mesenchymal Transition: At the Crossroads of Development and Tumor Metastasis. *Developmental Cell*, *14*(6), 818–829. https://doi.org/10.1016/j.devcel.2008.05.009

Yang, W., Gelles, J., & Musser, S. M. (2004). Imaging of single-molecule translocation through nuclear pore complexes. *Proceedings of the National Academy of Sciences of the United States of America*, *101*(35), 12887–12892. https://doi.org/10.1073/pnas.0403675101

Yang, W., & Musser, S. M. (2006). Nuclear import time and transport efficiency depend on importin β concentration. *Journal of Cell Biology*, *174*(7), 951–961. https://doi.org/10.1083/jcb.200605053

Yoshikawa, Y., Velichko, Y. S., Ichiba, Y., & Yoshikawa, K. (2001). Self-assembled pearling structure of long duplex DNA with histone H1. *European Journal of Biochemistry*, *268*(9), 2593–2599. https://doi.org/10.1046/j.1432-1327.2001.02144.x

Yu, J., Lei, K., Zhou, M., Craft, C. M., Xu, G., Xu, T., Zhuang, Y., Xu, R., & Han, M. (2011). KASH protein Syne-2/Nesprin-2 and SUN proteins SUN1/2 mediate nuclear migration during mammalian retinal development. *Human Molecular Genetics*, *20*(6), 1061–1073. https://doi.org/10.1093/hmg/ddq549

Yuh, M. C., & Blobel, G. (2001). Karyopherins and nuclear import. *Current Opinion in Structural Biology*, *11*(6), 703–715. https://doi.org/10.1016/S0959-440X(01)00264-0

Zanconato, F., Cordenonsi, M., & Piccolo, S. (2016). YAP/TAZ at the Roots of Cancer. *Cancer Cell*, *29*(6), 783–803. https://doi.org/10.1016/j.ccell.2016.05.005

Zhang, K., Grither, W. R., Van Hove, S., Biswas, H., Ponik, S. M., Eliceiri, K. W., Keely, P. J., & Longmore, G. D. (2016). Mechanical signals regulate and activate SNAIL1 protein to control the fibrogenic response of cancer-associated fibroblasts. *Journal of Cell Science*, *129*(10), 1989–2002. https://doi.org/10.1242/jcs.180539

Zhang, Qiuping, Ragnauth, C., Greener, M. J., Shanahan, C. M., & Roberts, R. G. (2002). The nesprins are giant actin-binding proteins, orthologous to Drosophila melanogaster muscle protein MSP-300. *Genomics*, *80*(5), 473–481. https://doi.org/10.1016/S0888-7543(02)96859-X

Zhang, Quiping, Skepper, J. N., Yang, F., Davies, J. D., Hegyi, L., Roberts, R. G., Weissberg, P. L., Ellis, J. A., & Shanahan, C. M. (2001). Nesprins: A novel family of spectrin-repeat-containing proteins that localize to the nuclear membrane in multiple tissues. *Journal of Cell Science*, *114*(24), 4485–4498. https://doi.org/10.1242/jcs.114.24.4485

Zhang, X., Lei, K., Yuan, X., Wu, X., Zhuang, Y., Xu, T., Xu, R., & Han, M. (2009). SUN1/2 and Syne/Nesprin-1/2 Complexes Connect Centrosome to the Nucleus during Neurogenesis and Neuronal Migration in Mice. *Neuron*, *64*(2), 173–187. https://doi.org/10.1016/j.neuron.2009.08.018

Zhang, Y. L., Frangos, J. A., & Chachisvilis, M. (2006). Laurdan fluorescence senses mechanical strain in the lipid bilayer membrane. *Biochemical and Biophysical Research Communications*, *347*(3), 838–841. https://doi.org/10.1016/j.bbrc.2006.06.152

Zhang, Y., Li, S., Zeng, C., Huang, G., Zhu, X., Wang, Q., Wang, K., Zhou, Q., Yan, C., Zhang, W., Yang, G., Liu, M., Tao, Q., Lei, J., & Shi, Y. (2020). Molecular architecture of the luminal ring of the Xenopus laevis nuclear pore complex. *Cell Research*, *30*(6), 532–540. https://doi.org/10.1038/s41422-020-0320-y

Zhao, B., Li, L., Lei, Q., & Guan, K. L. (2010). The Hippo-YAP pathway in organ size control and tumorigenesis: An updated version. *Genes and Development*, *24*(9), 862–874. https://doi.org/10.1101/gad.1909210

Zhao, B., Wei, X., Li, W., Udan, R. S., Yang, Q., Kim, J., Xie, J., Ikenoue, T., Yu, J., Li, L., Zheng, P., Ye, K., Chinnaiyan, A., Halder, G., Lai, Z. C., & Guan, K. L. (2007). Inactivation of YAP oncoprotein by the Hippo pathway is involved in cell contact inhibition and tissue growth control. *Genes and Development*, *21*(21), 2747–2761. https://doi.org/10.1101/gad.1602907

Zhao, B., Ye, X., Yu, J., Li, L., Li, W., Li, S., Yu, J., Lin, J. D., Wang, C. Y., Chinnaiyan, A. M., Lai, Z. C., & Guan, K. L. (2008). TEAD mediates YAP-dependent gene induction and growth control. *Genes and Development*, *22*(14), 1962–1971. https://doi.org/10.1101/gad.1664408

Zhao, X H, Laschinger, C., Arora, P., Szaszi, K., Kapus, A., & McCulloch, C. A. (2007). Force activates smooth muscle alpha-actin promoter activity through the Rho signaling pathway. *Journal of Cell Science*, *120*(Pt 10), 1801–1809. https://doi.org/10.1242/jcs.001586

Zhao, Xiao Han, Laschinger, C., Arora, P., Szászi, K., Kapus, A., & McCulloch, C. A. (2007). Force activates smooth muscle α-actin promoter activity through the Rho signaling pathway. *Journal of Cell Science*, *120*(10), 1801–1809. https://doi.org/10.1242/jcs.001586

Zhou, Z., Du, X., Cai, Z., Song, X., Zhang, H., Mizuno, T., Suzuki, E., Yee, M. R., Berezov, A., Murali, R., Wu, S. L., Karger, B. L., Greene, M. I., & Wang, Q. (2012). Structure of Sad1-UNC84 homology (SUN) domain defines features of molecular bridge in nuclear envelope. *Journal of Biological Chemistry*, *287*(8), 5317–5326. https://doi.org/10.1074/jbc.M111.304543

Zierhut, C., Jenness, C., Kimura, H., & Funabiki, H. (2014). Nucleosomal regulation of chromatin composition and nuclear assembly revealed by histone depletion. *Nature Structural and Molecular Biology*, *21*(7), 617–625. https://doi.org/10.1038/nsmb.2845

Zila, V., Margiotta, E., Turoňová, B., Müller, T. G., Zimmerli, C. E., Mattei, S., Allegretti, M., Börner, K., Rada, J., Müller, B., Lusic, M., Kräusslich, H. G., & Beck, M. (2021). Cone-shaped HIV-1 capsids are transported through intact nuclear pores. *Cell*, *184*(4), 1032-1046.e18. https://doi.org/10.1016/j.cell.2021.01.025

Zimmerli, C. E., Allegretti, M., Rantos, V., Goetz, S. K., Obarska-Kosinska, A., Zagoriy, I., Halavatyi, A., Hummer, G., Mahamid, J., Kosinski, J., & Beck, M. (2021). Nuclear pores dilate and constrict in cellulo. *Science*, *374*(6573), eabd9776. https://doi.org/10.1126/science.abd9776

Zink, D., Fischer, A. H., & Nickerson, J. A. (2004). Nuclear structure in cancer cells. *Nature Reviews Cancer*, *4*(9), 677–687. https://doi.org/10.1038/nrc1430

9. Appendix A: Note from Chapter 1

Modelling of mechanosensitive nucleocytoplasmic transport

Initial conceptual model

To obtain a first understanding of how mechanical force should affect nucleocytoplasmic transport of constructs with NLS sequences, we developed a simple conceptual model. For this, we simply assumed that:

$$\frac{n}{c} = \frac{f_i}{f_e} = \frac{f_p + f_f}{f_p} \quad \text{if} \quad \frac{n}{c} < \left(\frac{n}{c}\right)_{sat}$$

$$\frac{n}{c} = \left(\frac{n}{c}\right)_{sat} \quad \text{otherwise}$$

Where n/c is the nuclear-to-cytoplasmic concentration ratio of a given construct, f_i and f_e are the flow rates in and out of the nucleus respectively, f_p is a passive diffusive flow rate through NPCs which decreases with increasing MW (and is equal in the export and import direction), f_f is a facilitated diffusive flow rate which depends on the strength of the NLS sequence (and does not depend on MW) and $\left(\frac{n}{c}\right)_{sat}$ is a maximum value for n/c ratios, where saturation is reached. Such saturation would imply that any change in f_i is matched by an equivalent change in f_e, keeping the ratio constant. In this initial conceptual model, the underlying reason for this is not addressed. However, the detailed, kinetic model described below provides a justification for this, discussed in the text: as NLS affinities increase, cargo molecules can compete with Ran-GTP for binding importins, limiting the ability of Ran-GTP to disassemble the cargo-importin complex. This leads to the facilitated diffusion of importin-cargo complexes out of (and not only into) the nucleus. In this scenario, both influx and efflux are driven by facilitated diffusion, and respond in the same way.

Note that facilitated and passive diffusion are assumed to have additive contributions to total influx flow rates, and that for simplicity changes in nuclear/cytosolic volume compartments are not considered (unlike in the more detailed, kinetic model below). The effect of force applied to the nucleus is introduced by increasing f_p by two-fold at the lowest MW (arbitrarily set to have to have a value of f_p=1 in the absence of force) and by a progressively smaller amount as MW increases, until having a negligible effect at the highest MW (arbitrarily set to have a value of f_p=0.015 in the absence of force). Force also increases f_f by 2-fold, in this case independently of MW. After applying these effects of force, mechanosensitivity is calculated as:

$$mechanosensitivity = \frac{\left(\frac{n}{c}\right)_{stiff}}{\left(\frac{n}{c}\right)_{soft}}$$

Graphs in Fig. 4a,b were calculated by calculating n/c and mechanosensitivity for a range of values of f_p (1-0.015 before force application) and f_f, (16-0.12 before force application). The choice of values is arbitrary, and merely intends to show the relative effects when either f_f or f_p dominate the overall n/c ratio. Accordingly, no specific numerical values are shown in the graphs.

Kinetic mathematical model of transport.

The kinetic model of nucleocytoplasmic transport (Model Figure 1, Model Tables 1-3) was constructed following a canonical description of the nucleocytoplasmic transport process (Cautain et al., 2015; Görlich et al., 2003; Jovanovic-Talisman & Zilman, 2017; S. Kim & Elbaum, 2013a). A

system of ordinary differential equations (Model Table 1) is used to describe passive diffusion of unbound cargo molecules through NPCs; Ran-mediated facilitated diffusion of cargo:importin complexes through NPCs, and maintenance of the RanGTP gradient across the nuclear envelope through NTF2-mediated import of RanGDP (Katharina Ribbeck et al., 1998; A. Smith et al., 1998), RanGAP-mediated hydrolysis of RanGTP to RanGDP in the cytoplasm (Bischoff et al., 1994), and chromatin-bound RCC1 (RanGEF) mediated conversion of RanGDP to RanGTP in the nucleus (Renault et al., 2001). During passive diffusion, unbound cargo molecules diffuse in either direction at a rate proportional to their concentrations, in accordance with Fick's law (K. Ribbeck & Görlich, 2001; Timney et al., 2016). During facilitated diffusion, cargo:importin complexes interact with docking sites on NPCs, diffuse across the nuclear envelope and release cargo by interacting with RanGTP. Docking rate to the NPC is proportional to the number of available docking sites. Cargo and importin molecules also associate and dissociate spontaneously in a non-Ran dependent manner. Of note, the model does not consider competition of cargo with other, endogenous cargo molecules already present in cells (Kopito & Elbaum, 2009), due to the difficulty in estimating overall endogenous cargo concentrations or affinities. However, the main effect of this competition is to limit the availability of Ran, something which is already considered by modelling a finite Ran concentration.

Model parametrization: The kinetic model of transport provides a simplified minimal description of the transport process based on a set of canonical assumptions(Cautain et al., 2015; Görlich et al., 2003; Jovanovic-Talisman & Zilman, 2017; S. Kim & Elbaum, 2013a). It is not meant to reproduce precise empirical values, rather to characterize dependencies among key biophysical parameters that determine NPC transport kinetics on soft and stiff surfaces. Nonetheless, the model has been carefully parametrized to reproduce key features of transport, and it is remarkably robust to changes in its parameter values. Unless stated otherwise, all simulations were conducted using the mean measured nuclear and cytoplasmic volumes of 627 fL and 2194 fL in our dataset. Passive diffusion rates for different cargo molecules of different sizes were also obtained from measurements (Fig. 2e,f). The cargo concentration was estimated to be in the range 0.01-0.1 μM, based on comparison of GFP fluorescence values and reference fluorescence of purified GFP. This is much lower than the ~10 μM physiological concentrations of importins such as Kapß1 (Kapinos et al., 2017; Paradise et al., 2007), and the estimated 5-20 μM concentration of RanGTP concentration in HeLa cells (Görlich et al., 2003), thus precise values of these parameters are expected to have limited effect. Indeed, doubling or halving Ran concentration had limited qualitative effect on our model results. The Ran cycle kinetic parameters were fitted to reproduce a robust nuclear:cytoplasmic RanGTP ratio of >500 (Görlich et al., 2003), starting from a 1000:1 ratio. The number of dock sites per NPC was estimated from the thousands of FG binding sites per NPC and the large fraction of cargo and NTR molecules found in mass-spectrometry measurements in native NPCs (S. J. Kim et al., 2018).

Simulation code. Our simulations were implemented in Python (version 3.6). They are fully reproducible; the source code and the run parameters can be found in https://github.com/ravehlab/npctransport_kinetic (run03 was used to produce model results in this manuscript).

Model Table 1. Ordinary differential equations (ODEs) of a kinetic model of transport. Subscripts N and C indicate nuclear and cytoplasmic localization. Subscript NPC indicates localization to the NPC, and subscripts NPC-C and NPC-N indicate sub-localization at the nuclear and cytoplasmic sides of the NPC, respectively. Bracketed variables are in units of concentration (for either the nucleus or the cytoplasm) and non-bracketed variables indicate actual numbers of molecules (for NPC-docked molecules) (Table S1). N_A is Avogadro's number.

ODEs	Processes described
$[\dot{C}_N] = -\pi_{passive}[C_C] \cdot \frac{V_C}{V_N}$ $[\dot{C}_C] = -\pi_{passive}[C_N] \cdot \frac{V_N}{V_C}$	Passive diffusion of unbound cargo through the NPC
$\dot{CI}_{NPC-N} = \sigma_{on} \cdot (N_{dock} - CI_{NPC}) \cdot [CI_N] - \sigma_{off} \cdot CI_{NPC-N} + \varphi \cdot (CI_{NPC-C} - CI_{NPC-N}) - \alpha[GTP_N]CI_{NPC-N}$ $\dot{CI}_{NPC-C} = \sigma_{on} \cdot (N_{dock} - CI_{NPC}) \cdot [CI_C] - \sigma_{off} \cdot CI_{NPC-C} + \varphi \cdot (CI_{NPC-N} - CI_{NPC-C})$ $[\dot{C}_N] = [GTP_N] \cdot \left(\frac{\alpha CI_{NPC-N}}{N_A \cdot V_N} + \beta[CI_N]\right) + k_{off}[CI_N]$ $[\dot{CI}_N] = -\beta[GTP_N][CI_N] - k_{off}[CI_N] - \sigma_{on} \cdot (N_{dock} - CI_{NPC}) \cdot [CI_N] / (N_A \cdot V_N) + \sigma_{off} \cdot CI_{NPC-N}/(N_A \cdot V_N)$	Facilitated diffusion: - Docking and undocking of cargo:importin complexes to and from NPCs, resp. - NPC traversal of NPC-docked cargo:importin complexes between cytoplasmic and nuclear ends of the NPC - RanGTP-dependent and RanGTP-independent dissociation of cargo:importin complexes in the nucleus and NPC
$[\dot{C}_C] = k_{off}[CI_C]$ $[\dot{CI}_C] = -k_{off}[CI_C] - \sigma \cdot (N_{dock} - CI_{NPC}) \cdot [CI_C]/(N_A \cdot V_C) + \sigma_{off} \cdot CI_{NPC-C}/(N_A \cdot V_C)$	Non-RanGTP dependent dissociation of cargo molecules from importin molecules in the cytoplasm
$[\dot{CI}_N] = k_{on}[C_N]$ $[\dot{CI}_C] = k_{on}[C_C]$ $[\dot{C}_N] = -k_{on}[C_N]$ $[\dot{C}_C] = -k_{on}[C_C]$	Association of cargo molecules to importin molecules. assuming [I]>>[C] (see Model parametrization)
$[\dot{GTP}_N] = \gamma[GDP_N] - (\delta + \epsilon)[GTP_N] - [GTP_N] \cdot \left(\frac{\alpha CI_{NPC-N}}{N_A \cdot V_N} + \beta[CI_N]\right)$ $[\dot{GTP}_C] = \epsilon[GTP_N] \cdot \frac{V_N}{V_C} - \eta[GDP_C] + [GTP_N] \cdot \left(\frac{\alpha CI_{NPC-N}}{N_A \cdot V_C} + \beta[CI_N] \cdot \frac{V_N}{V_C}\right)$ $[\dot{GDP}_N] = \delta[GTP_N] + \zeta[GDP_C] \cdot \frac{V_C}{V_N}$ $[\dot{GDP}_C] = \eta[GTP_C] - \zeta[GDP_N] \cdot \frac{V_N}{V_C}$ $[\dot{GDP}_C] = -\zeta[GDP_N] \cdot \frac{V_N}{V_C}$	Ran cycle: - RCC1 (RanGEF) mediated exchange of RanGDP to RanGTP - RanGAP-mediated hydrolysis of RanGTP to RanGDP - Residual reverse conversion of nuclear RanGTP to RanGDP - NTF2-mediated transport of RanGDP (symmetric for export and import, results in net import due to concentration gradient) - export of importin-bound RanGTP following an import cycle (the exported importins are not modeled explicitly)

Model Table 2. Kinetic model variables.

Variable name	Description
C	cargo molecules (unbound)
CI	cargo:importin complex (bound)
GTP	RanGTP
GDP	RanGDP

Model Table 3. ODE model coefficients.

Model coefficient	Description	Value*	units
α	Rate of GTP-dependent conversion of NPC-docked cargo:importin complex to nuclear cargo	10^6	$M^{-1}sec^{-1}$
β	Rate of GTP-dependent conversion of nuclear cargo:importin complex to nuclear cargo	10^6	$M^{-1}sec^{-1}$
γ	Rate of exchange of GDP_N to GTP_N by RCC1	1000	sec^{-1}
δ	Rate of residual exchange of GTP_N to GDP_N by RCC1	0.2	sec^{-1}
ϵ	Rate of RanGTP passive export	0.5	sec^{-1}
ζ	Rate of NTF2-mediated RanGDP transport	1.0	sec^{-1}
η	Rate of RanGAP-mediated hydrolysis of RanGTP to RanGDP	500.0	sec^{-1}
k_{on}	Rate of cargo association to importin molecules	0.001-3.83**	sec^{-1}
k_{off}	Rate of dissociation of cargo:importin complexes	0.05	sec^{-1}
$\pi_{passive}$	Passive diffusion rate (permeability)	0.03-0.16***	sec^{-1}
σ_{on}	Rate of docking of cargo:importin complexes to NPC	$50x10^6$	$sec^{-1}M^{-1}$
σ_{off}	Rate of undocking of cargo:importin complexes from NPC	3000.0	sec^{-1}
φ	Traversal rate of cargo:importin complexes across the NPC	15.0 (soft) 150.0 (stiff)	sec^{-1}
N_{dock}	Number of docking sites on NPCs	500	-
N_{NPC}	Number of NPC molecules per cell	2000	-
$[Ran]_{cell}$	Total concentration of RanGTP and RanGDP in the entire cell	20	μM
$[C]_{cyto,t=0}$	Initial cytoplasmic concentration of cargo molecules****	0.1	μM
V_N	Nuclear volumen	$627x10^{-15}$	L
V_C	Cytoplasmic volume	$2194\ x10^{-15}$	L
Δt	Simulation timestep	0.001	sec
τ	Simulation time	100	sec

* unless stated otherwise for specific runs

** 0.054 sec^{-1} for weak NLS, 0.205 sec^{-1} for medium NLS

*** according to measurements of actual passive diffusion rates for different cargo molecules (Figure 5e,f)

**** the initial nuclear concentration is zero in all runs

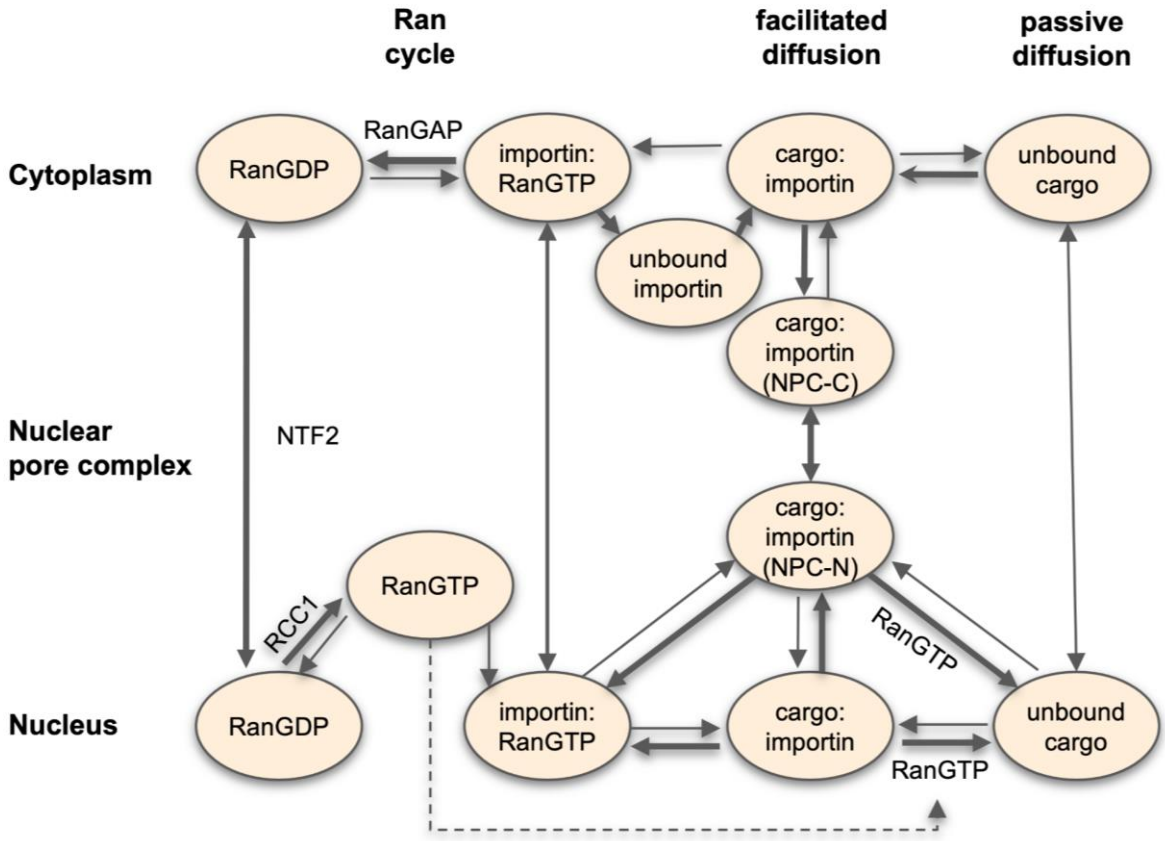

Model Figure 1. Kinetic model of import through the NPC. The concentration of importin molecules is not modeled explicitly (see Text), except to indicate whether cargo molecules are in the bound or unbound state, but they are shown here for completeness.

10. Appendix B: Cloning techniques

During the progress of this work in the Cellular and molecular mechanobiology laboratory I have faced many different scientific questions, many of them could be answered by using a plasmid vector encoding a mutant or heterologous protein. For this reason, I cloned more than a hundred *ad hoc* different plasmid vectors in this time. This gained experience is the knowledge I want to transmit in this appendix, which I hope to be minimally useful until the cost of synthesizing entire plasmids becomes futile.

The first step when facing a cloning process is to define if it is a deletion, an insertion, or a point mutation. In the case of the deletions, small insertions, and point mutations (side-directed mutagenesis) I found a method in the literature that is seamless (no need for restriction enzymes), quick and cheap. This method was published by Liu and Naismith in 2008 and consists in a simple PCR, followed by DpnI digestion, and *E. coli* transformation (H. Liu & Naismith, 2008). In the case of big insertions, the used method was Gibson Assembly protocol and reactives by New England Biolabs. Gibson Assembly is also a seamless method, but its efficiency is lower compared to Liu and Naismith method due to the need to attach different big pieces of DNA.

10.1. Liu & Naismith protocol

10.1.1. Protocol for primer design

The pair of primers for this type of mutagenesis process contain two types of regions: Non-Overlapping, that will bind the template plasmid; and Primer pair, placed at the 5' end, that will bind the other primer (see (H. Liu & Naismith, 2008),Figure 38a-c). There are several rules to achieve a successful primer design:

- Melting temperature of non-overlapping sequences ($T_{m\text{-}no}$) 5 to 10°C higher than the melting temperature of primer pair complementary sequences ($T_{m\text{-}pp}$).
- In my experience, all the space between the NO and the PP can be used for insertions, no matter if the primer lengths are vastly different or the insertion is very long (whose length is mostly limited by quality standards in oligonucleotide synthesis).
- In the case of deletions, they can be placed in any place of the PP region, in Figure ***38***b is placed in the middle.
- Regarding point mutations, if placed in the PP region there is no limit in the number of changes, since changing all the bases would become an insertion. However, if two single-base mutations are some 50bp apart we could fit them in the NO region, making sure there are enough bases on the 3' end to start polymerization in the first cycles.

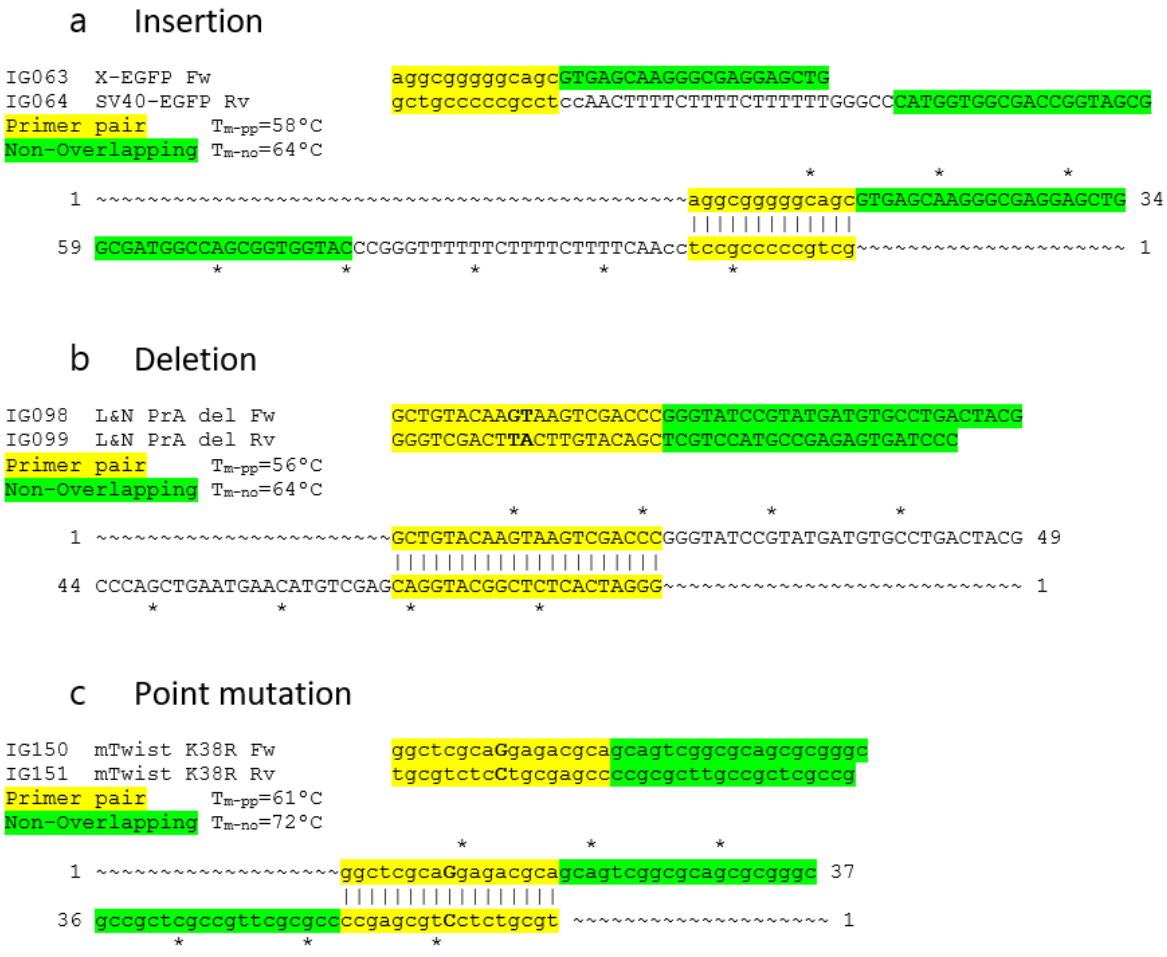

Figure 38 Primer pair examples for Liu and Naismith protocol, for insertion, deletion, and point mutagenesis.

10.1.2. PCR conditions

(Adapted from Liu and Naismith, 2008)

An essential characteristic of this PCR protocol is that it needs a non-strand-displacing polymerase, in our case we used Phusion.

PCR reaction

	10 µL Total	**20 µL Total**	**50 µL Total**
Nuclease-free water	5.2	Up to 20 µL (10.4 µL)	Up to 50 µL (26 µL)
5x HF buffer	2	4 µL	10 µL
10mM dNTPs	0.2	0.4 µL	1 µL

10µM Fw	1	2 µL	5 µL
10µM Rv	1	2 µL	5 µL
Template	8ng	16ng	40ng
DMSO	0.3	0.6 µL (3%)	1.5 µL (3%)
Phusion	0.3	0.6 µL	1.5 µL (3 units)

PCR Cycles (use two ram cycles)

94°C for 7 min

Ram 1. No. cycles 12
94°C for 1 min
Tm no -5 for 1 min
72°C for 30s/kb

Ram 2 No. cycles 3
95°C for 1min
Tm pp -5 for 1min
72°C for 30s/kb

Final amplification
72°C for 20min
4°C hold

Template DNA removal

In 20 µL from the PCR sample add 1µL (5 units) DpnI and incubate at 37°C for 4 hours (can also be done O/N to increase efficiency). PCR amplification can be checked by running an agarose gel.

Transformation

Use 50 µL of DH5 α or any other commercial competent cells + 5 µL of the reaction and then followed the standard transformation protocol. If colonies are too few, you filter the with a dialisis filter DNA from the Dpn I digested reaction and then do the transformation again (this protocol usually give a high mutation efficiency so you don't need too many colonies).

Colony PCR

In order to screen the outcome of the cloning process for insertions or deletions, we implemented a colony PCR technique that is able to detect changes in length of 40bp in 200bp fragments.

11. Appendix C: Data processing for Chapter 2

In this appendix I add the commented MATLAB codes used to compute all the measurements presented in 5 Results. Chapter 2: Study of the mechanical regulation of nucleocytoplasmic transport in multicellular systems. I have used three differentiated codes for three different processing steps.

1. The Measuring code. It has been used for measuring shape parameters of the nuclei and the fluorescence intensities, that are used in the next step to measure ratios. The zones where the intensities are measured are 2D areas placed in the z-slice where the nucleus is the widest in area. The OUT region is placed from 3 pixels outside of the mask to 1 pixel outside of the mask, it is a ring surrounding the nucleus. The IN region is the mask eroded 1 pixel. As an output it yields a table, with one row per nuclei.
2. The Calculation code. This code uses the output of the previous code and calculates more complex shape parameters and ratios for all the channels. It also calculates quality parameters that are then used for filtering bad data points. As an output it also yields a table, with one row per nuclei, but a higher amount of columns.
3. The Plotting code. This code is used for data binning and 2D and 3D plotting. As an output it yields the graphs for the chosen combination of variables and the table with the data. It can be run by section.

11.1. Measuring code

```
clear all; clc; close all
%addpath("C:/Users/igranero/OneDrive - IBEC/MATLAB");

%% PARAMETERS
n0=15; %starting image, in case you have stopped it and want to start from the n-
th image on the list

%%Channels
       Amount_of_channels=2;   %from 1 to 3
       Mask='*cp_masks.tif';
       Ch1='*c1.tif';         %file identifiers
       Ch2='*c2.tif';
       % Ch3='*c3.tif';
%%Regions to measure
       out2 = 3;  %% outer limit of outer ring in pixels %% 4 for pixel size
0.415, 7 for pixel size 0.247
       out1 = 1;   %% inner limit of outer ring in pixels %% 2 for pixel size
0.415, 3 for pixel size 0.247
       out1_2 = 2;   %% inner limit of outer ring in pixels %% 2 for pixel size
0.415, 3 for pixel size 0.247
       in = 1;     %% outer limit of the inner nucleus %% 2 for pixel size 0.415,
3 for pixel size 0.247

%%Imaging conditions
       z_corr=0.86;          %% 0.86 for airyscan 63x with immersol vs live cells;
z-correction factor calculated with Diel, E.E., Lichtman, J.W. & Richardson, D.S.
Tutorial: avoiding and correcting sample-induced spherical aberration artifacts
in 3D fluorescence microscopy. Nat Protoc 15, 2773-2784 (2020). https://doi-
org.sire.ub.edu/10.1038/s41596-020-0360-2
       voxel_xy_size=0.1412983*4;  %% voxel yx size
       voxel_z_size=0.4;      %% voxel z size
       interp_ratio=(voxel_z_size*z_corr)/voxel_xy_size;
```

```
%%Volume restriction on measuring
       threshold=2000; %%minimum amount of pixels for the nucleus mask to be
processed

%% Get folder where to get all the images, masks included
folder = uigetdir(pwd, 'Select a folder');

%% Identifying MASKS and channel files
files_mask = dir(fullfile(folder,Mask));
   for r=1:length(files_mask)
   filename_mask{r}={append(files_mask(r).folder,'\', files_mask(r).name)};
   end

files_ch1 = dir(fullfile(folder, Ch1));
   for r=1:length(files_ch1)
   filename_ch1{r}={append(files_mask(r).folder,'\',files_ch1(r).name)};
   end
      if Amount_of_channels>=2
      files_ch2 = dir(fullfile(folder, Ch2));
         for r=1:length(files_ch2)
         filename_ch2{r}={append(files_mask(r).folder,'\',files_ch2(r).name)};
         end
         if Amount_of_channels>=3
         files_ch3 = dir(fullfile(folder, Ch3));
            for r=1:length(files_ch3)

filename_ch3{r}={append(files_mask(r).folder,'\',files_ch3(r).name)};
            end
         end
      end

%% Checkpoint
   if length(filename_mask)==length(filename_ch1)
   else
      warning('Error in the list of files')
      return
   end

%% Here is where fun begins
tic

%pre-create results table
Results=table('Size', [50000,43],
'VariableTypes',{'string','double','double','double','double','double','double','
double','double','cell','cell','double','double','double','double','double','doub
le','double','double','double','double','double','double','double','double','doub
le','double','double','double','double','double','double','double','double','doub
le','double','double','double','double','double','double','double'},'Var
iableNames',{'filename_str','cell_num','Volume','Centroid','BoundingBox','EquivDi
ameter','Extent','PrincipalAxisLength','Orientation','EigenVectors','EigenValues'
,'Solidity','SurfaceArea','Volume_um3','Vol_in_p_Ch1','MeanIntensity_in_p_Ch1','M
inIntensity_in_p_Ch1','MaxIntensity_in_p_Ch1','Std_in_p_Ch1','Median_in_p_Ch1','V
ol_out_p_Ch1','MeanIntensity_out_p_Ch1','MinIntensity_out_p_Ch1','MaxIntensity_ou
t_p_Ch1','Std_out_p_Ch1','Median_out_p_Ch1','img_size_x','img_size_y','img_size_z
','img_size_x_interp','img_size_y_interp','Vol_in_p_Ch2','MeanIntensity_in_p_Ch2'
,'MinIntensity_in_p_Ch2','MaxIntensity_in_p_Ch2','Std_in_p_Ch2','Median_in_p_Ch2'
,'Vol_out_p_Ch2','MeanIntensity_out_p_Ch2','MinIntensity_out_p_Ch2','MaxIntensity
_out_p_Ch2','Std_out_p_Ch2','Median_out_p_Ch2'
});
Results=[];

%%for every POSITION and/or Timepoint
```

```
for n=n0:length(filename_mask) % number of images / sets of mask+channels
n/length(filename_mask)*100
V_mask = tiffreadVolume(filename_mask{n});
V_ch1 = tiffreadVolume(filename_ch1{n});
       if Amount_of_channels==2
       V_ch2 = tiffreadVolume(filename_ch2{n});
       Channels = {V_ch1, V_ch2};
       end
       if Amount_of_channels==3
       V_ch2 = tiffreadVolume(filename_ch2{n});
       V_ch3 = tiffreadVolume(filename_ch3{n});
       Channels = {V_ch1, V_ch2, V_ch3};
       end

%%Array of masks of cells one-by-one
   % %counting how many times a pixel value is present to filter the ones that
   % are very few times
u=unique(V_mask);
U= [u,histc(V_mask(:),u)];

cell_Amount=double(max(V_mask(:))); % to know the total amount of cells/particles
in the mask
n_chunk=10;
G=ceil(cell_Amount/n_chunk);  % calculate the amount of rounds of n_chunk
particles to compute at a time

   for g=1:G
      clear MASK
         if G==g
         cell_count_up=cell_Amount;
         cell_count_down=(g-1)*n_chunk+1;
         else
         cell_count_up=g*n_chunk;
         cell_count_down=(g-1)*n_chunk+1;
         end

      for i = cell_count_down:cell_count_up
         if U(U(:,1)==i,2)>=threshold
            for z = 1:size(V_mask,3)
                   % take a stack position
               img = V_mask(:,:,z);
               % i th cell at z th position
               img1 = img;
               img1(img1~=i)=0;
               MASK{i,z} = img1;
            end
         else
            img1=uint16(zeros(size(V_mask,1),size(V_mask,2)));
            for z = 1:size(V_mask,3)
               MASK{i,z} = img1;
            end
         end
      end

%% Create tables with data from nuclei shapes, in and out regions
stats_nuc = table('Size',[1
4],'VariableTypes',{'double','double','double','double'} );
stats_in =table('Size',[1
4],'VariableTypes',{'double','double','double','double'} );
stats_out =table('Size',[1
4],'VariableTypes',{'double','double','double','double'} );

          % % Radii of expansion and decrease of the nuclei
```

```
          disk_out2 = strel('disk',out2,0);
          disk_out1 = strel('disk',out1,0);
          disk_out1_2 = strel('disk',out1_2,0);
          disk_in = strel('disk',in,0);

clear M;
   %% Cell by cell analysis
   for cell_num=cell_count_down:cell_count_up
              % % Make an array for each cell
              for j = 1:size(V_mask,3)
                M(:,:,j) = MASK{cell_num,j};
              end

             % % Binarizing the cellpose mask and the cell specific mask
             binary = imbinarize(V_mask,0);
             binary_c = imcomplement(binary);
             bin_M = imbinarize(M,0);
   %%if there is something in the mask, look for the best plane
   if max(bin_M, [], 'all')==0
   else
             % % plane/s of maximal area
             plane_val=[sum(bin_M,[1 2])];
             [plane_max_val,plane_max_z]=max(plane_val);
             plane_vector=(plane_val~=plane_max_val);
             bin_M_plane=bin_M;
             bin_M_plane(:,:,plane_vector)=0;

             % % Creation of the nuclear an perinuclear areas
                %OUT =(imdilate(bin_M,disk_out2) -
imdilate(bin_M,disk_out1)).*binary_c;
                %IN = imerode(bin_M,disk_in);
             OUT_p =(imdilate(bin_M_plane,disk_out2) -
imdilate(bin_M_plane,disk_out1)).*binary_c;
             OUT_p_2 =(imdilate(bin_M_plane,disk_out2) -
imdilate(bin_M_plane,disk_out1_2)).*binary_c;
             IN_p = imerode(bin_M_plane,disk_in);
                    %  sliceViewer(bin_M);

             filename_str = convertCharsToStrings(filename_mask{n});
             Description = table(filename_str, cell_num);

             %%Correction of voxel size to get the right proportions for
             %%shapes.
             %%To calculate real volume multiply the result times the xy
             %%pixel size which becomes the voxel size for the calculated
             %%volume
                       A = double(bin_M);
                       [m1,n1,p1]= size(A) ;

                       if interp_ratio>1
                       z2=round(p1*interp_ratio);
                       Ai=imresize3(A,[m1 n1 z2]);
                       else
                       x2=round(m1/interp_ratio);
                       y2=round(n1/interp_ratio);
                       Ai=imresize3(A,[x2 y2 p1]);
                       end
                       bin_Ai = imbinarize(Ai,0.5);

             %% Nuclear properties. takes properties of the nuclei and keeps only
the biggest volume, in case it detects small separated voxels (same for in and
out)
```

```
            stats_nuc =
regionprops3(bin_Ai,'BoundingBox','Centroid','EigenValues','EigenVectors','EquivD
iameter','Extent','Orientation','PrincipalAxisLength','Solidity','Volume','Surfac
eArea');
                [~,l]= max(stats_nuc.Volume);
                stats_nuc = stats_nuc(l,:);
                %%conversion to um^3
                                if interp_ratio>1

stats_nuc.Volume_um3=stats_nuc.Volume*(voxel_xy_size*interp_ratio)^3;
                                else

stats_nuc.Volume_um3=stats_nuc.Volume*(voxel_z_size*z_corr)^3;
                                end
            cell_stats = [Description stats_nuc];

            % % for measuring several channels In and Out regions
            for c=1:length(Channels)
                ch=convertStringsToChars("_Ch"+c);

            % %measure IN and OUT  if there is something
            % % OUT_p
                if max(OUT_p(:))==1
                stats_out_p=
regionprops3(OUT_p,Channels{1,c},"Volume","MeanIntensity","MaxIntensity","MinInte
nsity","VoxelValues");
                    [~,l]= max(stats_out_p.Volume);
                    stats_out_p = stats_out_p(l,:);
                    if stats_out_p.Volume > 1

stats_out_p.Std_out_p=std(double(stats_out_p.VoxelValues{1}));

stats_out_p.Median_out_p=median(double(stats_out_p.VoxelValues{1}));
                        stats_out_p.VoxelValues=[];
                    else

stats_out_p.Std_out_p=std(double(stats_out_p.VoxelValues(1)));
                        stats_out_p.VoxelValues=[];
                    end
                else
                stats_out_p{:,:} = NaN;
                end



names_out_p={'Vol_out_p','MeanIntensity_out_p','MinIntensity_out_p','MaxIntensity
_out_p','Std_out_p','Median_out_p'};
                names_out_p_Ch=append(names_out_p,ch);
                stats_out_p.Properties.VariableNames = names_out_p_Ch;

            % % OUT_p_2
                if max(OUT_p_2(:))==1
                stats_out_p_2=
regionprops3(OUT_p_2,Channels{1,c},"Volume","MeanIntensity","MaxIntensity","MinIn
tensity","VoxelValues");
                    [~,l]= max(stats_out_p_2.Volume);
                    stats_out_p_2 = stats_out_p_2(l,:);
                    if stats_out_p_2.Volume > 1

stats_out_p_2.Std_out_p=std(double(stats_out_p_2.VoxelValues{1}));

stats_out_p_2.Median_out_p=median(double(stats_out_p_2.VoxelValues{1}));
```

```
                        stats_out_p_2.VoxelValues=[];
                    else

stats_out_p_2.Std_out_p=std(double(stats_out_p_2.VoxelValues(1)));
                        stats_out_p_2.VoxelValues=[];
                    end
                else
                stats_out_p_2{:,:} = NaN;
                end

names_out_p_2={'Vol_out_p_2','MeanIntensity_out_p_2','MinIntensity_out_p_2','MaxI
ntensity_out_p_2','Std_out_p_2','Median_out_p_2'};
                names_out_p_2_Ch=append(names_out_p_2,ch);
                stats_out_p_2.Properties.VariableNames = names_out_p_2_Ch;
            % % IN_p
                if max(IN_p(:))==1
                stats_in_p =
regionprops3(IN_p,Channels{1,c},"Volume","MeanIntensity","MaxIntensity","MinInten
sity","VoxelValues");
                    [~,l]= max(stats_in_p.Volume);
                    stats_in_p = stats_in_p(l,:);
                    stats_in_p.Std_in_p=std(double(stats_in_p.VoxelValues{1}));

stats_in_p.Median_out_p=median(double(stats_in_p.VoxelValues{1}));
                    stats_in_p.VoxelValues=[];
                else
                stats_in_p{:,:} = NaN;
                end

names_in_p={'Vol_in_p','MeanIntensity_in_p','MinIntensity_in_p','MaxIntensity_in_
p','Std_in_p','Median_in_p'};
                names_in_p_Ch=append(names_in_p,ch);
                stats_in_p.Properties.VariableNames = names_in_p_Ch;
                    % % Image Size
                        [y x z]=size(V_mask);
                        img_size=table(x, y, z, x/interp_ratio, y/interp_ratio);
                        img_size.Properties.VariableNames =
{'img_size_x','img_size_y','img_size_z',
'img_size_x_interp','img_size_y_interp'};
                    % % Data storage
                        if c==1
                        cell_stats = [cell_stats stats_in_p stats_out_p img_size];
%cell_stats = [cell_stats stats_in stats_out stats_in_p stats_out_p];
                        else
                        cell_stats = [cell_stats stats_in_p stats_out_p];
                        end
            end
    % Append results
        Results = [Results; cell_stats];
    end
    end
end

Date=datetime;
Date.Format = 'yyyy_MM_dd__HH_mm_ss';
name_export=append('Results_',char(files_mask(n0).name),'_p',char(Date),'_out2_',
""+out2,'_out1_',""+out1,'_in_',""+in,'.txt');
writetable(Results,name_export,'WriteRowNames',true,'Delimiter',';');
end

toc
```

11.2. Calculation code

```
tic
clear all;
addpath("C:\Users\igranero\OneDrive - IBEC\DiskStation backup\MetaDataset");

%%Name of the file out of a_Measure with the data from all the nuclei
nametable="Results_20220801_Metadataset.txt";
R1=readtable(nametable);
R1.filename_str=string(R1.filename_str); % convert first column to string

%% Parameters
par_volume=200; %minimal volume in um3
par_Solidity=0; %minimal Solidity
par_hoechst=4;  %minimal hoescht ratio to accept the nuclei
par_bg=50;      %background signal to noise ratio in the channel to measure
dist_density=100; %distance in pixels of the radius where to measure density for
each cell

%%Imaging conditions
       z_corr=0.86;          %% 0.86 for airyscan 63x with immersol vs live cells;
z-correction factor calculated with Diel, E.E., Lichtman, J.W. & Richardson, D.S.
Tutorial: avoiding and correcting sample-induced spherical aberration artifacts
in 3D fluorescence microscopy. Nat Protoc 15, 2773-2784 (2020). https://doi-
org.sire.ub.edu/10.1038/s41596-020-0360-2
       voxel_xy_size=0.1412983*4;  %% voxel yx size
       voxel_z_size=0.4;     %% voxel z size
       interp_ratio=(voxel_z_size*z_corr)/voxel_xy_size;

%image classification
code=["2205b" "2224" "2226" "2227" "2228" "2230"]; %code of experiment
acq_code_name=["2205b" "2224" "2226" "2227" "2228" "2230"];
acq_code=[1 2 3 4 5 6];

experiment=["2205b" "2022_06_16" "2022_06_17" "2226" "2022_07_08__10"
"2022_07_08__15" "2022_07_14__11" "2022_07_14__17"    "2022_07_28__12"
"2022_07_28__11"    "2022_07_28__17"    "2022_07_28__19"]; %type of experiment
11_21 is Sensor, 17_00 is YAP
acq_exp=[1  1   2   1   1   2   1   2   1   1   2   2];
acq_bgch2=[1    1   2   1   1   2   1   2   1   1   2   2];

positions=["pos1" "pos2" "pos3" "pos4"]; %type of experiment 11_21 is Sensor,
17_00 is YAP
acq_pos=[1 2 3 4];

% Correlation Sensor-YAP
c2224(:,1)=[97  87  57  86  38  37  36  120 100 213 60  40  102 61  43  41  74  79  46  45  44  47  89  106 107 122 108 101 162 272 299 300 334 188 222 211 355 182 268 181 237 332 221 474
443 273 331 210 436 354 353 414 537 389 513 583 461 460 550 623 1139    459 651 497 347 321 378 322 427 458 457 425 430 424 455 554 428 429 841 1060    686 735 1053    648 929 476 477
479 485 579 563 1018    539 659 793 695 1314    1069    795 1478    820 721 1451    1452    1087    1120    1480    855 1684    953 1392    1024    1129    1390    942 1086    1354    1323
1158    1598    1038    1815    1419    2068    1785    2070    1692    2024    1997    1859    1711    1987    1835    1864    1947    1842    1845    1951    1689    1908    1952    1793    2041
2204    2300    2314    2179    2493    2426    2465    2312    2397    1090    991 629 653 811 684 950 865 964 837 924 999 960 611 785 812 1025    1096    1227    864 1135    1027    1232
1029    1028    1289    1219    1167    1578    990 1335    1450    1765    1739    1721    1461    1520    1396    1186    1769    1297    1584    1394    1052    1259    1513    1820    1449    1572
1573    1544    1424    1585    1097    1288    1737    1616    1553    1764    1998    1543    1955    1969    1482    1855    1322    1811    1963    1734    1755    1714    1591    1834    1687
];
```

Only one correlation table is shown for space purposes.

```
   %cor_table is [code position correlations]
cor_table={2 1 c2224; 4 1 c2227; 5 1 c2228;6 1 c2230pos1;;6 2 c2230pos2;;6 3
c2230pos3};

%% code experiment and position

%CODE of the experiment
for i=1:height(R1)
   for j=1:length(code)
   cerca=strfind(char(R1.filename_str(i)),code(j));
   cerca1=isnan(cerca);
```

```
            if cerca1==0
               R1.code_name(i)=acq_code_name(j);
               R1.code(i)=acq_code(j);
            end
    end
end

%EXPERIMENT type
for i=1:height(R1)
    for j=1:length(experiment)
    cerca=strfind(char(R1.filename_str(i)),experiment(j));
    cerca1=isnan(cerca);
            if cerca1==0
               R1.experiment(i)=acq_exp(j);
            end
    end
end

%POSITION
for i=1:height(R1)
    for j=1:length(positions)
    cerca=strfind(char(R1.filename_str(i)),positions(j));
    cerca1=isnan(cerca);
            if cerca1==0
               R1.position(i)=acq_pos(j);
            end
    end
    if R1.position(i)==0
               R1.position(i)=1;
    end
end

%% Timepoint and position

R1.rel_time(:)=1;

%% Background

for i=1:height(R1)
    for j=1:length(experiment)
    cerca=strfind(char(R1.filename_str(i)),experiment(j));
    cerca1=isnan(cerca);
            if cerca1==0
               R1.r_bg_ch2(i)=acq_bgch2(j);
            end
    end
end

%% Volume filter
for i=1:height(R1)
    if R1.Volume_um3(i)>par_volume
    R1.r_Volume_filter(i)=1;
    else
    R1.r_Volume_filter(i)=0;
    end
end

%% Solidity filter
for i=1:height(R1)
    if R1.Solidity(i)>par_Solidity
R1.r_Solidity_filter(i)=1;
    else
       R1.r_Solidity_filter(i)=0;
```

```
    end
end

%% Hoechst filter
R1.r_Ratio_ch1=R1.MeanIntensity_in_p_Ch1./R1.MeanIntensity_out_p_Ch1;
for i=1:height(R1)
    if R1.r_Ratio_ch1(i)>par_hoechst
R1.r_Hoechst_filter(i)=1;
    else
        R1.r_Hoechst_filter(i)=0;
    end
end

%% Edge filter  -  Exclude nuclei touching the edges of the images, using the
values of bounding box
    Min_x =5 ;
    Min_y =5 ;
    Min_z =0.5 ;
for i=1:height(R1)
    min_x=R1.BoundingBox_1(i);
    max_x=R1.BoundingBox_1(i)+ R1.BoundingBox_4(i);
    min_y=R1.BoundingBox_2(i);
    max_y=R1.BoundingBox_2(i)+ R1.BoundingBox_5(i);
    min_z=R1.BoundingBox_3(i);
    max_z=R1.BoundingBox_3(i)+ R1.BoundingBox_6(i);

    Max_x=R1.img_size_x_interp(i)-5 ;
    Max_y=R1.img_size_y_interp(i)-5 ;
    Max_z=R1.img_size_z(i)-0.5;

    if min_x>Min_x & max_x<Max_x & min_y>Min_y & max_y<Max_y & min_z>Min_z &
max_z<Max_z
    R1.r_EdgeFilter(i)=1;
    else
    R1.r_EdgeFilter(i)=0;
    end
end

%% Channel 2 filter and ratio
for i=1:height(R1)
sn_in=R1.MeanIntensity_in_p_Ch2(i)/R1.r_bg_ch2(i);
sn_out=R1.MeanIntensity_out_p_Ch2(i)/R1.r_bg_ch2(i);
R1.ston_ch2(i)=min(sn_in,sn_out);
end

for i=1:height(R1)
R1.mtom_in_p_ch2(i)=(R1.Std_in_p_Ch2(i))/R1.MeanIntensity_in_p_Ch2(i);
R1.mtom_out_p_ch2(i)=(R1.Std_out_p_Ch2(i))/R1.MeanIntensity_out_p_Ch2(i);
end

for i=1:height(R1)
    if R1.ston_ch2(i)>par_bg
        R1.r_ch2_filter(i)=1;
        else
        R1.r_ch2_filter(i)=0;
    end

end

for i=1:height(R1)
    if
R1.r_ch2_filter(i)*R1.r_Volume_filter(i)*R1.r_Solidity_filter(i)*R1.r_Hoechst_fil
ter(i)*R1.r_EdgeFilter(i)==1
```

```
        R1.r_Ratio_p_ch2(i)=(R1.MeanIntensity_in_p_Ch2(i)-
R1.r_bg_ch2(i))./(R1.MeanIntensity_out_p_Ch2(i)-R1.r_bg_ch2(i));
    else
        R1.r_Ratio_p_ch2(i)=NaN;
    end
end

%% Separate ratios Sensor YAP

for i=1:height(R1)
    if R1.experiment(i)==1;
        R1.Sensor_ratio(i)=R1.r_Ratio_p_ch2(i);
           else
        R1.Sensor_ratio(i)=NaN;
    end
    R1.log2Sensor_ratio=log2(R1.Sensor_ratio);


    if R1.experiment(i)==2;
        R1.yap_ratio(i)=R1.r_Ratio_p_ch2(i);

    else
        R1.yap_ratio(i)=NaN;
    end
    R1.log2yap_ratio=log2(R1.yap_ratio);
end

%%  Parameters Nuclear Shape

for i=1:height(R1)
    if
R1.r_Volume_filter(i)*R1.r_Solidity_filter(i)*R1.r_Hoechst_filter(i)*R1.r_EdgeFil
ter(i)==1

R1.r_Nuc_shape(i)=(R1.PrincipalAxisLength_3(i))^2./R1.PrincipalAxisLength_1(i)./R
1.PrincipalAxisLength_2(i);
    else
        R1.r_Nuc_shape(i)=NaN;
    end
end

for i=1:height(R1)
    if
R1.r_Volume_filter(i)*R1.r_Solidity_filter(i)*R1.r_Hoechst_filter(i)*R1.r_EdgeFil
ter(i)==1
    R1.r_Sphericity(i)=pi^(1/3)*(6*R1.Volume(i))^(2/3)/R1.SurfaceArea(i);
    else
    R1.r_Sphericity(i)=NaN;
    end
end

for i=1:height(R1)
    if
R1.r_Volume_filter(i)*R1.r_Solidity_filter(i)*R1.r_Hoechst_filter(i)*R1.r_EdgeFil
ter(i)==1

R1.r_prolate(i)=2*R1.PrincipalAxisLength_3(i)^2/(R1.PrincipalAxisLength_3(i)^2+R1
.PrincipalAxisLength_2(i)^2)*(1-
(R1.PrincipalAxisLength_3(i)^2+R1.PrincipalAxisLength_2(i)^2)/(2*R1.PrincipalAxis
Length_1(i)^2));
    else
    R1.r_prolate(i)=NaN;
    end
```

```
end

for i=1:height(R1)
    if
R1.r_Volume_filter(i)*R1.r_Solidity_filter(i)*R1.r_Hoechst_filter(i)*R1.r_EdgeFil
ter(i)==1

R1.r_oblate(i)=2*R1.PrincipalAxisLength_2(i)^2/(R1.PrincipalAxisLength_2(i)^2+R1.
PrincipalAxisLength_1(i)^2)*(1-
(2*R1.PrincipalAxisLength_3(i)^2)/(R1.PrincipalAxisLength_2(i)^2+R1.PrincipalAxis
Length_1(i)^2));
    else
    R1.r_oblate(i)=NaN;
    end
end
%% Density
%Density of cells in a square centered at the cell and with side = 2+dist_density

for i=1:height(R1)
    if R1.r_Hoechst_filter(i)>0 & R1.r_Solidity_filter(i)>0 &
R1.r_Volume_filter(i)>0
          rows=find( R1.code==R1.code(i)& R1.experiment==R1.experiment(i)&
R1.position==R1.position(i)& R1.rel_time==R1.rel_time(i)&
R1.r_Hoechst_filter(i)>0 & R1.r_Solidity_filter(i)>0 & R1.r_Volume_filter(i)>0 &
abs(R1.Centroid_1-R1.Centroid_1(i))<dist_density & abs(R1.Centroid_2-
R1.Centroid_2(i))<dist_density);
       R1.preDensity(i)=height(rows);
       if interp_ratio<1

R1.pre_z_range_layer(i)=(max(R1{rows,'BoundingBox_3'}+R1{rows,'BoundingBox_6'})-
min(R1{rows,'BoundingBox_3'}))*voxel_z_size;
       R1.pre_z_range_cell(i)=(max(R1{rows,'BoundingBox_6'}))*voxel_z_size;
       else
           return
       end
    else
    R1.preDensity(i)=NaN;
    R1.pre_z_range_layer(i)=NaN;
    R1.pre_z_range_cell(i)=NaN;
    end


%Correction for cells close to the edge of the images

if abs(R1.Centroid_1(i)-R1.img_size_x_interp(i))< dist_density ||
abs(R1.Centroid_1(i)) < dist_density
    dx=min(abs(R1.Centroid_1(i)-R1.img_size_x_interp(i)),abs(R1.Centroid_1(i)));
    area=4*dist_density^2;
    if abs(R1.Centroid_2(i)-R1.img_size_y_interp(i))< dist_density  ||
abs(R1.Centroid_2(i))< dist_density
       dy=min(abs(R1.Centroid_2(i)-
R1.img_size_x_interp(i)),abs(R1.Centroid_2(i)));
          rest_a=(dist_density+dx)*(dist_density+dy);
          ratio_a=rest_a/area;
       R1.corDensity(i)=(R1.preDensity(i)/ratio_a);
    else
          rest_a= (dist_density+dx)*dist_density*2;
          ratio_a=rest_a/area;
       R1.corDensity(i)=(R1.preDensity(i)/ratio_a);
    end
else
    if abs(R1.Centroid_2(i)-R1.img_size_y_interp(i))< dist_density  ||
abs(R1.Centroid_2(i))< dist_density
```

```
    area=4*dist_density^2;
    dy=min(abs(R1.Centroid_2(i)-R1.img_size_y_interp(i)),abs(R1.Centroid_2(i)));
           rest_a= (dist_density+dy)*dist_density*2;
           ratio_a=rest_a/area;
       R1.corDensity(i)=(R1.preDensity(i)/ratio_a);
    else
       R1.corDensity(i)=(R1.preDensity(i));
    end
end
end

% filter for manually excluded zones due to bad hoechst signal, and
% transformation to International System units
R1.Density(:)=NaN;
for i=1:height(R1)
    %for 2224
    if R1.code(i)==2 & R1.experiment(i)==1 & R1.position(i)==1 &
R1.Centroid_1(i)<1260*interp_ratio
      R1.Density_filter(i)=0;
    %for 2228
    elseif R1.code(i)==5 & R1.experiment(i)==1 & R1.position(i)==1 &
R1.Centroid_1(i)<930*interp_ratio
      R1.Density_filter(i)=0;
    %for 2230
    elseif R1.code(i)==6 & R1.experiment(i)==1 & R1.position(i)==1 &
R1.Centroid_1(i)<680*interp_ratio
      R1.Density_filter(i)=0;
    else
       R1.Density_filter(i)=1;
    end

    if R1.Density_filter(i)==1
       R1.Density(i)=R1.corDensity(i);
       R1.Density_cell_um2 =R1.Density/(2*dist_density*voxel_xy_size)^2;
       R1.z_range_layer(i)=R1.pre_z_range_layer(i);
       R1.z_range_cell(i)=R1.pre_z_range_cell(i);
    end
end

%% correlate positions between live and staining

R1.cc_cell_num(:)=NaN;
for i=1:height(cor_table)
    clear temp_cor_table
    temp_cor_table=cor_table{i,3};
    for j=1:height(R1)
       if R1.experiment(j)==1 & R1.code(j)==cor_table{i,1} &
R1.position(j)==cor_table{i,2}
       isthere=find(temp_cor_table(:,1)==R1.cell_num(j));
          if isthere>0
          R1.cc_cell_num(j)=temp_cor_table(isthere,2);
          end
       end

    end
end

% Data from correlated cell

for i=1:height(R1)
     if R1.experiment(i)==1 & R1.cc_cell_num(i)>0
       j=find(R1.cell_num==R1.cc_cell_num(i) & R1.code==R1.code(i) &
R1.experiment==2 & R1.position==R1.position(i));
```

```
            if j>0
                R1.cc_log2yap_ratio(i)=R1.log2yap_ratio(j);
                R1.cc_Volume_um3(i)=R1.Volume_um3(j);
                R1.cc_Volume_dif(i)=(R1.cc_Volume_um3(i)-
R1.Volume_um3(i))/R1.Volume_um3(i);
                R1.cc_MeanIntensity_in_p_Ch2(i)=R1.MeanIntensity_in_p_Ch2(j);
                R1.cc_Density_cell_um2(i)=R1.Density_cell_um2(j);
                R1.cc_z_range_layer(i)=R1.z_range_layer(j);
                R1.cc_z_range_cell(i)=R1.z_range_cell(j);
            else
                R1.cc_log2yap_ratio(i)=NaN;
                R1.cc_Volume_um3(i)=NaN;
                R1.cc_Volume_dif(i)=NaN;
                R1.cc_MeanIntensity_in_p_Ch2(i)=NaN;
                R1.cc_Density_cell_um2(i)=NaN;
                R1.cc_z_range_layer(i)=NaN;
                R1.cc_z_range_cell(i)=NaN;
            end
        else
           R1.cc_log2yap_ratio(i)=NaN;
           R1.cc_Volume_um3(i)=NaN;
           R1.cc_Volume_dif(i)=NaN;
           R1.cc_MeanIntensity_in_p_Ch2(i)=NaN;
           R1.cc_Density_cell_um2(i)=NaN;
           R1.cc_z_range_layer(i)=NaN;
           R1.cc_z_range_cell(i)=NaN;
        end
    end

    %For cells with non-measurable density in Sensor images, and Density measurement
    in YAP: use YAP density measurement as the good one.
    for i=1:height(R1)
    if isnan(R1.Density_cell_um2(i)) & ~isnan(R1.cc_Density_cell_um2(i))
       R1.Density_cell_um2(i)=R1.cc_Density_cell_um2(i);
       R1.z_range_layer(i)=R1.cc_z_range_layer(i);
       R1.z_range_cell(i)=R1.cc_z_range_cell(i);
    end
    end

    for i=1:height(R1)
    R1.DNAq(i)=(R1.MeanIntensity_in_p_Ch1(i)/median(R1.MeanIntensity_in_p_Ch1(R1.code
    ==R1.code(i)& R1.experiment==R1.experiment(i),:)))*R1.Volume(i);
    end
    R1.LogDNAq=log(R1.MeanIntensity_in_p_Ch1.*R1.Volume);
    R1.NucProjected_area=R1.Vol_in_p_Ch2*voxel_xy_size^2;
    R1.Sha_Vol=R1.r_Nuc_shape./R1.Volume_um3;
    R1.OrientaionPA3=abs(R1.EigenVectors_9);

    %L and M values calculated for best specificity
    L1=prctile(R1.mtom_out_p_ch2(R1.experiment==1,:),85);
    M1=prctile(R1.ston_ch2(R1.experiment==1,:),15);
    L2=prctile(R1.mtom_out_p_ch2(R1.experiment==2,:),85);
    M2=prctile(R1.ston_ch2(R1.experiment==2,:),15);

    R2=R1( R1.r_Volume_filter==1 & R1.r_Solidity_filter==1 & R1.r_Hoechst_filter==1  &
    R1.r_EdgeFilter==1,:);

    R3=R2(R2.mtom_out_p_ch2<L1 & R2.ston_ch2>M1 & R2.experiment==1 |
    R2.mtom_out_p_ch2<L2 & R2.ston_ch2>M2 & R2.experiment==2,:);

    %% EXPORT
    Date=datetime;
    Date.Format = 'yyyy_MM_dd__HH_mm_ss';
```

```
name_export=append('PROCESSED_',nametable,'_',char(Date),'.txt');
writetable(R1,name_export,'WriteRowNames',true, 'Delimiter',';');

name_export=append('PROCESSEDandCURED_',nametable,'_',char(Date),'.txt');
writetable(R3,name_export,'WriteRowNames',true, 'Delimiter',';');
toc
```

11.3. Plotting code

```
%%I recommend to create a new folder to have graphs separated

%%to make graphs
addpath('C:\Users\igranero\OneDrive - IBEC\DiskStation
backup\MetaDataset\MATLAB_b_ExcelProxy'); %folder where the source table is
nametable="PROCESSEDandCURED_Results_20220801_Metadataset.txt_2022_08_07__12_25_2
7.txt";
R1=readtable(nametable);
clc

Rexp1=R1(R1.experiment==1,:); %%more filters can be added as in
R2=R1(R1.Density==5,:);
Rexp2=R1(R1.experiment==2,:);

%% 2D Graphs in batch
ytitle= {    'Volume um3','Nuclear projected area um2','Nuclear Shape index', 'Orientation shortest axis', 'Solidity',
'Sphericity', 'Oblateness', 'Prolateness', 'DNA quantity', 'Log2 Sensor ratio', 'Log2 Sensor ratio', 'Log2 Sensor ratio',
'Log2 Sensor ratio', 'Log2 Sensor ratio', 'Log2 Sensor ratio', 'Log2 Sensor ratio', 'Log2 Sensor ratio', 'Log2 Sensor
ratio', 'Log2 Sensor ratio', 'Log2 Sensor ratio', 'Log2 Sensor ratio', 'Log2 Sensor ratio', 'Log2 Sensor ratio', 'Log2 YAP
ratio', 'Log2 YAP ratio', 'Log2 YAP ratio', 'Log2 YAP ratio', 'Log2 YAP ratio', 'Log2 YAP ratio', 'Log2 YAP ratio', 'Log2
YAP ratio', 'Log2 YAP ratio', 'Log2 YAP ratio', 'Log2 YAP ratio', 'Log2 YAP ratio', 'Log2 Sensor ratio', 'Log2 YAP ratio',
'Cell thickness', 'Monolayer thickness', 'Log2 Sensor ratio', 'Log2 Sensor ratio', 'Log2 Sensor ratio', 'Log2 YAP ratio',
};
xtitle= {    'Density cell/um2', 'Density cell/um2', 'Density cell/um2', 'Density cell/um2', 'Density cell/um2', 'Density
cell/um2', 'Density cell/um2', 'Density cell/um2', 'Density cell/um2', 'Density cell/um2', 'Log2 Volume um3', 'Volume
um3', 'Log2 Nuclear projected area um2','Nuclear projected area um2','Nuclear Shape index', 'Orientation shortest axis',
'Solidity', 'Sphericity', 'Oblateness', 'Prolateness', 'DNA quantity', 'Cell thickness', 'Monolayer thickness', 'Density
cell/um2', 'Log2 Volume um3', 'Volume um3', 'Log2 Nuclear projected area um2','Nuclear projected area um2','Nuclear Shape
index', 'Orientation shortest axis', 'Solidity', 'Sphericity', 'Oblateness', 'Prolateness', 'DNA quantity', 'Log2 YAP
ratio', 'Log2 Sensor ratio', 'Density cell/um2', 'Density cell/um2', 'Solidity-Sphericity', 'Solidity-Sphericity',
'Shortest axis length', 'Shortest axis length',          };
y={ Rexp1.Volume_um3  Rexp1.NucProjected_area  Rexp1.r_Nuc_shape  Rexp1.OrientaionPA3  Rexp1.Solidity  Rexp1.r_Sphericity
Rexp1.r_oblate  Rexp1.r_prolate  Rexp1.DNAq  Rexp1.log2Sensor_ratio  Rexp1.log2Sensor_ratio  Rexp1.log2Sensor_ratio
Rexp1.log2Sensor_ratio  Rexp1.log2Sensor_ratio  Rexp1.log2Sensor_ratio  Rexp1.log2Sensor_ratio  Rexp1.log2Sensor_ratio
Rexp1.log2Sensor_ratio  Rexp1.log2Sensor_ratio  Rexp1.log2Sensor_ratio  Rexp1.log2Sensor_ratio  Rexp1.log2Sensor_ratio
Rexp1.log2Sensor_ratio  Rexp2.log2yap_ratio  Rexp2.log2yap_ratio  Rexp2.log2yap_ratio  Rexp2.log2yap_ratio
Rexp2.log2yap_ratio  Rexp2.log2yap_ratio  Rexp2.log2yap_ratio  Rexp2.log2yap_ratio  Rexp2.log2yap_ratio  Rexp2.log2yap_ratio
Rexp2.log2yap_ratio  Rexp2.log2yap_ratio  Rexp1.log2Sensor_ratio  Rexp1.cc_log2yap_ratio  Rexp1.z_range_cell
Rexp1.z_range_layer  Rexp1.log2Sensor_ratio  Rexp1.log2Sensor_ratio  Rexp1.log2Sensor_ratio  Rexp1.cc_log2yap_ratio
};
x={ Rexp1.Density_cell_um2  Rexp1.Density_cell_um2  Rexp1.Density_cell_um2  Rexp1.Density_cell_um2  Rexp1.Density_cell_um2
Rexp1.Density_cell_um2  Rexp1.Density_cell_um2  Rexp1.Density_cell_um2  Rexp1.Density_cell_um2  Rexp1.Density_cell_um2
log2(Rexp1.Volume_um3)  Rexp1.Volume_um3  log2(Rexp1.NucProjected_area)  Rexp1.NucProjected_area  Rexp1.r_Nuc_shape
Rexp1.OrientaionPA3  Rexp1.Solidity  Rexp1.r_Sphericity  Rexp1.r_oblate  Rexp1.r_prolate  Rexp1.DNAq  Rexp1.z_range_cell
Rexp1.z_range_layer  Rexp2.Density_cell_um2  log2(Rexp2.Volume_um3)  Rexp2.Volume_um3  log2(Rexp2.NucProjected_area)
Rexp2.NucProjected_area  Rexp2.r_Nuc_shape  Rexp2.OrientaionPA3  Rexp2.Solidity  Rexp2.r_Sphericity  Rexp2.r_oblate
Rexp2.r_prolate  Rexp2.DNAq  Rexp1.cc_log2yap_ratio  Rexp1.log2Sensor_ratio  Rexp1.Density_cell_um2  Rexp1.Density_cell_um2
Rexp1.Solidity-Rexp1.r_Sphericity  Rexp1.Solidity./Rexp1.r_Sphericity  Rexp1.PrincipalAxisLength_3
Rexp1.PrincipalAxisLength_3          };
binS= [ 24  24  24  24  24  24  24  24  24  24  40  30  30  33  30  30  30  30  32  33
30  30  30  24  40  30  30  33  30  30  30  30  32  33  30  30  30  24  24  30  30  30
30     ];

saving= ones(1,length(xtitle));                          %do you want them to be
saved? 1=yes 0=no
Errorbar=0; %0 std, 1 sem
n_threshold=5;
 %%%%%%%%%%%%%%%%%%%%%%%%%%%%%%%%%%%%%%%%%%%%%%%%%%%%%%%%%%%%%%%%%%%%%%%%%%%%%%%%
  % code for graph making
                    Date=datetime;Date.Format = 'yyyy_MM_dd__HH_mm_ss';
Date=char(Date);
for j=1:length(x)
   bin=round((max(x{:,j})-min(x{:,j}))/binS(j),2,'significant');%bin=binS(j);
   Min=floor(min(x{:,j})/bin);
   Max=ceil(max(x{:,j})/bin);
```

```
    clear c

 %%Data clustering
    for i=1:Max-Min
        clear temp_y
        temp_y=y{j};
    c(i,1)=(Min+(i-1))*bin;
    c(i,2)=(Min+(i))*bin;
    c(i,3)=mean(temp_y(x{:,j} >= (Min+(i-1))*bin & x{:,j} <
(Min+(i))*bin,1),'omitnan');
    c(i,4)=std (temp_y(x{:,j} >= (Min+(i-1))*bin & x{:,j} <
(Min+(i))*bin,1),'omitnan');
    c(i,5)=sum   (~isnan(temp_y(x{:,j} >= (Min+(i-1))*bin & x{:,j} < (Min+(i))*bin
& isnan(x{:,j})==0,1)),   'omitnan');
    c(i,6)=std (temp_y(x{:,j} >= (Min+(i-1))*bin & x{:,j} <
(Min+(i))*bin,1),'omitnan')/c(i,5);
          if c(i,5)<n_threshold
              c(i,:)=NaN;
          end
    end
    c2=array2table(c);
    tabletitle=ytitle(j)+" vs "+xtitle(j);
    names={'Low', 'Up', 'Mean', 'Std', 'N', 'SEM'};
    names=append(names,' ',tabletitle);
    c2.Properties.VariableNames=names;
    c2.Properties.Description=nametable;
    Data{j}=c2;

    %%Graph making
    close
    X = Min*bin:bin:(Max-1)*bin; %x-axis
    Y = c(:,3);

    if Errorbar==0
    E = c(:,4)/2;
    elseif Errorbar==1
    E = c(:,6)/2;
    end

    Fig=errorbar(X,Y,E,'o');
    hold on
    yyaxis right
    plot(X,c(:,5))
    ylim([0 max(c(:,5))+0.5])


    nonNaN=find(~isnan(c(:,3)));
    xlim([(Min+min(nonNaN)-1.5)*bin (Min+max(nonNaN)-0.5)*bin])


    title(ytitle(j)+" vs "+xtitle(j))

    hold off
    %%Saving
    if saving[j]==1
    Title=strrep(ytitle(j)+"_vs_"+xtitle(j)+"_"," ","_");
    savingname=strrep("fl"+j+"_"+Title+Date+".png","/","_");

savingname_table=strrep("fl"+j+"_"+Title+Date+extractBefore(nametable,40)+'.txt',
"/","_");
    saveas(Fig,savingname);
    writetable(Data{j}, savingname_table,'WriteRowNames',true,'Delimiter',';');
    end
```

```
    clear Fig
    close
end

%% 3D Graphs in batch
ytitle= {   'Solidity','log2 yap ratio',  'Sensor', 'Sensor', 'Sensor', 'Sensor',
'Log2 Sensor ratio', 'Log2 Sensor ratio', 'Log2 Sensor ratio', 'Log2 Sensor
ratio', 'Log2 YAP ratio', 'Log2 YAP ratio', 'Log2 YAP ratio', 'Log2 YAP ratio',
};
xtitle= {   'Density cell/um2','Density cell/um2', 'Density cell/um2',
'Solidity', 'Solidity', 'Solidity', 'Log2 YAP ratio', 'Log2 YAP ratio', 'Log2 YAP
ratio', 'Log2 YAP ratio', 'Log2 Sensor ratio', 'Log2 Sensor ratio', 'Log2 Sensor
ratio', 'Log2 Sensor ratio', };
ztitle= {   'Volume','Volume','Volume', 'Nuclear_shape', 'Volume', 'Sphericity',
'Density cell/um2','Volume', 'Sphericity', 'Solidity', 'Density
cell/um2','Volume', 'Sphericity', 'Solidity', };
y={ Rexp1.Solidity  Rexp2.log2yap_ratio  Rexp1.log2Sensor_ratio
Rexp1.log2Sensor_ratio  Rexp1.log2Sensor_ratio  Rexp1.log2Sensor_ratio
Rexp1.log2Sensor_ratio  Rexp1.log2Sensor_ratio  Rexp1.log2Sensor_ratio
Rexp1.log2Sensor_ratio  Rexp1.cc_log2yap_ratio  Rexp1.cc_log2yap_ratio
Rexp1.cc_log2yap_ratio  Rexp1.cc_log2yap_ratio    };
x={ Rexp1.Density_cell_um2  Rexp2.Density_cell_um2  Rexp1.Density_cell_um2
Rexp1.Solidity  Rexp1.Solidity  Rexp1.Solidity  Rexp1.cc_log2yap_ratio
Rexp1.cc_log2yap_ratio  Rexp1.cc_log2yap_ratio  Rexp1.cc_log2yap_ratio
Rexp1.log2Sensor_ratio  Rexp1.log2Sensor_ratio  Rexp1.log2Sensor_ratio
Rexp1.log2Sensor_ratio     };
z={ log2(Rexp1.Volume_um3)  log2(Rexp2.Volume_um3)  Rexp1.Volume_um3
Rexp1.r_Nuc_shape  Rexp1.Volume_um3  Rexp1.r_Sphericity  Rexp1.Density_cell_um2
Rexp1.Volume_um3  Rexp1.r_Sphericity  Rexp1.Solidity  Rexp1.Density_cell_um2
Rexp1.Volume_um3  Rexp1.r_Sphericity  Rexp1.Solidity   };

binS_x=   [20 20 20 20 20 20 20 20 20 20 20 20 20 20 20 20  ];
binS_z=   [20 20 20 20 20  20 20 20 20 20 20 20 20 20 20 20 20 20 20];
n_threshold=5;

saving= zeros(1,length(xtitle));                            %do you want them to
be saved? 1=yes 0=no
Errorbar=1; %0 std, 1 sem
 %%%%%%%%%%%%%%%%%%%%%%%%%%%%%%%%%%%%%%%%%%%%%%%%%%%%%%%%%%%%%%%%%%%%%%%%%%%
  % code for graph making
                    Date=datetime;Date.Format = 'yyyy_MM_dd__HH_mm_ss';
Date=char(Date);
for j=1:length(x)
    bin_x=round((max(x{:,j})-min(x{:,j}))/binS_x(j),2,'significant');
    Min_x=floor(min(x{:,j})/bin_x);
    Max_x=ceil(max(x{:,j})/bin_x);

    bin_z=round((max(z{:,j})-min(z{:,j}))/binS_z(j),2,'significant');
    Min_z=floor(min(z{:,j})/bin_z);
    Max_z=ceil(max(z{:,j})/bin_z);
    clear c
    c_gs=[];
    yy=[];
    %%Data clustering
    for k=1:Max_z-Min_z
        for i=1:Max_x-Min_x
            clear temp_y
            temp_y=y{j};
        c(i,1)=(Min_x+(i-1))*bin_x;
        c(i,2)=(Min_x+(i))*bin_x;
        c(i,3)=mean(temp_y(x{:,j}>=(Min_x+(i-1))*bin_x  &  x{:,j}<(Min_x+(i))*bin_x
&  z{:,j}>=(Min_z+(k-1))*bin_z  &  z{:,j}<(Min_z+(k))*bin_z,1),'omitnan');
```

```
        c(i,4)=std (temp_y(x{:,j}>=(Min_x+(i-1))*bin_x  &  x{:,j}<(Min_x+(i))*bin_x
&  z{:,j}>=(Min_z+(k-1))*bin_z  &  z{:,j}<(Min_z+(k))*bin_z,1),'omitnan');
        c(i,5)=sum   (~isnan(temp_y(x{:,j}>=(Min_x+(i-1))*bin_x  &
x{:,j}<(Min_x+(i))*bin_x   &  z{:,j}>=(Min_z+(k-1))*bin_z  &
z{:,j}<(Min_z+(k))*bin_z & isnan(x{:,j})==0,1)),   'omitnan');
        c(i,6)=c(i,4)/c(i,5);
            if c(i,5)<n_threshold
                c(i,:)=NaN;
            end
        end
        c_g=c;
        c_gs=[c_gs c];
    end

    X=Min_x*bin_x:bin_x:(Max_x-1)*bin_x;
    Z=Min_z*bin_z:bin_z:(Max_z-1)*bin_z;
    [zz,xx]=meshgrid(Z,X);
    for k=1:Max_z-Min_z
    yy=[yy c_gs(:,3+(k-1)*6)];
    end
    s1=figure
    surf(xx,zz,yy);
    xlabel(xtitle{j})
    ylabel(ztitle{j})
    zlabel(ytitle{j})

        %% Graph making
        grid on
        clear im
        az = 45;
        az_0=az;
        el = 90;
        el_0=el;
        view([az,el])
        degStep = 5;
        detlaT = 0.1;
        f = getframe(gcf);
        [im,map] = rgb2ind(f.cdata,256,'nodither');
        k = 1;

        % tilt down
        for i = el:-degStep:15
          el = i;
          view([az,el]);
          f = getframe(gcf);
          im(:,:,1,k) = rgb2ind(f.cdata,map,'nodither');
          k = k + 1;
        end
        % spin left
        for i = az:-degStep:-120
          az = i;
          view([az,el]);
          f = getframe(gcf);
          im(:,:,1,k) = rgb2ind(f.cdata,map,'nodither');
          k = k + 1;
        end
        % spin right
        for i = az:degStep:90
          az = i;
          view([az,el]);
          f = getframe(gcf);
          im(:,:,1,k) = rgb2ind(f.cdata,map,'nodither');
          k = k + 1;
```

```
        end
        % spin left
        for i = az:-degStep:az_0
          az = i;
          view([az,el]);
          f = getframe(gcf);
          im(:,:,1,k) = rgb2ind(f.cdata,map,'nodither');
          k = k + 1;
        end

        % tilt up to original
        for i = el:degStep:el_0
          el = i;
          view([az,el]);
          f = getframe(gcf);
          im(:,:,1,k) = rgb2ind(f.cdata,map,'nodither');
          k = k + 1;
        end

        %%Saving
    if saving[j]==1
    Title=strrep(ytitle(j)+"_vs_"+xtitle(j)+"_vs_"+ztitle(j)+"_"," ","_");
    savingname=strrep("gif"+j+"_"+Title+Date+".gif","/","_");

savingname_table=strrep("gif"+j+"_"+Title+Date+extractBefore(nametable,40)+'.txt'
,"/","_");
    imwrite(im,map,savingname,'DelayTime',detlaT,'LoopCount',inf)
    writetable(array2table(c_gs),
savingname_table,'WriteRowNames',true,'Delimiter',';');
    end
%     clear Fig
%     close
end
```